UNIVERSITAT DE BARCELONA

Engineering poly (ethylene glycol) diacrylate-based microstructures to develop an *in vitro* model of small intestinal epithelium

Albert Garcia Castaño

Tesi doctoral

ENGINEERING POLY (ETHYLENE GLYCOL) DIACRYLATE-BASED MICROSTRUCTURES TO DEVELOP AN *IN VITRO* MODEL OF SMALL INTESTINAL EPITHELIUM

Memòria presentada per

ALBERT GARCIA CASTAÑO

Per a optar al grau de **Doctor en Biomedicina**

Universitat de Barcelona
Departament d'Enginyeries: Secció d'Electrònica

Programa de doctorat en Biomedicina
2012 – 2016

Tesi doctoral dirigida per
Dr. Elena Martínez Fraiz

Tutor de la tesi
Prof. Josep Samitier Martí

Barcelona, 2017

Index

Abstract

Most of the current *in vitro* cell culture models do not accurately reproduce the physiological behavior of cells *in vivo*. Therefore, they do not represent the functional properties of the corresponding tissues. Increasing evidences support the hypothesis that, by providing cells with a biomimetic cell culture environment, physiological characteristics improve, approaching *in vivo* situation. Such complex tissue-like microenvironments should approach the 3D architecture, biochemical and mechanical properties of *in vivo* tissues. Tissue engineering based approach combined with microfabrication techniques provide unprecedented opportunities to go one step beyond the conventional 2D *in vitro* tissue culture models and reliably reproduce *in vivo* tissue microenvironments.

Epithelial barriers protect the body against physical, chemical, and microbial insults. The small intestinal epithelium is a multicellular tissue with barrier characteristics, these meaning: cell polarization and limited intercellular space for effective barrier function. Functional *in vitro* models of intestinal epithelium have been pursued for a long time. They are key elements in basic research, disease modelling, drug discovery, and tissue replacing and have become prime models for adult stem cell research. In 2D cell cultures, intestinal epithelial cell lines achieve polarization using Transwell® microporous filters. However, this simplified model leads to a poor correlation between *in vitro* and *in vivo* drug absorption tests. *In vivo*, intestinal epithelial cells are organized into crypt-villus units, finger-like protrusions which are key elements in the functionality of the tissue and absent in standard 2D models. Therefore, the development of *in vitro* 3D tissue equivalents accounting for the dimensions, architecture, and cell physiology of the *in vivo* human intestinal tissue still remains a challenge.

Here we describe a simple and cost-effective method to fabricate soft 3D villi-like microstructures with the anatomical architecture and dimensions. We employ poly (ethylene glycol) diacrylated (PEGDA) and acrylic acid that copolymerize and form soft hydrogels upon crosslinking through UV photolithography. Hydrogels are networked materials with high water content, which allow easy diffusion of soluble factors and oxygen. PEG-based hydrogels possess highly tunable chemical and mechanical properties and have become trendy materials to mimic and are the extracellular matrix and tissue basement membranes. To get 3D villi-like microstructures, 2D photomasks were used in a UV light-dependent polymerization process. During this process, several factors,

such as UV exposure time, photoinitiator concentration, and PEGDA molecular weight and concentration, were studied to understand the mechanisms that allow the formation of high aspect ratio soft microstructures. Then, these variables were adjusted to control the microstructure dimensions and to obtain villi-like microstructures resembling the dimensions, biochemical and mechanical properties of villi in native tissues.

To allow cell adhesion and growth, we copolymerized PEGDA with acrylic acid and we took advantage of the exposed carboxylic groups of the acrylic acid to covalently incorporate laminin through the EDC/NHS coupling reaction. We have stablished the ratio between PEGDA and acrylic acid to obtain on the one hand, a successful copolymerization and villi-like structures formation and, on the other a proper protein functionalization of the hydrogel.

Functionalized villi-like microstructured hydrogels have proven suitable for epithelial cell growth. MDCK and Caco-2 cells, two epithelial cell lines have proven to attach, grow and form monolayers of epithelial polarized cells lining the villi-like microstructured hydrogels. Cell polarization was assessed by cell morphology (cell columnar shape and position and orientation of the nuclei) and the expression of polarization markers (villin, ZO-1 and β catenin) at the proper location. Finally, we used Caco-2 cells to validate the functionality of our construct as an *in vitro* model of intestinal epithelium. Caco-2 cells are the standard cells to model the small intestinal barrier. Measurements of the transepithelial resistance (TEER) of Caco-2 cell monolayers formed on the villi-like microstructures showed values closer to *in vivo* situation than those found in Caco-2 monolayers cultured on Transwell® inserts. These results are promising toward the use of our in vitro model in drug absorption and toxicity tests, as well as biological studies and disease modelling.

Glossary

ATR	Attenuated total reflectance
Caco-2	Human epithelial colorectal adenocarcinoma (caco-2) c
EDC	(1-ethyl-3-(3′-dimethylaminopropyl)-carbodiimide
EDTA	ethylenedinitrilo-tetraacetic acid
ECM	Extracellular matrix
FTIR	Fourier transform infrared spectroscopy
GelMA	Methacrylated gelatin
I2959	2 hydroxy-4'-(2-hydroxy-ethoxy)-2-methylpropiophenone
LGR5	Leucine-rich repeat-containing G-protein coupled receptor 5
MDCK	Madin-Darby canine kidney
MeHA	Methacrylated hyaluronic acid
MES	2-(N-morpholino)ethanesulfonic acid
MUC	Mucin
NHS	N Hydroxysuccinimide
PBS	Phosphate buffered saline
PDMS	Polydimethylsiloxane
PEG	Poly (ethylene glycol)
PEGDA	Poly (ethylene glycol) diacrylate
PEGMA	Poly (ethylene glycol) monoacrylate
PI	Photoinitiator
PLA	Poly (lactic acid)
PLGA	Poly (lactic-co- glycolic acid)
PMMA	Poly (methyl methacrylate)
PNIPAm	Poly (N-isopropylacrylamide)
SEM	Scanning electron microscopy
TBO	Toluidine blue O
TEER	Transepithelial electrical resistance
UV	Ultraviolet light
ZO-1	Zonula occludens-1

1 Introduction

1.1 ANATOMY AND BIOLOGY OF SMALL INTESTINE

The small intestine is a long tube, being the largest component of the gastrointestinal tract. Its average length in an adult human is 7 m, varying from 2.7 m to 9.8 m, and it is approximately 2.5–3 cm in diameter.[1] It is the major site where digestion and absorption of nutrients take place. The small intestine is preceded by the stomach, and followed by the large intestine, and it comprises three parts: the duodenum, jejunum and ileum (Fig. 1.1a). To maximize the efficiency of its functions, the inner wall of the small intestine shows highly adapted anatomical features: circular folds (Fig. 1.1a), which contain finger-like projections called villi, and cells that have membrane protrusions called microvilli. These structures increase the total surface area in contact with the lumen (the inside of the tube) up to about 400 m^2.[2,3] The wall of the small intestine is composed of four layers: mucosa, submucosa, *muscularis*, and serosa. The mucosa is the innermost layer and it is in direct contact with the lumen. The submucosa is a dense layer of connective tissue, which irradiates branches of blood vessels, lymphatic vessels, and nerves into the mucosa. The *muscularis* consists of two smooth muscle layers. The outer is a thinner layer that is arranged in longitudinal muscle fibers; the inner is a thicker layer which contains circular muscle fibers. Such muscle layers enable the digested food to be pushed along the small intestine by waves of muscle contractions, called peristalsis. Finally, the serosa consists of several layers of connective tissue which completely surround the small intestinal tub (Fig. 1.1a).[4]

The intestinal mucosa is composed of three layers: epithelium, lamina propria, and *muscularis mucosae*. The epithelial layer is a simple columnar epithelium, which serves as physical and biochemical barrier, permitting metabolic and digestive absorption of nutrients, electrolytes and water, while maintaining a defense against pathogenic agents, and the immune homeostasis.[2,5] Also, it is responsible of the secretion of numerous hormone regulators of digestive function, mucus, and antimicrobial proteins. The mucosa is highly connected to the immune system, and has abundant immune cells underlying the epithelium. The lamina propria is a connective tissue that lies under the epithelium. It contains many blood and lymphatic vessels, which constitute the routes that the absorbed nutrients follow towards other tissues of the body. It also contains the cells of the immune system. The deepest layer of the mucosa is a thin layer of smooth muscle cells (*muscularis mucosae*), which provides movements to ensure that all epithelial cells are fully exposed to the lumen (Fig. 1.1b).

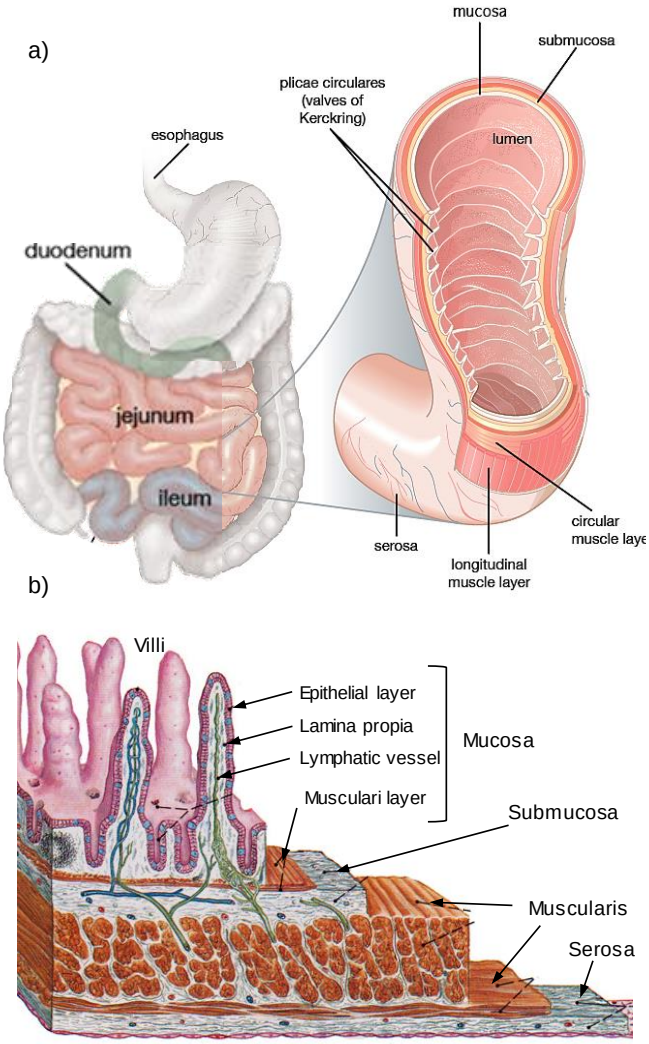

Figure 1.1: a) Drawing of the gastrointestinal tract and anatomy of small intestine (adapted from Encyclopædia Britannica Online).[6] b) Detailed illustration of four layers of small intestinal wall: mucosa, submucosa, *muscularis*, and serosa (http://faculty.southwest.tn.edu).

The small intestinal mucosa is made up of circular folds (*plicae circularis*). These folds have many finger-like projections of the mucosa, known as villi, extending from the luminal surface into de lumen of the small intestine. Villi play an essential role in increasing the surface area for the absorption of nutrients (Fig. 1.2a,b).[4]

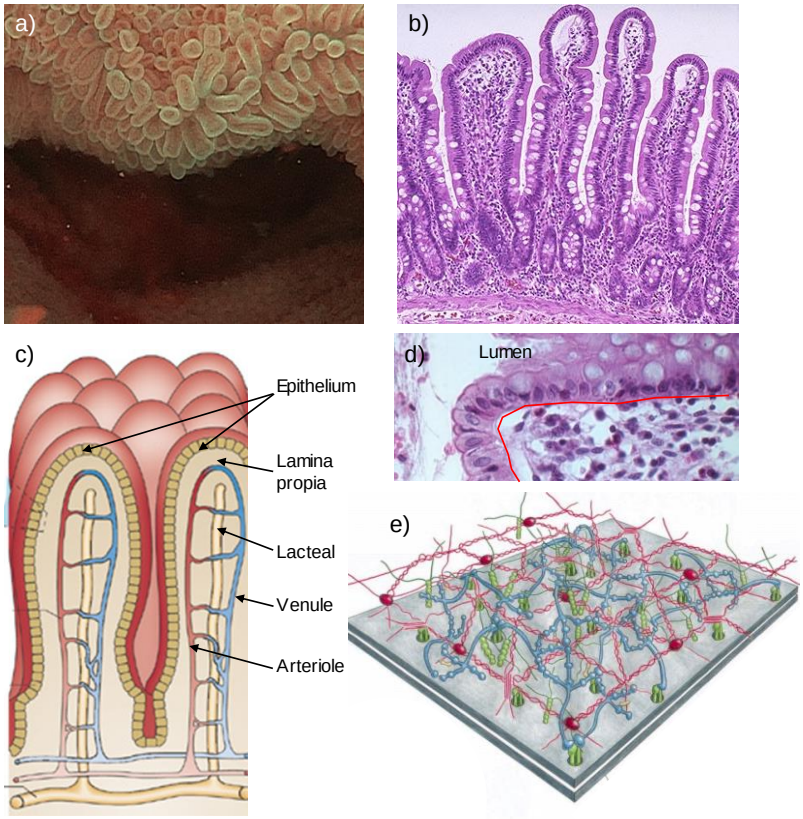

Figure 1.2: a) Terminal ileum in a colonoscopy, where the villi can be easily appreciated covering the surface (https://www.youtube.com/watch?v=SDbjwMS_1vI). b) Longitudinal cross section of small intestinal mucosa with long villi. (library.med.utah.edu). c) Schematics of cross-section of the villi. (adapted from Viswanathan *et al.*).[7] d) Longitudinal cross section of villi highlighting the basement membrane (red line). e) Schematic model of the basement membrane (adapted from Alberts *et al.*)[8]

Villi have dimensions of 0.2–1 mm in height,[4,9] 125 µm in diameter,[9,10] and show a density of 20-40 villi/mm^2.[4,11] Each villus is composed by a core of lamina propria covered by epithelial cells. The lamina propria is composed basically of collagen type I and type III, which form the scaffolding for the villus.[12] Inside the lamina propria there are an arteriole, a venule, a blood capillary network, and a lymphatic capillary or lacteal. The network of capillaries is in charge of taking the amino acids and the glucose produced by digestion and the lymphatic capillary absorbs fatty acids and glycerol, the products of fat digestion, into direct circulation (Fig. 1.2c). Lamina propria forms a loosely packed connective tissue that allows the presence of several cell types such as fibroblasts, and immune system related cells, such as neutrophils, macrophages, dendritic

cells, and lymphoid cells.[13] At the outer part of the lamina propria and underlining the layer of epithelial cells, there is a thin structure (hundreds of nm) called basement membrane. This is a specialized form of extracellular matrix (ECM) that forms stable sheets through self-assembly, which supports and separates the epithelium from the lamina propria (Fig. 1.2d,e). The basement membrane gives structural support and reinforces the epithelium and helps it to resist stretching and tearing. Also, it is important for the anchoring, migration, and differentiation of epithelial cells and influences their behaviour.[14]

Attached on the basement membrane, columnar epithelial cells are arranged in a monolayer. These cells are tightly packed and form a continuous sheet called columnar epithelium (Fig. 1.2c).[8] Once the nutrients are in the small intestine, epithelial cells contain enzymes that help break down them into components small enough to be transported into the bloodstream.[4] The intestinal epithelium layer also acts as a permeable barrier, separating luminal contents from the underlying tissue compartments thanks to strongly joined epithelial cells and avoiding the free entrance of harmful agents.[2]

Besides the absorptive and selective barrier functions of the epithelial cells, intestinal epithelium is the first line of defense to prevent pathogen invasion. The first barrier pathogens encounter is a highly-hydrated mucus layer (700 μm in height) (Fig. 1.3a).[15] Mucus covers the epithelium surface and protects the epithelial cells against chemical, enzymatic or microbial harming.[16] Under the mucus layer, the cells have a dense membrane-anchored matrix (30 – 100 nm), called the glycocalyx (Fig. 1.3b).[17] Main mucus and glycocalyx compounds are the mucins, glycoproteins that are free in the mucus (MUC2) and membrane-bound in the glycocalyx (MUC1, MUC3, MUC17).[18] Bacteria enter into the mucus and can be trapped in their pores, so they are excluded from the epithelial surface (Fig. 1.3a). In addition, small intestinal epithelial cells express innate immune receptors and antimicrobial peptides and they can be activated to produce mediators that recruit, activate and condition cells of the immune system.[19] They also allow colonization for the trillions of commensal bacteria, which are essential for health.[2] Moreover, the epithelium contains T cells (cell-mediated effectors) located at the basement membrane between epithelial cells at a frequency of about 1-2 per 20 epithelial cells.[20] Also, the lamina propria is a part of the immune system and contains lymphocytes (B cells and T cells), dendritic cells, macrophages, eosinophils and mast cells.[21] Because of the majority of immunological processes at the small intestine take place in the mucosa, the lack of epithelial barrier integrity allows the pass of harmful substances, which can lead to inflammation, infection, autoimmune diseases or cancer.[2,22]

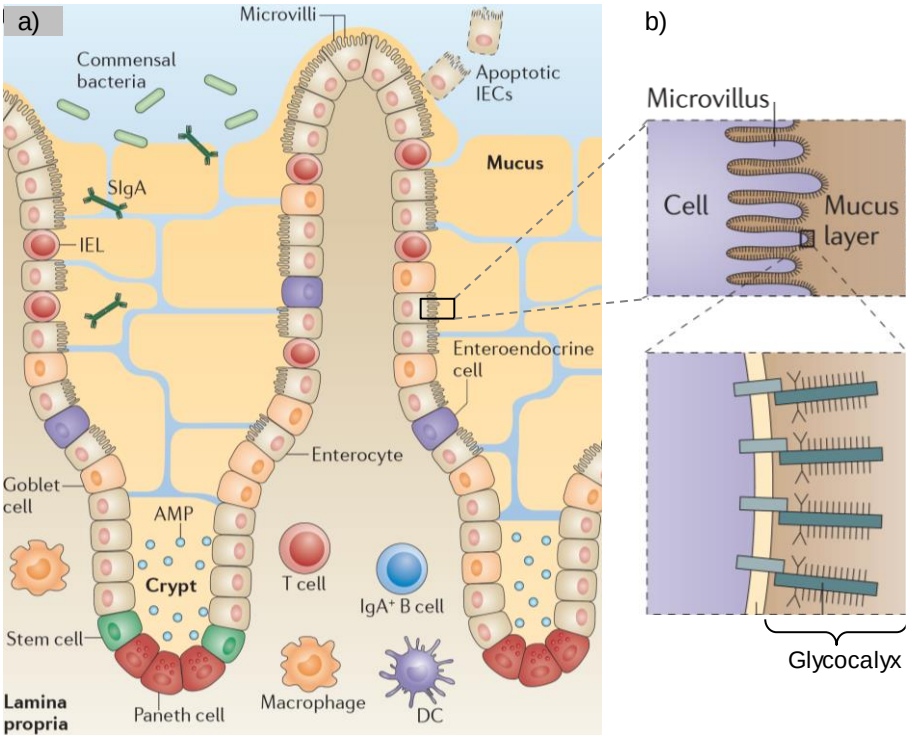

Figure 1.3: a) Schematics of the anatomy of the intestinal mucosa and its immune apparatus. Also, it is detailed the location of mucus and bacteria. Intestinal epithelial cells (IECs), antimicrobial peptides (AMPs), intraepithelial lymphocytes, dendritic cells (DC); secretory immunoglobulin A (SIgA). b) schematic detail of the glycocalyx anchored to epithelial cell membranes (adapted from Mowat *et al.* and McGuckin. et al).[21,23]

The small intestinal epithelium, in adults, is continuously renewed in a turnover of around 2-6 days. Proliferative cells are called intestinal stem cells (ISC) and reside within invaginations at the base of villi known as the crypts of Lieberkühn (Fig. 1.4a). The intestinal stem cells give rise to several types of epithelial cells: absorptive cells (enterocytes), Paneth cells, intestinal globet cells, and enteroendocrine cells. The Paneth cells reside within the stem cell niche at the bottom of the crypt, while the other three types of intestinal epithelial cells migrate toward the tip of the villus (1.4b).[28-31] These architectural crypt-villi unit is relevant in the epithelial cell differentiation, and evidences the biochemical gradients generated along the crypt–villus axis.[26] Intestinal stem cells are located at the bottom of the crypts, where they replicate for continuous self-renewal and are responsible for cell population maintenance,[25,27] generating all lineages of mature intestinal epithelial cells.[28,29]

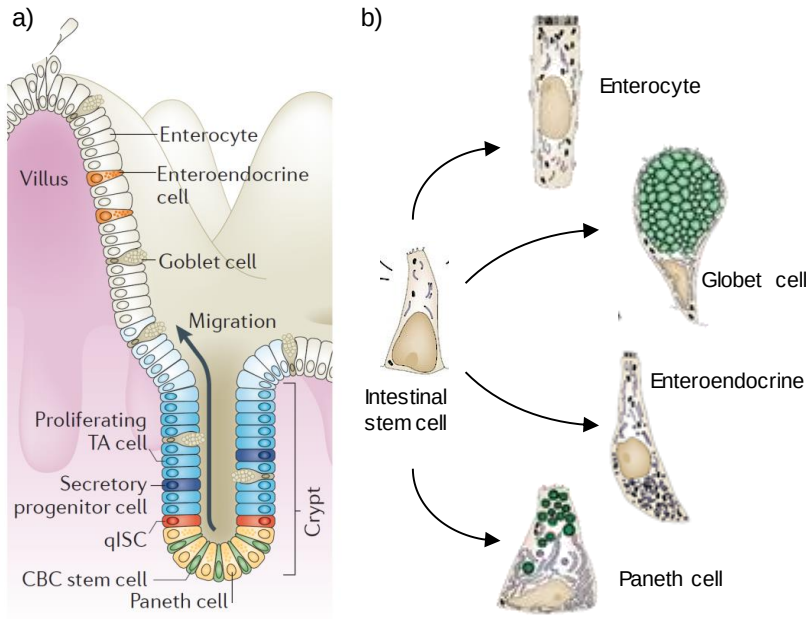

Figure 1.4: The distribution of epithelial cell types in the small intestine epithelium. Intestinal stem cells (ISC) are located near the crypt base and produce transient-amplifying (TA) cells, which proliferate in the mid-crypt and terminally differentiate to produce the different intestinal epithelial cell types. Crypt base columnar (CBC) stem cells are interdigitated with Paneth cells at the crypt base. Quiescent intestinal stem cells (qISCs). (Adapted from Goodell *et al.* and Crósnier *et al.*)[24,25]

Intestinal stem cells can be identified by the expression of leucine-rich repeat-containing G-protein coupled receptor 5 (LGR5 gene).Recent findings in stem cell identification and characterization have made possible to obtain crypt–villus structures and all epithelial cell lineages from culturing single Lgr5+ stem cells *in vitro*.[30,31] Paneth cells are intercalated among the intestinal stem cells and are thought to have a role in regulating host–microbial interactions by the secretion of antibacterial proteins into the lumen, thereby providing protection for the stem cell niche.[32] Goblet cells are balloon-like cells with the nucleus at the base and the rest of the cytoplasm occupied by secretory granules containing mucin, the major component of the mucus.[24] Enteroendocrine cells comprise about 1% of cell population in the intestinal epithelium, produce hormones and peptides in response to various stimuli and release them to initiate digestive actions and protective responses.[24,33]

Enterocytes are the dominant cell lineage (90% of total cells). Enterocytes secrete hydrolytic enzymes to facilitate the efficient breakdown of digested food and the absorption of nutrients. Enterocytes differentiate and migrate up the tip where are shed off the villi in about 4 days.[24,34] Enterocytes are

columnar cells, with a vertically elongated nucleus located just below the center of the cell. They are highly polarized cells, meaning that their upper part, which is called apical side, and it is in contact with the lumen, is separated from their lower part, called basolateral side, which is in contact with the basement membrane (Fig. 1.5a).[35] At the apical domain, enterocytes show a large number of cylindrical projections of the membrane, called microvilli, which increase absorption surface area and contain the enzymes and transporters that are needed for the digestion and absorption. The microvilli are easily identified on bright field or fluorescence microscope as they form a diffused line called the brush border.[8] Each microvillus measures ~1 μm in height (Fig. 1.5b) and it is composed of 20–30 actin filaments and associated proteins such as villin or ezrin. Cell apical membranes exhibit a density of $2 \cdot 10^{10}$ microvilli/cm^2 (Fig. 1.5c). At the basal surface, enterocytes are attached to the basement membrane.

Enterocytes fit close together by tight junctions, adherent junctions and desmosomes and form a continuous monolayer. All epithelial cells express tight junction proteins and form tight junctions with other epithelial cells. Tight junctions are located on the lateral membrane, close to the apical side, and create the closest contact between cells in nature. At these areas cell membranes join and seal the apical and basolateral compartments when epithelial sheets are generated, thus creating a selective permeable barrier (Fig. 1.5d). Tight junctions are composed by transmembrane adhesion proteins such as occludin or claudin that join directly one to another in neighboring cells to occlude the intercellular space. They also have a cytoplasmic plaque of proteins such as the *zonula occludens* (ZO-1) that anchor to the strands to the actin cytoskeleton (Fig. 1.5e).[36]

Enterocytes transport selected nutrients across the epithelium from the lumen into the connective tissue underneath by different mechanisms. Paracellular transport happens across the tight junctions between adjacent epithelial cells. This transport route is characteristic of hydrophilic molecules (Fig. 1.6a).[37] Epithelial cells modulate their tight junctions to permit a flow of solutes and water through spaces between neighboring cells.[8,36] Passive diffusion transports molecules through the cellular membrane driven by a concentration gradient. It is the route for small and lipophilic molecules, such as of oxygen, carbon dioxide and water (Fig. 1.6b).[38] The transcellular transport uses specific transporter proteins of the membrane that bind to the molecule to be transported. Examples include luminal amino acids, iron and glucose (Fig. 1.6c).[39] Finally, endocytosis refers to the uptake of particles or large macromolecules forming a vesicle. This vesicle is transported to the other side of the cell and then released. Examples include the transport of insulin and cholesterol (Fig. 1.6d).[38] Overall, tight junctions help to avoid the free pass of molecules through the space between cells.

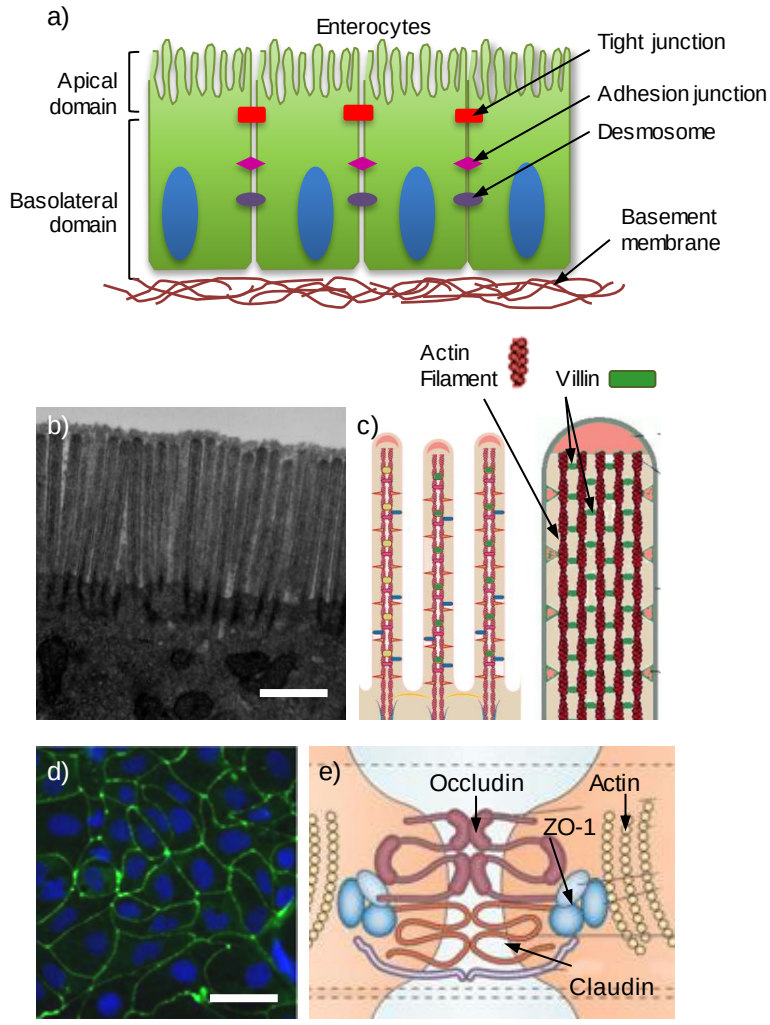

Figure 1.5: a) Schematics of the enterocyte morphology, tight junctions and microvilli. b) Transmission electron microscopy (TEM) image of microvilli (http://remf.dartmouth.edu). Scale bar = 50 nm. c) Detailed drawing of the microvilli (adapted from Delacour *et al.*, and Alberts *et al.*).[8,40] d) Top view of an epithelial monolayer, where ZO-1 is stained in green). e) Tight junction complex, showing the main protein components. ZO, *zona occludens*. Scale bar = 20 µm (adapted from Lozovatsky *et al.*).[41] Schematics of tight junction complex (adapted from Neunlist *et al.*).[42]

Since the integrity of the epithelial barriers determines their functionality, many techniques have been developed to quantify the barrier integrity of epithelial monolayers grown on porous membranes. On the one hand, permeability for small hydrophilic molecules is measured by sucrose or low molecular weight fluorescent dyes. On the other hand, transepithelial electrical

resistance (TEER) is a widely accepted quantitative technique to measure the integrity dynamics of tight junction.[43]

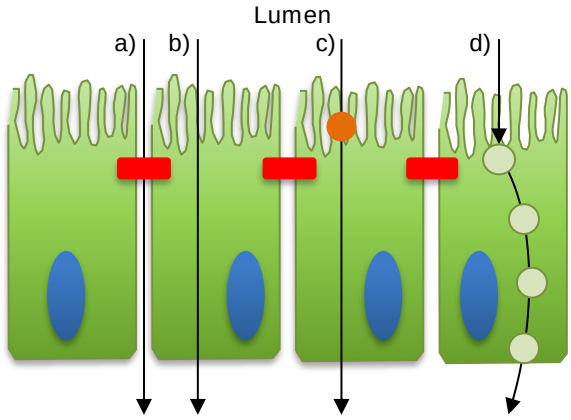

Figure 1.6: Mechanisms of transport across intestinal mucosa. a) Paracellular transport, b) passive diffusion, c) transcellular transport, and d) endocytosis. Tight junctions in red, and active transporter in orange.

1.1.1 SMALL INTESTINE PATHOLOGY

The small intestinal epithelium can be affected by disorders such as infections, lymphomas and tumors, obstructions, food intolerances, and inflammatory diseases. These disorders alter the functionality of the epithelium and its morphology. Alterations of the size and properties of villi produce defects on the epithelium that have detrimental effects on their functions.[44]

Enteric infections interfere in the digestion and absorption of food. They also cause a lot of unpleasant symptoms like diarrhea, bleeding, bloating, nausea, vomiting, abdominal pain, and obstructions. Gastroenteritis is considered as one of the leading causes of illness and death in children under 5 years' age, worldwide, but especially in developing countries. It caused over one million deaths in 2010.[45,46] In most of the enteric infections, the mucosa suffers architectural alterations: villi become shorter and blunt and crypts hypertrophied.[47] This is the case of *Salmonella typhimurium*, as it was found that villus height and surface area decreased and goblet cell density increased significantly after 14 days of infection.[48] Also *Staphylococcus aureus* produce a shortening of villi (20% in height reduction) and the elongation of crypts (35% in depth increasing).[49–51] Other bacteria such as *Bacillus cereus* and enteroaggregative *Escherichia coli* also cause a shortening of villi by the necrosis in the tip.[52–54]

Food intolerances such as celiac disease also have a relevant prevalence, affecting more than 1% of the people in Europe, with an increasing incidence of 15% every year.[55] Celiac disease is essentially sensitivity to gluten, which is a component of wheat. It is believed that there is an immunological response to components of gluten, which results in abnormalities and inflammation of the lining of the small intestine.[56] Villi are shortened or even completely absent because of the rapid loss of epithelial cells from the villus tip (Figure 1.7a).[57,58] As a result, the mucosa becomes "leaky"; water and salts can leak out of the cells into the intestinal lumen and they will be lost though diarrhea.

Crohn's disease is classified as an autoimmune disorder. It causes chronic inflammation of the in the intestinal wall, and results in villus destruction due to a lymphoid aggregation in villi (Fig. 1.7b).[59] Complications of Crohn's disease can include bowel obstructions, inflamed ulcerous tracts, and fistulas. Most Crohn's patients have episodes of disease activity followed by remissions. This stress leads to the anxiety and social withdrawal of more than 12.7 per 100,000 person/year in Europe.[60]

Cancers of the small intestine (adenocarcinomas, carcinoid tumors, lymphoma and sarcoma) are not the most common (0.42% of total cancer cases). However, colorectal cancer is the third most common cancer worldwide and the fourth most common cause of death. 1.4 million new cases and almost 694,000 deaths estimated to have occurred in 2012.[61,62]

Two other diseases that erode villi morphology are lymphangiectasis and amyloidosis. Lymphangiectasis is an abnormality of lymphatic channels which cause edema and diarrhea. When lymphatic channels become blocked, they dilate, break and discharge their contents into the lumen. Characteristic white-tipped villi together with low and round villi with a normal color illustrate this disease (Fig. 1.7c).[63] Amyloidosis is characterized by the deposition of fibrils composed of variety of serum proteins, which form the so called amyloid deposits. Such deposits infiltrate the lining of the intestine interfering cell function and impeding digestion and absorption. Amyloid deposits infiltrated at the tip of villi (Fig. 1.7d), erode their morphology and affect epithelium functions.[64]

The quality of life in patients who suffer enteric infections, food intolerances, Crohn's disease, or intestinal cancers, is severely affected, thus demanding better therapeutics. Pharmacological treatments and palliative cares do not benefit patients or elicit diminishing effect over time.[65] A better understanding of epithelium physiology and pathology is required to improve the treatments, model diseases and investigate in new drug developments. Also, because the loss of the highly specialized intestinal epithelium is associated with high morbidity and mortality,[66] there is a lot interest in tissue engineering and

regenerative medicine applications,[67] specially in the case of the short bowel syndrome, characterized by the loss of more than 70% of the intestinal length.[68] For this purposes predictive models of the small intestinal epithelium are required.[69]

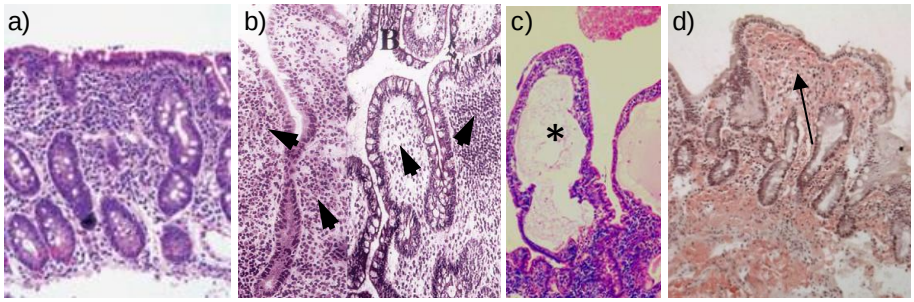

Figure 1.7: Effects of small intestine diseases on villi. a) Celiac disease from several grades (from Gujral *et al.*).[57] b) Lymphoid aggregates in the mucosa from a Crohn's disease patient's ileum. The villus is broader than surrounding classical villi, and the lamina propria is packed with lymphocytes (adapted from Naganuma *et al.*).[59] c) Lymphangiesctasia. Lymphatic channels (*) dilated and anastomosed in the mucosa, containing lined by flat epithelium. Villi are broader and the lamina propria is packed with lymphocytes. (from Omhiya *et al.*).[63] d) Amyloid deposits in villi (arrow) (from global.britannica.com, PEIR Digital Library, and www.healcentral.org)

1.2 *IN VIVO* AND *IN VITRO* MODELS OF SMALL INTESTINE EPITHELIUM

Because oral drug administration remains the most prevalent and used method for drug therapy,[70] the pharmaceutical industry demands models to accurately predict the *in vivo* absorption of a drug. The current small intestinal models can be grouped in *in situ-in vivo*, explants and slices, and *in vitro* models.

1.2.1 *IN SITU-IN VIVO* MODELS

Many intestinal diseases are studied in animal models because of practical and ethical concerns associated with human experimentation, and the need of observing the overall effects of the drug in a living subject. To study intestinal disorders a wide variety of mammalian models are used, from mice to pigs. As mice show similar intestinal development than human intestine, mice-based models are the preferred for Crohn's disease,[71] autoimmune gastritis,[72] intestinal inflammation,[73] intestinal and colorectal cancer,[74,75] celiac disease,[76] and gastroenteritis.[77] Also, animal models are widely used in the study of

intestinal drug transport.[78] For this purpose, intestinal perfusion and pharmacokinetic studies of plasma are usually carried out (Fig. 1.8).[79]

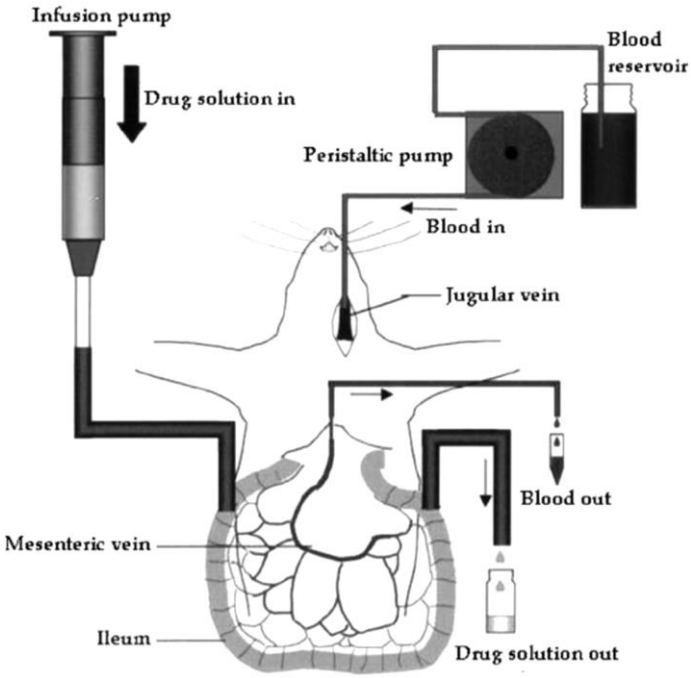

Figure 1.8: Schematic representation of intestinal perfusion and pharmacokinetic studies of plasma (Figure adapted from Singh *et al.*).[80]

Animal models are needed to mimic the extremely complex physiology of the intestinal epithelium and can serve as an important source of *in vivo* information. However, due to their complexity, it is not possible to control and study the independent contributions of the microbiota, intestinal epithelium, and immune system due to their synergic interactions. The small intestine is a complex organ and it is inaccessible to experimental manipulation and observation *in vivo*. In addition, using numerous live animals is expensive and have a lot of ethical concerns. On the other hand, drug efficacy and toxicity must be estimated from *in vivo* clinical pharmacokinetics. Unfortunately, *in vivo* data are usually unavailable at the early stages of drug discovery and development, so *in vitro* models have become invaluable tools at these phases.

1.2.2 EXPLANTS AND INTESTINAL SLICES

As an alternative to animal models, the culture of intact small intestine sections offers the closest scenario to the *in vivo* conditions. This methodology

has the advantages of using the native environment and cell population, and allow manipulation and observation, hindered when the tissue resides in the body. In addition, large surface areas are available, and they preserve the mucus layer. However, the limited diffusion of extracellular molecules into thick tissues restricts the tissue viability, which could be limited from 2 hours to 14 days.[81,82]

The everted gut sac is a technique that consists on preparing the intestinal sac by inverting a segment of the intestine. The segment is turned inside out, resulting in the epithelium with the villi at the outer part (Fig. 1.9a).

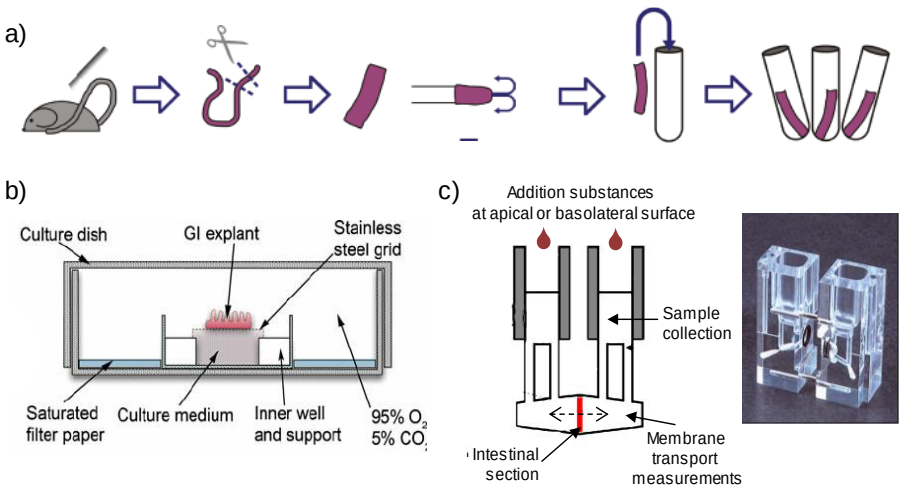

Figure 1.9: Schematic representation of the a) everted explant gut procedure (Figure adapted from Carvalho *et al.*).[83] b) A diagrammatic representation of the intestinal explant culture on air–liquid interface (Figure adapted from Randall *et al.*)[82]. c) Schematic representation of the Ussing chamber. Intestinal sections (red) are mounted between two chambers. The two chambers respectively simulate blood stream and gut lumen. The mounted intestinal mucosa actively pumps molecules from one chamber to the other and the resultant molecular gradient between chambers can be measured. Picture of a market Ussing chamber (www.warneronline.com).

Everted gut sac model is used to study the mechanisms and kinetics of drug absorption.[84,85] Another option are the explants formed by biopsies (3 mm in diameter) that are rapidly placed, mucosal-side up, onto cell culture systems (Fig. 1.9b).[82] The minimal forms of explants are the intestinal slices which are obtained by precision-cut techniques. Intestinal slices (~400 μm thick) are usually prepared by filling rat intestines with liquid agarose following cooling and cutting and they can be cultured *in vitro* for 4 hours.[86,87] This model is widely used to test the transport of molecules, metabolism, and toxicology through the intestinal barrier.[88] Intestinal slices are characterized by the so called Ussing

chambers. Ussing chambers consist of two halves separated by the intestinal section, which is previously opened as flat sheet.

The sample is placed in such a way that the apical membrane is facing one half of the chamber, whereas the basolateral is facing the other half, thus separating the solutions that independently bath each chamber (Fig. 1.9c).[89] They are used to measure the transport of electrolytes, nutrients, and drugs across the intestinal barrier. A miniaturized version of the Ussing chambers is used, together with precision-cut intestinal slices, to predict drug absorption, to monitor drug effects on the function of ion channels, and to measure possible interactions with the absorption of nutrients.[89,90]

1.2.3 *IN VITRO* MODELS OF INTESTINAL EPITHELIA

In vitro culture models are valuable tools for the study of the intestinal barrier, epithelial cell differentiation, intestinal development, intestinal pathologies, toxicity testing, drug development, and regenerative medicine. The most used *in vitro* model of the small intestinal epithelium relies on culturing intestinal epithelial cell monolayers in the so-called Transwell® inserts. A Transwell® insert consist of a permeable porous membrane that separates two compartments in a cell culture well.[91] The upper compartment mimics the environment of the apical cell side, facing the lumen, while the lower compartment mimics the basolateral cell side, facing the basement membrane (Fig. 1.10a). These membranes can contain pores ranging from 0.1 to 12 μm in diameter to ensure appropriate porosity and permeability for medium and cell metabolites.[92,93] They are made of polycarbonate, polystyrene, polyethylene terephthalate (PETF), and cellulose derivatives. In addition, membrane surfaces can be coated by several proteins to enhance cell adhesion, as a mimicking of the basement membrane. The proteins used most frequently are collagen (type I/III or IV), laminin, or Matrigel™, a mixture of ECM proteins that have been extracted from Englebreth-Holm-Swarm tumors in mice. Cells are seeded and cultured on the inserts and form, upon their confluence, a barrier between the two compartments (Fig. 1.10b). This system can be used to quantify the transcellular transport, both the uptake of molecules into the cells from the apical compartment and the efflux of molecules from the cells to the basolateral compartment (Fig. 1.10b). It is also used to determine and monitor transcellular transport changes upon barrier disruptors, and the electrical properties of the cell monolayer such as the transepithelial electrical resistance (TEER) (Fig. 1.10b). Permeability and TEER are both indicators of the integrity of epithelial

barrier, but they determine different parameters and should not be directly compared.[94]

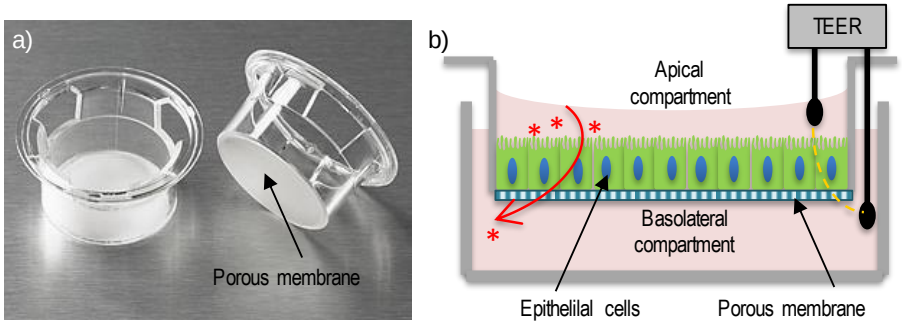

Figure 1.10: a) Transwell® insert of polycarbonate membrane (Corning). b) Schematic illustration of *in vitro* 2D Transwell® assay, a monolayer of epithelial is formed on a porous membrane separating two compartments. This system allows the permeability quantification by using fluorescent dyes, or the electrical properties measurements of the epithelial monolayer.

Transepithelial electrical resistance (TEER) measurement is a widely accepted quantitative method to assess the barrier function and permeability of intestinal epithelial monolayers cultured on permeable membranes.[94] Since the epithelial barriers are characterized by the presence of tight junctions, they are able to specifically regulate the flow of molecules through the paracellular space.[95] Paracellular transport regulates the flow of hydrophilic molecules, including the ions, and TEER is related to the ionic conductance of the paracellular pathway in the epithelial monolayer. For this reason, TEER and the integrity of an epithelial barrier can be directly correlated.

TEER measurements have been carried out for many years using a conventional Voltohmmeter and an electrode pair, called chopstick electrode, which applies a voltage difference (12.5 Hz square-wave AC signal) between both sides the porous membrane. The resulting current (through the cells, on both transcellular and paracellular pathways) is measured, leading to an ohmic resistance. While transcellular resistance is made up by the apical and basal cell membrane, the paracellular resistance comes from the cell-cell contacts and the lateral intercellular space. Due to the high resistance of cell membranes, the current predominantly flows through the paracellular pathway, describing the global resistance of an epithelial monolayer as the resistance associated to their tight junctions (Fig. 1.11).[37] Resistances coming from the medium, the electrode-medium interface, and the semipermeable membrane influence TEER measurements and are removed by measuring the resistance of the system without cell monolayers.

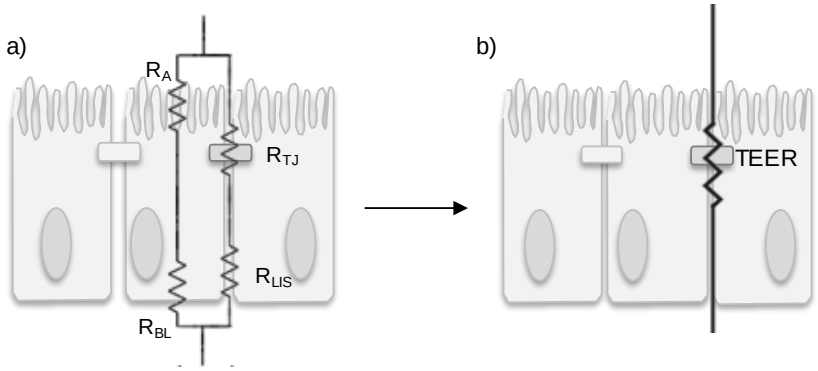

Figure 1.11: a) Scheme of the electrical resistances associated to the intestinal epithelium. Cell membranes resistances, at the apical (R_A) and basal (R_{BL}) location, and the resistance of tight junctions (R_{TJ}) that determines whether the transepithelial resistance is high or low. Theoretically, the lateral intercellular space (R_{LIS}) could contribute a resistance in series with the tight junction, but there is little evidence that this is physiologically significant.[96] b) Scheme of the simplified electrical resistance associated to intestinal epithelium contemplated by conventional Voltohmmeter measurements.

Despite the simplicity of the experimental measurements using Voltohmmeter, measurements depend a lot on the positioning of the chopsticks and the surface of the inserts. Impedance spectroscopy can be used to determine TEER in a more robust manner and to have a more complete picture of the electrical behavior of the system. In impedance spectroscopy the frequency of an applied AC voltage is swept while measuring the amplitude and the phase of the resulting AC current.[43] This methodology measures the complex ratio of voltage to current, and includes contributions from resistive, capacitive, and inductive components of the circuit. It has the advantage of complementing TEER measurements recording the electric capacitance (at 1 -10^5 Hz) of the epithelial cells. Within the considered frequency range, the high resistance of the membrane causes the current to flow across the capacitor and allows ignoring the membrane resistance and summarizing the apical and basolateral membranes in one capacitance (C_{Cl}).[43] Considering this, the electrical circuit diagram can be simplified as shown Figure 1.12a. The typical impedance spectra of epithelial monolayers are characterized by high impedances at mid-range frequencies, related to TEER and capacitance C_{Cl}, and low impedance values at high frequencies related to the impedance of the medium (Fig. 1.12b). Cell capacitance provides additional information about the epithelial barrier properties. For example, the abundance of brush layers, which consist mainly of microvilli, correlates to a larger capacitance, because it increases the surface area of the cell membrane.[97]

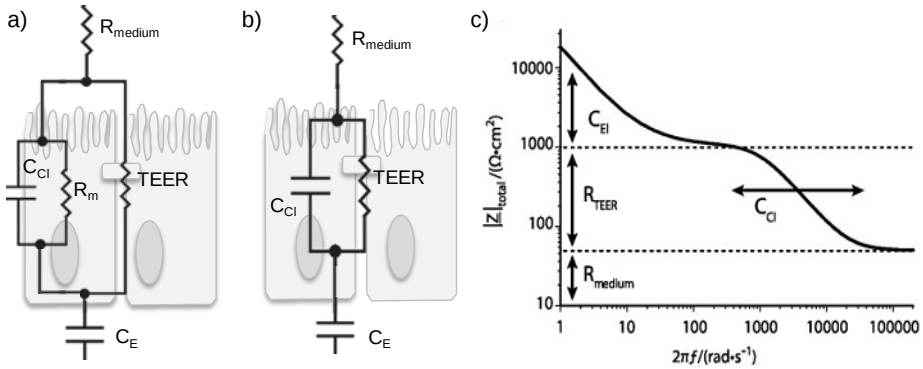

Figure 1.12: a) Diagram of the equivalent circuit describing the contribution of the transcellular and paracellular pathway to the total impedance, of the epithelial monolayer. C_{Cl}, capacitance of the cell layer; R_{medium}, ohmic resistance of the medium; R_m, ohmic resistance of the membranes. Capacitance of electrodes C_E, and ohmic resistance of the medium are also represented. b) Simplified equivalent electrical circuit diagram for an epithelial monolayer. c) Schematic impedance spectrum of a cell monolayer at different frequencies (adapted from Benson *et al.*).[43]

The first attempt of culturing intestinal epithelial cells *in vitro* was done at the 80s, when Qauroni *et al.* cultured cells from rat gut.[98] Nowadays, primary intestinal epithelial cells can be obtained with high purity from intestinal tissue, but cells only survive for short periods of time.[99] However, recent publications have generated stable genetically modified intestinal epithelial cell lines, useful for testing absorption of drug candidates.[100] Alternatively, cell lines derived from colorectal tumor are a proved effective option for developing enterocyte-like cultures. Colorectal tumor derived cell lines, mainly Caco-2, are standardized as preclinical experimental models to study drug transport processes through the intestinal epithelium.

Caco-2 is a human colon adenocarcinoma-derived cell line that is used as a model of the human small intestinal mucosa for the high-throughput screening of drug permeability.[101,70] Caco-2 cells are typically cultured on Transwell® inserts, have a fast proliferation and develop to a confluent differentiated epithelial cell monolayer. This cell line, when differentiates, establishes tight junctions, develop microvilli at the apical membrane, and produces enzymes appearing in normal enterocytes, such as alkaline phosphatase.[102] Caco-2 cells are widely applied for studying intestinal permeability,[103] drug absorption,[104] intestinal metabolism and transporters,[105] and toxicity.[106] Caco-2 cells have shown good correlation and prediction of intestinal permeability of passively absorbed drugs.[107] On the contrary, predictions in the case of drugs that are absorbed by active transporters have shown low accuracy.[104] HT-29 cells show the typical morphology of epithelial cells, but they do not differentiate to

enterocyte-like cells and a large portion of them is made up of goblet-like cells; hence this line produces large amounts of mucin and is used for studying bacterial adhesion.[108] T84 is another cell line from cells of intestinal crypt used for the study of food proteins.[92]

Co-cultures are used to improve the *in vitro* models by adding the diverse cell population of the small intestinal epithelium. To this end, several cell types have been co-cultured on Transwell® inserts, such as Caco-2 and HT29 for the production of a mucus layer.[109] Caco-2, dendritic cells and monocytes have been co-cultured to study immune processes in the inflamed intestinal mucosa.[110,111] In addition, co-culture can be compartmentalized by seeding Caco-2 cells on the upper part of Transwell® and other cell types, such as macrophages[112] or endothelial cells,[113] on the basal compartment. In these systems, immune cells,[114] and pathogenic and non-pathogenic bacteria can be added.[115] On the other hand, Transwell® insert can be modified to improve cell physiology , like Shen *et al.*, who developed a 3D printed insert for hanging culture of Caco-2 cells.[116]

However, colorectal tumor derived cell lines are not derived from small intestinal epithelium and have severe limitations. These limitations are related to their inconsistent expression of transporters and metabolic proteins depending on the culture conditions.[117] In addition, Caco-2 cell monolayers lead to an "artificial" transepithelial electrical resistance (TEER) values greater than 300 $\Omega \cdot cm^2$ compared to the native human small intestine which is 40-90 $\Omega \cdot cm^2$.[118,119] The absence of small intestinal stem cells and other epithelial cell types limits the relevance of the physiology and functionality of these standard *in vitro* models.

Despite many advantages such as easy cell culture and high reproducibility, conventional *in vitro* models lack small intestine 3D structural features, involved in the nutrient absorbance and the epithelium remodeling, and relevant small intestine epithelial cell types such as goblet cells or stems cells. The routinely culture platform used, Transwell®, also lacks the environment complexity and transport activity associated with the native small intestinal tissue. Porous membranes have flat surfaces, not comparable with the characteristic 3D villus-crypt units of the small intestine. Even though many approaches have been adapted to fill the gap between the conventional 2D culture and native intestine, the complexity of *in vivo* is not represented in these models.

To overcome the limitations of the standard Caco-2 models cultured on Transwell® inserts, new trends and emerging strategies have been attempted to model small intestine in complex constructs, using biomaterials and microtechnologies. These new models incorporate the mimicking of the basement membrane, the development of the 3D architecture of the small intestine, and the development of dynamic environments to apply fluid flow and

peristalsis. We will consider the components needed to develop such complex systems in what follows.

1.3 HYDROGEL MATERIALS FOR THE CULTURE OF SMALL INTESTINE EPITHELIAL CELLS

The extracellular matrix (ECM) is a complex 3D fibrous meshwork, with hydrogel-like structure composed of fibers and pores made of a variety of proteins and polysaccharides.[8] Its heterogeneous composition provides cell anchoring support, tissue structure, and directs cell fate.[120] The small intestinal epithelium is anchored to a specialized ECM, the basement membrane. The basement membrane is a thin layer composed of laminin, collagen (predominantly collagen IV), proteoglycans, and other structural and adhesive proteins that create pores of 10 nm in size and small cavities of 1-5 μm in diameter.[14,121,122] The major non-collagenous component, laminin,[123,124] forms a thick and almost continuous line, conformal with the villi architecture, along the walls of the villi.[125] The basement membrane controls the epithelial cell shape, gene expression, adhesion, migration, proliferation, and apoptosis.[126] Thus, an engineered material for the cell culture of the intestinal epithelium should mimic the chemical composition and structure of the basement membrane. To this aim, hydrogels have become the most popular biomaterial.

Hydrogels are composed of hydrophilic polymer chains that form three-dimensional networks upon cross-linking via covalent bonds or via physical attraction, either intramolecular or intermolecular. These hydrophilic polymer networks can absorb high amounts of water (often more than 90%) and swell without dissolving, increasing their volumes in the swollen state (up to 10^3 times, ratio swollen gel volume / dry gel volume).[127] Hydrogels show a wide range of porosities, from less than 100 Å to more than 10 μm.[128] Their porosity facilitates the transport of nutrients and waste.[129] Hydrogels have been widely used for biological applications due to structural similarities to the native ECM (Fig. 1.13).[130–132] Hydrogels can be made using a variety of polymeric materials, which can be of natural or synthetic origin. Natural polymers have as advantages their inherent bioactivity, biocompatibility, and biodegradability. They are usually fabricated from ECM components.

To mimic the basement membrane for epithelial cell cultures the most used proteins are collagen and Matrigel™. Collagen matrices are widely used because of their abundance in the basement membrane.[133] Matrigel™ is a mixture of ECM proteins, mainly laminin, collagen IV and enactin.[134] However, Matrigel™ has limited availability, batch-to-batch variability, pathogen transmission, immunogenicity, technical challenges in handling, and experimental inertness.[135] In addition, other natural-derived materials such as laminin, fibronectin,

hyaluronic acid, and chitosan have been used in intestinal tissue engineering.[136–138] Despite several intestinal cell types, including stem cells, have been successfully cultured on natural hydrogels, it is often difficult to tailor their mechanical, chemical, and degradation properties.

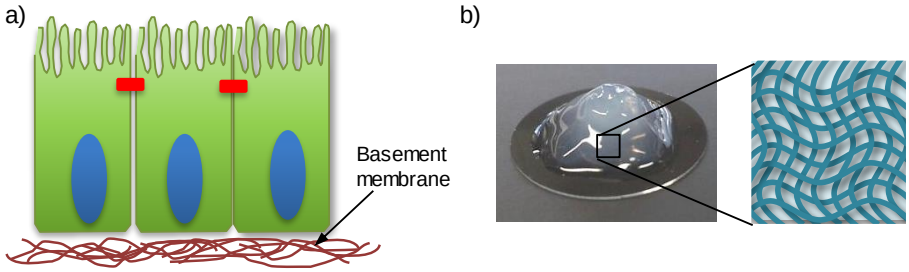

Figure 1.13: a) Schematic representation of an epithelial cell on the basement membrane of heterogeneous fibrillar network. b) Synthetic hydrogel, and an illustration of the polymeric network.

Hydrogels from synthetic polymers are attractive materials because they offer greater control over physicochemical properties, low immunogenicity, minimized batch-to-batch variations and long-term stability. However, most of them often fail to recapitulate essential biological features such as biodegradability or biological recognition.[139,140] These hydrogels are made of monomers or polymers that create a cross-linked network mainly based on poly (ethylene glycol) (PEG), poly (N-isopropylacrylamide) (PNIPAm), poly (2-hydroxyethyl methacrylate) (PHEMA), and poly (vinyl alcohol) (PVA) (Fig. 1.14).[141,142] These materials are usually combined with natural derived materials or cell-adhesive ligands to improve their bioactivity.

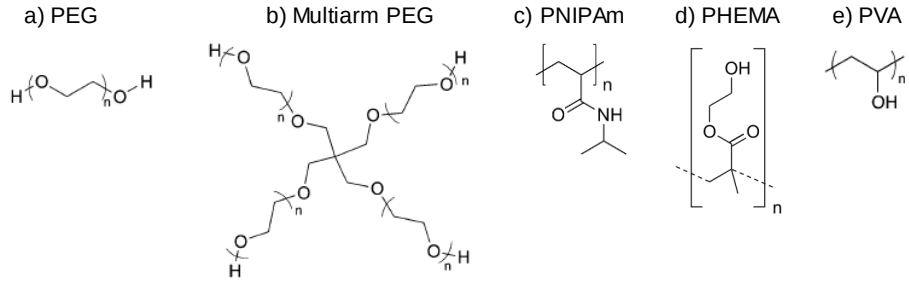

Figure 1.14: Molecular structures of polymer repeat units used for preparing synthetic hydrogels: a) linear poly (ethylene glycol) (PEG), b) four-arm PEG, c) poly (N-isopropylacrylamide) (PNIPAm), d) poly (2-hydroxyethyl methacrylate) (PHEMA), and e) poly (vinyl alcohol) PVA (adapted from Kharkhar *et al.*).[142]

Hydrogel cross-linking strategies are based on chemical (covalent) or physical (non-covalent) interactions among monomer or polymer chains.

Physical cross-links include entangled chains, hydrogen bonding, ionic bonding, hydrophobic interactions and crystallite formation.[142] Even though they are not permanent junctions, they keep the hydrogel from dissolving in aqueous media. Natural-derived hydrogels are typically formed by physical cross-links. For example, Matrigel™ gels with temperature, it forms liquid solutions at low temperatures and gels at room temperature. Gelatin and collagen form liquid solutions at high temperatures and gel at low temperatures. Polysaccharides, such as alginate, form gels in the presence of Ca^{2+}.

Chemical cross-links, on the other hand, are permanent junctions formed by covalent bonds. One common way to create a covalently cross-linked network is using chain or step growth polymerization mechanisms, in which end-functionalized mono/macromers react to form oligomers and long chain polymers.[143] For example, click reactions are a class of reactions to covalently link two reactants in a straightforward, modular and high-yielding manner, which have become popular for synthesizing hydrogels. They use highly reactive functional pairs such as thiol-vinyl, thiol-maleimide, and azide-alkyne. One attractive feature of this type of cross-linking mechanism is that it does not require any additional components, such as an initiator, but the gelation rates are typically slow.[142,144] By free radical polymerization, polymers modified with one or more vinyl groups react, in the presence of a photoinitiator and suitable light wavelength, to create high-molecular-weight chains that are covalently cross-linked in the network. Radical chain polymerizations are fast, and happen at time scales from seconds to several minutes.[145]

1.3.1 NETWORK STRUCTURE OF HYDROGELS

The chemical properties of the repeating units, monomers (or macromers), and the method of cross-linking determine the three-dimensional structure of hydrogels.[132] Many of their properties, including the equilibrium water content, compressive modulus, and diffusivity depend on the hydrogel cross-linking density (ρ_x), which refers to the number of chains in a given volume of hydrogel. Cross-linking density determines important parameters used to define the network structure of hydrogels: the swelling ratio (Q), the polymer volume fraction in the swollen state ($\upsilon_{2,s}$), the average (or effective) molecular weight between cross-links (M_c), and the network mesh size (ξ). The swelling ratio is the ratio between the volumes of water-swollen hydrogel to dry volume and it affects the mechanical properties of the hydrogel. The polymer volume fraction in the swollen state describes the amount of liquid than can be imbibed in the hydrogel. The mesh size dictates the diffusivity of molecules through the

network.[131] For their characterization, hydrogel networks are usually considered an "ideal" collection of chains between junction points (cross-links), but in reality these networks contain defects such as loops, physical junctions, entanglements, and dangling ends (Fig. 1.15).[146,147]

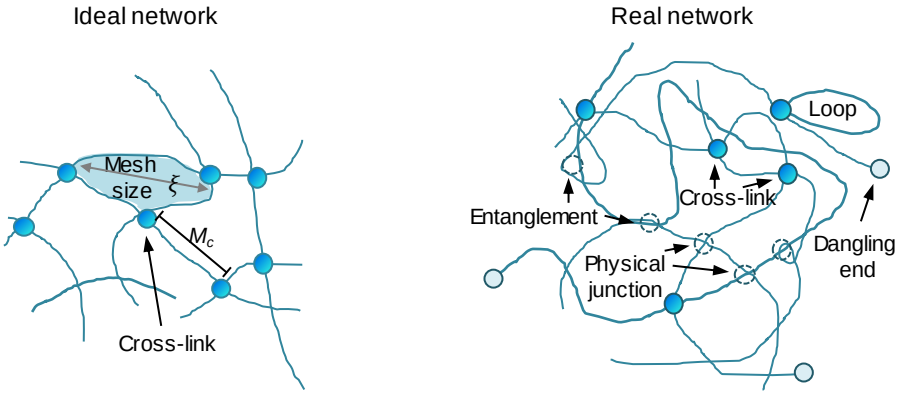

Figure 1.15: Ideal and real network structure of hydrogel showing cross-links (blue circles), mesh size (ξ) and molecular weight between cross-links (Mc), physical junctions, entanglements, loops, and dangling ends.

Hydrogel swelling parameters can be determined using the equilibrium swelling theory proposed by Flory-Rehner.[148] The Flory-Rehner equation is typically employed to relate the hydrogel swelling ratio, which is the inverse of the polymer volume fraction, to its cross-linking density. Hydrogels can be assumed as highly swollen systems (Q > 10), and neglecting polymer chain ends, the Flory-Rehner equation simplifies to:

$$Q = \rho_x^{-3/5}\left[\frac{1/2 - 2\chi_1}{V_1}\right]^{3/5} \qquad \text{Eq. 1}$$

where V_1 is the molar volume of the solvent and χ_1 represents the interaction between the polymer and the solvent. Finally, the mesh size can be estimated following equation:

$$\xi = v_{2,s}^{(-1/3)}\ \frac{2M_cC_n}{M_r}l \qquad \text{Eq. 2}$$

where M_r is the molecular weight of the monomer, C_n is the Flory characteristic ratio and l the length of the bond along the polymer backbone. Mesh size at the equilibrium swelling dictates the diffusivity of molecules through the network,

and can be compared to the hydrodynamic radius of a molecule to determine whether diffusion would take place (Eq. 3)

$$\frac{D_g}{D_0} = \left(1 - \frac{r_s}{\xi}\right) \qquad \text{Eq. 3}$$

D_g is the solute diffusivity in the hydrogel swollen state, D_0 is the unhindered solute diffusivity in the swelling solvent, and r_s is the radius of the solute.[149]

1.3.2 POLY (ETHYLENE GLYCOL) (PEG) -BASED HYDROGELS

Poly (ethylene glycol) (PEG) is one of the most popular synthetic materials used in biomedical applications, tissue regeneration, cell culture, tissue models for wound healing, and cancer drug delivery.[150,151] Because of its high hydrophilicity, bioinert structure, lack of toxic or immunogenic response, low cost, and water solubility is suitable for cell culture applications. In addition, it has been approved by the food and drug administration (FDA). Also, PEG-based hydrogels provide adjustable mechanical properties as their elastic modulus can be tuned over a broad range of values to mimic the moduli of soft tissues (e.g., E ~ 5 kPa to E ~ 900 kPa).[152] However, PEG-based hydrogels have no bioactive sites for cells interaction, so they do not support cell adhesion and proliferation. It is common to incorporate cell adhesive peptides to make them bioactive.[139]

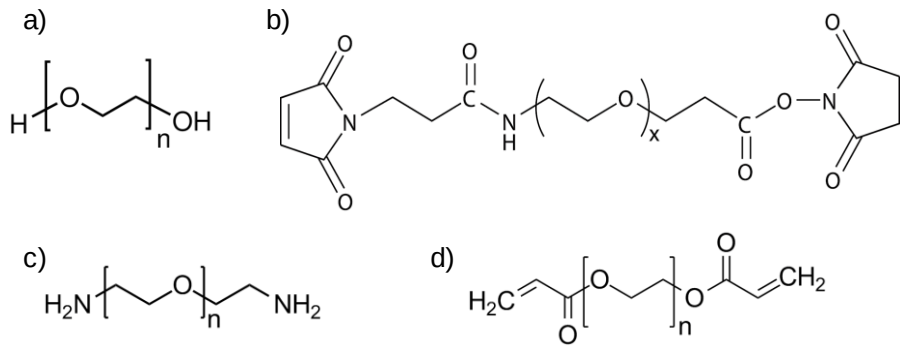

Figure 1.16: a) Poly (ethylene glycol), b) poly (ethylene glycol) dimaleimide, c) poly (ethylene glycol) diamine, and d) poly (ethylene glycol) diacrylate.

PEG macromers are often chemically modified to support cross-linking mechanisms. These modified macromers are commercially available or can be prepared in house.

It is common the modification of the hydroxyl end groups by, maleimide, thiol, amide, azide, sulfovinyl, or acrylate groups that can be cross-linked by click reactions or free radical polymerization (Fig. 1.16).[153] In addition, cell adhesive molecules can be PEGylated to be anchored in these systems.[154]

Also, interpenetrating networks of gelatin methacrylate and hyaluronic acid methacrylate polymerized with polyethylene glycol have been reported to improve PEG cell adhesion properties. All these engineered PEG hydrogels have demonstrated to support cell functions such as adhesion, migration, proliferation, and the regulation of stem cell fate.[155–157] In addition, basement membrane-mimetic PEG hydrogels have been developed to replicate basement membrane topography,[158] the vascular basement membrane to study the neutrophil extravasation,[159] to provide a basement membrane model of the alveolar-capillary barrier,[160] to study the epithelial morphogenesis,[161] and as intestinal basement membranes to assess organoid growth.[162]

1.4 FREE-RADICAL PHOTOPOLYMERIZATION OF PEGDA

The most common method of cross-linking to form PEG-based hydrogels is based on the use of PEG-acrylates, especially PEG-diacrylate (PEGDA) through UV initiated free radical photopolymerization. This reaction has as main advantage mild reaction conditions. In addition, it provides temporal and spatial control over the hydrogel formation. Free radical photopolymerization initiates without the need for high temperatures or extreme pH conditions and in a non-purged environment.[163] Also, in contrast to click reactions that are spontaneous, photopolymerization can be controlled over time.

Free radical polymerization forms polymers by the addition of free radical building blocks (Fig. 1.17).[164] UV-initiated free radical polymerization is described by three reaction steps: initiation, propagation, and termination (Table 1.1). It is initiated by the combination of irradiation with the appropriate wavelength (usually UV) and the presence of a photoinitiator (PI). The photoinitiator absorbs energy and decomposes with an efficiency f and rate constant k_d into two reactive free radicals (R*) with unpaired electrons. Acrylate groups of the monomers (M) are sensitive to free radicals and unpaired electron swipe carbon-carbon double bond (-C=C-) creating a new free radical monomer (RM*). The constant rate for chain initiation is k_i. Free radical monomers propagate the reaction at a rate k_p, creating polymer chains (P_m). These chains have an unpaired electron and can again serve as free radicals. The last step is the termination, which occurs when two unpaired electrons find each other creating stable polymer chains as a rate k_t. This reaction is inhibited in the presence of

oxygen because it captures the radical species formed from the PI, forming peroxides and avoiding polymer polymerization. Oxygen reacts with radicals under the rate constant k_{O_2}.

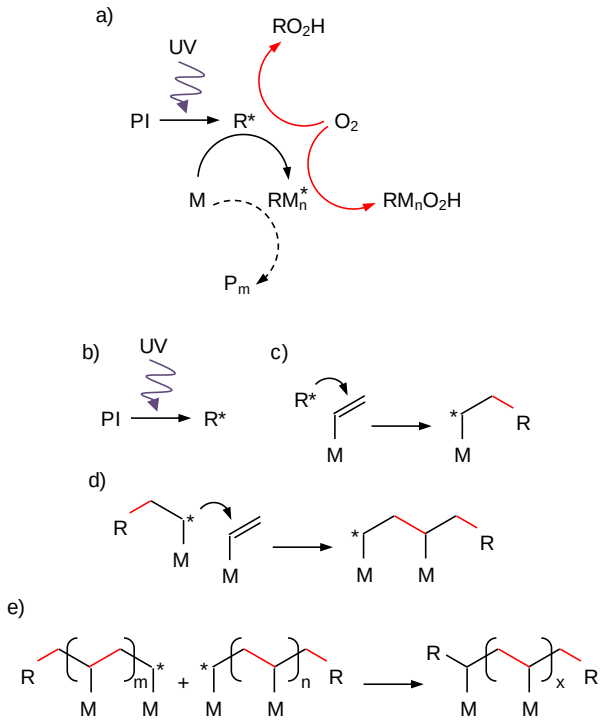

Figure 1.17: a) Schematics of free radical polymerization reaction (black) and oxygen inhibiting mechanism (red). Radicals (R*) are generated from photoinitiator molecules (PI) by the UV light. Acrylate monomers (M), react with radicals in free radical monomers (RM*), which create polymer chains (P_m). Oxygen (O_2), reacts with radicals creating peroxide molecules (RO_2H, RM_nO_2H). M is the acrylate monomer, and red line represents the new formed bonds.

Description	Reaction
Initiation:	
Decomposition	$PI \xrightarrow{k_d} 2fR^*$
Chain initiation	$R^* + M \xrightarrow{k_i} RM^*$
Propagation	$RM_n^* + M \xrightarrow{k_p} RM_{n+1}^*$
Termination:	$RM_n^* + RM_m^* \xrightarrow{k_{tc}} P_{n+m}$

Oxygen inhibition	$R^* + O_2 \xrightarrow{k_{O_2}} RO_2H$

Table 1.1: Kinetics and reaction steps in free radical photopolymerization. Photoinitiator (PI), radicals from photoinitiator (R*), photoinitiator efficiency (f), acrylate monomers (M), free radical monomers (RM*), polymer (P_n), oxygen (O_2), peroxide molecules (RO_2H, RM_nO_2H).[165]

The photoinitiator decomposition k_d depends on its quantum yield (ϕ) (ratio of molecules decomposed to the number of photons absorbed), molar attenuation coefficient (ε) (or molar absorptivity, ability of a chemical species to attenuate light at a given wavelength), the intensity of the light absorbed (I) at given wavelength (λ), Avogadro's number (N_A), Planck's constant (h) and the speed of light (c) (Eq. 4).

$$k_d = \frac{\phi(2.303\varepsilon)I\lambda}{N_{AV}hc} \qquad \text{Eq. 4}$$

The dynamic concentration of all the species in a well-mixed bulk reaction volume can be defined by a set of differential equations::[166]

$$-\frac{dPI}{dt} = k_d[PI] \qquad \text{Eq. 5}$$

$$\frac{d[R^*]}{dt} = 2k_d f[PI] - k_p[R^*][M] - 2k_t[R^*][RM^*] - 2k_t[R^*]^2 - k_{O_2}[R^*][O_2] \qquad \text{Eq. 6}$$

$$\frac{d[M]}{dt} = -k_p[R^*][M] - k_p[R^*][RM^*] \qquad \text{Eq. 7}$$

$$\frac{d[RM^*]}{dt} = k_p[R^*][M] - 2k_t[RM^*]^2 - 2k_t[R^*][RM^*] - k_{O_2}[RM^*][O_2] \qquad \text{Eq. 8}$$

$$\frac{d[P]}{dt} = 2k_t[RM^*]^2 + 2k_t[R^*][RM^*] + k_{O_2}[RM^*][O_2] \qquad \text{Eq. 9}$$

$$\frac{d[O_2]}{dt} = -k_{O_2}[RM^*][O_2] - k_{O_2}[R^*][O_2] \qquad \text{Eq. 10}$$

Combining these equations the rate of polymerization R_p can be estimated by:[165]

$$R_p = k_p[M]\sqrt{\frac{2fk_d[PI]}{k_t}} \qquad \text{Eq. 11}$$

Polymerization can be computed as the total fraction monomer conversion (p) given by equation 12, where $[M]_0$ is the initial concentration of the monomer:

$$p = \frac{[M]_0 - [M]}{[M]_0} \qquad \text{Eq. 12}$$

To determine fraction monomer conversion, the concentration of monomer as a function of time has to be computed. Because of polymerization (Eq. 11), monomer concentration will disappear over time, therefore:[167]

$$\frac{d[M]}{dt} = R_p = -k_p[M]\sqrt{\frac{2fk_d[PI]}{k_t}} \qquad \text{Eq. 13}$$

The concentration of photoinitiator also depends on the time and can be obtained from integrating equation 5, considering the initial concentration $[PI]_0$. By this, equation 15 is obtained.

$$[PI] = [PI]_0\, e^{-k_d t} \qquad \text{Eq. 14}$$

$$\frac{d[M]}{dt} = -k_p\,[M]\sqrt{\frac{2k_d f[PI]_0}{k_t}}e^{-\frac{k_d}{2}t} \qquad \text{Eq. 15}$$

By integrating equation 15, isolating (Eq. 16) and substituting in equation 12 the fractional monomer conversion as a function of time can be computed as:[167]

$$\ln\left(\frac{[M]}{[M]_0}\right) = \left(\frac{8k_p^2 f[PI]_0}{k_d k_t}\right)^{\frac{1}{2}}\left[e^{\left(-\frac{k_d t}{2}\right)} - 1\right] \qquad \text{Eq. 16}$$

$$[M] = [M]_0 e^{\left(\frac{8k_p^2 f[PI]_0}{k_d k_t}\right)^{\frac{1}{2}}\left[e^{\left(-\frac{k_d t}{2}\right)}-1\right]} \qquad \text{Eq. 17}$$

$$p = 1 - e^{\left(\frac{8k_p^2 f[PI]_0}{k_d k_t}\right)^{\frac{1}{2}}\left[e^{\left(-\frac{k_d t}{2}\right)}-1\right]} \qquad \text{Eq. 18}$$

By looking at this equation is evidenced that free radical photopolymerization is controlled through photoinitiator-related parameters such as its concentration, and through the intensity of light (energy dosage) and the propagation and termination rate constants. In addition, oxygen plays a key role because it diminishes the number of radical species that drive the

polymerization, inhibiting the reaction. To take profit of free radical polymerization, terminal hydroxyl groups of the PEG can be substituted by acrylates to from PEG-diacrylate (PEGDA). PEGDA is the type of macromer most used for photopolymerization. By free-radical polymerization, PEGDA repeating units, often called monomers even if they are actually macromers, cross-link to form long branched chains and cross-linked networks (hydrogels). This contrasts with poly (ethylene glycol) monoacrylate (PEGMA), which creates linear chains resulting in a soluble polymer network, because PEGDA monomers are bifunctional and PEGMA are monofunctinal.[166,168] PEGDA hydrogels are highly tunable, by varying their molecular weight or polymer concentration the mechanical properties can be controlled.[169]

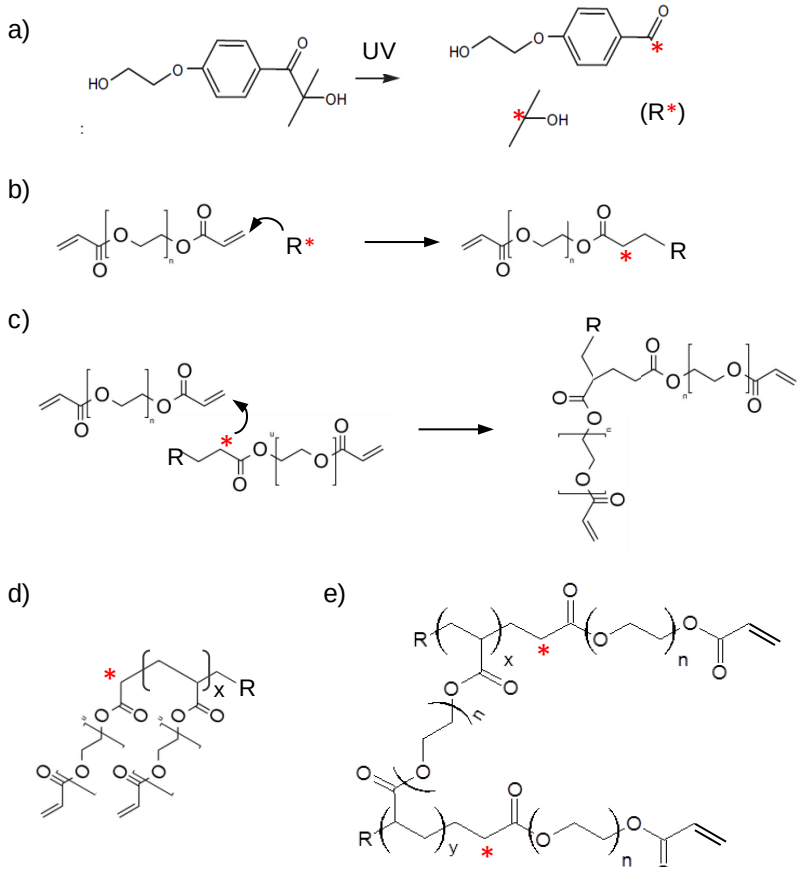

Figure 1.18: Scheme of free-radical polymerization of PEGDA by the activation of I2959. a) Cleavage of I2959 into radicals (R*), b) initiation of polymerization by the radicalization of monomers. c) Propagation of the polymerization in d) linear chains or e) branched chains. Red dots relate to unpaired electrons, x and y relate to the size of the poly(acrylate) domains, and n relates to the size of the PEG domains.

For biomedical applications, PEGDA hydrogels are usually fabricated using 2-hydroxy-4'-(2-hydroxyethoxy)-2-methylpropiophenone, known as I2959 (Ciba® IRGACURE® 2959, Switzerland) as photoinitiator. Figure 1.18 shows the free-radical photopolymerization reaction described in Figure 1.17 adapted to the PEGDA free-radical polymerization in presence of I2959.

PEGDA and I2959 have been used in mimicking many tissues, such as the cornea,[170] bone,[171] cartilage,[172] or hair follicle.[173] It is a water soluble photoinitiator with a limited solubility (~1% w/v)[174] and it possesses a high molar absorption at UV medium-wavelengths (200 – 320 nm). However, its molar absorptivity spectrum (Fig. 1.19) limits the generation of radicals at wavelengths up to 370 nm, with a value of 4 M^{-1} cm^{-1} at 365 nm.[175] At wavelengths below 350 nm, cellular encapsulation is precluded because of its phototoxic and mutagenic characteristics.[176]

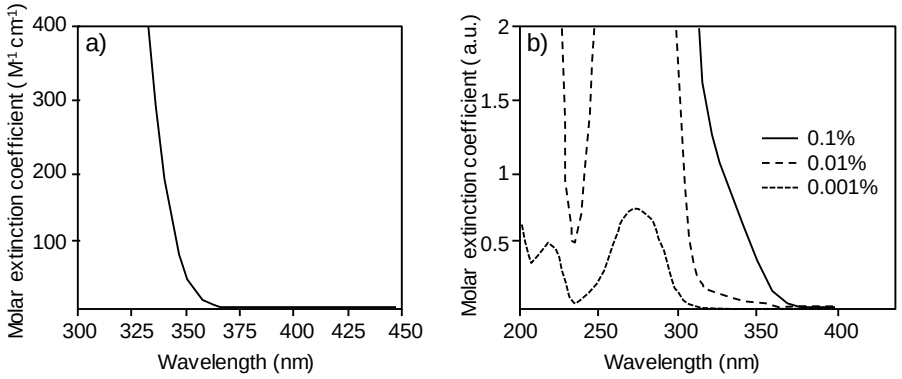

Figure 1.19: (a) Molar absorptivity of I2959.[177] (b) Molar absorptivity at different I2959 concentrations. Absorption spectrum of Ciba® IRGACURE® 2959 as % in acetonitrile.[178]

1.5 MICROSTRUCTURING OF HYDROGELS

Hydrogels are usually fabricated and used as films or bulk structures. Some cell engineering applications require the miniaturization of hydrogel structures and the fine tuning of their architecture. Considering the small intestinal epithelium, the crypt-villi architecture has proved to be relevant in the physiology of this tissue. Thus, this three-dimensionality has to be considered when fabricating a biomimetic hydrogel. Several methods are employed to microstructure hydrogels and reviews classify them in micromolding, microfluidics, stereolithography, 3D bioprinting, and photolithography.[179–181]

The functionality of many tissues is related to their 3D architecture, such as the spongy part and the canaliculus of bone tissue, the palisades of the corneal

limbus, the compartmentalized hair follicle, and the crypt-villi unit. For all of them, relevant geometrical features are in the range of tens to hundreds of micrometers. So, microstructuring techniques must work within this range. Traditional microfabrication techniques have been extensively used and optimized for hard materials,[182] but the implementation of these methodologies for soft materials impose specific challenges. The main specific care is the manipulation, because hydrogels are very soft, and can easily break. Many hydrogels are sticky, which could also restrict the use of molds.

1.5.1 MICROMOLDING

Micromolding is an extensively used technique based on the use of hard templates or molds from which the microstructure is transferred to another material. These molds are usually fabricated by photolithography, soft lithography (a technique used for replicating structures using elastomeric molds), etching or laser ablation.[183,184] Molds from polydimethylsiloxane (PDMS), poly(methyl methacrylate) (PMMA), polyurethanes, polyimines, or Teflon have been employed as templates to produce hydrogels with topographic features.[170,173,185–187] One of the preferred materials used in micromolding is PDMS due to its inertness, optical transparency and flexibility.[188] A variety of hydrogel shapes, morphologies and sizes can be precisely fabricated on a template, ranging from less than 1 μm to larger than 500 μm.[189,190] Polymeric solutions are placed on the mold, and after cross-linking, hydrogels replicate the shape of the template, being a negative of the original mold (Fig. 1.20). In micromolding, hydrogels are cross-linked by temperature such as agarose, or light, such as PEGDA, gelatin methacrylate or hyaluronic acid methacrylate.[190–193]

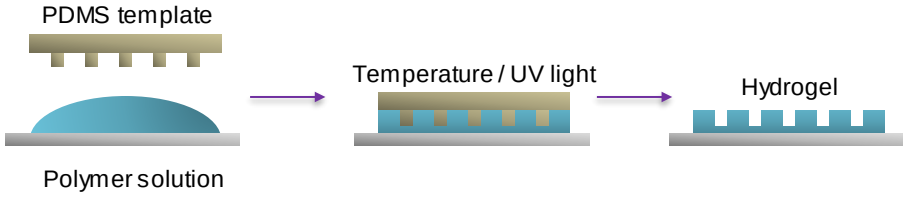

Figure 1.20: Schematic presentation of hydrogel micromolding using a PDMS template.

The main problem when using molding with hydrogels is demolding, as they might be sticky or very soft, so microstructures can be deformed or broken. To overcome this restriction, molds can be coated with other polymers, or anti-sticking layers. PNIPAAm is a temperature responsive polymer that has been used as a coating for PDMS molds to demold agarose hydrogel microstructures.[194]

An alternative option, useful for high aspect-ratio microstructures, it is proposed the use of intermediate molds made of soluble materials such as gelatin,[195] poly L-lactic acid,[196] agarose,[197] or PNIPAAm.[198] These intermediate molds are used as sacrificial layers and are destroyed to demold the hydrogel of interest.

Micromolding is usually costly affordable and allows obtaining large-surface areas with microstructures but with soft materials sometimes require several demolding steps to create complex architectures.

1.5.2 3D BIOPRINTING

3D bioprinting is a rapid-prototyping method to create three-dimensional architectures with high precision due to the accurate deposition of wide range of materials to a desired location.[199–201] In addition, it allows the printing of multiple cell types previously diluted in the polymer solution. 3D bioprinting can be performed by inkjet bioprinting, microextrusion bioprinting, and laser-assisted bioprinting.[179]

Hydrogels can be made by inkjet bioprinters (Fig. 1.21a), which consist on a syringe that ejects the polymer solution on a surface where a cross-linking method is applied.

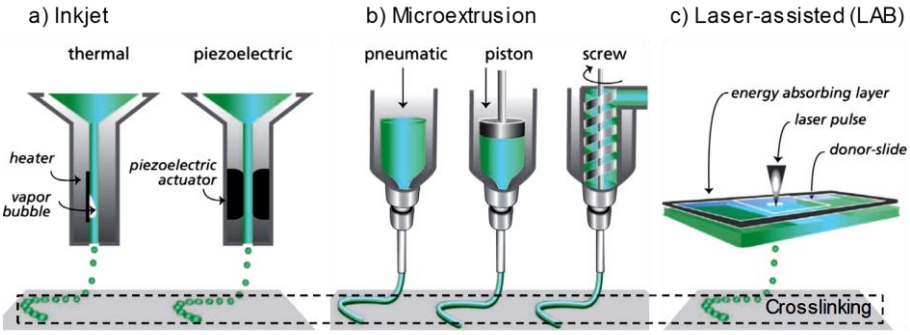

Figure 1.21: Schematic illustration of the 3D bioprinting approaches. a) Inkjet, b) microextrusion, and c) laser-assisted bioprinting. Polymer solutions cross-link once they reach the substrate. (adapted from Malda *et al.*)[202]

Depending on cross-linking method (temperature or UV light) different materials can be fabricated such as PEG-based polymers,[203] gelatin, alginate and hyaluronic acid.[204,205] This technology reaches resolutions of 50 µm – 1 mm and is able to work at high speed.[206] For temperature-based cross-linking, the time for hydrogel forming has to be reduced. Additional issues related to the technique are clogging of the needle and formation of bubbles. Microextrusion bioprinting uses a piston-dispenser to deposit the material (Fig. 1.21b). Hydrogels cross-link

after their deposition, by ionic cross-linking such as alginate, thermal cross-linking such as agarose, or photocross-linking such as PEGDA and GelMA.[201,207] Again, clogging of the nozzles and their size limit its resolution to 5 μm – 1 mm.

	3D bioprinting technique		
	Inkjet-based	Extrusion	Laser-assisted
Resolution/droplet size	50 μm–1 mm	5 μm–1 mm	>10 μm
Material viscosity/density	Low	High	Low–High
Printing speed	Fast	Slow	Medium-fast

Table 1.2: Characteristics of inkjet, microextrusion, and laser-assisted technologies. [208]

Laser assisted bioprinting does not use nozzles and can achieve high resolution, less than 10 μm.[209] This technique uses focused laser beam pulses on the absorbing layer of a ribbon, which is covered by a layer of pre-hydrogel material, to generate a high-pressure bubble that propels the material toward the collector substrate, where it gelifies (Fig. 1.21c). The most commonly used hydrogels are alginate and collagen.[208,210,211] Comparative considerations between 3D bioprinting techniques are listed in Table 1.2.

1.5.3 MICROFLUIDICS

Microfluidics is a technology that aims the manipulation of fluids at the submillimeter scale using a microscale devices built with microtechnologies. Microfluidics offers the ability to work with small reagent volumes, confers miniaturization, and can be used to perform experiments not possible at the macroscale. Microfluidics relies on fluid handling using laminar flow, as the small dimension of the channels usually hampers turbulent regime.

Devices containing microfluidic channels are usually made of PDMS.[212] This technology has been applied for the fabrication of building-blocks and microfiber hydrogels with a very good control of the size and shape of the fabricated structures. These precise dimensions are mainly controlled by the fluid flow rate. The simplest methodology is the fabrication of hydrogel microspheres by emulsion. These microspheres can be made of PEGDA, agarose, and alginate.[213] For the fabrication of more complex architectures, these microspheres are assembled in 3D hydrogel structures at the millimeter scale.[214] A particular application of microfluidics for hydrogel microstructuring is the development of complex microfiber networks.[215] These microfibers fabricated from various polymers such as alginate, collagen, PEGDA, and PLGA due to their rapid cross-linking.[179,216–219] Microfluidics can be combined with photopolymerization in the

so-called flow lithography process, to fabricate large numbers of hydrogel microparticles. These methodology requires the use of photocross-linkable materials such as PEGDA, gelatin methacrylate or methacrylated hyaluronic acid.[220] In addition, microfluidics have allowed the development of specific devices that mimic highly controlled environments for cell culture, the so-called lab on chip devices. The application of these devices to intestinal *in vitro* models will be reviewed later on in this document.

1.5.4 STEREOLITHOGRAPHY-BASED TECHNIQUES

Stereolithography creates 3D shaped materials by using photopolymerization by the precise irradiation of layer-by-layer materials. It enables the fabrication of complex architectures and geometries in a very precise way. The first layer of photopolymerized hydrogel is adhered to a built platform, which is moved a defined step height for the polymerization of the subsequent layer. This process is repeated until the shape of the desired structure is achieved (Fig. 1.22). Microstructuring can be completed by two different methods: the shape of each layer can be controlled by a computer and drawn by a laser beam, or by applying different photomask at each exposition.[179,221] In the case of photosensitive hydrogels stereolithography has been used to encapsulate cells in three-dimensional structured PEGDA, gelatin methacrylate or poly(ethylene glycol) dimethacrylate (PEG-DMA) hydrogels.[222–224] Despite the excellent three-dimensional control of the microstructures obtained, the additive one-layer-at-a-time approach is laborious and time-consuming.

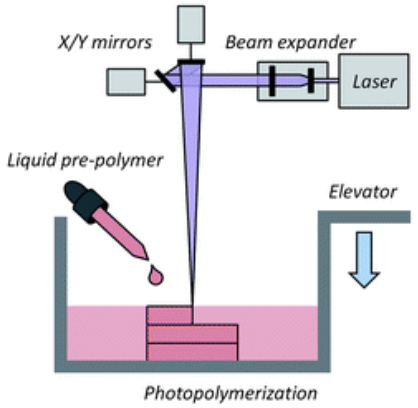

Figure 1.22: Schematics of the stereolithography technique where a polymer solution is polymerized layer-by-layer and controlled by the specific position of a platform.

Moreover, cross-linking only occur at the surface of the photopolymerizable material (within the first few micrometers). In addition, the lateral resolution is between 150 and 200 μm and the minimum distance between two adjacent layers is 50 μm, which gives quite a poor resolution in the z-dimension.[225]

Two-photon polymerization can be also considered as a stereolithography technique, and it can be used to create three-dimensional microstructures in a simple and fast manner. Polymerization occurs in a liquid based material which receives high power near-infrared (NIR) or infrared (IR) femtosecond lasers. When two photons provide, simultaneously, sufficient power at the focal point, free radical polymerization can be initiated into the volume of the photosensitive material. Instead of the physical movement of a platform, two-photon technique creates three-dimensional microstructures by changing the laser focus position (Fig. 1.23). This technique enables the fabrication of hydrogels with chemical patterns using polymers with different cross-linking end groups, or cleavage groups. It also has the advantage of creating features as small as 100 nm.[226] As an example, Anseth and coworkers, have developed chemical-micropatterned and physically microstructured hydrogels (PEG and bis(azide)-functionalized polypeptides) for cell culture, tissue regeneration, and biological arrays and/or assays.[175,227–229] As drawbacks, this technique is complex, expensive, and limited to photosensitive materials.

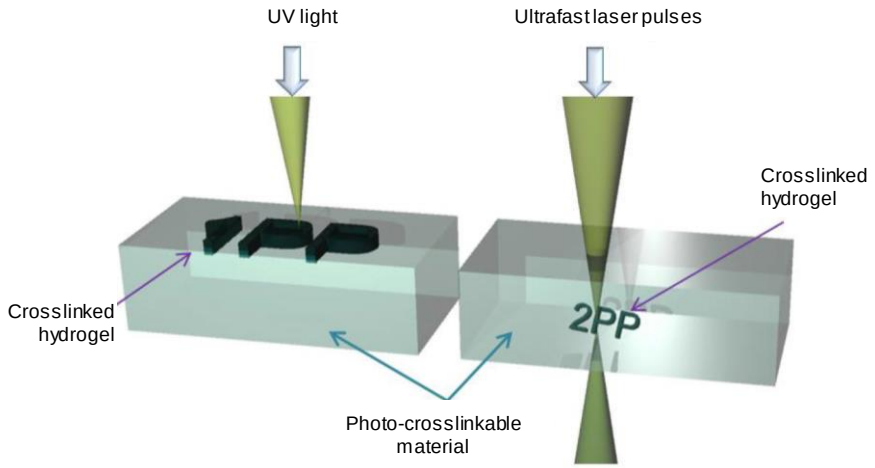

Figure 1.23: Drawing of the stereolithographic (left) and two-photon (right) techniques (adapted from Koskela *et al.*).[230]

1.5.5 PHOTOLITHOGRAPHY

Photolithography is the microfabrication technique most used in microelectronics to create integrated circuits. The procedure consists on depositing a thin layer of a photoresist on the top of the material to be microstructured. Then, a photomask with a desired pattern, with light opaque and transparent regions, is placed on top of the photoresist and it is exposed to UV light through the mask. Photomasks can be made of metal or glass, but also high-quality acetate sheets can be used if the dimensions of the microstructures are relatively large (> 50 μm). The illuminated regions become either cross-linked (negative photoresist) or degraded (positive photoresist), and a replica of the design in the photoresist is developed with a solvent. At this point etching techniques are used to transfer the pattern to the underneath material and finally, the photoresist layer is removed (Fig. 1.24a).[231] The technique is parallel in nature and it allows the microfabrication of large-surface areas in a simple step. The energy dosage is controlled by the intensity of the light source (usually prefixed) and by the exposure time. However, the resolution of conventional photolithographic techniques is limited by light diffraction to be on the order of half the wavelength of the light employed (< ~200 nm).

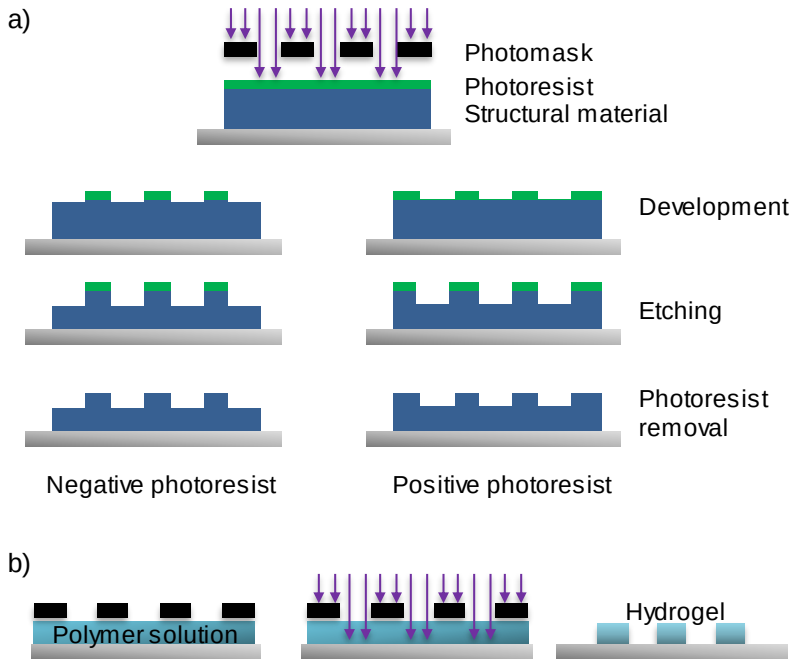

Figure 1.24: a) Schematic representation of conventional photolithography. b) Direct photopolymerization of a hydrogel through a photomask.

These diffraction phenomena are differentiated in Fraunhofer diffraction, which occurs at far-field distances of the slits of the mask, and Fresnel diffraction, which occurs when the light passes through an aperture and diffracts in the near field. It occurs due to the short distance in which the diffracted waves propagate. As example, mask and photoresist are usually separated by an air gap or glass of some thickness (20 to 200 μm), which affects the transfer of the mask pattern. This limits the transferable minimal structure sizes at about 1 to 5 μm in lateral resolution.[232]

Application	Refs.
Cell encapsulation in microscaled hydrogels	190
Photopatterning for guiding cell behavior	233
Cell-laden microgels	220
Cell encapsulation	177
Hydrogel to mimic cartilage	234
Multilayer microfluidic hydrogels	235
Hydrogel stiffness and permeability studies	236
Aggregation of Pancreatic b-Cells	237
Stem Cell Culture and Gene Delivery	238
Cell migration in synthetic extracellular matrices	239
Protein encapsulation	240
Patterned vascular networks	241
Matrix Metalloproteinase-2 Mediated Release	242
Bone tissue engineering scaffold	171
Cornea engineering hydrogel	170
3D hair follicle-like hydrogel	173
Osteogenic differentiation	243
Smooth muscle cell proliferation	244
Vascularization of tissue Constructs	245
In vitro Model for Ductal Carcinoma	246

Table 1.3: Different applications of microstructured PEGDA hydrogels in the field of cell/tissue engineering.

Conventional photolithography resolution is enough for most cell culture applications, because three-dimensional structures are in the range of tens of microns to millimeters. To be used with photocross-linkable hydrogels, the

photomask is placed on top of the hydrogel solution and UV is exposed through the photomask. So, only UV irradiated areas will polymerize (Fig. 1.24b). Exposure time must be precisely controlled because overexposition causes the polymerization of areas that are under the masked regions, which may create undesired patterns.[220] This technique has been successfully used to produce microstructures on several hydrogels, mainly those containing acrylate groups in their backbone, such as PEGDA, methacrylated hyaluronic acid, gelatin methacrylate, and mixtures of these polymers.[247–258] The cells can be cultured on the hydrogel surface, but more often these materials have been widely used for cell-laden applications.[187,220,257] They have been also used to create chemical micropatterns on hydrogels.[233,259–261] A example of use in tissue engineering, are honeycomb structures fabricated by several photolithographic steps, which supported and surrounded individual hepatic microtissues.[262] Although photolithography is a very simple and low-cost process, this approach is not straightforward when applied to create complex 3D structures on soft and thick hydrogels. Microstructuring of PEGDA with high aspect ratio shape has been carried out using pure PEGDA or highly concentrated solutions of PEGDA.[263–265] These microfabrication techniques have been extensively used to microstructure hydrogels, and in particular, they have been applied to PEGDA hydrogels for biomedical applications (Table 1.3).

The combination of the elements explained in this section (hydrogels and microstructures) to design new *in vitro* models of small intestinal epithelium is reviewed in what follows.

1.6 COMPLEX *IN VITRO* MODELS OF SMALL INTESTINAL EPITHELIUM

1.6.1 INTESTINAL ORGANOIDS

The identification of small intestinal stem cells by using the Lgr5 gene marker has recently allowed the formation of intestinal organoids, called mini-guts, cultured *in vitro*. Sato *et al.*, developed the generation of long-term culture of organoids with crypt-villi architecture from small intestine crypts, cultured in a three-dimensional extracellular matrix (Matrigel™) (Fig. 1.25).[31,266]

These organoids contain all the main intestinal epithelial cell types, including the stem cells. Intestine-like organoids can be obtained from adult or neonatal mice small intestine tissue,[267] human embryonic stem cells, and induced pluripotent stem cells.[268] Despite organoids serve as a model that mimics the physiology and functionality of the small intestinal epithelium, they are closed

structures that do not allow the access to the lumen, thus hampering their potential applications.[269]

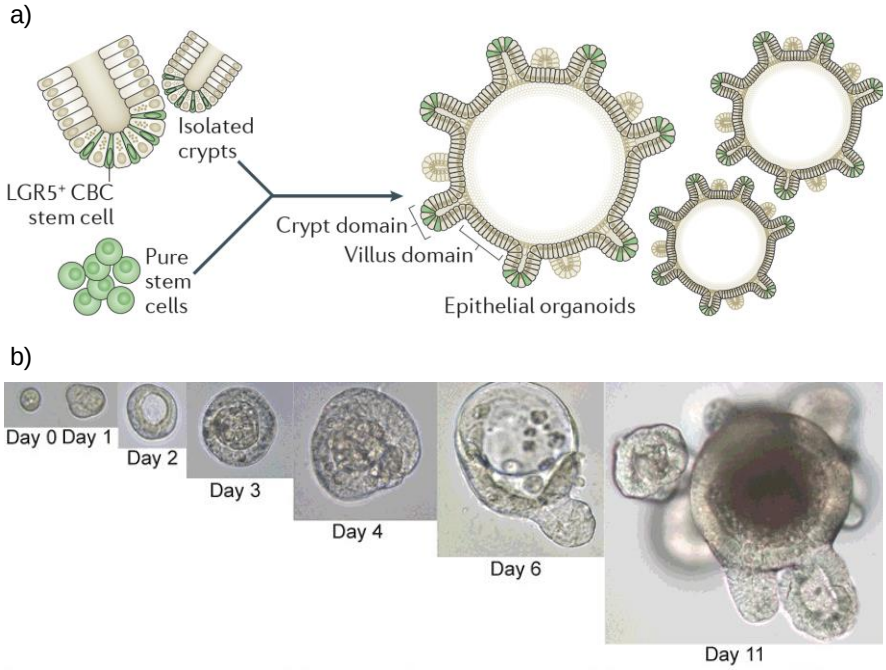

Figure 1.25: a) Schematic drawing of the culture of crypts or isolated intestinal stem cells to develop intestinal organoids. b) Intestinal organoids grown *in vitro*. While grow organoids increase the number of crypt-like domains (differential interference contrast images). The lumen is filled with dead cell material (dark gray) (adapted from Buske. Et al)[270]

1.6.2 GUT-ON-A-CHIP MODELS

For the last decade, microfluidics has been used to study, in miniaturized systems called lab-on-chip devices, physiological mechanisms and cellular behavior in ways that have not been possible before. These microdevices can be used to test the efficacy and toxicity of drugs and chemicals in automated, high-throughput, approaches and to create *in vitro* models of human diseases. *In vitro* models of small intestine have also been integrated in microfluidic chips, thus creating the so-called gut-in-a chip models.

Kimura *et al.* fabricated a micropumped microfluidic device with two compartments divided by a semipermeable membrane to mimic *in vivo* conditions and study the transport activity of Caco-2 cells. This system integrated optical fiber sensors on each compartment for fluorescence detection of labeled

molecules. By measuring *in-situ* the labeled molecules, this system provides a useful platform for drug screening and toxicity testing in dynamic environments (Fig. 1.26a).[271] Kim *et al.* developed a microfluidic device to mimic peristaltic motions and intestinal shear stress (Fig. 1.26b). They obtained a confluent layer of Caco-2 cells on a porous membrane and reported the development of villi-like structures over long time periods. The permeability of the paracellular way and Caco-2 differentiation were higher than in conventional 2D models and similar to *in vivo*. In addition, they achieved a successful co-culture of commensal bacteria (*Lactobacillus rhamnosus GG)* with Caco-2 cells.[269] Surprisingly, markers of goblet cells, mucus production, enteroendocrine cells, and Paneth cells were found on Caco-2 cells. These findings on gut-on-a chip devices suggest that dynamic conditions have dramatic effects on cell phenotype and differentiation, and improve *in vitro* models of small intestine.[272]

Other integrated microfluidic platform, called NutriChip, also reproduced a confluent layer of Caco-2 cells separated from a co-culture of immune cells by a permeable membrane to mimic the activation of immune cells in response to the transfer of nutrients across the epithelial layer (Fig. 1.26c). This system allowed monitoring of the response of immune cells to pro-inflammatory stimuli by the Caco-2 activation against the pathogen agent LPS (lipopolysaccharide) and it was observed an increase on the production of inflammation biomarkers (IL-6).[273] Considering the interaction of the intestinal function with other organs, many authors have attempted to integrate within the same chip different tissue models. Recently, Esch *et al.* have fabricated a modular pumpless device that allowed combining Caco-2 cells with liver tissue (Fig. 1.26d). This system also incorporates transepithelial electrical resistance sensors to monitor the gut epithelial barrier function.[274] Shuler and co-workers developed a microscale cell culture analog system (μCCA)[275] that contained interconnected compartments (lung, liver, and other tissues) in a chip. Then, intestinal Caco-2 cell model was integrated (Fig. 1.26e),[276] and recently, villi-like structures have also been incorporated .[277]

Complex *in vitro* models, including organoids, 3D synthetic villi and gut-on-a-chip have proved that the mimicking of physiological features enhance the cell differentiation processes, and maintain epithelium and commensal bacteria co-culture. In particular, the mimicking of the crypt-villus architecture small intestinal epithelium has demonstrated its physiological relevance by the improvement of paracellular permeability correlation. Microfluidic devices allow for tight regulation of the cellular microenvironment, including fluid shear and gradients of biochemical molecules, and offer high-throughput culture and analysis of 3D tissues. However, for the most part, microfluidic devices remain similar to 2D cell culture in the fact that the cells are seeded in a monolayer

without surrounding support cells or encasement in extracellular matrix. Moreover, these devices provide a limited space for cell growth and are difficult to combine with conventional biological testing techniques.

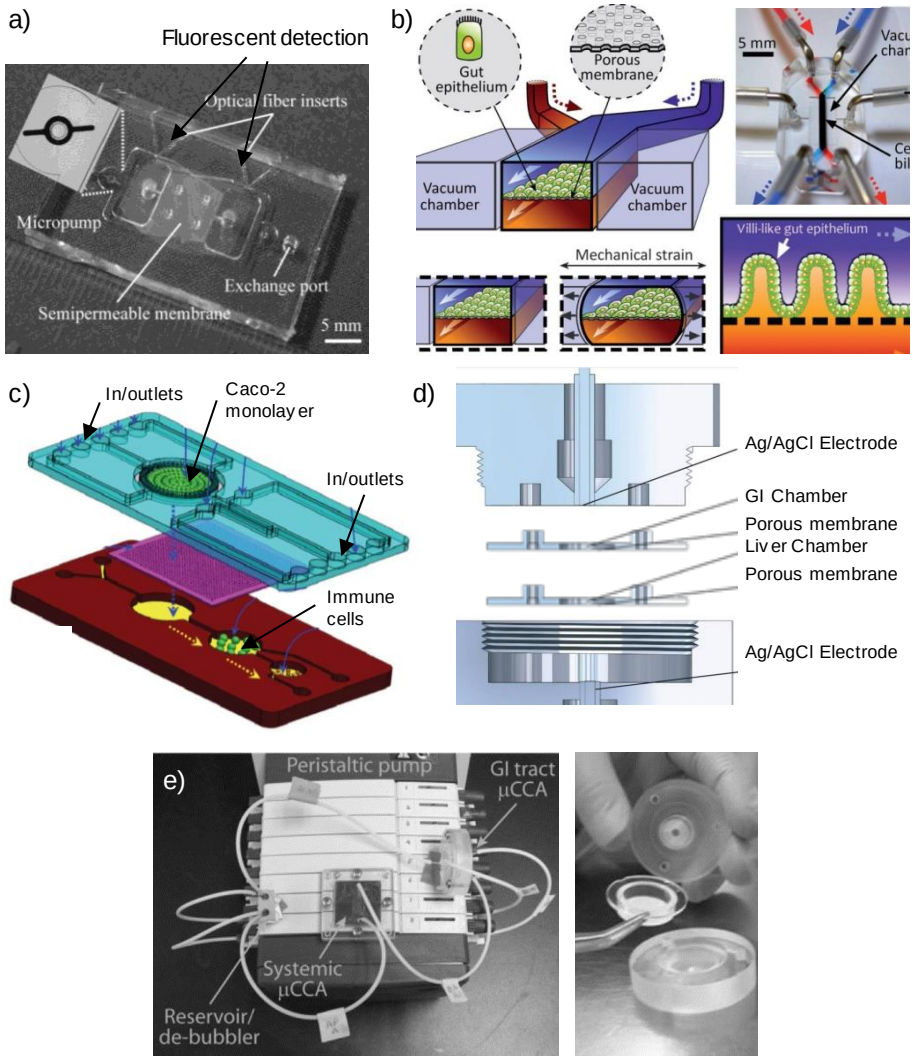

Figure 1.26: a) Photograph of the micropumped microfluidic device reported by Kimura *et al.* which incorporates optical sensors for the measuring of fluorescent dyes.[271] b) The human gut-on-a-chip. Schematic of the gut-on-a-chip device showing the flexible porous ECM-coated membrane lined by gut epithelial cells cross horizontally through the middle of the central microchannel. (Upper right) A photographic image of the gut-on-a-chip device composed of PDMS elastomer that allows providing peristaltic-like motion. Schematic showing transformation of a planar intestinal epithelium into villus structure (from Kim *et al.*).[160] c) Schematic of the NutriChip forming the miniaturized gastrointestinal tract. The device contains epithelial cells and immune cells in different compartments. d) Cross section of modular, pumpless body-on-

a-chip platform for the co-culture of GI tract epithelium and 3D primary liver tissue (from Esch *et al.*).[274] e) Image of the microscale GI tract cell culture analog system consisting in a porous membrane integrated in microfluidic system in contact with other tissue models (from Mahler et al).[156]

1.6.3 THREE-DIMENSIONAL MODELS OF SMALL INTESTINAL EPITHELIUM

Recent developments in biomaterials and microfabrication methods have fostered the development of *in vitro* models that mimic the 3D features of the small intestinal epithelium.[278,279–281] Crypt-like topography has been produced by photolithography and transferred to poly(dimethylsiloxane) (PDMS) (Fig. 1.27a). Caco-2 cells cultured on these substrates showed lower levels of differentiation on the micro-wells compared to flat substrates, attributed to significant influence of crypt-like topography on intestinal cell phenotype.[281] Wang *et al.* also, fabricated type I collagen membranes with crypt-like micro-well topography (Fig. 1.27b).[280] Slightly lower TEER values were found for Caco-2 cells cultured on crypt-like micro-well membranes, compared to flat collagen, suggesting that crypt-like topography affects tight junctions, as *in vivo*, where on the crypts permeable tight junctions are found.[282] Villi architecture has also been produced by several techniques. Lee *et al.* fabricated villi scaffolds made of porous poly (lactic-co- glycolic acid) (PLGA) by 3D printing.[283] However, the technique resolution did not allow the fabrication of small enough microstructures, which had considerably larger dimensions (1 mm in width and 700 μm in height) than villi, and pores of about 100 μm. Even though the scaffold mimics the shape, dimensions and pore size are far away from the *in vivo* situation.

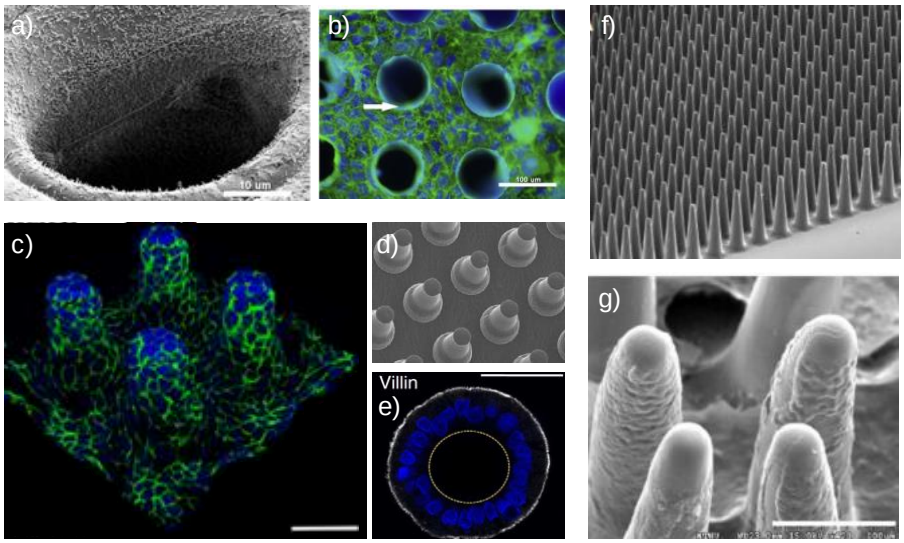

Figure 1.27: Crypt and villi architecture reproduced on hard substrates. a) PDMS well and b) collagen membrane with crypt-like topography (Wang *et al.*).[280,281] c) Caco-2 cells cultured on PDMS inserts with villi-like topography, d)

scanning electron microscopy image of PDMS villi inserts, and e) confocal microscopy analysis of villin distribution on Caco-2 cells grown on PDMS villi inserts (from Salomon *et al.*).[284] f,g) Scanning electron micrographs of the PLA biomimetic villus array (from Yang *et al.*).[285]

Molding techniques combining laser ablation and sacrificial molding have allowed the fabrication of villi-like structures on soft materials such as collagen (1 – 800 MPa) (Fig. 1.28a).[183] This system was adapted to a custom-made culture insert, so TEER and permeability measurements were performed.[286] Results suggested that the 3D intestinal model could improve the correlation between *in vitro* models and native human small intestine.[104] This approach also proved that the expression of MUC17 was highly enhanced in the 3D villi model, compared to a monolayer culture (fig. 1.28b). This finding suggests that the architecture of the villi induces physiological changes in human intestinal cells.[287]

Although topographic features of villi were recreated in collagen, this can form a barrier to the diffusion of some drugs, and can be biodegraded after short term-cell culture. To overcome these issues, alternatives such as PLGA have been proposed. PLGA porous scaffolds allowed the diffusion of biomolecules. They also allowed cell attachment and were suitable for the differentiation of primary cells from crypt mice, mimicking the differentiation process *in vivo* (Fig. 1.28c).[197] Epithelial cells were at different stages of differentiation along the crypt–villus axis, and this altered where bacteria reside.[288] Also, strains of commensal bacteria can live and exert their effects against pathogenic *Salmonella* (Fig. 1.28d,e). Recently, organoids were incorporated into these PLGA synthetic intestinal niches, together with other cells including macrophages. It was seen that lactobacillus enhance enterocyte differentiation, and bacteria (*E. coli*) negatively affects growth and differentiation. 3D scaffold was also tubularized to be implanted in mucosal defects in animals. Mucosa regeneration was achieved with native-like characteristics (Fig. 1.28f,g).[289] Other approaches use polyethersulfone (PES) hollow fibers to mimic small intestinal tube. Caco-2 cells formed cell monolayers on the inner surface and showed higher degree of differentiation than conventional 2D models. However, the diameter of fibers was too small (900 μm) compared to diameter of human small intestine (2.5 cm), and no three-dimensional features were incorporated on the inner surface.[290] Silk-based porous scaffolds were fabricated with a screw-patterned hollow lumen (400 μm ridge-like features) and were used as architectural and functional construct by culturing several intestinal cell types (1.28h). Primary human intestinal myofibroblasts were seeded within the scaffold and Caco-2 and HT29 cells were cultured on its surface. These synthetic intestinal tissues permit the accumulation of mucus, and interact with *Lactobacillus rhamnosus GG* strain. However, the three-dimensional architecture based on ridges do not faithfully mimic the finger-like morphology of villi. In addition, TEER and permeability

assays are difficult to implement. Moreover, tissue functions tend to decrease after a few weeks of cell seeding.[291]

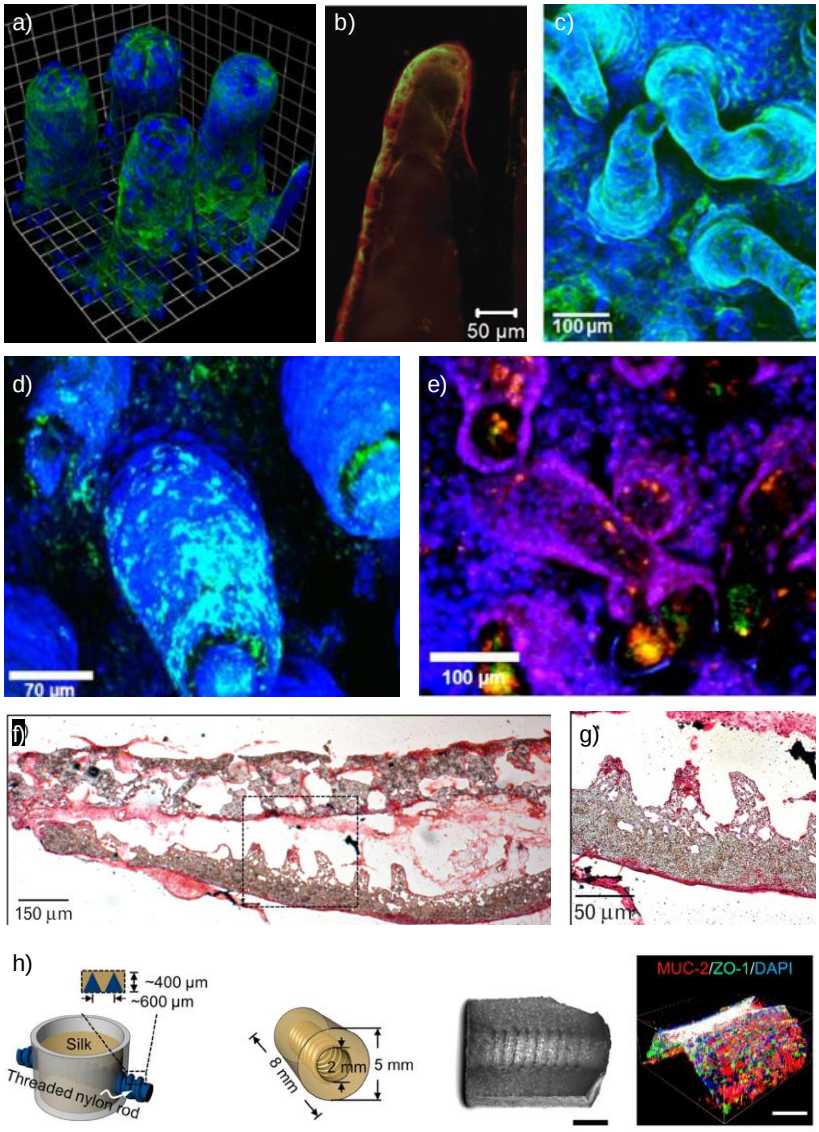

Figure 1.28: 3D synthetic small intestine scaffolds based on laser ablation and sacrificial molding techniques. a) 3D villi with Caco-2 cells (from Yu *et al.*) [286] b) Expression of MUC17 in Caco-2 cells (red: actin, green: MUC17) in 3D collagen scaffold (from Kim *et al.*).[146] c) Cell full coverage over a section of a PLGA villus. d) Confocal microscopy image of PLGA scaffolds cultured for 21 days with Caco-2 (blue), and bacteria (red), and e) Caco-2 cells with probiotic (red) and pathogen (green) (from Costello *et al.*).[87,147] f) Hematoxylin-eosin micrograph of the mucosa of mouse 28 days after implantation of synthetic scaffold seeded with mouse-derived progenitor cells showing intact villus

structure. g) Higher magnification of the highlighted area (from Shaffiey *et al.*).[148] h) Fabrication process for silk-based porous scaffolds for 3D human intestine engineering, and a fluorescence image of a cell covered ridge.

The architecture of small intestine has been also captured into *in vitro* models using decellularized animal small intestine segments. Native tissue has been used as a template to generate scaffolds with three-dimensional intestinal features. Chemical vapor deposition of silica was used to mimic the topography of the intestinal basement membrane.[292] However, due to the fragile nature of silica, the replicas were unsuitable for cell culture or to serve as molds. Recently this method has been improved using poly (p-xylylene) polymer, which can serve as a mold to fabricate PDMS replicas with the tissue architecture used as cellular growth substrates.[293]

Overall, microfabrication techniques have proved that better *in vitro* epithelial models can be developed by recapitulating the *in vivo* 3D tissue architecture. However, to be of practical use in the *in vitro* modelling of diseases, the preclinical screening for drug toxicity and the understanding of organ development, these systems should be easy to fabricate and be compatible with conventional cell culture and biological characterization techniques. This thesis aims to further accelerate this shift from 2D to 3D biomimetic models by providing a new cell culture platform for intestinal epithelial tissue.

2

Hypothesis and objectives

In vitro assays are recently shifting from the use of 2D cell monolayers to the use of organotypic, 3D cell cultures, as it is becoming increasingly evident that the "flat biology" approach is not predictive of *in vivo* tissue responses. In particular, the current *in vitro* human intestinal models provide data that is not predictive of the *in vivo* behavior. Our hypothesis is that, by developing a new model that recapitulates the 3D architectural features of the native tissue in an appropriate biomaterial, advanced *in vitro* models of the intestinal epithelium can be produced. Therefore, the overall aim of this thesis is to engineer a small intestinal *in vitro* model that mimics the villi-like architecture and the mechanical properties of the intestinal epithelium able to support the growth of a functional epithelial intestinal cell barrier. Towards this objective, specific objectives are defined as:

- To fabricate hydrogel microstructures by photolithography, obtaining in a single-step process self-standing villi-like microstructures resembling the small intestine 3D architecture. To define the relationships between the material properties, the process parameters and the obtained 3D structures.

- To provide the hydrogels with the proper biochemical, mechanical and physicochemical properties for their successful bioactivity. To investigate the effects of processing parameters in the formation of the 3D villi-like microstructures.

- To evaluate the interactions between epithelial cells and the functionalized microstructured hydrogels, analyzing the cell behavior and the formation of a functional epithelial cell barrier. To determine the relationship between the fabrication parameters and the epithelial phenotype. To design and implement engineering processes leading to interface the new *in vitro* models with conventional testing approaches.

3

Materials and Methods

3.1 FABRICATION OF PEGDA HYDROGELS IN A CLOSED CHIP

3.1.1 POLYMER SOLUTION FOR HYDROGEL FORMATION

Hydrogels were fabricated by the photopolymerization of diacrylate-terminated poly (ethylene glycol) (PEGDA) molecules under ultraviolet (UV) irradiation in a reaction called free radical polymerization, as described in section 1.5 (Fig. 3.1).

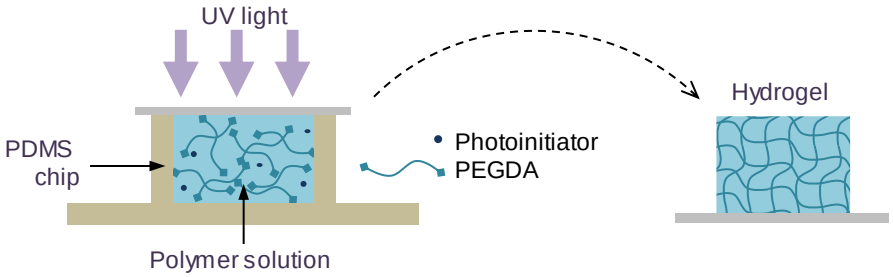

Figure 3.1: Simplified scheme of PEGDA photopolymerization in a closed chip.

The polymer solutions were based on PEGDA (Sigma-Aldrich, USA) of either 575 Da ($PEGDA_{575}$) or 6000 Da ($PEGDA_{6000}$) of molecular weight diluted in phosphate buffered saline (PBS) with a concentration of 10 mM PO_4^{3-}, 137 mM NaCl, and 2.7 mM KCl, at pH 7.4 (ThermoFisher Scientific, Spain). 2-hydroxy-4'-(2-hydroxy-ethoxy)-2-methylpropiophenone (I2959) (Sigma-Aldrich, Spain) was the photoinitiator added to the polymer solution. PEGDA concentrations studied range between 5% w/v and 20% w/v, and I2959 concentrations between $5 \cdot 10^{-4}$% w/v and 1% w/v. PEGDA and I2959 were diluted in PBS at 65°C for 1 hour in a glass vial (VWR, Spain), previously cleaned with ethanol 96% v/v (Panreac Applichem, Spain), and dried under nitrogen air flow. Polymer solutions were protected from light and stored at 4°C until further use (maximum storage time 1 week). When precipitates were observed, the solutions were filtered by a 0.22 µm filter (Merck-Millipore, Spain).

3.1.2 PEGDA POLYMERIZATION SET-UP

The detailed experimental set-up designed for hydrogel polymerization is outlined in Figure 3.2. We fabricated a chip formed by a polydimethylsiloxane (PDMS, Sylgard 184 Silicon Elastomer, Dow Corning, Germany) container. The chip was sealed by a flat sheet of PDMS at the bottom side and covered by a glass coverslip (Fig. 3.2a,b). After UV irradiation and cross-linking, the hydrogel was

formed and it kept attached to the coverslip. Then, the sample was flipped up to access the hydrogel surface. PDMS prepolymer was prepared by mixing the base liquid prepolymer with the curing agent in a 10:1 ratio and degassing the mixture under vacuum for 1 h. The prepolymer was then placed between two flat poly (methyl methacrylate) (PMMA) (Goodfellow, UK) pieces spaced 1 mm and cured for 24 h at room temperature and 2 h at 65°C. We then created a circular hole of 10 mm in diameter by a punch of 10 mm in diameter (AcuPunch, USA) to contain hydrogel solution. Two channels were fabricated using a scalpel to facilitate the polymer flow inside the PDMS container, and two inlets were cut out by a 1.5 mm punch (Uni-Core, GE Healthcare Life Sciences, Spain) (Fig. 3.2c). PDMS container was thoroughly rinsed in ethanol 96% v/v, and blown dried with a nitrogen stream before sealing. As the hydrogels are very soft and are difficult to handle, they were polymerized on a coverslip that will act as a support. Glass coverslips 12 mm in diameter (Neuvitro, USA) were used for this purpose. Coverslips were rinsed in ethanol 96% v/v, blown dried with a nitrogen stream, and then placed on top of PDMS container, creating a space which was filled by the hydrogel solution (Fig. 3.2d-f). For the cross-linking of the hydrogel, the chip was then exposed to UV light in a Mask aligner instrument (SUSS MicroTec MJB4, Germany) at the IBEC nanotechnology platform (Fig. 3.2g-i). Samples were placed 5 mm below the light source of Mask aligner and exposed to UV light using a mercury short arc lamp (OSR HBO 350 W/S, Germany), which has intensity peaks within the spectral range of 250-435 nm (Fig. 3.3).

The mask aligner was calibrated for a power density of 25 mW/cm^2 by an UV intensity meter (SUSS MicroTec, Germany) placed at same position of the sample. After UV exposure, hydrogels adhered to the glass coverslips (Fig. 3.2k,l) were rinsed with PBS to remove non-cross-linked polymer and unreacted photoinitiator, placed in a 24-well plate (Nunc™, ThermoFisher Scientific, Spain), submerged in PBS, and kept at 4°C for the swelling process. According to previous experiments carried out in our laboratory,[294] hydrogels were allowed to swell for at least 3 days to reach equilibrium swelling. During this swelling period, PBS was changed every day to fully remove any non-cross-linked molecules.[295] To increase the experimental throughput, a parallel version of the chip was designed and fabricated. The parallel chip had nine PDMS containers arranged on the same piece of PDMS (Fig. 3.2j).

Depending on the final properties desired for the hydrogels, the exposure time and I2959 concentration were controlled to ensure an appropriated degree of polymerization.

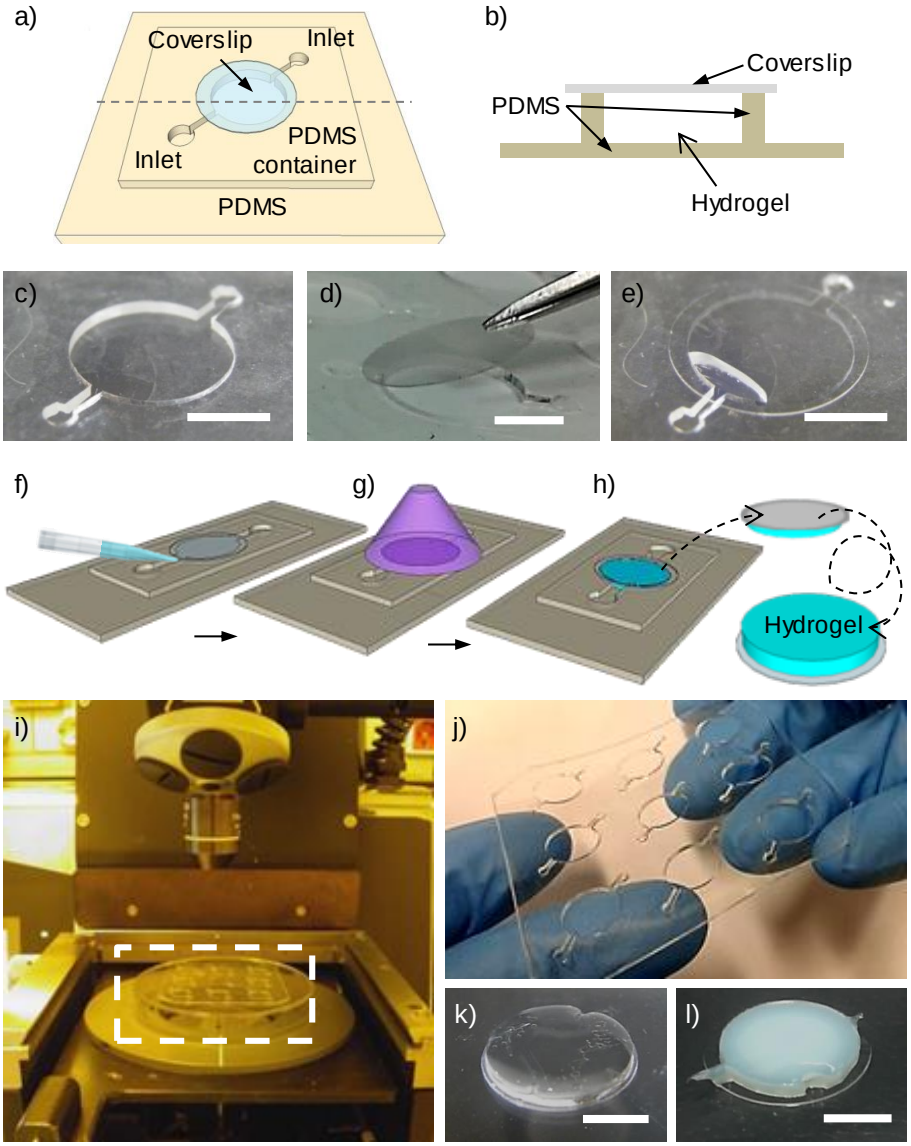

Figure 3.2: Schematics of the hydrogel fabrication set-up. a) Detailed top view and b) cross-section of the chip. Photographs of c) a PDMS container, d) coverslip placing on the PDMS container, and e) polymer solution flown inside of the PDMS container. Diagram of the fabrication procedure: once the coverslip is placed on top of the chip, the PDMS container is filled with the polymer solution (f). Then, the chip is exposed to UV light (g). Finally, the coverslip is removed and the disc-shaped hydrogel kept adhered on the coverslip (h). Image of i) the set-up placed on the Mask aligner instrument. j) PDMS array of nine containers. Photographs of k) 6.5% w/v $PEGDA_{6000}$ and l) 20% w/v $PEGDA_{575}$ hydrogels. Scale bars = 5 mm.

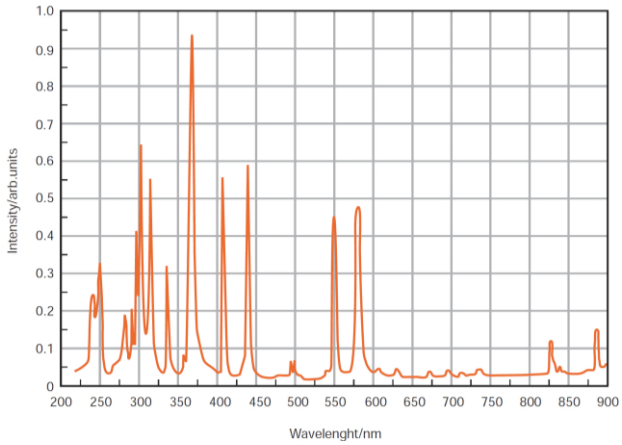

Figure 3.3: Intensity distribution at the spectral region of the mercury short arc lamp set in the Mask aligner. Extracted from OSRAM datasheet.[296]

3.1.3 EFFECT OF THE PHOTOINITIATOR CONCENTRATION ON PEGDA PHOTOPOLYMERIZATION

To study how the amount of photoinitiator affects PEGDA polymerization, disc-shaped hydrogels were photopolymerized by using different I2959 concentrations. Solutions of $PEGDA_{575}$ or $PEGDA_{6000}$ at 5%, 10% and 20% w/v in PBS were used for this purpose. These polymeric solutions were mixed with several concentrations of photoinitiator ($5 \cdot 10^{-4}$% w/v, 0.05% w/v, and 0.5% w/v of I2959) and were exposed to UV light for 150 s. The color (transparent/white) of hydrogels was used as a parameter to qualitative assess the polymerization degree. To clarify the relationship between polymerization degree and the photoinitiator concentration, the fractional monomer conversion (p) was theoretically estimated using equation 14 (section 1.4).

$$p = 1 - \exp\left[\left(\frac{8k_p^2 f[PI]_0}{k_d k_t}\right)^{\frac{1}{2}}\left[\exp\left(-\frac{k_d t}{2}\right) - 1\right]\right] \qquad \text{Eq. 14}$$

where rate constants of decomposition, propagation and termination are defined by k_d, k_p, and k_t. The initial photoinitiator concentration $[PI]_0$ and the photoinitiator efficiency (f) were also considered. The photoinitiator characteristics are incorporated in the definition and quantification of k_d (Eq. 3), where ϕ is the photoinitiator quantum yield, ε the photoinitiator molar absorptivity, I the intensity of UV light, N_A the Avogadro's number, h the Planck´s constant, c the speed of light, and λ the wavelength of initiating light (λ).[166]

$$k_d = \frac{\phi(2.303\varepsilon)I\lambda}{N_A hc} \qquad \text{Eq. 3}$$

Taking into account that photoinitiator I2959 shows the highest molar absorptivity (400 M^{-1} cm^{-1}) at wavelengths below 340 nm,[177] and the spectral emission of the lamp is centered at 313 nm, this wavelength and ε = 400 M^{-1} cm^{-1} were selected for the calculations. In addition, 25 mW/cm^2 of UV intensity were measured with a probe at 365 nm. Then, integrating the area under the intensity curve between 286 nm and 340 nm (Fig. 3.3), an intensity of 37.5 mW/cm^2 was estimated as total intensity irradiating the sample.

3.1.4 EFFECTS OF THE EXPOSURE TIME ON HYDROGEL HEIGHT

Disc-shaped hydrogels were used to investigate the effects of UV exposure time on polymerization. For this purpose, 10% w/v $PEGDA_{575}$, and 10% w/v $PEGDA_{6000}$ solutions were prepared in PBS, and 1% w/v I2959 was added as photoinitiator. Polymer solutions were UV exposed during several times: 10 s, 25 s, 40 s, 100 s, and 150 s. To obtain images of the profile of disc-shaped hydrogels suitable for height measurements, the imaging set-up of the OCA15 Plus Contact Angle apparatus (DATAPHYSICS, Germany) was used. After letting the hydrogels to swell for three days in PBS, wet samples were placed at the center of the contact angle sample holder and photographs were taken. Then, images were analyzed by ImageJ free software (http://rsb.info.nih.gov/ij, National Institutes of Health, USA). The Height was measured describing a line from the coverslip to the top of the hydrogel and a PDMS piece of 10 mm was used as reference. Data was plotted and analyzed with OriginPro 8.5 software.

3.2 FABRICATION OF PEGDA MICROSTRUCTURED HYDROGELS

3.2.1 SET-UP FOR THE FABRICATION OF HYDROGEL MICROSTRUCTURES

To produce microstructures on PEGDA hydrogels a photomask was placed on top of the glass coverslip (Fig. 3.4a). The photomask pattern design consisted on a 0.5 x 0.5 mm^2 array of circular UV-transparent windows. Two diameters of windows and window spacing were used: 1) a large one of 300 μm in diameter and spaced 300 μm, which had a density of 4 windows/mm^2 (Fig. 3.4b,c) and made easier characterizations. 2) 100 μm in diameter and spaced 100 μm, which had a density of 25 windows/mm^2 (Fig. 3.4d,e), based on the anatomical geometry of human villi (about 125 μm in diameter),[9,10] and on villi

surface density (20-40 villi/mm²).[4] Photomasks were designed using AutoCAD software (Autodesk) and printed on acetate films (CAD/Art Services, USA). To use the parallel version of the chip (nine containers arranged on the same piece of PDMS) photomask designing was also arranged in nine arrays of circular windows in same photomask.

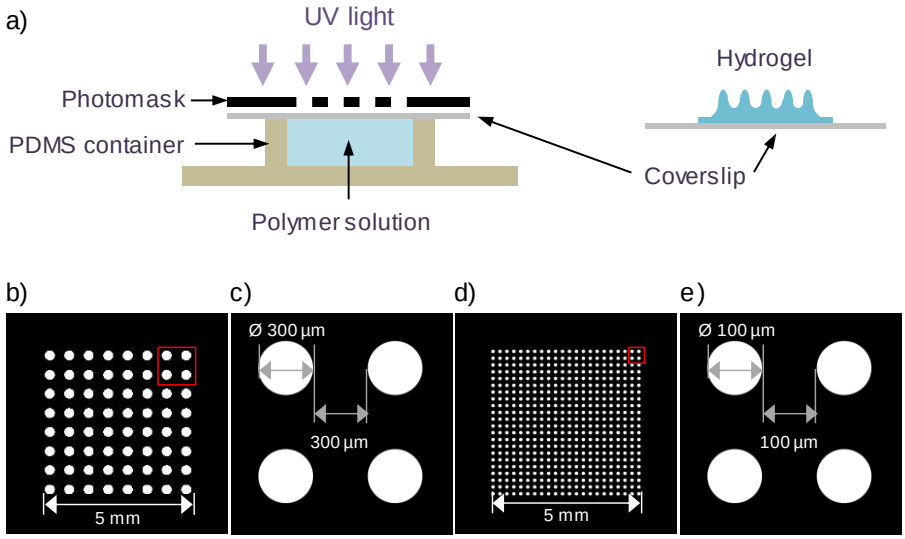

Figure 3.4: Simplified scheme of the fabrication set-up of the hydrogel microstructures. (a) Drawing of the photomask design used to microstructure hydrogels. Detail of photomask pattern with UV-transparent windows of 100 µm (b,c) and 300 µm (d,e) in diameter.

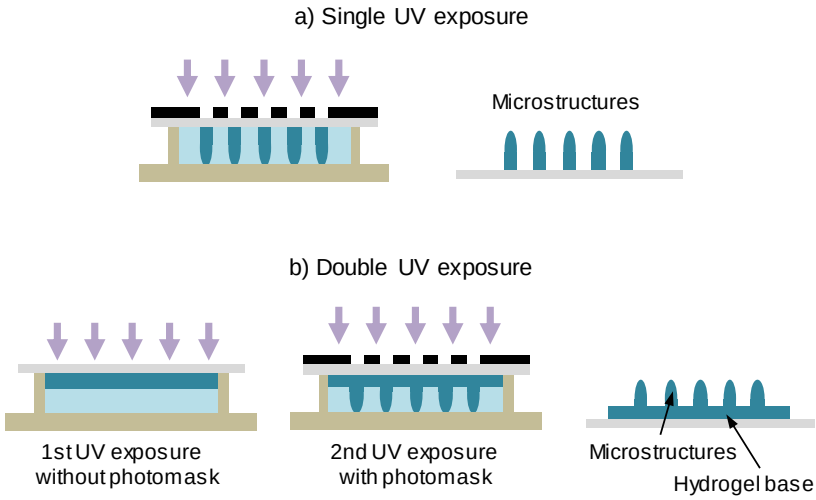

Figure 3.5: Schematics of UV exposure alternatives for hydrogel microstructuring. a) Single UV exposure and b) UV exposure in two steps.

For hydrogel microstructuring two alternatives were tried: 1) UV light exposure in a single step, or 2) UV light exposure in two steps. In the first alternative, hydrogels were exposed once with a photomask resulting in microstructures that were not connected among them (Fig. 3.5a). The second alternative was carried out to create a homogeneous hydrogel surface instead of the dual hydrogel-glass (coverslip) surface of the first one. When performed in two steps, the chip was UV exposed without photomask to create a thin layer of hydrogel that we called a base (Fig. 3.5b) and, immediately, a second UV exposure took place with the photomask for the microstructuring of the hydrogel.

3.2.2 GROWTH DYNAMICS OF THE HYDROGEL MICROSTRUCTURES

To study the growth of microstructures 10% w/v $PEGDA_{575}$ in PBS was used as polymer solution. Hydrogels were fabricated using a photomask with windows 300 μm in diameter to make the analysis easier. Microstructures were fabricated by single UV exposure, at different exposure times ranging from 70 to 110 s at intervals of 5 s. Then, microstructures were imaged by bright field microscopy in wet, taking top view captions to measure the diameter of the microstructures. Five samples were imaged for each exposure time, measuring at least 100 microstructures per sample. In addition, ten microstructures of each exposure time were imaged by SEM to compute their height, following the protocol described in section 3.2.4. Height and diameter values as a function of the UV exposure time, and the contours of the microstructures as a function of height and diameter were plotted with OriginPro 8.5 software.

3.2.3 EFFECTS OF THE FABRICATION PARAMETERS ON THE MORPHOLOGY AND HEIGHT OF THE MICROSTRUCTURED HYDROGELS

Effects of the exposure times used to form the base (ranging 0-15 s) and the microstructures (ranging 70-150 s) were analyzed by comparing the resulting morphologies and dimensions of microstructures. Shape and dimensions were also compared as a function of the PEGDA molecular weight (575, 6000), and polymer concentration (5%, 7.5%, and 10% w/v). All experimental conditions are listed in Table 3.1.

After fabrication, microstructures were imaged by optical microscopy and their morphology and height were assessed following the protocol described in section 3.2.5. At least three microstructures of two samples were analyzed for each condition.

First UV exposure (Hydrogel base) + Second UV exposure (Microstructuring)	$PEGDA_{575}$			$PEGDA_{6000}$		
	5%	7.5%	10%	5%	7.5%	10%
	0 s + 70 s	0 s + 70 s	0 s + 70 s	0 s + 70 s	0 s + 70 s	0 s + 70 s
	0 s + 90 s	0 s + 90 s	0 s + 90 s	0 s + 90 s	0 s + 90 s	0 s + 90 s
	0 s + 110 s	0 s + 110 s	0 s + 110 s	0 s + 110 s	0 s + 110 s	0 s + 110 s
	0 s + 130 s	0 s + 130 s	0 s + 130 s	0 s + 130 s	0 s + 130 s	0 s + 130 s
	0 s + 150 s	0 s + 150 s	0 s + 150 s	0 s + 150 s	0 s + 150 s	0 s + 150 s
	5 s + 70 s	5 s + 70 s	5 s + 70 s	5 s + 70 s	5 s + 70 s	5 s + 70 s
	5 s + 90 s	5 s + 90 s	5 s + 90 s	5 s + 90 s	5 s + 90 s	5 s + 90 s
	5 s + 110 s	5 s + 110 s	5 s + 110 s	5 s + 110 s	5 s + 110 s	5 s + 110 s
	5 s + 130 s	5 s + 130 s	5 s + 130 s	5 s + 130 s	5 s + 130 s	5 s + 130 s
	5 s + 150 s	5 s + 150 s	5 s + 150 s	5 s + 150 s	5 s + 150 s	5 s + 150 s
	10 + 70 s	10 + 70 s	10 + 70 s	10 + 70 s	10 + 70 s	10 + 70 s
	10 + 90 s	10 + 90 s	10 + 90 s	10 + 90 s	10 + 90 s	10 + 90 s
	10 + 110 s	10 + 110 s	10 + 110 s	10 + 110 s	10 + 110 s	10 + 110 s
	10 + 130 s	10 + 130 s	10 + 130 s	10 + 130 s	10 + 130 s	10 + 130 s
	10 + 150 s	10 + 150 s	10 + 150 s	10 + 150 s	10 + 150 s	10 + 150 s
	15 + 70 s	15 + 70 s	15 + 70 s	15 + 70 s	15 + 70 s	15 + 70 s
	15 + 90 s	15 + 90 s	15 + 90 s	15 + 90 s	15 + 90 s	15 + 90 s
	15 + 110 s	15 + 110 s	15 + 110 s	15 + 110 s	15 + 110 s	15 + 110 s
	15 + 130 s	15 + 130 s	15 + 130 s	15 + 130 s	15 + 130 s	15 + 130 s
	15 + 150 s	15 + 150 s	15 + 150 s	15 + 150 s	15 + 150 s	15 + 150 s

Table 3.1. List of UV exposure times and polymer solutions used to study their effects on the morphology of microstructures.

3.2.4 MORPHOLOGY ASSESSMENT BY SCANNING ELECTRON MICROSCOPY (SEM)

Scanning Electron Microscopy (SEM) was used to image the geometry and the surface morphology of microstructured hydrogels. As this technique works under high vacuum, water must be removed from the samples without affecting their three-dimensional structure. Two preparation methods were assayed. In a first attempt, freeze-drying technique was used. For this purpose, hydrogels were first rinsed in Milli-Q water to remove salts. Then, hydrogels were immersed in liquid nitrogen and freeze-dried for 1 week at -50°C and 0.06 mbar of pressure (Christ Alpha 1-4 SC, SciQuip, UK). As a second approach, critical point drying was used. For this purpose, hydrogels were rinsed in Milli-Q water to remove salts, and dehydration was carried out by their sequential immersion in graded ethanol solutions in Milli-Q water: 30%, 50%, 70%, 80%, 90%, and 96% v/v for 5-15 min each and twice for 100% ethanol. Then, samples were placed in the chamber of a critical point dryer (K850, Quorum technologies, UK), sealed and cooled. Ethanol was replaced completely by liquid CO_2, and by slowly heating. CO_2 achieved gas phase equilibrium at 35°C and 85.06 atm to be slowly drained.

After either freeze-drying or critical point drying, hydrogels were imaged by ultra-high resolution scanning electron microscopy (Nova™ NanoSEM 230, FEI Company, The Netherlands) operating in low vacuum mode (0.5 mbar of water vapor pressure). No conductive coating was required for imaging. Images were analyzed by ImageJ free software to obtain microstructure dimensions. To obtain the height of the microstructures, SEM images of tilted samples were used. The real height was calculated by considering the tilting angle. In the images, height was measured as the distance from top of the microstructure to its median (Fig. 3.6b).

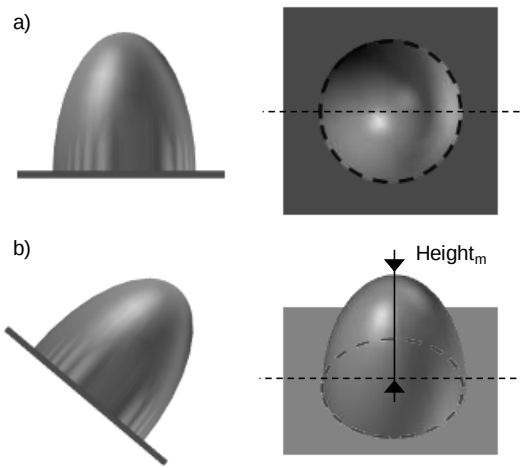

Figure 3.6: SEM image processing to measure the height of microstructures. Schematics of cross-section and top view and of a) non-tilted samples and b) tilted samples. Dash line is the median of the microstructure in the image. Height of microstructures was calculated by measuring the distance between the median and the top of the microstructure. Then, heights were corrected by the tilting angle.

3.2.5 MORPHOLOGY ASSESSMENT BY OPTICAL MICROSCOPY

To analyze the shape and dimensions of the hydrogel microstructures at equilibrium swelling, samples were imaged by bright field microscope (Nikon Eclipse Ts2, Japan) or stereoscope microscopy (Leica MZ10, Germany) in wet conditions. To measure the dimeter, top view images were collected and then measured. On the other hand, for the complete morphology analysis, microstructured samples were vertically cross-sectioned and then imaged.

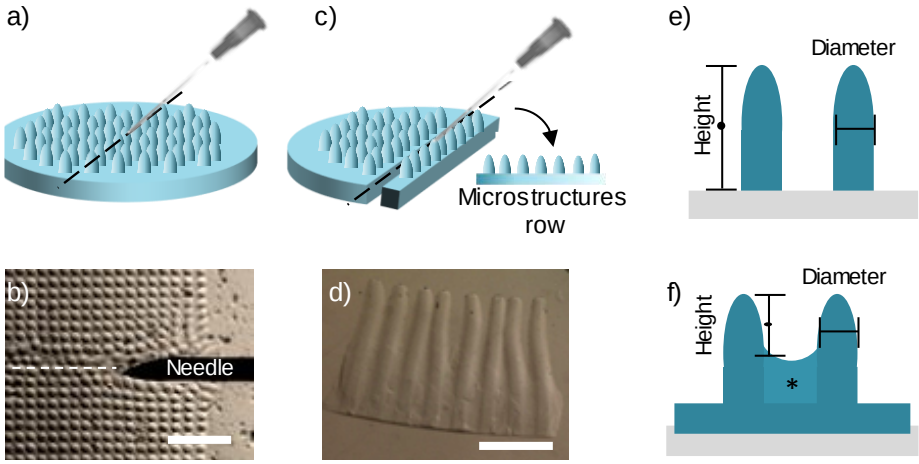

Figure 3.7: Schematics of the sectioning process of microstructured hydrogels. a,b) cross-sectioning of the hydrogels. c,d) Cut to obtain a single row of microstructures. e) Height and diameter determination of microstructures, f) when interstitial hydrogel (asterisk) is polymerized between microstructures. Scale bars: b = 1 mm, d = 0.5 mm.

First of all, hydrogels were sectioned in two pieces using a needle of 27G ¾" (0.4 mm in diameter) (BD Microlance, Spain) as a scalpel (Fig. 3.7a,b). Then, thin slices containing individual rows of microstructures were sectioned with the same needle and used to image the cross-section of the microstructures (Fig. 3.7c,d). The cutting process was carried out keeping hydrogels submerged in PBS and was monitored using a stereoscope or bright field microscopy.

The difficulties of this process were based on the manipulation of the samples to avoid destroying hydrogels using the needle. Rows containing microstructures with undesired fractures or uncompleted were discarded. One row of each sample was imaged, containing more than ten microstructures. ImageJ free software was used to measure the dimensions of the microstructures. The height was determined by the distance between the tip of microstructures and the base. When there was hydrogel between the microstructures, the height was determined as the distance between the tip of microstructure and the profile of the interstitial hydrogel. The diameter was measured at half of the microstructure height (Fig. 3.7e,f).

3.3 COPOLYMERIZATION OF PEGDA AND ACRYLIC ACID

PEGDA hydrogels need to be modified to support cell adhesion and culture. Since PEGDA backbone does not have any functional group that would

allow the incorporation of peptides or proteins, acrylic acid was added into the polymer solutions. On the one hand, acrylic acid has a vinyl group, so it can copolymerize with PEGDA by photopolymerization (Fig. 3.8). On the other hand, acrylic acid has a carboxylic group, which serves as a functional site to incorporate proteins by a carbodiimide-mediated reaction.[297,298]

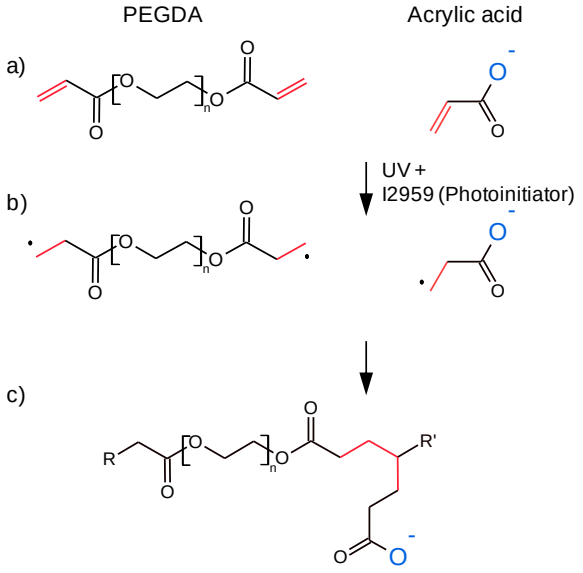

Figure 3.8: Scheme of acrylic acid and PEGDA copolymerization. a) PEGDA and acrylic acid monomers. Vinyl bond (red) takes part in free radical polymerization. Reactive oxygen for the protein coupling. b) Radicalized (•) monomers after radical attack. c) Copolymerization resulting from acrylic acid and PEGDA.

3.3.1 POLYMER SOLUTION FOR PEGDA-ACRYLIC ACID HYDROGEL FORMATION

The polymer solution was based on PEGDA of either 575 Da ($PEGDA_{575}$) or 6000 Da ($PEGDA_{6000}$), and acrylic acid (Merck Millipore, Spain) diluted in PBS and containing I2959 as a photoinitiator. PEGDA concentrations ranged between 5% w/v and 20% w/v, acrylic acid concentration ranged between 0.06% w/v and 2.4% w/v and I2959 concentration between 0.1% w/v and 1% w/v. PEGDA and I2959 were diluted in PBS at 65°C for 1 hour in a glass vial previously cleaned with ethanol 96% v/v and dried under nitrogen air flow. Then, acrylic acid was added and allowed to dilute for 1 hour at 65°C. Polymer solution was protected from light and stored at 4 °C until use (maximum storage time 1 week). In the case of observing precipitates, the solutions were filtered by a 0.22 µm filter.

3.3.2 CHARACTERIZATION OF PEGDA-ACRYLIC ACID COPOLYMERIZATION

To analyze the success of the copolymerization reaction between PEGDA and acrylic acid, the chemical modifications on the structure of the resulting hydrogels were monitored by Attenuated total reflectance - Fourier transform infrared spectroscopy (ATR–FTIR). This technique is based on measuring the absorption of IR light when its frequency matches the vibrational frequency of chemical bonds. To reduce water contribution in the recorded spectrum, hydrogels had to be dried. As hydrogels suffered a dramatic shrinking after drying because of their high-water content, large pieces of hydrogels were used. Disc-shaped hydrogels were fabricated using a PDMS container of 2 mm in height and 12 mm in diameter. Polymer solutions containing 10% w/v $PEGDA_{575}$ or $PEGDA_{6000}$, and 0.3% w/v or 1.2% w/v acrylic acid in PBS with 1% w/v I2959 were prepared. PEGDA solutions without acrylic acid were also prepared and used as a reference. Hydrogels were polymerized by 300 s of UV exposure to ensure the full cross-linking of the 2 mm in height. After fabrication, hydrogels were removed from the coverslip and placed in a 12-well plate. Then, hydrogels were first rinsed thoroughly with Milli-Q water, and then they were allowed to dry during 24 h in a vacuum desiccator.

Fourier transform spectroscopy was performed on a spectrophotometer (Nicolet iS 10, ThermoFisher Scientific, Spain) by using an ATR diamond and the deuterated triglycine sulphate (DTGS) detector. ATR avoids the problem of strong attenuation of the IR signal in highly absorbing media, such as aqueous solutions. An average of 16 scans per hydrogel in the range of 500-4000 cm^{-1} with a resolution of 4 cm^{-1} were performed. Raw data was processed and spectra were plotted as an average of at least two samples per condition with OriginPro 8.5 software.

3.3.3 TOLUIDINE BLUE O (TBO) ASSAY TO QUANTIFY THE DENSITY OF CARBOXYLIC GROUPS

Toluidine blue (tolonium chloride) is an acidophilic dye that reversibly binds to acidic molecules (sulfates, carboxylates, and phosphates) in a pH-dependent manner, and has been previously used in the detection of carboxylic groups (Fig. 3.9).[299,300]

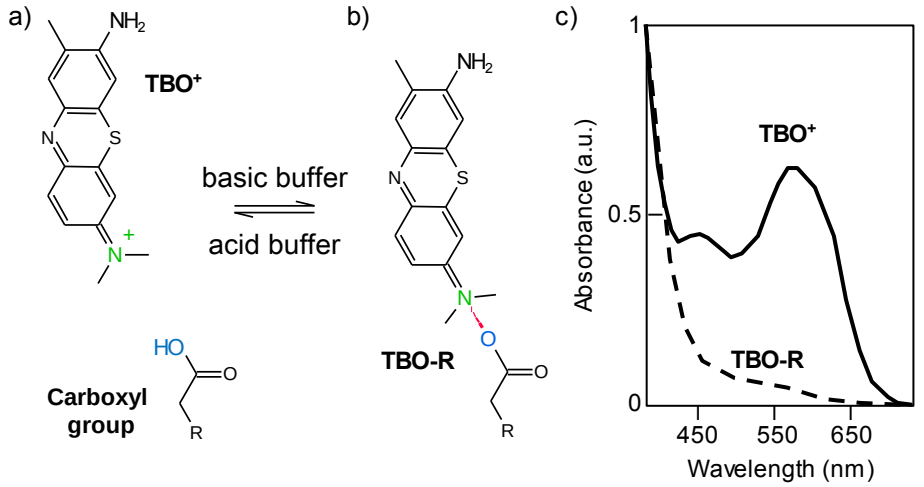

Figure 3.9: Simplified scheme of the reversible reaction between TBO and carboxylic groups. a) The TBO molecules in acidic solutions exist as protonated positively-charged species. b) In alkaline solutions, deprotonated forms of TBO and carboxylic groups can react. c) Absorption spectra of free TBO^+ in acidic solution that shows an intense peak at about 633 nm (solid line), and the TBO anchored to acid group TBO-R in alkaline solution (dashed line).[301]

For the quantification of the carboxylic groups in the PEGDA - acrylic acid copolymerized hydrogels, disc-shaped samples (10 mm in diameter and 1 mm in height) were prepared. $PEGDA_{575}$ and $PEGDA_{6000}$ at 5% w/v or 10% w/v in PBS solution containing 1% w/v of photoinitiator (I2959) were used. Acrylic acid was added at concentrations of 0.06% w/v (8.3 mM), 0.12% w/v (16.7 mM), 0.3% w/v (41.6 mM), 0.6% w/v (83.3 mM), 1.2% w/v (166.5 mM), and 2.4% w/v (333 mM). PEGDA solutions cross-linked without acrylic acid were used as controls. After fabrication hydrogels were removed from the coverslip and allowed to swell in PBS at pH 10 at 4°C in a 12-well plate. To perform the TBO assay three hydrogels of each condition were incubated overnight in 1.5 mL of a solution containing 15 mM toluidine blue O (Sigma-Aldrich, Spain) in PBS at pH 10 and at room temperature in a rotating plate (Heidolph Rotomax 120, Spain) set at 100 rpm. To remove any unbound dye, samples were frequently rinsed with PBS at pH 10 for 3 days. Thereafter, hydrogels were immersed in 2 mL of 50 vol.% glacial acetic acid (Panreac Applichem, Spain) in Milli-Q water for 2 h. The acidic medium caused the release of TBO solution from the hydrogel into the solution.[300]

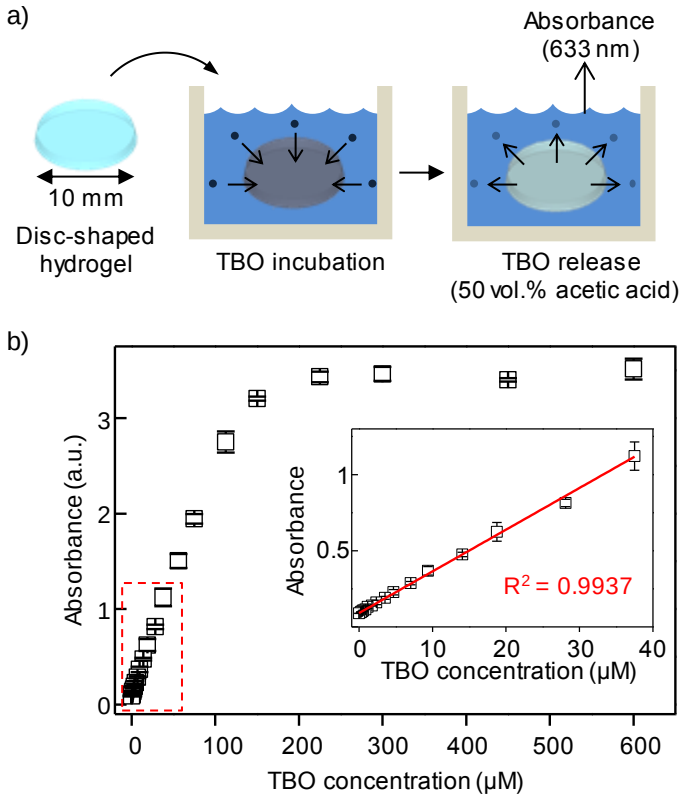

Figure 3.10: a) Scheme of the TBO assay. After fabrication, hydrogels were left to react overnight in toluidine blue. Finally, hydrogels were soaked in acetic acid, TBO was released and the absorbance of the resulting solution was measured at 633 nm. b) Calibration curve for the concentration of toluidine blue dye using optical density at wavelength of 633 nm. Detail of linear fitting at the region between 0 and 40 μM.

Finally, the absorbance of the solution at 633 nm was measured with a plate reader (Tecan infinite M200 PRO Multimode Microplate Reader, Switzerland) (Fig. 3.10a). To get quantitative date, a calibration curve was generated using solutions of TBO in 50 vol.% glacial acetic acid in Milli-Q water with concentrations ranging from 0 to 600 μM. Figure 3.10b shows the light absorbance of solutions containing a known amount of TBO at a 633 nm. The linear portion of the graph was confined to the region between 0 and 37.5 μM TBO. When sample solutions were more opaque than 37.5 μM TBO solution, they were diluted until absorbance fitted within the range of detection. Then, the dilution factor was multiplied if necessary to extract the final molarity of the hydrogel samples. The average number of total COOH moles in the hydrogels was plotted as a function of the total number of acrylic acid moles in the polymer

solution. As a non-parametric study, Mann-Whitney U test and Kruskal Wallis test were used to perform the statistical analysis.

3.3.4 MECHANICAL PROPERTIES OF PEGDA – ACRYLIC ACID HYDROGELS

To determine the effects of acrylic acid on the stiffness of PEGDA-acrylic acid hydrogels, their mechanical properties were characterized by a compression test. Disc-shaped hydrogels of 10 mm in diameter and 2 mm in height were fabricated for these measurements. The samples tested were fabricated using 6.5% w/v $PEGDA_{6000}$ solutions in PBS with 1% w/v of I2959 and acrylic acid in concentrations ranging from 0.06% w/v to 1.2% w/v (Table 3.2). Polymer solutions without acrylic acid were used as a control. Polymeric solutions were photopolymerized by exposing them for 150 s under UV light. To ensure a precise diameter for the mechanical measurements, swollen hydrogels that increased their diameter were punched to obtain samples 10 mm in diameter.

Acrylic	0%	0.06% w/v	0.12% w/v	0.3% w/v	0.6% w/v	1.2% w/v
acid conc.	0 mM	8.3 mM	16.6 mM	41.6 mM	83.3 mM	166.5 mM

Table 3.2: Acrylic acid concentrations used in the fabrication of hydrogels for the mechanical testing.

Stress-strain curves were obtained in compression mode with a mechanical testing machine (Zwick-Roell Zwicki Z0.5TN, Germany). This instrument provides up to 10 N in the load cell and has 30 mm in diameter compression plates (Fig 3.11a,b). Swelled hydrogels were placed at the center of the compression plates for the measurements. To avoid loss of hydration during the test, a few drops of PBS were added just before the beginning of the measurements. Stress-strain curves were measured under unconfined compression using a velocity of compression of 2 mm/min. The strain rate was limited to 1%/min and the maximum strain was limited to 10%, in agreement with similar procedures found in literature.[302,303] A small initial load of 5 mN was used to promote an adequate contact between the hydrogel samples and the compression plate. The stress, σ, was calculated by dividing the normal force, F, over the hydrogel cross-sectional area, A. The strain, ε, was calculated as the variation in the hydrogel height or plates distance, Δh, divided by the original height or plate distance, H. Young's modulus was calculated from the slope of the linear part of the stress–strain curve, from 0 to 10% strain, where the samples displayed elastic behavior (Fig. 3.11c). Three independent samples per condition were used and statistically compared by Kruskal-Wallis test.

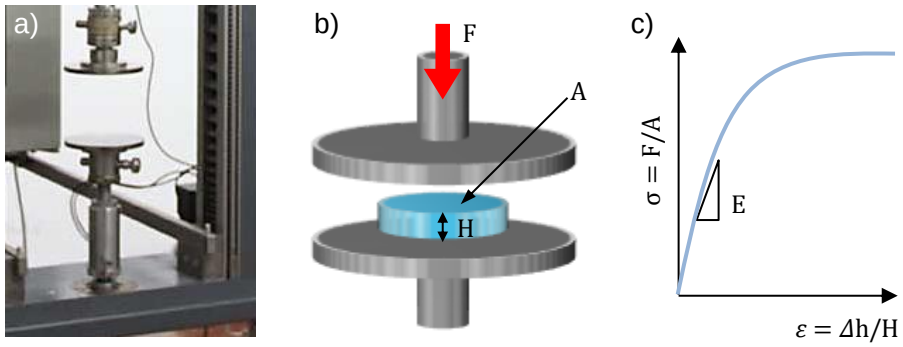

Figure 3.11: Mechanical testing scheme: a) Picture of the Zwicki testing machine, b) drawing of uniaxial compression test where F is the normal force applied, A is the hydrogel cross-sectional area, and H the initial height of the hydrogel. c) Typical stress-strain curve followed by Young's modulus determination (E), where stress is defined by σ and strain by ε.

3.3.5 EFFECT OF ACRYLIC ACID ON THE MORPHOLOGY OF MICROSTRUCTURED HYDROGELS

To determine the effects of acrylic acid on the shape of hydrogel microstructures, a solution of 6.5% w/v $PEGDA_{6000}$ in PBS with 1% w/v I2959 was selected. To this solution, acrylic acid was added in concentrations ranging from 0.06% w/v (8.3 mM) to 1.2% w/v (166.5 mM) (Table 3.3). Polymer solutions without acrylic acid was used as a control.

Acrylic acid concentration						
0%	0.06% w/v	0.12% w/v	0.3% w/v	0.6% w/v	0.9% w/v	1.2% w/v
0 mM	8.3 mM	16.6 mM	41.6 mM	83.3 mM	125 mM	166.5 mM

Table 3.3: Acrylic acid concentrations used in the fabrication of hydrogels for the study of the effects of acrylic acid on the morphology of the hydrogel microstructures.

The solutions were used to fabricate hydrogel microstructures with the photomasks containing windows of 100 µm in diameter, following the procedure described in section 3.2. Microstructured hydrogels were fabricated by UV exposure in two steps, using 10 s of exposure for the formation of the hydrogel base and 70 s of exposure for the formation of the microstructures. After three days of swelling, samples were cut into cross sections and the microstructures were imaged in a bright field or stereoscope microscope. The height of microstructures was determined between their top and the base as described in

section 3.2.5. The diameter of microstructures was measured as an average of the diameters at the tip and diameter at the bottom. Two samples per condition were tested, with at least three measurements. Measurements were done by ImageJ free software. Height and diameter were plotted as a function of acrylic acid content with OriginPro 8.5 software.

3.4 PROTEIN FUNCTIONALIZATION OF PEGDA–ACRYLIC ACID HYDROGELS

Proteins were coupled by carbodiimide reaction by taking profit of the exposed carboxylic groups of PEGDA-acrylic acid hydrogels. (1-ethyl-3-(3′-dimethylaminopropyl)-carbodiimide (EDC) (Sigma-Aldrich, Spain) and N-Hydroxysuccinimide (NHS) (Sigma-Aldrich, Spain) were used as activator agents (Fig. 3.12).[297] Hydrogels were placed in a 24-well plate and they were allowed to swell for three days. Then, they were rinsed in 500 µL of 0.1 M MES buffer at pH 4.7 (ThermoFisher Scientific, Spain) for 10 min and incubated in 500 µL of EDC/NHS (50 mM/30 mM) solution in MES buffer for 30 min for the activation of the carboxylic groups. After that, hydrogels were rinsed twice with Milli-Q water and they were incubated with a protein solution (several proteins were tested). Proteins solutions were prepared in 50 mM HEPES (Sigma-Aldrich, Spain) and 137 mM NaCl (Sigma-Aldrich, Spain) buffer at pH 8.5, and hydrogels were incubated for 1-2 hours to covalently couple the protein to the hydrogels.

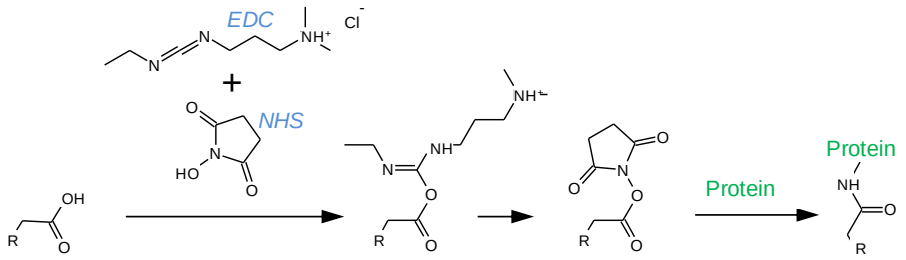

Figure 3.12: Cross-linking strategy used for the coupling of proteins to hydrogels. Carboxyl groups of hydrogels were first activated with EDC and modified with NHS to form a semi-stable NHS-ester. Subsequent amine-coupling of the protein results in a covalent bond (amide bond) between the protein and the hydrogel.

Three strategies were used for protein incubation. The first one was immersing the hydrogels in 500 µL of the protein solution (Fig. 3.13a). This approach is the most used in literature,[297] but it implies a waste of proteins. A second alternative was based on placing a drop of 20 µL of highly concentrated

protein solution (>0.1 mg/mL) on top of hydrogel (Fig. 3.13b). As confinement of the drop on top of the hydrogels was an issue we used a sliced pipette tip as a container, filling it with 50 µL of high concentrated protein solution (Fig. 3.13c). Different proteins were used to functionalize the hydrogels: collagen type I (Sigma-Aldrich, Spain), Streptavidin Texas Red® (ThermoFisher Scientific, Spain), fibronectin (Sigma-Aldrich, Spain) and laminin (Sigma-Aldrich, Spain). To determine the success of the protein coupling reaction, hydrogels were functionalized with fluorescent-conjugated proteins and imaged.

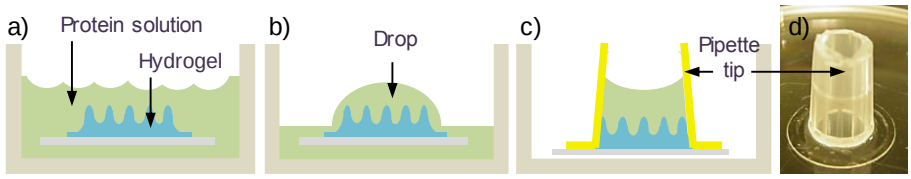

Figure 3.13: Protein incubation strategies. a) Soaking hydrogels in the solution, b) placing a drop on top of hydrogel, and c) using of sliced pipette tip as a container. d) Photograph of the sliced pipette tip placing on the hydrogel sample.

3.4.1 CHARACTERIZATION OF HYDROGEL FUNCTIONALIZATION BY INFRARED SPECTROSCOPY (ATR-FTIR)

ATR-FTIR was used to verify each step of the functionalization process described above. To this end, polymer solutions of 10% w/v $PEGDA_{6000}$ in PBS containing 1.2% w/v acrylic acid (166.5 mM) and 1% w/v I2959 were prepared. Disc-shaped hydrogels of 2 mm in height and 12 mm in diameter were fabricated by exposing the solutions for 300 s to UV light. Then, hydrogels were activated with EDC/NHS solutions of two molarities (6 mM/5 mM and 50 mM/30 mM). After that, the samples activated with 50 mM/30 mM EDC/NHS were functionalized with 500 µL of protein solutions containing collagen type I at two concentrations (0.04 and 0.4 mg/mL). A sample of 4 mg/mL collagen type I solution was analyzed as a reference. Samples were first rinsed thoroughly with Milli Q water, and then, they were allowed to dry during 24 h in a vacuum desiccator. IR spectra were acquired by a spectrophotometer (Nicolet iS 10, ThermoFisher Scientific, Spain). Samples were scanned in the range of 500-4000 cm^{-1} with a resolution of 4 cm^{-1}. 16 scans were performed per hydrogel and the average data were collected. Spectra were plotted with OriginPro 8.5 software and correspond to the average of at least two samples.

3.4.2 PROTEIN FUNCTIONALIZATION AS A FUNCTION OF THE ACRYLIC ACID CONTENT

To study the effect of acrylic acid content in the amount of protein coupled to the hydrogel, disc-shaped hydrogels were prepared. The polymer solution contained 7.5% w/v $PEGDA_{6000}$ in PBS with 1% w/v I2959, and either 0.12% w/v (16.6 mM) or 0.6% w/v (83.3 mM) acrylic acid. Samples were activated following the EDC/NHS protocol and then functionalized with 500 µL of 0.05 mg/mL Streptavidin Texas Red® protein solution. As controls to test unspecific protein adsorption a set of samples without EDC/NHS activation were also incubated with the protein solution. The amount of coupled protein was analyzed by fluorescence microscopy. Hydrogels were mounted with Fluoromont-G (BioNova científica, Spain), and a coverslip was directly placed on top them. They were imaged with a Nikon Eclipse E1000 microscope (Nikon, Japan) using the G-2A filter. Ten pictures/sample (magnification: 10X) were taken keeping same capture parameters of three replicas per condition. Pictures were processed on ImageJ free software. The mean gray value of each image was obtained by the sum of gray values of all the pixels in the image divided by the number of pixels. The intensity average values and standard deviation were plotted with OriginPro 8.5 software. As a non-parametric study, Mann-Whitney U test and Kruskal Wallis test were used to perform the statistical analysis

3.4.3 STUDY OF THE STABILITY OF PROTEIN FUNCTIONALIZATION

Fluorescence microscopy was used to determine the robustness of the protein coupling reaction by evaluating its stability after repeating rinsing. To this end, disc-shaped hydrogels (10 mm in diameter) were fabricated from a solution of 10% w/v $PEGDA_{575}$ and 0.9% w/v acrylic acid (1.25 mM) in PBS containing 1% w/v I2959. The solution was exposed 150 s under UV light. Then, hydrogels were functionalized with 500 µL of 0.05 mg/mL Streptavidin Texas Red® protein solution following the protocol described previously. After the functionalization, hydrogels were thoroughly rinsed with PBS 1, 3, or 10 times. After these rinsing cycles the fluorescence of the samples was measured. For this purpose, hydrogels were mounted with Fluoromont-G, and a coverslip was directly placed on top of them. Three samples of each condition were prepared and observed on a fluorescence microscope (Nikon Eclipse E1000, Japan) using the G-2A filter. At least 5 pictures/sample (magnification: 10X) were taken, keeping same capture parameters (MetaMorph software, USA). Then, images were analyzed by ImageJ free software. The mean gray value of each image was obtained by the sum of gray

values of all the pixels in the image divided by the number of pixels. The intensity average values and standard deviation were plotted with OriginPro 8.5 software.

On the other hand, another set of hydrogels were prepared using the same polymer solutions and fabrication parameters to evaluate the influence of storage time on the protein functionalization. Hydrogels were stored at 4°C in PBS for 1, 3, or 7 days, changing the buffer solution every day. The fluorescence of the samples for each time point was analyzed as described above.

3.5 CELL CULTURE AND CHARACTERIZATION

3.5.1 CELL CULTURE OF NIH-3T3 FIBROBLASTS

NIH-3T3 fibroblasts were purchased from American Type Culture Collection (ATCC, US). Passages 3 to 5 were expanded in 75 cm^2 Nunc™ flasks (ThermoFisher Scientific, Spain) in low glucose Dulbecco's Modified Eagle Medium (DMEM) (Gibco/Brl Life Technologies, Paisley, UK) supplemented with 10% v/v foetal bovine serum (FBS) (Gibco, UK), 1% v/v penicillin/streptomycin (Invitrogen, CA, USA), 1% v/v L-glutamine (Invitrogen, CA, USA) and 1% v/v sodium pyruvate (Invitrogen, CA, USA). When cells achieved 90% of confluence they were detached from the flask by treating them with Trypsin-EDTA (0.25% w/v) (25200, ThermoFisher Scientific, Spain) and incubating them at 37°C for 5 min. Then, the cell suspension was diluted in cell medium and centrifuged at 1000 rpm. Finally, the supernatant was removed and the cells were resuspended in 5 mL of cell medium. The cell density was adjusted by counting cells in a Neubauer chamber (Sigma-Aldrich, Spain). Cell seeding on microstructured or flat hydrogels was carried out by as described in section 3.5.4. After seeding, cells on hydrogels were maintained in an incubator (Galaxy® 14S, Eppendorf, Spain) at 37°C and 5% CO_2 and cell culture medium was exchanged every 2 days.

3.5.2 CELL CULTURE OF MADIN-DARBY CANINE KIDNEY (MDCK) CELLS

MDCK (Madin-Darby canine kidney) cells were a kind gift of the Integrative cell and tissue dynamics group of IBEC. Passages 2 to 4 were expanded in 75 cm^2 Nunc™ flasks in low glucose Dulbecco's Modified Eagle Medium (DMEM) supplemented with 10% v/v foetal bovine serum (FBS), 1% v/v penicillin/streptomycin, 1% v/v L-glutamine, and 1% v/v sodium pyruvate. When cells achieved 70% they were treated with Trypsin-EDTA (0.25% w/v) under incubation at 37°C for 15 min. To stop the effect of the Trypsin-EDTA, cell suspension was diluted in cell medium and centrifuged for 5 min at 1000 rpm,

and supernatant eliminated. Then, the cell pellet resuspended in 5 mL of cell medium. A Neubauer chamber was used to count cell density and adjust it. The cell seeding on hydrogels was carried out as described in section 3.5.4. After seeding, cells on hydrogels were maintained in an incubator at 37°C and 5% CO_2 and cell culture medium was exchanged every 2 days.

3.5.3 CELL CULTURE OF HUMAN EPITHELIAL COLORECTAL ADENOCARCINOMA (CACO-2) CELLS.

Caco-2 cells were kindly provided by the Physiology department from the Faculty of Pharmacy (University of Barcelona). Passages 74 to 77 were expanded and maintained in 75 cm^2 flasks in Dulbecco's Modified Eagle Medium with sodium pyruvate, glutamine, and 4.5 g/L glucose (41965 Gibco, Spain) supplemented with 10% foetal bovine serum (FBS), containing 1% v/v penicillin/streptomycin, and 1% v/v non-essential amino acids (Gibco, UK). Cells were maintained in an incubator at 37°C with 5% CO_2 with medium exchange every 2 days. When they achieve confluence values of 50% to 75%[304] they were treated with 0.02 mM Trypsin-0.5 mM EDTA (25300, ThermoFisher Scientific, Spain) and incubated at 37°C until cells were fully detached (15-20 min). Then, the cell suspension was diluted in cell medium and centrifuged. Finally, the supernatant was removed and cells were resuspended in cell medium. Cell density was adjusted by counting cells in a Neubauer chamber. Cell seeding on hydrogels was carried out as described in section 3.5.4. Caco-2 cells were seeded at low ($2.5 \cdot 10^4$ cells/cm^2) and high ($5 \cdot 10^5$ cells/cm^2) densities. After seeding on the hydrogels, the samples were also maintained at 37ºC in an incubator with 5% CO_2 with regular medium change every 2 days.

3.5.4 CELL SEEDING STRATEGIES

After fabrication, hydrogels were left to swell at least 3 days in PBS. Before cell seeding, hydrogels were immersed in 1 mL of 10% v/v penicillin/streptomycin (Invitrogen, CA, USA) in PBS for 1 h in a new 24-well plate. UV sterilization was avoided to prevent damaging proteins. Cell seeding was carried out by adding 1 mL of a cell suspension, at different cell densities as a function of the cell type and the experiment, on a 24-well plate containing the hydrogels (Fig. 3.14a) and placing carefully the plate in the incubator to let the cells deposit homogeneously everywhere. After 1 day of cell culture, hydrogels were placed in a new sterile 24-well plate. Surface cell seeding density (cell/cm^2)

was calculated by multiplying cell suspension density (cell/mL) per well area (1.9 cm^2).

In addition, two other cell seeding alternatives were explored. The first one was placing a drop of a highly-concentrated cell suspension (> 10^6cells/mL) on top of the hydrogels for 1 hour to allow cell adhesion (Fig. 3.14b), to confine cell adhesion to the hydrogel. Then, 1 mL of culture medium was added to fully cover the hydrogels. However, this strategy sometimes resulted in an inhomogeneous cell seeding. The last strategy consisted on covering the hydrogels with 500 µL of a low-density cell suspension (< 10^5cells/mL) and placing the samples on a rotating plate at 100 rpm for 10 min, to concentrate most of the cells at the center of the well plate and ensure hydrogel cell coverage (Fig. 3.14c). Unfortunately, very often a lot of cells moved and located under the coverslip during spinning.

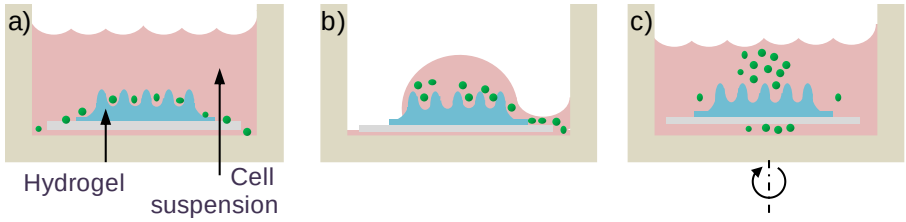

Figure 3.14: Cell seeding strategies for hydrogel cell culturing. a) Simple deposition, b) placing a drop of cell medium on top of hydrogel, and c) rotating the samples to concentrate the cells at the center.

3.5.5 NIH-3T3 CELLS ADHESION ON MICROSTRUCTURED HYDROGELS

Fibroblasts were used as a cell model to assess if PEGDA-acrylic acid hydrogels supported cell culture, meaning that cells were able to attach and cover the microstructures forming a monolayer. To this aim, flat samples were used. Hydrogels were fabricated from 20% w/v $PEGDA_{575}$ in PBS solution containing 2.5% w/v acrylic acid and 0.1% w/v I2959. Samples were exposed 200 s under UV light. After letting the hydrogels swell for 3 days, samples were cut in 7x7 mm squares. Then, they were functionalized with 500 µL of 100 µg/mL fibronectin solution in PBS. Polymer solution without acrylic acid was used as a control. NIH-3T3 fibroblasts were seeded at a density of 10^5 cells/cm^2 and cultured for 4 hours. For NIH-3T3 fibroblasts, nuclei and F-actin were chosen as markers to study cell adhesion and morphology. Samples (with and without acrylic acid) were fixed and nuclei were stained with Hoechst and F-actin with Phalloidin (a high-affinity fluorescence-conjugated F-actin probe), following the protocol described in

section 3.5.8. Three replicas for both conditions were used, and three images were taken at 10X magnification for each sample for randomly selected areas using a fluorescence microscope (Eclipse E1000). Images were analyzed by ImageJ free software. Cell adhesion was obtained by counting the cell nuclei per area. Then, the cell adhesion relative to cell seeding density was calculated and plotted with OriginPro 8.5 software as average of nine pictures. Mann-Whitney U test was used to perform the statistical analysis.

To determine if fibroblasts covered the microstructures forming a monolayer, polymer solutions of 10% w/v $PEGDA_{575}$ in PBS containing 1.25% w/v and 0.1% I2959 were used. Microstructured hydrogels were fabricated using a photomask with windows of 300 µm in diameter and a single UV exposure time of 170 s. Samples were functionalized with 500 µL of 50 µg/mL fibronectin solution in PBS. Fibroblasts were seeded at a density of $2.5 \cdot 10^4$ cells/cm^2 and were cultured for 7 days. Then, hydrogels were fixed and nuclei were stained with Hoechst and F-actin with Phalloidin, following the immunostaining protocol described 2.5.3, and fluorescence images were taken with a Nikon E1000 and a Leica SPE microscopes. Cell coverage was calculated by counting of cell nuclei on three microstructures of three samples, and on the glass coverslip as a control, and was plotted with OriginPro 8.5 software. In addition, confocal microscopy (Leica SPE) was used to obtain detailed images of the cells at different sections of the microstructures.

3.5.6 MDCK CELLS COVERAGE ON MICROSTRUCTURED HYDROGELS

MDCK cells were used as an epithelial cell model to optimize the protein concentration for cell adhesion on our hydrogels. Cells were seeded on PEGDA-acrylic acid hydrogels functionalized with several laminin concentrations. Polymer solutions of 10% w/v $PEGDA_{575}$ in PBS containing 1.25% w/v acrylic acid and 1% I2959 were used. Disc-shaped samples of 10 mm in diameter were fabricated by UV exposure of 150 s. Hydrogels were functionalized with 500 µL of laminin solutions at concentrations of 10, 50, or 100 µg/mL of laminin. MDCK cells were seeded at a density of $2 \cdot 10^5$ cells/cm^2 and cultured for 24 h. As control, MDCK cells were cultured on a 24-well plate without hydrogels. Cell surface coverage was assessed by bright field microscopy (Leica DM IRBE, Germany). At least three images of randomly selected areas were taken of three identical replicas using a 10X magnification. Then, images were analyzed by ImageJ free software. Cell covered areas were measured and the relative covered surface areas (cell covered area/image area) were calculated and plotted with OriginPro 8.5 software. Mann-Whitney U test was used to perform the statistical analysis

In addition, MDCK cells were used to study cell polarization on the microstructured hydrogels fabricated with different conditions. First, two polymer solutions were used to test the influence of polymer concentration on cell polarization: (1) 5% w/v $PEGDA_{575}$ and 0.6% w/v acrylic acid in PBS containing 1% w/v I2959, and (2) 10% w/v $PEGDA_{575}$ and 1.25% w/v acrylic acid in PBS containing 1% w/v I2959. Microstructures were fabricated by a single UV exposure of 170 s, using a photomask with windows of 300 μm in diameter. Hydrogels were functionalized with 500 μL of 100 μg/mL laminin solution. Then, MDCK cells were seeded at $2.5 \cdot 10^4$ cells/cm^2 and the cell coverage on microstructures was checked by bright field microscopy at days 7, and 14. At day 14 samples were imaged by fluorescence and confocal microscopy to evaluate cell morphology and the presence of epithelial cell markers. For this purpose, cell nuclei were stained with Hoechst and F-actin with Phalloidin following the same staining protocol as in the case of fibroblasts. To evaluate cell polarization, the expression of a tight junction-related protein, ZO-1, and cell-cell adhesion-related protein, β-catenin, were studied following the immunostaining protocol described in section 3.5.8.

To test the influence of the microstructure size on the cell coverage, microstructures were fabricated using two photomasks with windows of 100 μm and 300 μm in diameter and identical polymer solutions and exposure times (10% w/v $PEGDA_{575}$-1.25% acrylic acid, and 5% w/v $PEGDA_{575}$-0.6% acrylic acid, exposure time 170 s).

On the other hand, the influence of the hydrogel base on cell coverage was studied using photomasks with windows of 100 μm in diameter. Polymer solutions of 5% w/v $PEGDA_{575}$ and 0.15% w/v acrylic acid in PBS containing 1% w/v I2959 were microstructured by double UV exposure of 10 s for the formation of a hydrogel base and 150 s for the formation of the microstructures. These samples were compared to equivalent microstructures without hydrogel base. Functionalization was done by placing a drop of 20 μL of a 500 μg/mL laminin solution on top of microstructures. MDCK cells were seeded at $2.5 \cdot 10^4$ cells/cm^2 and cultured for 21 days. Cell coverage was checked at day 14 and 21 and cell nuclei and F-actin were analyzed by fluorescence microscopy, and confocal microscopy.

Finally, to test the influence of PEGDA molecular weight on the cell coverage, polymer solutions of 10% w/v $PEGDA_{6000}$ and 0.6% w/v acrylic acid in PBS containing 1% I2959 were used and compared to microstructured hydrogels made of $PEGDA_{575}$. Hydrogels were fabricated using photomasks of 100 μm windows under UV light exposure of 10 s for the formation of a hydrogel base and 150 s for the microstructuring. Then, hydrogels were functionalized with a 20 μL drop of 500 μg/mL laminin solution, on top of microstructures. MDCK cells were

seeded at $1.5 \cdot 10^4$ cell/cm^2 and cultured for 14 days. Hydrogels were qualitatively assessed by stereoscope microscopy and cell nuclei and F-actin by confocal microscopy. Experimental conditions tested are listed in Table 3.4.

Samples were mounted using the holder mounting described in section 3.5.8. Through an inverted confocal microscope, Leica SPE, serial sections at 10X magnification were taken and stacked to obtain three-dimensional reconstructions. The size of z-sections varied depending on the sample, ranging from 1to 5 µm.

Study	Polymer Solutions	Photomask window diameter
Polymer concentration	5% w/v PEGDA575 - 0.6% w/v acrylic acid 10% w/v PEGDA575 - 1.25% w/v acrylic acid	300 µm
Microstructure size (diameter)	5% w/v PEGDA575 - 0.6% w/v acrylic acid 10% w/v PEGDA575 - 1.25% w/v acrylic acid	100 µm 300 µm
Hydrogel base	5% w/v $PEGDA_{575}$ - 0.15% w/v acrylic acid	100 µm
PEGDA molecular weight	10% w/v PEGDA6000 - 0.6% w/v acrylic acid	100 µm

Table 3.4: Experimental conditions for the study of MDCK cells coverage on microstructured hydrogels.

3.5.7 CACO-2 CELL POLARIZATION ON MICROSTRUCTURED HYDROGELS

As Caco-2 cell requirements are different from those of fibroblasts and MDCK, cell adhesion was tested using two protein concentrations for functionalization. Disc-shaped hydrogels were fabricated from 6.5% w/v $PEGDA_{6000}$ and 0.3% w/v acrylic acid (41.6 mM) in PBS containing 1% I2959. PEGDA-acrylic acid hydrogels were functionalized in 500 µL of laminin solutions with concentrations of 50 and 100 µg/mL. Finally, hydrogels were seeded at a density of $5 \cdot 10^5$ cells/cm^2 and cultured for 24 h. Cell adhesion and spreading measured as surface coverage was assessed by bright field microscopy (Nikon Eclipse Ts2).

To study the cell polarization and the coverage of the 3D surface, PEGDA-acrylic acid hydrogels were microstructured using the polymer solutions and fabrication parameters producing the shape and dimensions closest to the villi of native intestinal tissue. Microstructured hydrogels were fabricated from 6.5% w/v $PEGDA_{6000}$ and 0.3% w/v acrylic acid (41.6 mM) in PBS containing 1% w/v I2959. A photomask with windows of 100 µm in diameter was used. The fabrication process was carried out by 10 s of UV light exposure of 10 s for the

formation of the hydrogel base and 70 s of UV exposure for the formation of the microstructures. Then, the hydrogels were functionalized by using a sliced pipette tip and a drop of 50 µL of a 250 µg/mL laminin solution placed on top of the microstructures for 1 h. Cells were seeded at a density of $5 \cdot 10^5$ cells/cm^2. Cell culture was imaged at 7, 14 and 21 days by bright field microscopy (Nikon Eclipse Ts2) to determine the cell coverage. Cell polarization was assessed by cell morphology, so cell nuclei and F-actin were stained and imaged. In addition, epithelial cell markers, ZO-1, β-catenin, and villin (the major protein associated with actin in the microfilament core of intestinal microvilli)[305] were stained. Cell markers were analyzed by fluorescence and confocal microscopies. As controls, Caco-2 cells were cultured on Transwell® inserts of 12 mm in diameter containing polycarbonate porous membranes of 0.4 µm in pore size (Sigma-Aldrich CLS3401, Spain). Cells were seeded at same cell density as on hydrogels and cultured for 21 days.

Samples containing microstructured hydrogels were mounted using a holder mounting described in section 3.5.8, and samples from Transwell® were prepared cutting the membranes and mounting them between two coverslips with mounting medium. Through inverted confocal microscopes (Leica SPE, SP2) serial sections at 10X magnification were taken and stacked to obtain three-dimensional reconstructions. The size of z-sections varied depending on the sample, ranging between 0.5 and 2 µm.

3.5.8 IMMUNOSTAINING

Cell morphology and cell polarization were studied through the immunostaining of nuclei, filamentous actin (F-actin), and epithelial cell markers and were performed in the 24-well plates used for cell culture. Cells on hydrogels were fixed with 500 µL of 4% w/v paraformaldehyde (Sigma-Aldrich, Spain) at room temperature (RT) for 30 min on a rotating plate set at 100 rpm. Then, samples were rinsed twice with 500 µL of 50 mM Tris-Cl and 150 mM NaCl buffer saline (TBS) solution (ThermoFisher Scientific, Spain) at RT for 5 min on a rotating plate (100 rpm).

To permeabilize the cell membrane, cells were washed with 500 µL of TBS containing 0.1% v/v Triton X-100 (Sigma-Aldrich, Spain) (T+) at RT for 30 min on a rotating plate (100 rpm). To prevent nonspecific binding of the antibodies, samples were blocked. Blocking was carried out incubating the samples in 500 µL of TBS containing 3% v/v donkey serum (Gibco, UK) and 0.3% v/v Triton X-100 (T++) at RT for 2 hours on a rotating plate (100 rpm). After blocking, samples were incubated in 500 µL of T++ containing the primary

antibodies. Goat anti-ZO-1 (ab190085 Abcam, UK) was used at 2 µg/mL, rabbit anti-β-catenin (ab2365 Abcam, UK) at 5 µg/mL and mouse anti-villin (ab201989 Abcam, UK) at 1 µg/mL. The incubation was performed for 2 hours at room temperature on a rotating plate (100 rpm) and overnight at 4°C. Then, the samples were washed three times with 500 µL T+ for 5 min at 100 rpm. After that, samples were blocked by the incubation in 500 µL of T++ for 2 hours at room temperature.

Then, samples were incubated with secondary antibodies or 160 nM Alexa Fluor® 568 Phalloidin (ThermoFisher Scientific, Spain) in 500 µL of T++ 2 hours at room temperature. Anti-goat Alexa 568 (A11057, ThermoFisher Scientific, Spain) was used at 2 µg/mL, anti-rabbit Alexa 647 (Jackson Immunoresearch, USA) was used at 2 µg/mL, and anti-mouse Alexa 488 (A21202, ThermoFisher Scientific, Spain) at 2 µg/mL. Then, samples were washed three times in 500 µL of T+ and incubated in 500 µL of T++ containing 16.2 µM Hoechst 33342 (ThermoFisher, Spain) or 300 nM DAPI (ThermoFisher Scientific, Spain), which stain nucleic acid, for 15 min on a rotating plate (100 rpm) and washed twice in 500 µL of TBS.

Considering the full height of hydrogels, a mounting holder was designed and fabricated to prevent the squashing of the microstructures (Fig. 3.15).

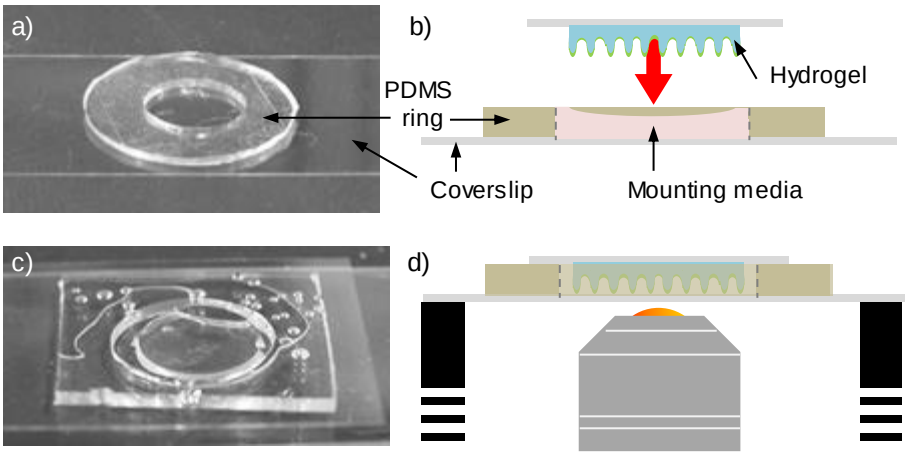

Figure 3.15. Schematics of mounting set-up for the microscopy imaging of microstructured hydrogels. a) Picture of the PDMS ring placed on a coverslip. Cross-section (b) of the mounting. c) Picture of the hydrogel sample mounted in the PDMS ring. d) Illustration of how samples were placed on the confocal microscope.

A PDMS ring of 10 mm in its inner diameter and 1 mm in height was fabricated and placed on a large coverslip (600 x 24 mm) (Menzel Gläser, ThermoFisher Scientific, Spain). The PDMS ring and coverslip were sonicated in

ethanol 96% v/v for 5 min and then blown dried with a nitrogen stream before sealing it without any treatment. The container was then filled with Fluoromont-G and the microstructured hydrogels, which are adhered on a coverslip after fabrication, were placed on top, embedded in the mounting medium (Fig. 3.14). This set-up allowed the imaging of the microstructures by confocal microscopy.

3.5.9 ANALYSIS OF CELL NUCLEI MORPHOLOGY AND ORIENTATION

Cell nucleus is deformed and oriented by the spatial disposition of the cell.[306] Therefore, nuclei morphology and orientation with respect to the basal cell surface could be used as markers for cell polarization. For this purpose, the shape and orientation of the nucleus of Caco-2 cells cultured for 14 and 21 days on microstructured hydrogels were analyzed and compared to cells cultured on Transwell® (0.4 μm pore size polycarbonate membrane) for 21 days (negative control) and on representative images of a cross section through the center and a longitudinal cross section of a villous of small intestine (positive control), from the medical cell biology web site of the Yale School of Medicine.[307]

Microstructured hydrogels and Transwell® samples were observed under a Leica SPE and SP2 laser-scanning microscopes. Samples after 14 days (3 replicas) and 21 days (2 replicas) of cell culture were used. Confocal z-stack images were acquired at 1 μm intervals, and processed using ImageJ to identify each nucleus individually (Fig. 3.16a). First, the image threshold was adjusted to isolate the nucleus from the background. Second, thresholded images were converted to binary (Fig. 3.16b). Finally, nuclei were fitted to ellipses by using the analyze particles tool (Fig. 3.16c). Aspect ratio (major axis/minor axis) and orientation (α) of the ellipses in the image framework were measured by default (ImageJ software). However, such angle (α) does not directly correspond to the angle described between the nuclei and the surface of the microstructure. To obtain the normal angle of the nuclei to the hydrogel surface (θ) we proceeded as follows (Fig. 3.16d). First, the contour and center of the microstructures were identified for each image. Secondly, the position vectors between the position of the center of the microstructure and the center of each nucleus (ellipse) were evaluated. Then, the angle defined by these vectors in the image framework (β) was measured (Fig. 3.16c). Finally, we could obtain the nuclei orientation on the surface (θ) by subtracting the angle of the ellipse (α) from the angle of the position vector (β), as equation shows (Fig. 3.16d). The same procedure was carried out with the images of cross section through the center of native villi.

$$\theta = \beta - \alpha \qquad \text{Eq. 19}$$

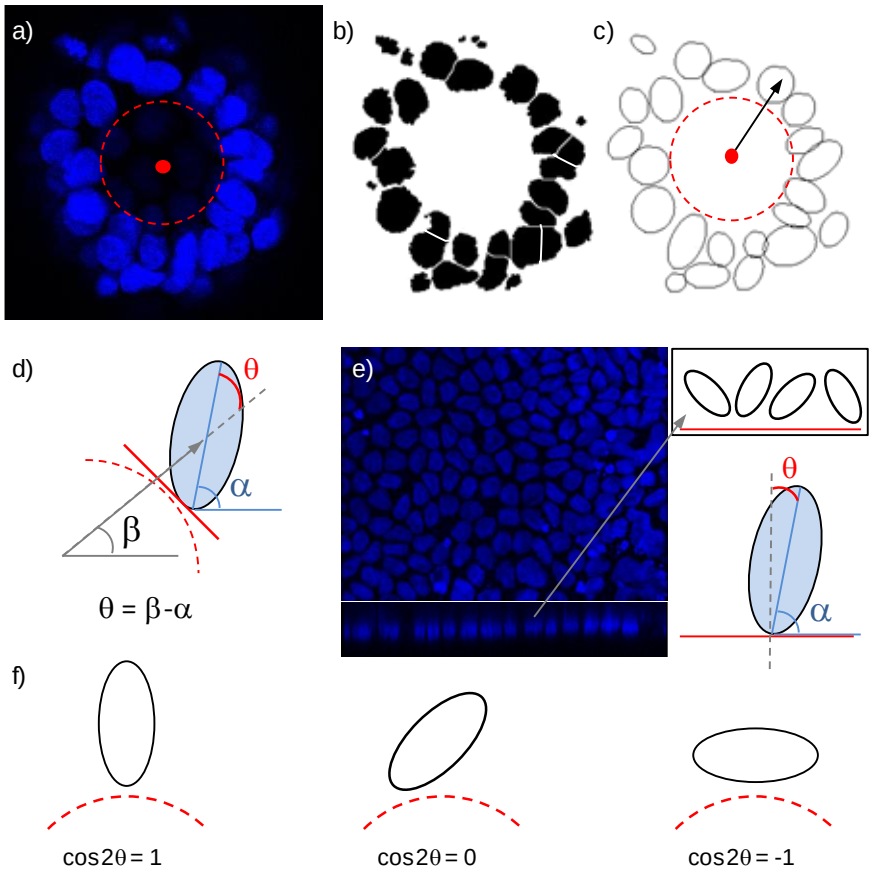

Figure 3.16. Schematic representation of image processing in the nuclei orientation analysis. a) Confocal stack of microstructured hydrogel, showing the nuclei in blue, b) binary image, and c) ellipse fitting. Microstructure contour is depicted as a dashed red line, and its center as a red dot. The arrow in c) represents a vector from the center of the microstructure to the center of an ellipse (nucleus). d) Drawing of the nuclei angle estimation. Angle of the nuclei major axis (α) and the vector (β) with respect to horizontal axis, and normal nuclei angle with respect to the microstructured surface (θ). e) Confocal stack of cells on a Transwell®, showing the nuclei in blue. Orthogonal views were used to the ellipse fitting. f) Drawings relating cos2θ with nuclei orientation.

In the case of Transwell® (3 replicas) cross sections were obtained by using the orthogonal view tool (ImageJ) from the confocal reconstructions. Nuclei were ellipse fitted and the angle of the ellipse orientation (α) was taken as nuclei orientation, because Transwell® has a flat surface which was aligned with the

horizontal axis. To obtain θ, complementary angle was subtracted (Fig. 3.16e). The same procedure was carried out with the images of longitudinal cross section of native villi.

The nuclei aspect ratio of Caco-2 cells cultured on Transwell® and on hydrogel, were plotted and compared with the aspect ratio of the nuclei from the images of cross-sectioned native villi. The angle of nuclei respect to the surface was plotted in a wind rose diagram, and the alignment between the nuclei orientation and the direction normal to the surface was assessed by the order parameter <cos 2θ>. If nuclei were perpendicular to the surface, <cos 2θ> value was 1, whereas if nuclei were parallel to the surface, its value was -1 (Fig. 3.16f). Graphs were plotted with OriginPro 8.5 software and Mann-Whitney U test and Kruskal Wallis test were used to perform the statistical analysis.

3.6 TRANSEPITHELIAL ELECTRICAL RESISTANCE (TEER) MEASUREMENTS OF CACO-2 CELL MONOLAYERS

3.6.1 TEER MEASUREMENTS BY A VOLTOHMMETER

Transepithelial electrical resistance (TEER) is a quantitative technique widely used to measure the integrity of semipermeable cell barriers. TEER of epithelial monolayers is usually measured in a standardized set-up which consists on cell monolayers cultured on semipermeable filter inserts (Transwell®) that creates two separate compartments (upper and lower compartment) (Fig. 3.17a). An electrode can be introduced in each of the compartments to measure the electrical resistance between them when the cell monolayer is formed (Fig. 3.17). At the end, TEER expressed in $\Omega \cdot cm^2$, is calculated as the measured resistance multiplied by the surface area of the cell monolayer. In the present study, electrical measurements were performed in collaboration with the Physiology department of the Faculty of Pharmacy (UB). We used an Epithelial Voltohmmeter (Millicell-ERS system, Merck-Millipore, Spain), which applies an AC square wave of 20 mV of amplitude at a frequency of 12.5 Hz (Fig. 3.17b). Measurements are carried out using alternating current (AC) because direct current (DC) can damage both the cells and the electrodes. A pair of electrodes popularly known as “chopstick” electrodes was used. Each stick of the electrode pair (4 mm wide and 1 mm thick) contains a silver/silver chloride pellet to measure voltage and a silver electrode to allow the pass of current. STX3/“chopstick” silver electrode pair was used, which allows adjusting the distance between electrodes to avoid sample damaging and inaccurate measurements (Fig. 3.17c). To use our hydrogels with the standard Transwell®-

based approach, we had to be sure that once hydrogels were installed in the upper compartment all the electrical current was forced to pass through them, as shortcuts due to bad sealing between the hydrogels and the Transwell® walls would return false results.

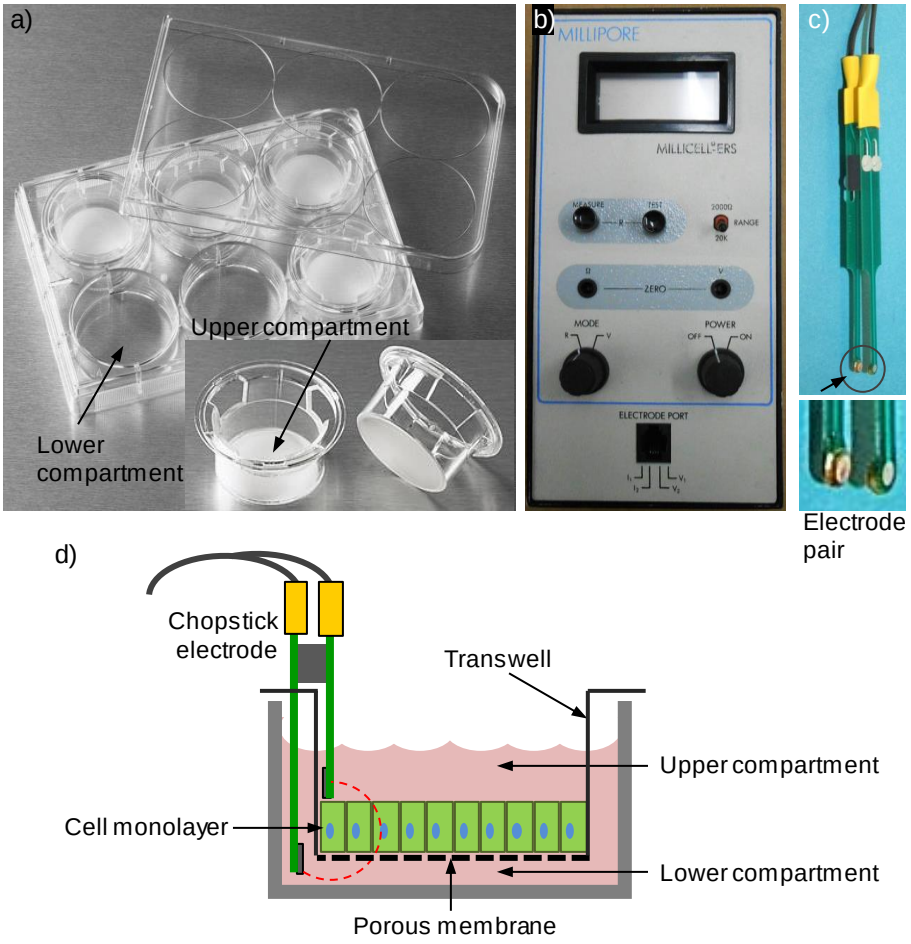

Figure 3.17: Standardized set-up of TEER measurements by voltohmmetry. a) 6-well plate of Transwell® porous membrane with inserts of 24 mm in diameter. b) Voltohmmeter, and c) STX3/"chopstick" silver electrode pair. d) Scheme of TEER measurements on Transwell® membrane system with a cell monolayer. Pass of current is drawn by a red dash line.

Two experimental approaches were assayed: 1) *in situ* hydrogel polymerization and 2) outside polymerization and posterior sealing. *In situ* polymerization consisted in filling Transwell® inserts of 12 mm in diameter with polycarbonate membranes with pores of 0.4 µm in size (Sigma-Aldrich CLS3401,

Spain) with the polymer solution. Then, a coverslip and a photomask were placed just below the Transwell®. This set-up did not allow the use of the Mask aligner because the system had to be irradiated from the bottom part (Fig. 3.18a). As an alternative UV source, a UV spot cure lamp (Excelitas Technologies UV omnnicure s1000, Germany) was used, which made possible to place the UV source at the bottom of the Transwell® (Fig. 3.18b).

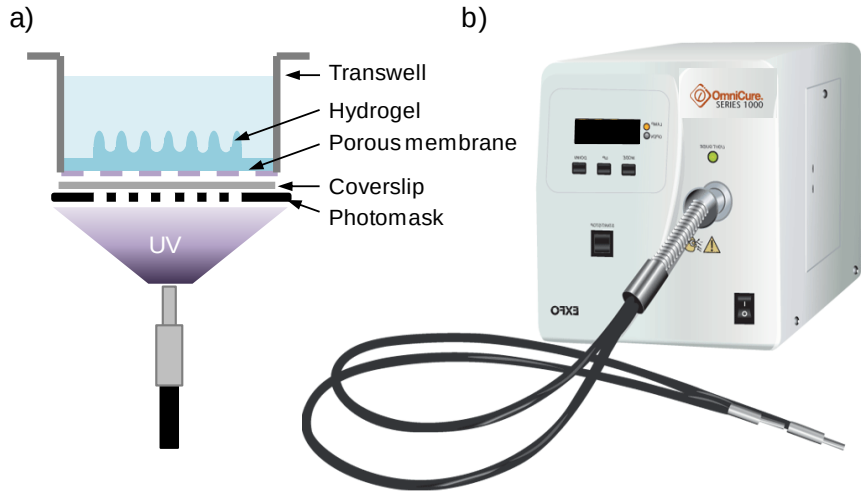

Figure 3.18: a) Scheme of the *in situ* hydrogel polymerization approach In situ hydrogel polymerization approach. b) UV spot cure lamp.

The second approach was implemented on Transwell® inserts of 24 mm with polycarbonate membranes with pores of 0.4 µm. Firstly, the insert was reversed and the outer part of the porous membrane was sealed with PDMS. PDMS prepolymer was prepared by mixing the base polymer with the curing agent in a 10:1 ratio and degassing the mixture under a vacuum for 1 h. The prepolymer was then deposited on the boundaries of the outer part of porous membrane, leaving a circular PDMS-free space of about 10 mm in the center (Fig. 3.19a-c). Transwell® and PDMS were left to dry in a tissue culture cabinet hood (Class II Type A2 Biological Safety Cabinet) for 24 hours, in sterile conditions. Then, microstructured hydrogels, fabricated onto coverslips, were detached from them by a scalpel and placed carefully inside the Transwell® (in the inner part) (Fig. 3.19d-f). Then, the hydrogels placed in the Transwell® inserts were left to dry the excess of PBS by placing them in the tissue culture cabinet hood for 15 min, in sterile conditions. After that, a ring-shaped pressure sensitive adhesive of 300 µm in height (Lintec, Japan) was cut (10 mm inner diameter, 20 mm outer diameter) and was placed around the hydrogel, to seal the system (Fig. 3.19g-i). To test TEER with this system, microstructured hydrogels were fabricated using

polymer solutions of 6.5% w/v $PEGDA_{6000}$ in PBS containing 0.3% w/v acrylic acid and 1% w/v I2959. Polymer solutions were exposed at UV for 10 s to form the hydrogel base, and then 70 s to form the microstructures. After fabrication and swelling for 3 days, samples were removed from the coverslips and placed in the Transwell® membranes. Then, functionalization was carried out by placing a sliced pipette tip as a container on top of hydrogel, and filling with 50 µL of a 250 µg/mL laminin for 1 hour. Caco-2 cells were seeded at $5 \cdot 10^5$ cells/cm^2 and samples kept at 37°C and 5% CO_2 and filled with culture medium, changed every two days.

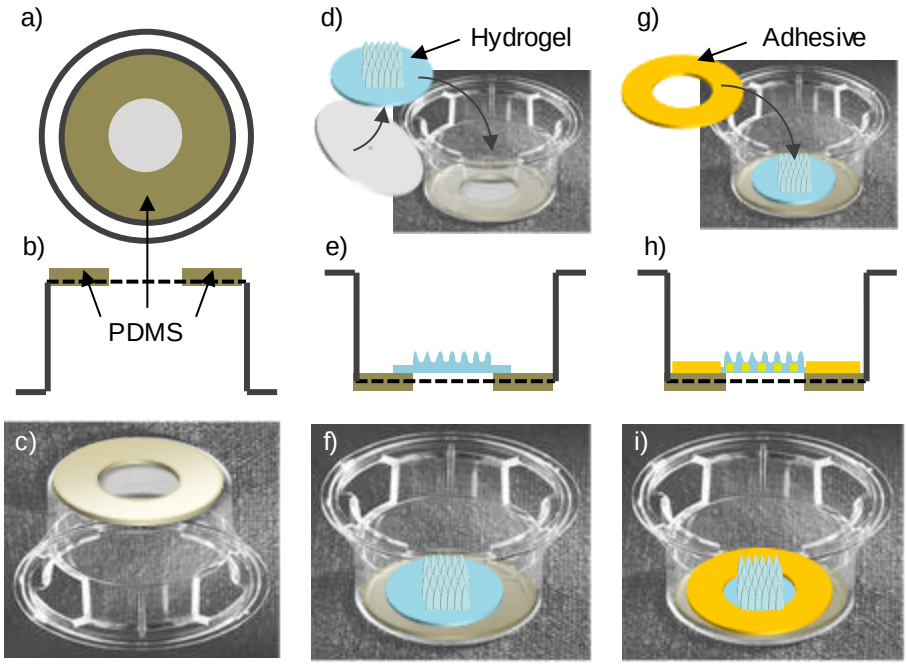

Figure 3.19: Overview of hydrogel sealing on Transwell®. a) Top view, and b) cross-section after PDMS (brown) deposition on the outer part of the porous membrane (dashed line). d) Scheme of hydrogel (blue) placing in the inner part of Transwell® and e) cross-section. g) Scheme of the sealing of the inner part by the use of an adhesive (yellow), and h) cross-section. Modified pictures of Transwell® after c) PDMS deposition f) hydrogel incorporation and i) addition of the adhesive.

TEER measurements were carried out at day 7 and day 21 of culture. To increase the accuracy of the results, readings were done per triplicate for each sample. To subtract the effect of hydrogel material on the resistance measurements, hydrogels without cells were also measured. Transwell® without cells as a negative control of barrier formation, and Transwell® cultured with Caco-2 cells as a positive control of barrier formation were also used. In addition,

at day 21 ethylenedinitrilo-tetraacetic acid (EDTA) treatment was applied by incubating the samples in a 50 µM EDTA solution for 5 min at 37°C, and then measuring the TEER. Three samples for each condition were used. The experimental layout is shown below (Fig. 3.20).

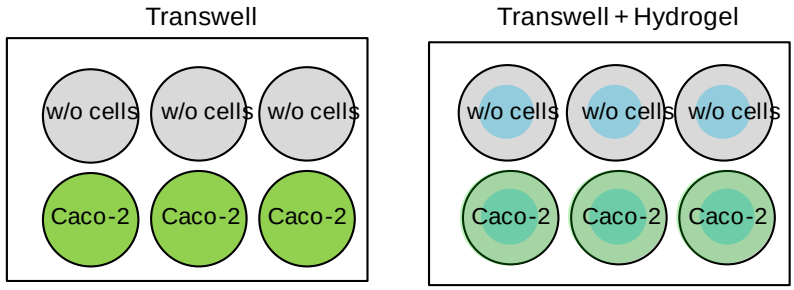

Figure 3.20: Experimental layout of the TEER assay on Transwell® inserts. Control samples (with and without cells) on Transwell® without hydrogels were placed in the same 6-well plate, as the samples with hydrogel (with and without cells) were placed in a different 6-well plate.

The resistance of the cell monolayer ($R_{monolayer}$) was calculated by subtracting the resistance measured on cell-free inserts (Transwell® or Transwell® with hydrogel) (R_{blank}) from the total resistance measured across the cell monolayer for both the samples with and without hydrogel (R_{total}), see equation 20. Results were then multiplied by the total surface area of the insert or hydrogel (estimated from confocal microscopy experiments) to express TEER in $\Omega \cdot cm^2$ (equation 21). Data analysis and plots were carried out with OriginPro 8.5 software. Mann–Whitney U test was used on the statistical comparison of two conditions.

$$R_{monolayer} = R_{total} - R_{blank} \quad \text{Eq. 20}$$

$$TEER_{monolayer} = R_{monolayer} \times \text{total surface area} \quad \text{Eq. 21}$$

3.6.2 TOTAL SURFACE AREA QUANTIFICATION BY CONFOCAL MICROSCOPY

For the microstructured hydrogels, their total surface area is an important parameter. Here, we estimated this value by reconstructing 3D images of the microstructures by fluorescent confocal microscopy z-stacks. After fabrication, samples were activated and functionalized with 500 µL of 0.05 mg/mL Streptavidin Texas Red® protein solution.

Through an inverted confocal microscope (TCS SPE, Leica, Germany) serial sections of about 1 µm in thickness at 10X magnification were taken and stacked to obtain three-dimensional reconstructions of the samples. The samples were oriented in such a way that microstructures were close to the objective (Fig. 3.15d). Thanks to the working distance of the 10X objective (3 mm) the whole height of the microstructures was imaged. One representative sample of each type of microstructured hydrogels was used to obtain three-dimensional reconstructions. Once obtained 3D reconstructions, at least five different regions of the rendering, containing different number of microstructures, were analyzed. The total surface area of 3D microstructures was determined by the surface tools of IMARIS software. To relate the 2D and the 3D surface areas (Fig. 3.21), a surface corrector factor (SCF) was determined as the fraction between these two measurements (Eq. 21).

$$SCF = \frac{\text{3D total Surface area}}{\text{2D Hydrogel area}} \qquad \text{Eq. 22}$$

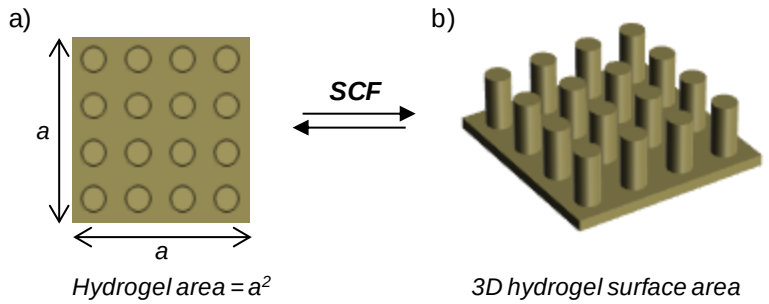

Figure 3.21: Illustration of the 2D 3D total surface area, parameters used in the calculation of the surface corrector factor (SCF).

3.6.3 TEER MEASUREMENTS BY IMPEDANCE SPECTROSCOPY ANALYSIS

Impedance spectroscopy is usually performed by the application of AC of small amplitude signal within a frequency range and measuring the amplitude and phase response of the impedance as a function of the frequency.[94] When applied to cell monolayers, impedance spectroscopy provides additional information about the capacitance of the cell layer with respect to the single frequency method (Voltohmmeter). Impedance, Z, is the ratio of the voltage to the current in on AC circuit. Impedance is a complex function and can be expressed by a real (R) and imaginary part (j is the imaginary unit and X the reactance)

(equation 23) or, on the polar form, as a modulus |Z| and an angle (θ) that gives the phase difference between voltage and current (equation 24).

$$Z = R + jX \quad \text{Eq. 23}$$

$$Z = |Z| \cdot e^{j\theta} \quad \text{Eq. 24}$$

Impedance spectroscopy measurements were performed in collaboration with the Biomedical Applications Group from the Centro Nacional de Microelectrónica (CNM) of the CSIC (Spanish National Research Council). This group has developed a bioreactor with two chambers and integrated electrodes for impedance spectroscopy measurements and the electronics for monitoring the impedance of cell barriers along the time and within a range of frequencies (Fig. 3.22). This system has been successfully used to perform electrical impedance spectroscopy (EIS) measurements on a model of blood brain barrier model.[308] This device consists of two plates with interdigitated electrodes that are sealed together with a porous membrane in between. This sealing creates two separated compartments in a similar way that a Transwell®. Cells are cultured on the porous membrane which with the help of two sheets of pressure-sensitive adhesives (PSA) (Adhesive Research, UK). Silicone gaskets of 0.5 mm in height define three independent cell culture chambers (4 x 20 mm in size) in a circular device of 45 mm in diameter (Fig. 3.22).[308] To ensure the correct supply of cell medium while measurements take place, upper and lower plates have a microfluidic system. To use this system, we adapted the fabrication process to perform the *in-situ* polymerization of our hydrogels with and without microstructures. For this purpose, a porous membrane with two adhesive (PSA) covers was used instead of a coverslip. The dimensions and layout of the PDMS container of our fabrication chip were also modified and a new version with three individual channels of dimensions 7 x 30 mm was produced (Fig. 3.23). In addition, the photomasks were also redesigned now to contain three areas (7 x 30 mm) of arrays of windows 100 μm in diameter that aligned with the membrane areas (Fig. 3.23a). The pools created by PDMS were filled with the polymer solution and exposed under UV light using the Mask aligner instrument.

Three types of membranes were used: polycarbonate of 1 μm pore size (WHA70604710, Sigma-Aldrich, Spain) and 0.4 μm pore size (HTTP04700, Merck–Millipore, Spain), and 1 μm pore size polytetrafluoroethylene (JAWP04700, Merck-Millipore, Spain). A nylon mesh was also used instead of the porous membrane, and was homemade cut and placed between the adhesive sheets. To test the influence of the porous membrane on the microfabrication

process, UV absorbance of the membranes was measured by a spectrophotometer (UV-VIS JASCO, Spain) within the range of 260 – 600 nm and 0.1 nm resolution. In addition, the intensity of UV light through membranes was measured at 365 nm by a UV intensitymeter (Model 100, Suss Microtec, Germany) and compared to the intensity measured directly under the light source.

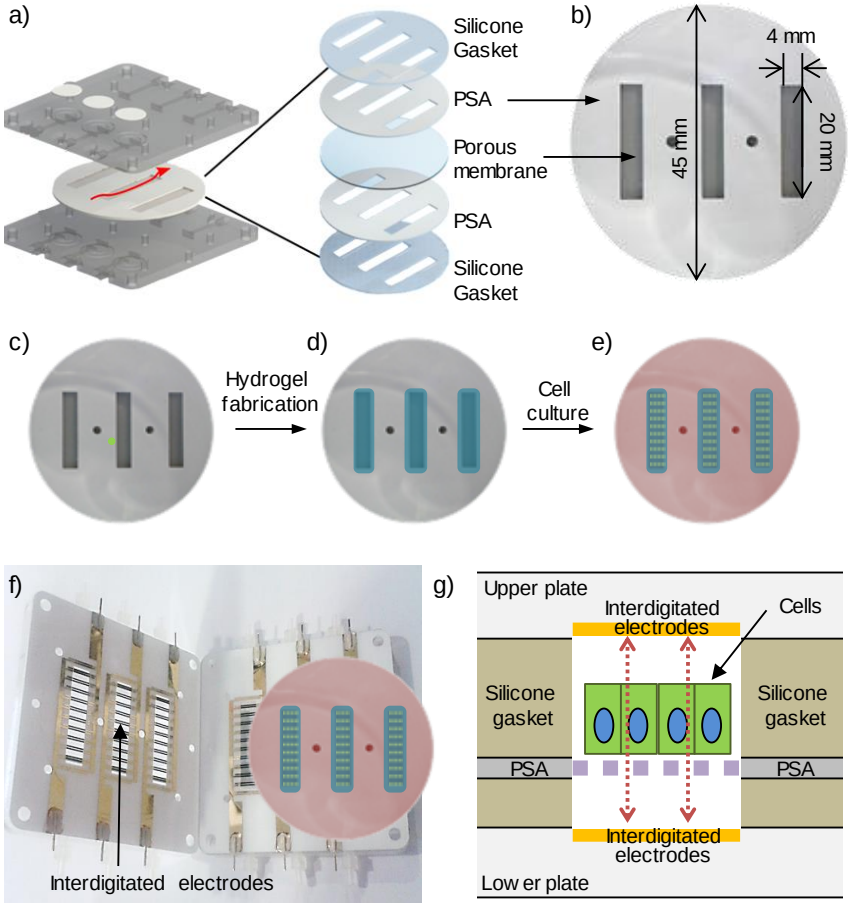

Figure 3.22: Schematic set-up for electrical impedance spectroscopy measurements of cells grown on hydrogels. a) Assembling parts of the bioreactor (modified from Yeste *et al.*)[308] including a schematic decomposition of the b) circular device containing the porous membrane. Experimental set-up procedure for mounting the hydrogels in the chamber. Using circular insert (c), hydrogels (in cyan) are fabricated on the surface of a porous membrane (d), and Caco-2 cells (green dots) are cultured on them (e). Finally, the circular insert was placed within the bioreactor. f) Picture of upper and lower plates where interdigitated electrodes are shown. g) Drawing of cross-section of one of the channels of the device. The porous membrane (violet dash line) fitted by adhesive (PSA) and silicone gaskets to develop cell culture wells. Interdigitated electrodes are represented in yellow, and pass of current in red dash double arrows.

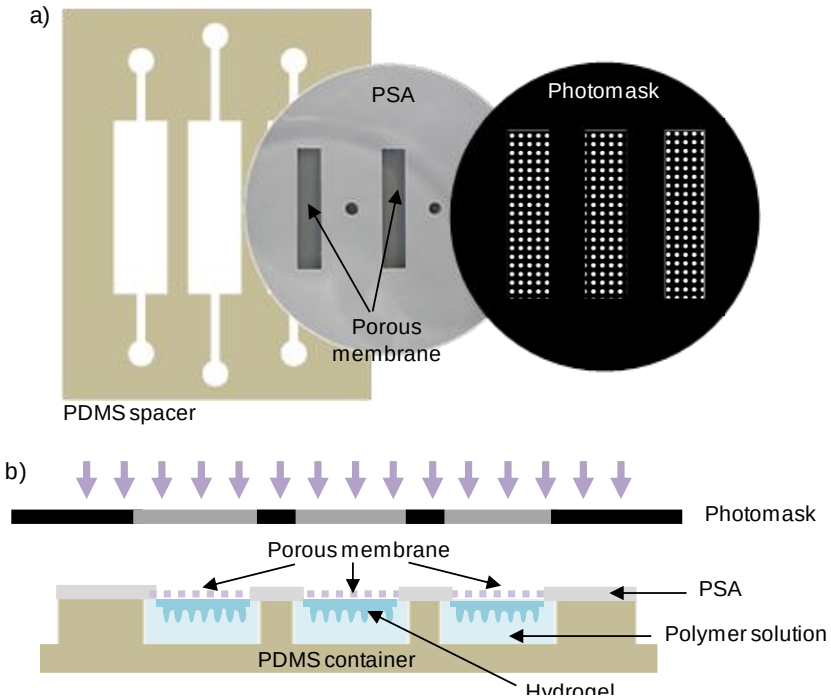

Figure 3.23: Hydrogel Fabrication set-up modified for EIS measurements. a) Illustration of the modified pieces of set-up. PDMS stencil in brown, porous membrane fixed by PSA in gray, and a circular photomask with three arrays of windows. b) Cross-section of the final fabrication device.

After fabrication, the swelling of the hydrogel can make them detach from the membranes and produce current leakages in TEER measurements. To keep hydrogels well adhered to the porous membranes, polycarbonate membranes were silanized using 3-(trimethoxysilyl)propyl methacrylate (TMSPMA, Sigma-Aldrich, Spain). We selected this silane because polycarbonate surface can be photo-chemically activated[309] by the immobilization of silanes In addition, TMSPMA has an acrylate group that can bind PEGDA and keep hydrogels covalently attached. Two protocols were used for the silanization procedure. In the first one, membranes were dried in the oven at 65°C for 30 minutes. Then, their surface was activated by placing them in an oxygen plasma cleaner (Harrick Scientific, Expanded Plasma Cleaner PDC-002, USA) for 2 min. Immediately after that, the membranes were immersed in the silane solution for 10 min. Silane solution was made by diluting TMSPMA at 2% v/v in absolute ethanol and 3% v/v of glacial acetic acid (1:10 acetic acid:Milli-Q water). Then, membranes were thoroughly rinsed by ethanol absolute and dried in the oven at 65°C for 30 min. The second protocol was based on the use of an UV cleaner (Bioforce Nanoscience, UV.TC.220, USA) for 15 min to photo-chemically activate the surface

of membranes.[309] The same silane solution was used and membranes were immersed for 1 to 2 hours. Then, membranes were thoroughly rinsed by ethanol absolute and dried in the oven at 65°C for 30 min. Polymerization on PFTE membranes and nylon mesh was attempted without further modifying these membrane materials.

Impedance spectroscopy measurements were carried out on 1 μm pore size polycarbonate membranes silanized by the second protocol. Microstructured hydrogels were fabricated using polymer solutions of 6.5% w/v $PEGDA_{6000}$ in PBS containing 0.3% w/v acrylic acid and 1% w/v I2959. Three channels were filled with the polymer solution and were exposed at UV for 10 s to form the hydrogel base, and then 70 s to form the microstructures. The hydrogels attached on membranes were rinsed in PBS and allowed to swell in PBS for at least 3 days. Functionalization was done by immersing the porous membranes in 5 mL of 50 μg/mL laminin solution for 1 hour. Caco-2 cells were then seeded on each of the three individual hydrogels by carefully depositing 250 μL of cell suspension containing $2.5 \cdot 10^6$ cells/mL, to achieve a density of approximately $5 \cdot 10^5$ cells/cm^2. To ensure cell attachment at the proper location, membranes were placed in an incubator but not fully covered by the cell medium for 1 hour. Then, porous membranes where placed on a 96 mm in diameter TPP petri dish (Sigma-Aldrich, Spain) covered by cell medium and placed inside an incubator, changing the cell medium every two days. After 14 days of cell culture, membranes were placed between two silicon gaskets and then the "sandwich" was placed in the modular bioreactor closed using screws.

TEER assays were performed by the measurement of impedance spectra at 20 frequencies, ranging from 100 Hz to 1 MHz, using an a portable 4 wire bioimpedance meter.[310] First, measurements were done in parallel at the three channels of the circular device and the resulting impedance (of each channel) across the cell monolayer on the hydrogel $Z_{measured}$ was recorded. Then, the hydrogels containing cells were removed from the porous membrane and the impedance of the silanized membranes (Z_{sm}) was measured. In addition, the impedance of the porous membrane alone Z_{blank} was used as a control. To obtain impedance spectra of cell barriers, the Z_{sm} was subtracted from the $Z_{measured}$ and fitted (using the least-square method in Matlab) to an equivalent electric circuit that describes the impedance spectra of a cell barrier.[43] Equivalent circuit analysis of the measured impedance spectra was performed to obtain the electrical parameters that can be applied to characterize the cellular barrier properties. In this circuit, the current flows through the junctions between cells (paracellular route) or through the cell membrane of the cells (transcellular route). The tight junction proteins in the paracellular route contribute to an ohmic resistance (TEER) in the equivalent circuit.

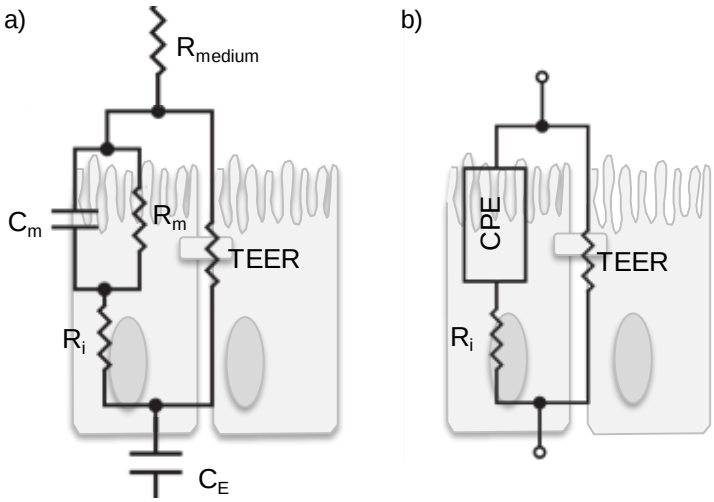

Figure 3.24: Diagram of impedance-based equivalent circuit a cellular monolayer that includes capacitance of the cell membrane (C_m), resistance of the cell membrane (R_m), resistance of the paracellular route (TEER), resistance of the medium (R_{medium}), and electrode capacitance (C_E). This circuit can be simplified because high membrane resistance force current through the other paths, total impedance, Z, results in a contribution of transepithelial electric resistance (TEER) of the paracellular electrical pathway, the ohmic resistance of the membranes (R_i), and the capacitance of the constant phase element (b).

The lipid bilayer in the transcellular route contributes to a parallel circuit consisting of an ohmic resistance (R_i) and an electrical capacitance, modeled by a constant phase element (CPE), which describes faithfully the dielectric properties of many cell membranes (Fig. 3.24).[311] To obtain $TEER_{monlayer}$ expressed in $\Omega \cdot cm^2$, the impedance at 100 Hz and surface area of microstructured hydrogel were multiplied (Eq. 21). Data analysis and plots were carried out with OriginPro 8.5 software.

3.7 STATISTICAL ANALYSIS

All statistical analysis were carried out taking into account the normality of the samples and their variance to choose between parametric or nonparametric methods. In the case of parametric methods, for 2 samples comparison t-test was used, and for more than 2 samples comparison One-Way ANOVA tests. In the case of non-parametric methods, for 2 samples comparison Mann-Whitney U test was used, and for more than 2 samples comparison Kruskal-Wallis test was used. All tests were performed using Matlab 2010 software and OriginPro 8.5 software.

4 Results and Discussion

4.1 PREPARATION AND CHARACTERIZATION OF PEGDA HYDROGELS IN A CHIP

We first validated the experimental set-up designed for the fabrication of PEGDA hydrogels. As hydrogels are very soft materials, a critical point was handling after fabrication. To solve this practical issue, we decided to use as cover on our chip a material to which hydrogels will adhere during polymerization. Later, this cover with the hydrogel will be retrieved and flipped to work with the sample. Despite previous works reported the use of silanized glass coverslips to keep the hydrogel covalently attached on them[187,263,312], we found out that hydrogels adhered well to non-treated coverslips.The chip designed is efficient and allows the successful polymerization of PEGDA solutions in hydrogels. The main factors that influence the polymerization process, such as the concentration of the photoinitiator, the time of UV exposure, and the presence of oxygen are studied in this section.

4.1.1 THE CONCENTRATION OF PHOTOINITIATOR RULES THE DEGREE OF POLYMERIZATION IN PEGDA HYDROGELS

PEGDA photopolymerization is initiated by the activation of the photoinitiator (I2959) under UV light. We first studied the polymerization of PEGDA as a function of I2959 concentration. To do this, different concentrations of $PEGDA_{575}$ and $PEGDA_{6000}$ were polymerized in the presence of several concentrations of I2959: $5{\cdot}10^{-4}$% w/v, 0.05% w/v, and 0.5% w/v. Disc-shaped hydrogels were fabricated by exposing them at 150 s under UV light. Figure 4.1 shows pictures of the hydrogels obtained for each polymerization condition. For the smallest percentage of photoinitiator used, no polymerization was observed regardless the polymer concentration of the solution. For the other concentrations, hydrogels were obtained.

Depending on polymer concentration and photoinitiator concentration hydrogels showed different opacity. For each PEGDA molecular weight, the most opaque samples were found with the highest polymer concentrations and largest values of photoinitiator content. The hydrogel opacity has been reported to increase with its cross-linking density when using PEGDA solutions with polymer concentrations of up to 60% w/v.[313] This means that for the same UV exposure time the degree of polymerization depends on the concentration of the photoinitiator.

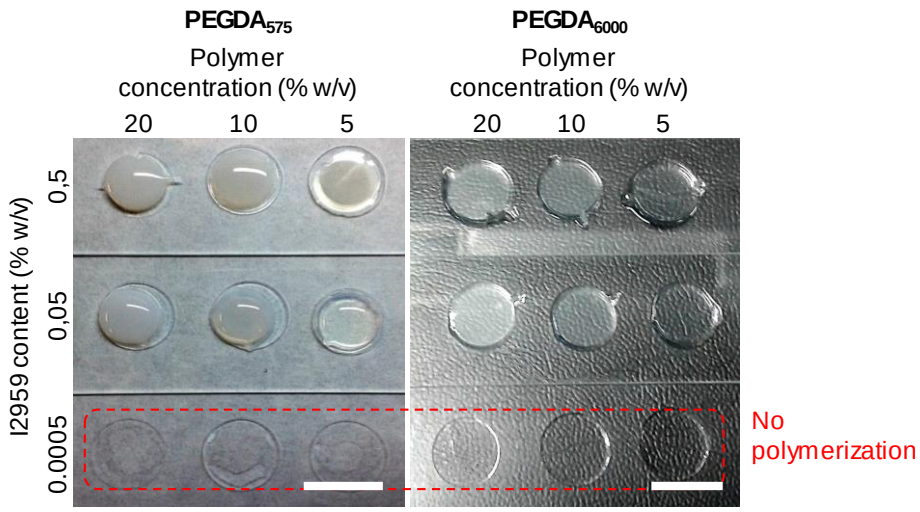

Figure 4.1: Photographs of photopolymerized PEGDA hydrogels fabricated from solutions containing several concentrations of photoinitiator (I2959). Note that at smallest photoinitiator concentration no polymerization was observed. Scale bar = 12 mm.

To better understand the role of I2959 concentration on the photopolymerization process, fractional monomer conversion was theoretically estimated from equation 18 (section 1.4) and plotted as a function of the exposure time for increasing I2959 concentrations (Fig. 4.2). Values of constants and parameters related to I2959 and the UV light source experimentally used are listed in Table 4.1. Photoinitiator concentration was limited to 1% w/v because it is reported as the limit of solubility of I2959 in water–based solutions.[178]

Parameter	Value	Units	Reference
k_p	21.65	$m^3\ mol^{-1}\ s^{-1}$	314–316
k_t	2516	$m^3\ mol^{-1}\ s^{-1}$	314–316
f	0.5	-	317
Φ	0.29	-	318
ε	40	$m^2\ mol^{-1}$	12, 13
I	375	$Kg\ s^{-3}$	measured
N_A	$6.022\ 10^{23}$	mol^{-1}	320
h	$6.63\ 10^{-34}$	$Kg\ m^2\ s^{-1}$	320
c	$3\ 10^8$	$m\ s^{-1}$	320
λ	$3{,}13 \cdot 10^{-7}$	m	15, 16

Table 4.1: Free radical polymerization related parameters used in this work converted to international units.

Fractional monomer conversion for the different I2959 concentrations describes an exponential function that levels off long UV exposure time. This saturation value depends on the actual I2959 concentration. It does not reach 100% in all cases, just for the highest I2959 concentrations (1% and 0.5% w/v). The graph also shows that for concentrations of photoinitiator below 0.05% w/v, fractional monomer conversion saturates at low values, while the time required for to achieve saturation is out of the experimental range considered.

The relationship between the photoinitiator concentration and UV exposure time required for the cross-linking of hydrogels, has been previously reported and it is reproduced in our experimental system.[259,321] We observed that for the smallest photoinitiator concentration assayed ($5 \cdot 10^{-4}$% w/v), even if theoretically the monomer conversion with 150 s of UV exposure is about 10%, experimental no hydrogel formation was found. This is in agreement with the results found by Dendukuri *et al.*, who reported that a minimum degree of monomer conversion is needed to obtain polymer gelation.[316] We also observe from Figure 4.2b that, for the UV exposure time used experimentally (150 s), the fractional monomer conversion predicted by the theoretical plot agrees with the less cross-linking in samples fabricated with photoinitiator concentration of 0.05% w/v with respect to 0.5% w/v (Fig. 4.1).

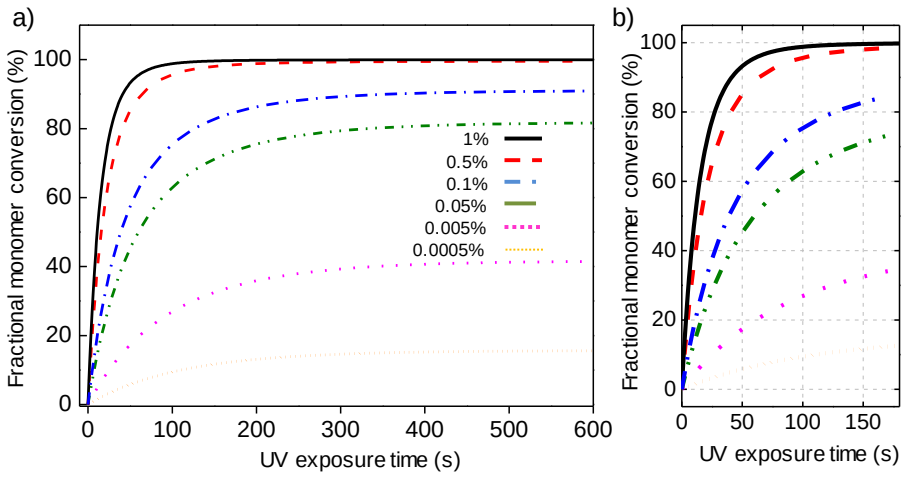

Figure 4.2: a) Theoretical plot of fractional monomer conversion of PEGDA polymer solutions as a function of UV exposure time. Different I2959 concentrations were used, 1% (black), 0.5% (red), 0.1% (blue), 0.05% (green), 0.005% (magenta), and $5 \cdot 10^{-4}$% (orange). b) Zoom of the time interval of interest.

To experimentally analyze the cross-linking degree in hydrogels, FTIR measurements were performed. The FTIR spectra of the hydrogels (10% w/v PEGDA and 1% w/v I2959) were used to study the double bond conversion, using

as a reference the C=C peak at 1600 cm^{-1} (Fig. 4.3). While the number of carbonyl groups do not change during photopolymerization, vinyl groups are reduced as much as polymerization advances. The low intensity peak of C=C compared to carbonyl stretching demonstrate the high cross-linking ratio of the fabricated hydrogels and that the conversion of C=C is almost complete (Fig. 4.3c).

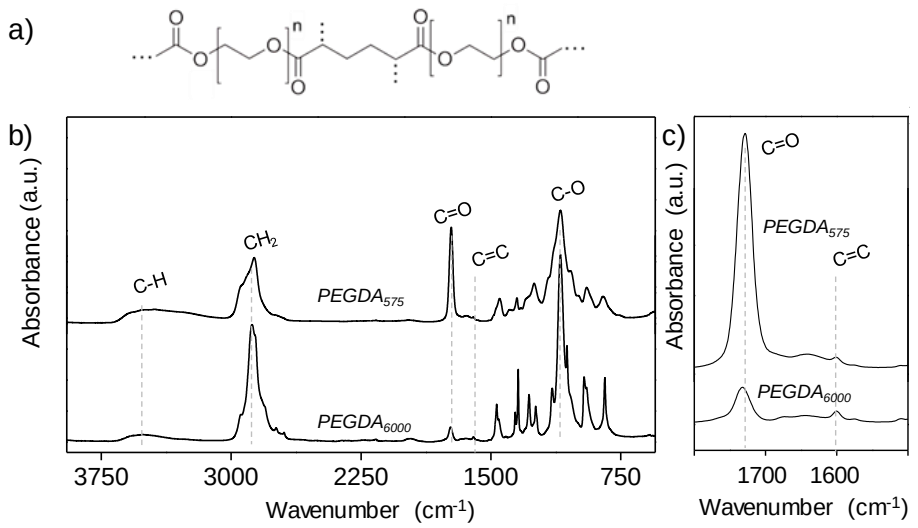

Figure 4.3: a) Drawing of the molecular structure of the PEGDA hydrogel. b) FTIR spectra of PEGDA hydrogels with absorption bands of C-H stretch vibration at 3508 cm^{-1},[322] CH_2 stretch at 2880 cm^{-1} ,[322] C=O stretch at 1729 cm^{-1},[323] C = C stretch at 1600 cm^{-1},[324] and C-O at 1100 cm^{-1}.[325] Main representative peaks of the PEGDA remain unaltered. c) Detail of the region of interest. Vinyl related peak show a very low intensity, meaning a high degree of cross-linking.

I2959 is a photoinitiator widely used in the fabrication of PEGDA hydrogels for biomedical applications. I2959 has been successfully used for cell encapsulation of a wide range of cell types from fibroblast to stem cells.[175,326] I2959 is cytocompatible at low concentrations (< 0.05% w/v) but its cytotoxicity increases with increasing photoinitiator concentrations.[326,327] In addition, free radicals formed in the presence of the photoinitiator and UV light cause significant levels of cell death in encapsulated cells.[327] In our experiments, cells will be placed on top of the hydrogels after fabrication, and most of the non-reacted radicals and non-decomposed I2959 molecules would be washed away, thus minimizing the potential cytotoxic effects on cell culture. In what follows, I2959 concentrations from 0.1% to 1% will be considered, which would lead to fractional monomer conversion rates of 0.980 to 0.995 for the exposure times explored (~150 s).

4.1.2 UV EXPOSURE TIME ENABLES TO CONTROL THE HEIGHT OF THE HYDROGELS

The total energy applied to the polymer solutions controls their polymerization degree. In our experimental set-up, for a container of 10 mm in diameter, the energy dose applied is 29.5 mJ/s. To study the effects of UV exposure time on the fabrication of PEGDA hydrogels, samples were exposed a set of times ranging from 10 to 150 s. Disc-shaped hydrogels were produced in a container of 1 mm in height. We found out that the height of the polymerized hydrogel increased quickly within the range of exposure times employed (Fig. 4.4). This is consistent with the amount of photoinitiator employed in this process (1% w/v), which, according to Figure 4.2, leads to 80% - 100% of fractional monomer conversion after just 50 s of UV exposure time. Indeed, the pictures of the profiles of the hydrogel obtained (Fig. 4.4) and their heights show polymerized structures achieving the height of the total container after 50 s of UV exposure (Fig. 4.4c). These results demonstrated that in our set-up UV exposure time plays a critical role in controlling the height of the hydrogels. This is in agreement with previous studies of the effects of UV exposure time on PEG hydrogel thickness, which determined that polymerization depth increases with the energy dosage and UV exposure time, and strongly depends on photoinitiator content. [224,321,328]

Pictures and measurements of Figure 4.4 correspond to samples in equilibrium swelling. Hydrogels swell and can retain a significant amount of water within their structure. The time for equilibrium swelling was determined in previous experiments as 2 to 3 days for $PEGDA_{6000}$.[294] Due to swelling, the maximum hydrogel heights reported in Figure 4.4 are higher than the height of the PDMS container. Swelling ratio for $PEGDA_{6000}$ (40%) is larger than for $PEGDA_{575}$ (16%), being this reflected in the pictures of the hydrogels and their heights.[236] In our case, hydrogels grow from the upper part (glass coverslip), where the free radical reaction is initiated, toward the bottom part of the container. Our results, in agreement with previous studies,[177,223] suggest that polymerization takes place differently as a function of depth. To initiate polymerization, a sufficient amount of photoinitiator need to be activated, which requires a minimum energy dosage. As the total energy received by the sample depends on time, short periods of UV exposure will not provide enough energy to polymerize the whole polymer solution. This is the case of UV exposure of 10 s (Fig. 4.4).

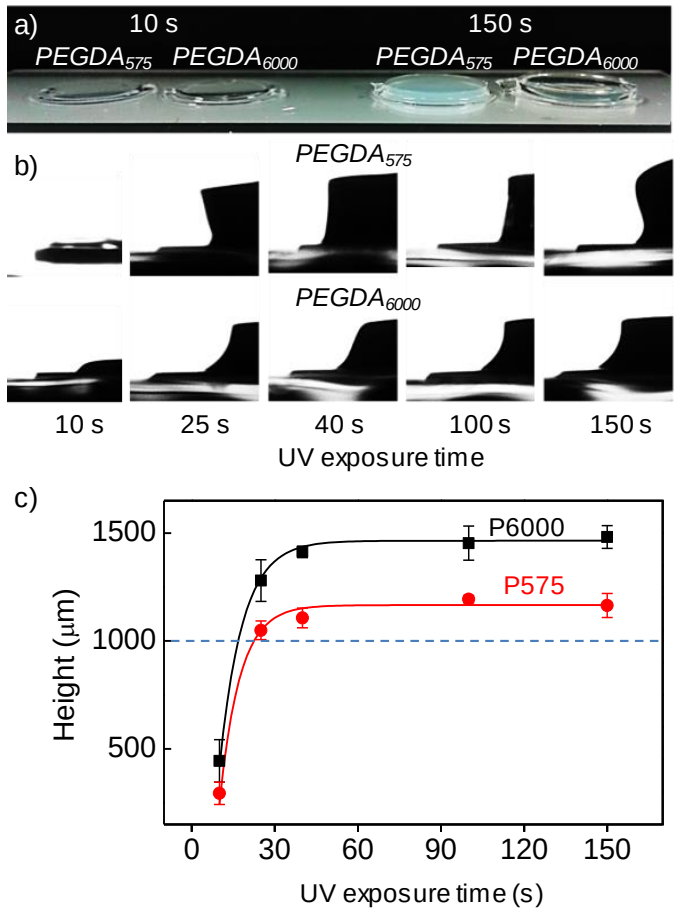

Figure 4.4: Effect of UV exposure time on the hydrogels height. a) Pictures of disc-shaped hydrogels after swelling process obtained at 10 s and 150 s of UV exposure. b) Pictures of the hydrogel profiles made at different UV exposure times. c) Graph showing the height of hydrogels after swelling as a function of UV exposure time (mean ± SD). The dash blue line shows the height of PDMS container.

In fact, light goes through the polymer solution until reaching the photoinitiator molecules, which absorb the light producing reactive species (free radicals) that drive the polymerization. This absorption leads to a gradual decrease of light intensity along the propagation direction (z) that can be calculated using the Beer–Lambert law. Then, the light intensity (I) at a specific depth in a thick sample is described by equation 25, which ignores the diffusion of both the initiator and bleached initiator degradation products at the polymerization time scale.[177]

$$I = I_0 e^{-2.303\,\varepsilon\,C\,z} \qquad \text{Eq. 25}$$

In this equation, I_0 is the intensity of radiation at the upper surface, ε is the molar extinction coefficient of the photoinitiator, and C is the concentration of the photoinitiator. Considering I2959 concentrations within the range of 0.1% to 1% w/v, equivalent to 4.46 and 44.6 mol·m^{-3}, we have estimated the intensity profile along the depth of the polymer solution (Fig. 4.5a). For 1% w/v of I2959, at 1 mm of distance from the surface, the irradiation is only 17% of the UV light intensity at the upper surface, while for 0.1% w/v of I2959, the UV intensity reach 84% of the surface value. As a consequence of this gradient of light intensity, a gradient of photoinitiator molecules and radicals formed is created along the vertical direction (Fig. 4.5b).[177] This fact implies that if 1% w/v of I2959 is used, to produce enough radicals at large distances from the UV source, long exposure times are required to reach the energy needed to initiate radical formation.

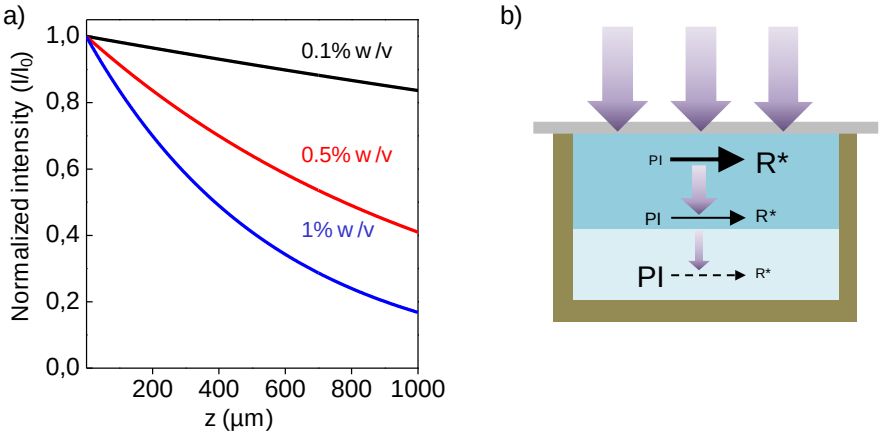

Figure 4.5: Normalized UV light intensity profile I/Io (a) as a function of depth of the PDMS container (z), for 0.1% w/v (black), 0.5% w/v (red), and 1% w/v I2959 (blue). b) Schematic model of light intensity decay leading to a vertical gradient of photoinitiator molecules (PI) and molecules converted to radicals (R*).

Considering the measurements of the height of hydrogels for different UV exposure times (Fig. 4.4), the energy received can be easily estimated for a given depth by multiplying the intensity and the UV exposure time:

$$E(z,t) = I_0 e^{-2.303\,\varepsilon\,C\,z} t \qquad \text{Eq. 26}$$

Figure 4.6a shows the energy dosage calculated from equation 26 and the estimated energy dosages from the experimental measurements. For these calculations, the initial intensity used was the calculated above, I_0 = 29.5 mJ/s and the second of exposition. The x axis of the graph represents the total thickness of

the sample (Fig. 4.6). To minimize the errors that might arise from using the height values measured after swelling, values from $PEGDA_{575}$ are used because it shows the lowest swelling ratio (Fig. 4.4). These approximation yields excellent agreement between theory and experiments. It is noticeable that, while hydrogel heights are still increasing (10 to 40 s), the estimated energy dosages received at each of the measured heights remains within the same range (80 – 250 mJ) without significant differences. One can then infer that such a value is the minimal energy needed to initiate enough radical formation for the formation of a gel.

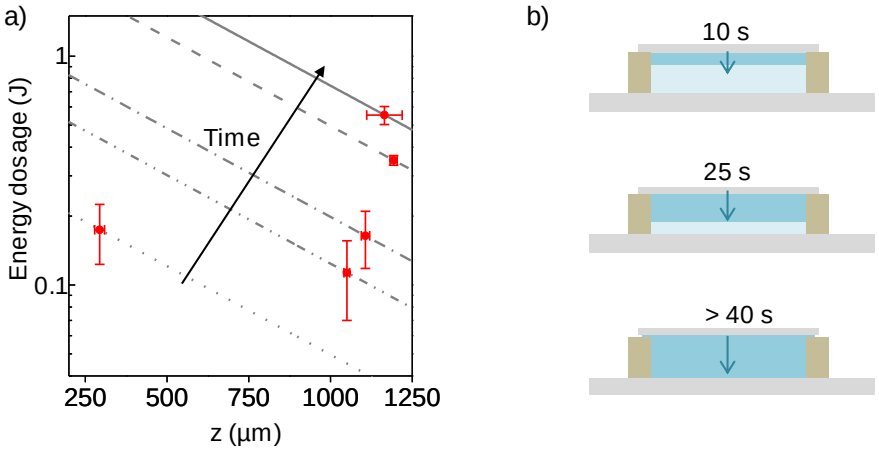

Figure 4.6: Plot of energy dosage (a) as a function of depth of the PDMS container (z) for 10 s (dotted line), 25 s (dot-dot-dashed line), 40 s (dot-dashed line), 100 s (dashed line), and 150 s (black line) of UV exposure time. Estimated values from experimental data are in red (mean ± SD). d) Schematic representation of the hydrogel growth progression.

4.1.3 EFFECTS OF OXYGEN IN THE POLYMERIZATION OF PEGDA HYDROGELS

In a free radical polymerization process, the lifetime of radicals is highly sensitive to the presence of oxygen.[316] The reaction rate of PEGDA with radicals is two orders of magnitude smaller ($k_i = 10^6$ L mol^{-1} s^{-1}) than the reaction rate of oxygen with radicals ($k_{O2} = 10^8$ L mol^{-1} s^{-1}). As a consequence, oxygen is scavenged by the radicals, inhibiting polymerization.[329,330] Therefore, the initial presence of oxygen in the polymer solution and the oxygen diffusion within the system must be considered for the success of polymerization. In the present set-up, an initial oxygen concentration of 0.27 mM[331] is present in the polymer aqueous-based solution, and oxygen can diffuse through the PDMS walls of the container (oxygen diffusion ≈ 10^{-9} m^2 s^{-1})[332] and through the air-liquid interfaces created by the inlets that deliver the polymer solution inside the chip (Fig. 4.7).

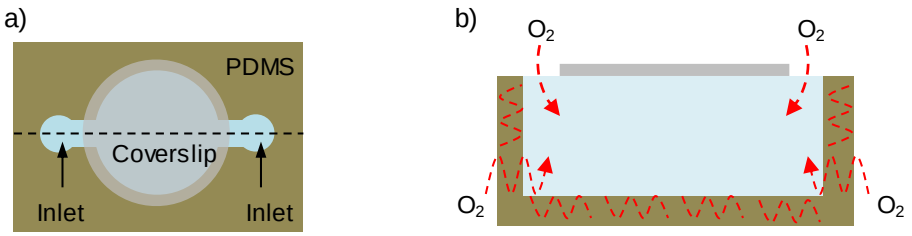

Figure 4.7: Schematics of a) top view and b) cross section of the experimental set-up. Red dash lines illustrate the sources of oxygen diffusion into the polymer solution.

In our system, despite the presence of initial oxygen dissolved within the polymer solution and the oxygen diffusion, PEGDA photopolymerization takes place, as it has been demonstrated. The explanation is that oxygen is quickly consumed by radicals, which are continuously generated by UV irradiation, and such as local oxygen depletion allows the polymerization.[329] However, the oxygen consumed can be renewed by the oxygen diffusing through the air-liquid interfaces and PDMS walls. To estimate if such oxygen diffusion has an effect on PEGDA polymerization in our experimental set-up, we computed the so-called Damköhler number (Da) to determine the relationship between oxygen diffusion and oxygen depletion in the system.[265] The Damköhler number can be computed as:

$$\mathrm{Da} = \frac{R^2/D_O}{[O_2]_0/\phi\varepsilon[PI]I} \qquad \text{Eq. 27}$$

Where R is the radius of the region exposed to the UV, D_0 is the diffusion coefficient of oxygen within the polymer solution, ϕ is the quantum yield of the photoinitiator, ε is the molar extinction coefficient of the photoinitiator, [PI] is the molar concentration of the photoinitiator, I is the intensity of the UV light, and $[O_2]_0$ is the molar concentration of oxygen initially dissolved in the polymer solution. When Da << 1, the oxygen diffusion in the system is fast, so the oxygen concentration can be considered as constant, and it is never depleted, therefore polymerization is inhibited. On the other hand, if Da >> 1, the oxygen diffusion is slow, so oxygen concentration is locally depleted and polymerization can occur.[265]

For a PDMS container of 10 mm in diameter, 0.1% to 1% w/v of photoinitiator I2959 (Table 4.1), polymer solutions containing between 5% and 20% w/v of PEGDA, and 37.5 mW/cm^2 of light intensity (power density), the Da has been calculated using the values listed in Table 4.2.

Parameter	Value	Units	Source
R	$5 \cdot 10^{-3}$	m	Measured
D_o	10^{-9}	$m^2\ s^{-1}$	31, 32
$[O_2]_0$	0.27	$mol\ m^{-3}$	331
[PI] range	4.46 - 44.6	$mol\ m^{-3}$	Measured
Φ	0.29	-	318
ε (λ=313 nm)	40	$m^2\ mol^{-1}$	12, 13
I (λ=313 nm)	$9.75 \cdot 10^{-4}$	$mol\ m^{-2}\ s^{-1}$	Measured

Table 4.2: Parameters used in the calculation of Damköhler number. D_o was approximated by a linear interpolation from the values corresponding to oxygen diffusion in PEGDA at 40% w/v ($D_O^{PEGDA\ 40\%} = 10^{-10}\ m^2\ s^{-1}$) and in the buffer without PEGDA ($D_O^{PBS} = 2 \cdot 10^{-9}\ m^2\ s^{-1}$).[333,334] $[O_2]_0$ was considered as the oxygen concentration in water at 1 atm and 20°C.[331]

With the values of Table 4.2, the Damköhler number was calculated to be in the range of $4.7 \cdot 10^3$ to $4.7 \cdot 10^4$ on the surface of the chip, depending on the concentration of the photoinitiator, and between $3.9 \cdot 10^3$ and $9.6 \cdot 10^3$ at the bottom of the chip (1 mm of distance). As Da >> 1 with our experimental set-up and photoinitiator concentration range, oxygen diffusion would not be a limiting factor for polymerization, even considering amount of the intensity decay at the bottom of the PDMS container.

4.2 FABRICATION OF MICROSTRUCTURED PEGDA HYDROGELS

Once checked that in our experimental set-up PEGDA solutions polymerize and form hydrogels, trials were performed to ensure that by the use of photomasks hydrogels could be polymerized forming microstructures. Several photomasks containing arrays of UV transparent windows of 500, 300, 200, and 100 μm in diameter were used to polymerize polymer solutions of PEGDA (5% w/v and 10% w/v). A PDMS container of 2 mm in height was used to avoid being limited in the vertical size by the spacer of the chip. Figure 4.8 shows the bright field microscopy images of the microstructures obtained. Microstructures are arrays of individual, high aspect ratio pillars attached to the glass coverslip. The pillars were grown at a density of 100, 270, 625, and 2500 pillars/cm^2 for UV transparent windows having 500, 300, 200 or 100 μm in diameter, respectively. It is remarkable that they show a quite homogeneous shape except at the borders of the mask area, where microstructures were smaller than the ones outside the edges (Fig. 4.8e).

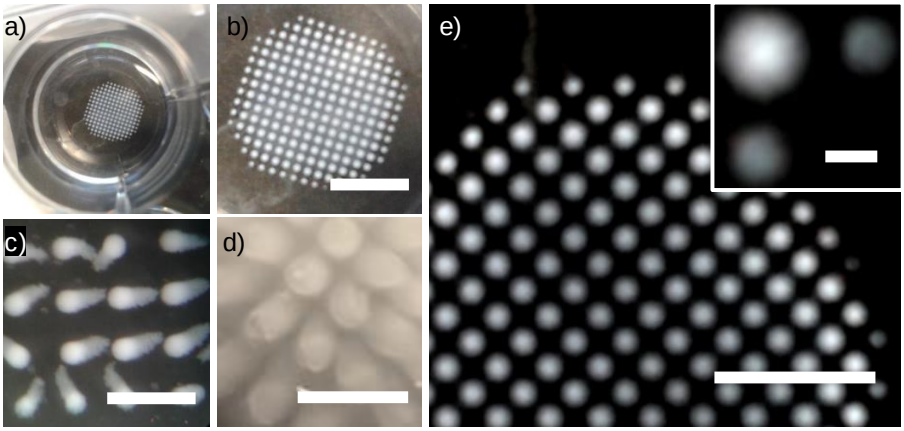

Figure 4.8: Top view of microstructured hydrogels after fabrication using photomasks with windows of a-b) 500 µm, c) 300 µm, and d) 200 µm. e) Top view image of an array of microstructures fabricated by using a photomask with windows 300 µm in diameter. The inset shows the boundary where microstructures were smaller. Scale bar: b = 5 mm, c = 1 mm, d = 500 µm, e = 2.5 mm, inset = 300 µm.

These pillars keep standing up and, in addition, when the well plate is shaken, the pillars move following the direction of the buffer and they even show a slight bending. This behavior is because they are formed by a very soft material. In fact, studies carried out at our group showed that hydrogels formed from polymer solutions with concentration in the range of 5 % to 10% w/v of $PEGDA_{6000}$ have elastic modulus values ranging 3 kPa to 11 kPa (Altay, internal report), in agreement of recently reported measurements (10% w/v $PEGDA_{6000}$ < 30 kPa).[236] Although $PEGDA_{700}$ with concentrations of 20% w/v have been used to replicate accurately complex 3D microenvironments to study 3D geometric and mechanical cues *in vitro*,[222] most of the reports that fabricate PEGDA microstructures by photolithography use 100% w/v PEGDA or highly concentrated PEGDA solutions. Such polymers lead to microstructures with elastic modulus in the range of MPa.[335] As an example, Dang *et al.* fabricated pillars of 1 mm in height and 500 µm in diameter using pure PEGDA and use this sample as a mold.[263] High aspect ratio microstructures have also been fabricated from $PEGDA_{250}$ (microneedles array)[264] and $PEGDA_{575}$.[265]

We have seen that the fabrication of microstructures with both the high aspect ratio features and the mechanical properties of the intestinal epithelium is possible. In what follows, we report the systematic study of the formation of these microstructures and the factors that rule the polymerization (UV exposure time, molecular weight and polymer concentration of PEGDA, and the presence of oxygen) when producing them.

4.2.1 GROWTH DYNAMICS OF MICROSTRUCTURES IN PEGDA HYDROGELS

The initial stages of growth of the microstructures were analyzed by measuring their diameters and heights at the several time points. To do this, 10% w/v $PEGDA_{575}$ hydrogels were microstructured by using a photomask with windows 300 μm in diameter (to facilitate the measurements). The hydrogels were fabricated by a single UV exposure, exposing samples to times comprised within 70 s to 110 s, at 5 s intervals. Polymer solutions were prepared in PBS containing 0.1% w/v of I2959. According to Figure 4.2, these exposure times are considered to obtain a fractional monomer conversion between 75% and 85%. For the range of UV exposure times studied, it was found that hydrogel microstructure height increased as the exposure time also increased (Fig. 4.9). In agreement with the observations for the non-microstructured hydrogels, pillars grow from the upper portion of the polymer solution and, when increasing the UV exposure time (energy dosage), the growth propagates in the vertical direction. In addition, it was observed that microstructures acquired rounded caps, and their walls were not vertical, but displaying a biomimetic rounded profile.

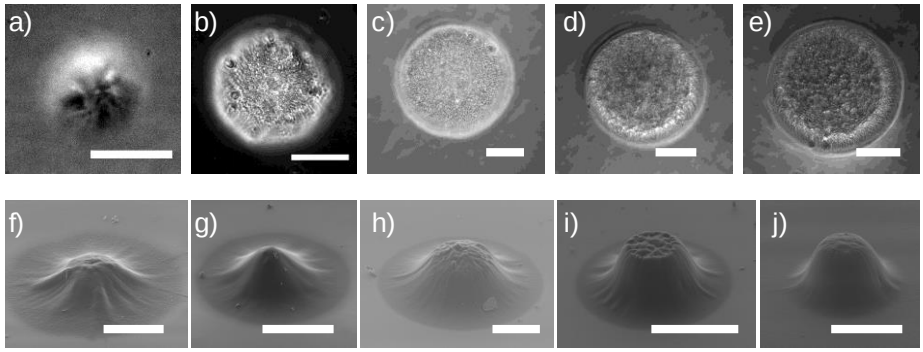

Figure 4.9: Pictures of the hydrogel microstructures at initial stages of growth. Top view and SEM images of representative microstructures fabricated by a,f) 70 s, b,g) 80 s, c,h) 90 s, d,i) 100 s, and e,j) 110 s of UV exposure. Scale bars: a-e,g,h = 100 μm, f = 50 μm, i,j = 200 μm.

Figure 4.10 shows the experimental measurements of the diameter (by bright field microscopy) and the height (by SEM) of the microstructures within the UV exposure time range assayed. We observed that images from optical microscopy led to values of the pillar diameter that were similar with those obtained by SEM. Therefore, we assumed that structures were not modified significantly by SEM sample preparation and used SEM images to get the values of height for the growing microstructures. The diameter of polymerized

microstructures was initially ~60% smaller than the window diameter of the photomask. As the UV exposure time increased, both the height and diameter of the pillars increased. The diameter became stable after 95 s of exposure, reaching a maximum value of around 320 µm, in close agreement to the diameter window of the photomask used. On the other hand, the height increased also with the exposure time, reaching maximum values of 190 µm, far from being limited by the height of the container (1 mm). We did not reach saturation in height because for the I2959 concentration (0.1% w/v) and the exposure time used (110 s), we were not at the maximum of the fractional monomer conversion (Fig. 4.2) yet. Figure 4.10b combines both diameter and height data representing the contours of the microstructures obtained for each UV exposure time. Profiles do not represent the exact microstructure contours, just schematic plots. These contours show the bullet-like shape of the growing microstructures. These pillars keep standing up and, in addition, when the well plate is shaken, the pillars move following the direction of the buffer and they even show a slight bending.

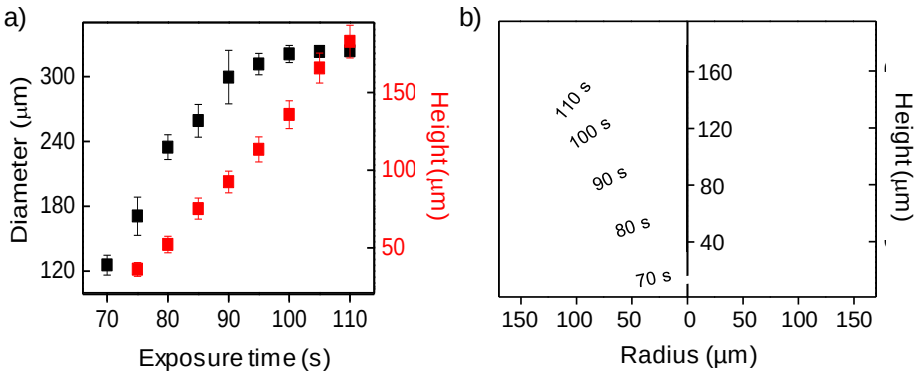

Figure 4.10: a) Plot of the diameters (black) and heights (red) of microstructures as a function of the UV exposure time (mean ± SD). b) UV exposure time-dependent contours of the microstructures.

In view of these results another set of microstructures was fabricated by exposing polymer solutions at 110 s, 125 s and 150 s to UV light. This time, structures were detached from the surface and their dimensions were measured in wet conditions by bright field microscopy. While the diameter of the microstructures did not change significantly, their height in wet conditions increased from 275 ± 3 µm to 384 ± 5 µm after 110 s and 150 s of UV exposure, respectively (Fig. 4.11). This growth dynamics observed on the hydrogel microstructures fabricated with our experimental set-up is in agreement with the work published by Jariwala *et al.*, who used a windows diameter of 16 mm and spacer of 1 mm in height to polymerize materials made of acrylated monomers.[336]

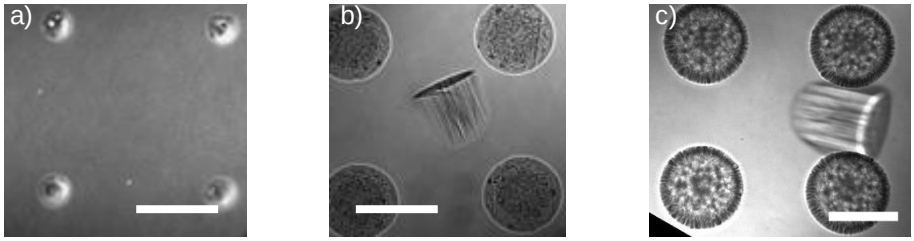

Figure 4.11: Pictures of the hydrogel microstructures at initial stages of growth. Top view pictures taken by bright field microscopy after a) 70 s, b) 85 s, and c) 150 s of UV exposure that illustrate the change in size as a function of exposure time. Scale bars =300 μm.

They found that materials grew in diameter and height until reaching the diameter of the photomask, and from there they were still increasing their height. In addition, the same growth behavior was published by Li *et al.*, who fabricated smaller (below 25 μm in height) microstructured PEGDA hydrogels, with a high aspect ratio (3:1). They reported that the diameter and the height of the structures increased as a function of the UV exposure time producing pillars with bullet-like shape contours similar to the ones found here.[337] On the other hand, although we expected fractional monomer conversions close to 100% for the 150 s of UV exposure time and the 0.1 % w/v of photoinitiator concentration employed (see Fig. 4.2), samples did not reach the total height of the container for this time. This could be explained because photomask acts a filter absorbing about 24% of UV light, according to experimental measurements.

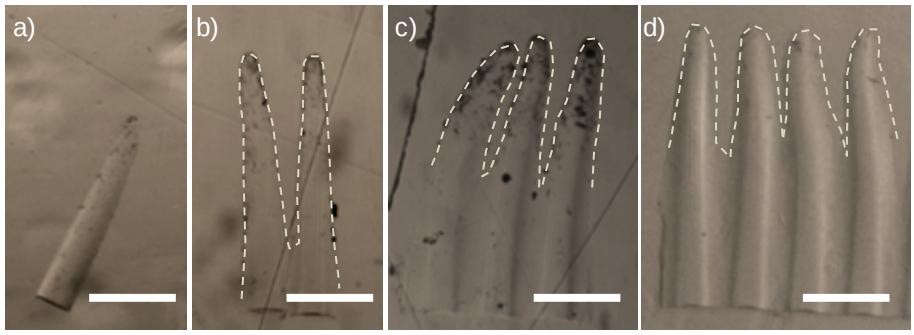

Figure 4.12: Effects of the UV exposure time on hydrogel microstructuring. Pictures of the microstructure profiles fabricated using a 7.5% w/v $PEGDA_{6000}$ polymer solution and a single UV exposure of a) 90 s, b) 110 s, c) 130 s, and d) 150 s. Scale bar = 300 μm.

To produce hydrogel microstructures with dimensions close to those of native villi of the intestinal epithelium, we focused our efforts in producing microstructures from photomasks of windows 100 μm in diameter, using

different polymers solutions of $PEGDA_{575}$ and $PEGDA_{6000}$ and 1% w/v of I2959. Then, we studied the effects of UV exposure time on these microstructures. It can be observed that isolated pillars are found for 90 s of exposure while for larger UV exposure times, hydrogel polymerized on regions that are theoretically unexposed (Fig. 4.12). A closer look-up at this process by SEM microscopy revealed that microstructures fabricated using photomasks with windows of 300 µm formed a continuous thin film of hydrogel material that covers the surface surrounding the microstructures (Fig. 4.13).

To visualize this thin layer of hydrogel, the sample was cross-sectioned. This hydrogel layer was already reported when arrays of PEGDA microstructures were polymerized using photomasks with windows (1 µm in diameter) too close (spaced 3 µm).[338]

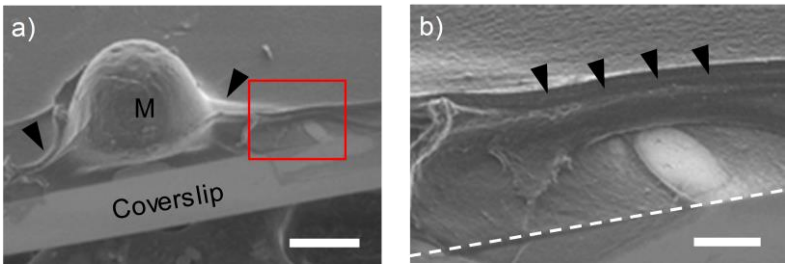

Figure 4.13: SEM images of hydrogel microstructures and the hydrogel thin layer. a) A hydrogel microstructure (M) and the hydrogel extent (arrowheads). b) Inset from image (a) (red square). The dash line marks the limit with the coverslip. Scale bars: a = 100 µm, b = 25 µm.

For exposure times longer than 130 s, this uncontrolled polymerization filled almost half of the space between the microstructures. At 150 s, on polymer concentrations above 7.5% w/v, unexposed regions fully polymerized and resulted in a completely polymerized block of hydrogel (Fig. 4.14). Because of this uncontrolled polymerization, at some point the effective height of the microstructures starts to reduce until the upper part becomes flat and their effective height can be assumed as zero.

Overall, these observations suggest that the morphology of the microstructures depends on the photomask and the UV exposure time, but there are other factors affecting the polymerization of the microstructures, which may also affect their shape and dimensions. This deserves to be understood in our experimental system for a better control over the morphology of the microstructures.

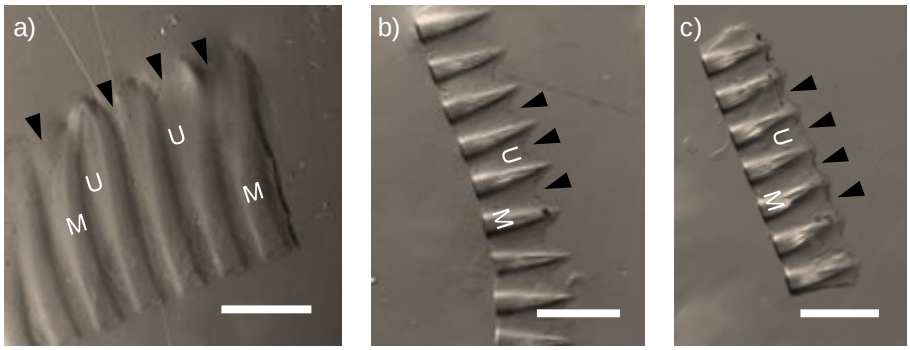

Figure 4.14: Effects of the interstitial polymerization on the height of the microstructures. Pictures of the microstructure profiles fabricated by the UV exposure times of 150 s, using a) 10% w/v $PEGDA_{6000}$, b) 7.5% w/v $PEGDA_{575}$, and c) 10% w/v $PEGDA_{575}$ polymer solutions. The M indicates the microstructures formed on the UV exposed region; the U indicates the polymerized hydrogel on unexposed regions, and the arrowheads indicate the boundaries of the polymer formed on the unexposed areas. Scale bar = 400 μm.

4.2.2 DETERMINING THE FACTORS RULING THE POLYMERIZATION OF PEGDA MICROSTRUCTURES

Light intensity acts as a catalyst in free-radical photopolymerization, so it is important to determine how the light transmission through the slit apertures of the binary photomask is. In our set-up, light must go through the acetate mask and the glass coverslip before reaching the polymer solution. Light passing through a slit may experience diffraction, and be partially deflected to unexposed regions. As the diameter of our apertures (windows = 10^{-4} m) is >> than the wavelengths of the light passing through, ($\lambda = 3 \cdot 10^{-7}$ m), Franhoufer diffraction effects can be neglected.[339] On the other hand, the edges of the photomask patterns usually generate diffraction effects, which follow the Fresnel diffraction, especially if there is a gap between the photomask and polymer solution. Gumuscu *et al.* found these effects to be relevant on fabricating PEGDA microstructures, and tried to solve it by reducing the spacing between the photomask and polymer solution, and thereby the diffraction of UV light at the edges of mask patterns.[259] In our experimental set-up, a coverslip of a thickness of 130 – 160 μm is placed between the photomask and the polymer solution. This distance was found to be enough for producing a 45% width error.[340] In addition, the acetate photomask can produce light scattering before the light exits the slit. The result is that light might invade unexposed regions near to the slit edge and polymer solution may cross-link between microstructures, while the opposite extreme (far away, at the bottom of the PDMS container) is not affected.[259,341] The

light passing through the slit of the photomask has a Gaussian intensity distribution, the cross-linking starts earlier in the central region between two adjacent opaque regions, where the light intensity is maximum (Fig. 4.15). In addition, on unexposed areas a few free radicals are generated because UV light is difficult to completely block at the edge of the slit, which may enhance the polymerization .[342,343]

Although the light intensity profile could partially give response to the microstructures shape and interstitial polymerization, photoinitiator, free radicals, and monomers also play an important role to explain this phenomenon.

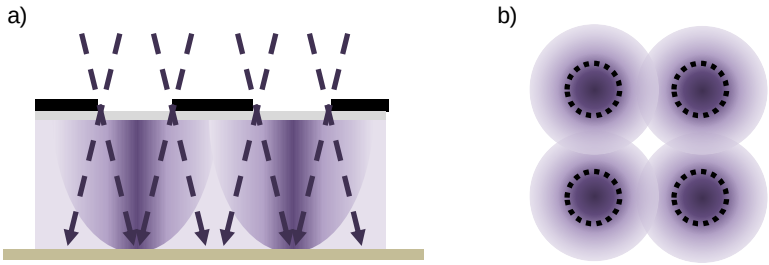

Figure 4.15: Effects of the photomask on the profile of the intensity light. a) Cross section of the chip, and b) top view, where dashed line indicates the boundaries of the windows of the photomask.

Recent publications have also described polymerization under unexposed regions of photomasks, which result in microstructures not faithfully reproducing the photomask pattern.[259,344] These phenomena are attributed to the diffusion of radicals at the boundaries between the polymerized and the non-polymerized solution. Indeed, this can be explained by the so-called polymerization-induced diffusion, a model proposed by Leewis *et al.*[345] On the one hand, during UV exposure the formation of free radicals produces that radicals radially diffuse from the irradiated region where they are generated, to the boundaries of the irradiated and non-irradiated regions. These radicals may lead to the cross-linking of such unexposed region.[346] On the other hand, the rapid consumption of the monomers at the irradiated region generates a gradient concentration of them, and as a result monomers diffuse from the surrounding area toward the center of the exposed area. The diffusion of radicals and monomers in opposite directions results in the formation of a gradient of polymerization, which may lead to the formation of a thin layer of is not fully polymerized hydrogel at the boundaries of the microstructures.[347] This is consistent with our observations of soft material located at the boundaries of the microstructures and the fact that the material observed between the pillars (at the non-irradiate areas) seems to be softer that the hydrogel forming the core of

the pillars. The amount of polymer formed between the microstructures is larger when using photomasks with windows more densely packed (100 µm vs 300 µm). Because of diffusion takes place from the center to the edges, the microstructures are much more cross-linked than that interstitial material.

Another consideration is that diffusion is a time-dependent process, and following our observations, longer exposure times would allow more diffusion and also more interstitial polymerization than shorter UV exposure times. First, dense microstructures are created at the center of the UV-exposed areas, with a thin base around the microstructures. For longer UV exposure times, the space between microstructures is fully polymerized (Fig. 4.12, Fig.3.13, Fig. 4.14). Figure 4.16 serves as an illustration of the radical and monomer diffusion theory.

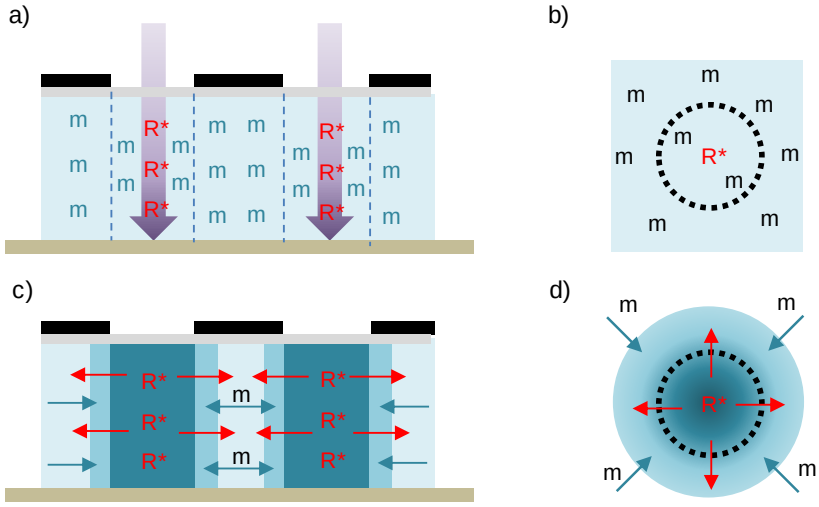

Figure 4.16: Schematic diagram of the polymerization on unexposed areas enhanced by the radicals (R*) and monomers (m) diffusion. Radical formation after UV light exposure, a) cross section and b) top view. Radical and monomer diffusion creates a lateral concentration gradient, which will result in a dense and thick microstructure at the center of the exposed area, and less dense and thinner layer at the boundary of the microstructure. c) Cross-section and d) top view. The dashed line indicates the boundaries of the windows of the photomask.

In addition, the polymerized material (cross-linked hydrogel) produce scattering effects. This theory is supported by Orakdogen *et al.*, who reported that the scattering light intensity from hydrogels is always larger than that from the polymer solution.[348] and the production of radicals attenuates the light intensity along the light propagation direction, as it has been seen in the fabrication of flat hydrogels, and generates a gradient of radicals in the z direction (Fig. 4.5). The convolution of the attenuation effects in z, and the lateral diffusion, may explain

that the formation of the interstitial material depends on the depth (Fig. 4.17). This hypothesis is in agreement with reports that showed microstructures with soft or roundish shapes when photopolymerizing PEGDA or other hydrogels.[259,343,344,349]

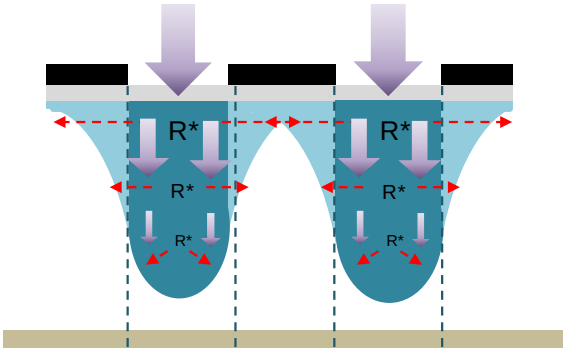

Figure 4.17: Schematics of the convolution of the attenuation of light (violet arrows), and the radial diffusion of radicals (R*). Dashed line indicates the boundary of photomask windows.

Even though the pattern of light intensity and the diffusion profile of reactants may account for the shape of PEGDA microstructures on our experimental set up, there is still a crucial factor that might affect the polymerization: the presence of oxygen. As it has been described, oxygen inhibits polymerization, and our set-up allows the oxygen diffusion through the PDMS walls and through the air-liquid interfaces created by the chip inlets.

Now, the Damköhler number was again calculated (Eq. 27) considering the size of the UV transparent windows of the photomasks. Using a photomask of windows 100 µm in diameter, Da = 4.7 (1% w/v I2959) at the upper region close to the mask while employing windows of 300 µm in diameter Da = 42 (1% w/v I2959). Shim and co-workers observed oxygen inhibition effects when Da < 50.[265] The Damköhler number was the recalculated considering Beer-Lambert equation to get information about the oxygen effects with increasing depth (z distance from the exposed surface). Figure 4.18a shows a plot of Da number as a function of z when using photomasks with windows of 100 µm or 300 µm compared to values obtained without photomask (flat hydrogels). Using photomasks, Da shows values under 50, where polymerization takes place but oxygen inhibition plays a non-negligible role. Considering windows of 100 µm, at 1 mm far away from the surface, Da decreases to values lower than 1. This means that a gradient of oxygen concentration is generated along the vertical direction of the reaction site and oxygen strongly inhibits the polymerization at such depths, thus limiting

the height of the microstructures to values much smaller than the total thickness of the chip.

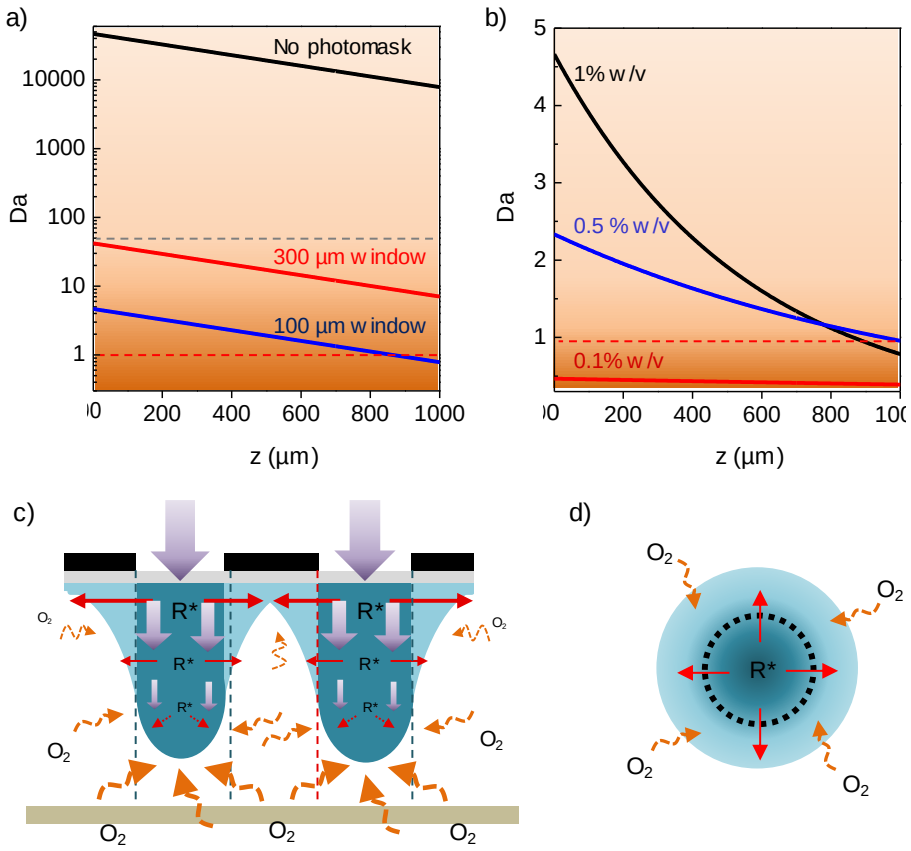

Figure 4.18: Oxygen effects on the microstructuring process. Plots of Damköhler number as a function of depth (z) varying the window diameters (a) and the concentration of I2959 (b). Grey dashed-line indicates Da = 50, the limit where oxygen inhibition effects are not negligible, and red dashed-line (Da = 1) indicates when the oxygen concentration gradient is generated, and oxygen inhibition lead the reaction. c) Cross section and d) top view of the schematic model of microstructures growth. After UV light exposure, diffusion of radicals (R*) enhances the polymerization on unexposed regions. Oxygen inhibition (orange dot arrows) is more prevalent far away from the UV light source. Both radical and oxygen gradients allow the fabrication of rounded shapes with soft boundaries. Dashed line indicates the boundary of photomask windows.

In addition, the effect of oxygen is enhanced when reducing the photoinitiator concentration (Fig. 4.18b), and becomes important up to the point of inhibiting polymerization for concentrations smaller than 0.1% w/v. It has to be considered that, in our experimental set-up, oxygen can diffuse from all directions except from the upper part of the device, where it is avoided by the

glass coverslip. Therefore, roundish tips and structure profiles as well as the presence of soft material at the boundaries between the exposed and non-exposed regions could be due in part due to oxygen inhibition at the hydrogel boundaries (Fig. 4.18c) This effect has been reported by Viswanathan and co-workers, who used a similar experimental system, but poly (hydroxyethyl methacrylate) (PHEMA) hydrogels instead of PEGDA.[344]

As a summary, polymerization agents (radicals) show a decreasing gradient in z and in the radial direction while the inhibition agent (oxygen) produce gradients from the bottom and the lateral sides of the chip. The convolution of these factors would explain the formation of bullet-like microstructures with roundish shapes and smooth profiles.

4.2.3 EFFECTS OF THE UV EXPOSURE TIME ON HYDROGEL MICROSTRUCTURING

To systematically study the effects of UV exposure time on the morphology and height of hydrogel microstructures, we selected those fabricated from photomasks of windows 100 µm in diameter. Polymer solutions of PEGDA (either 575 or 6000) at different concentrations (from 5% to 10% in w/v) were used. In these experiments, we used 1% w/v of I2959, so UV exposure times were selected to lead to fractional monomer conversion ratios of 95% to 100% (Fig. 4.2), so fully cross-linked structures are obtained. Therefore, UV exposure times ranging from 90 s to 150 s were applied. Figure 4.19a compares the real height of microstructures and the height of all hydrogel.

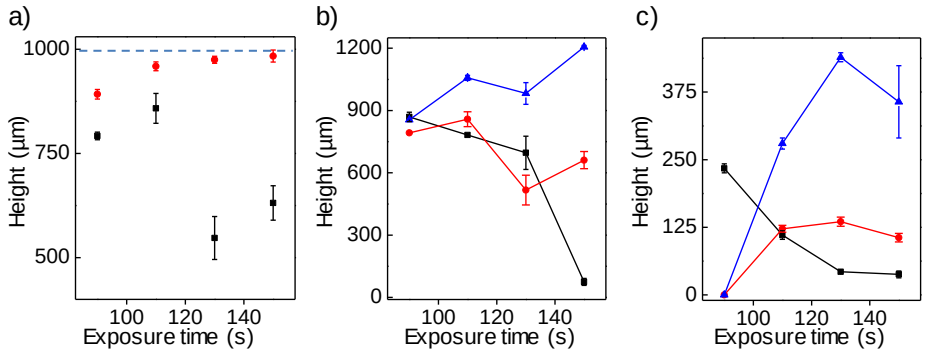

Figure 4.19: a) Growth of full hydrogel (red) and the height of microstructures (black) as a function of UV exposure time (mean ± SD) on 7.5% w/v $PEGDA_{6000}$. Evolution of height of microstructures on b) $PEGDA_{6000}$, and c) $PEGDA_{575}$ at 10% w/v (black), 7.5% w/v (red), and 5% w/v (blue).

We observed that from a certain exposure time, and while the full height of the microstructures increases, their effective height does not decrease due to the interstitial polymerization. Therefore, after a threshold of energy, the extra of irradiation serves to polymerize the space between microstructures. Even though the polymer solutions were exposed for 150 s, the full height of the hydrogel only reached or surpassed the PDMS height (1 mm) in the case of 5% w/v $PEGDA_{6000}$. Focusing only on the effective heights of the microstructures, for most of the experimental conditions studied it was found this value increased up to a maximum, and then it starts decreasing due to the polymerization at non-exposed areas. This biphasic behavior was more visible for $PEGDA_{575}$ than for $PEGDA_{6000}$ (Fig. 4.19b,c), and also more noticeable for polymer solutions concentrations equal or higher than 7.5% w/v.

Because of polymerization at unexposed regions, we decided to limit UV exposure times to the minimum required to achieve almost fully polymerized structures, which was determined by the maximum height of pillars. This aims to gain a better control of the shape and dimensions of the pillars fabricated. However, we found out that isolated pillars did not stand upright in a robust way, as often they fell, intertwined and stuck to each other. Therefore, we redesigned our fabrication process to perform two polymerization steps. A double UV exposure process was used to first create a hydrogel base to keep the hydrogel microstructures joined together, and then to ultimately produce the microstructures. To create such a base the first UV exposure was done without the photomask (Fig. 4.20).

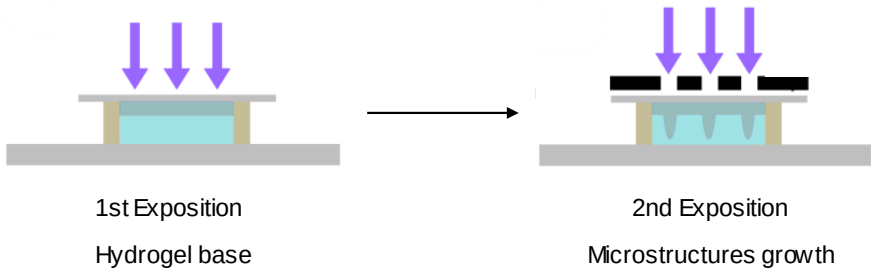

Figure 4.20: Schematic representation of the fabrication of hydrogel microstructures in two sequential exposures.

Also, and avoid the an anisotropic stiffness of hydrogel glass surfaces, which has been demonstrated that induce directional epithelial growth and guide cell migration along the direction of greatest rigidity.[350] To evaluate the effects of the UV exposure time for the base formation, microstructured hydrogels were fabricated by exposures of 5, 10, and 15 s for the hydrogel base, and 70 s for the microstructures. As Figure 4.21 shows, higher thicknesses of the hydrogel base were achieved by increasing the base exposure time. On the other hand,

increasing the hydrogel base lead to shorter microstructures (Fig. 4.21d-f). In addition, as the total time of UV exposure was increased, the interstitial polymerization also increased. $PEGDA_{575}$ showed a biphasic behavior with the exposure time used for the base, characterized by an increase of the height followed by a decrease (Fig. 4.21g). Therefore, 5 and 10 s were considered long enough to keep joined the microstructures while avoiding the base covering them. Even though 5 s of base exposure resulted in higher microstructures, these usually bended when using low polymer concentrations. For this reason, 10 s was also a time considered for further experiments.

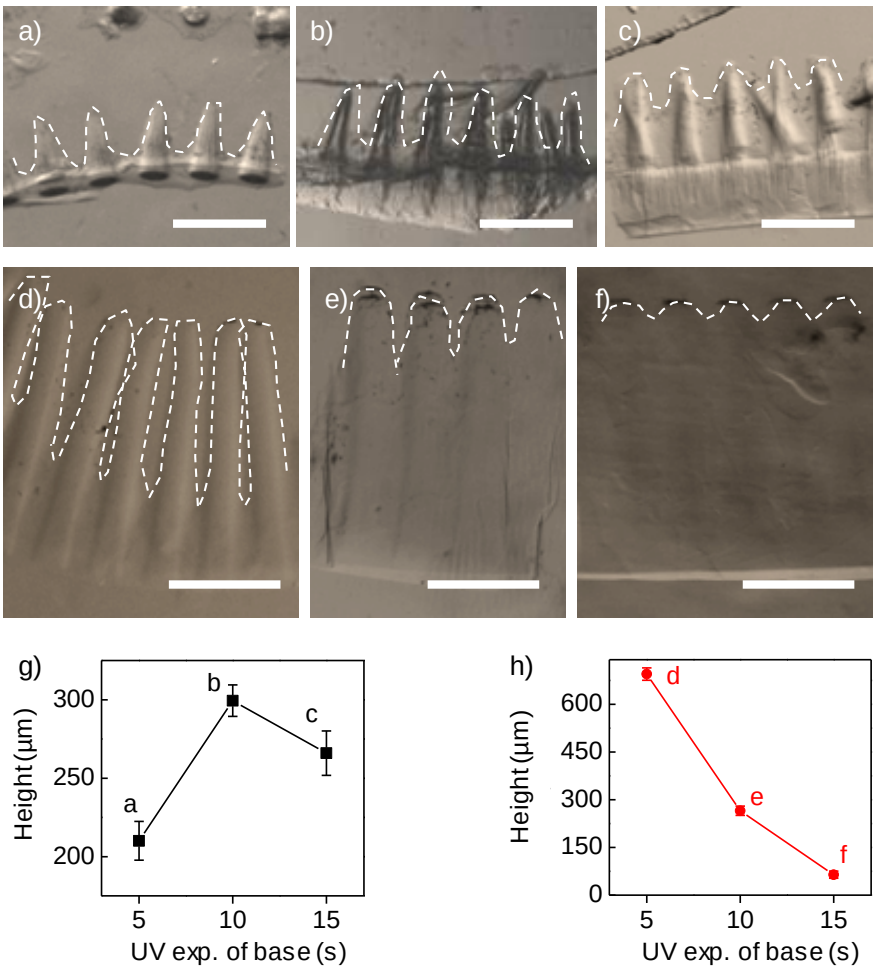

Figure 4.21. Effects of the hydrogel base on the effective height of the microstructures. Images of microstructures fabricated using 5 s, 10 s, and 15 s for the hydrogel base formation, and 70 s of UV exposure for the microstructuring; made of 10 % w/v $PEGDA_{575}$ (a-c) and 7.5 % w/v $PEGDA_{6000}$ (d-f). Scale bar = 400 µm. Plots of the microstructure heights, g) $PEGDA_{575}$, and h) $PEGDA_{6000}$, (mean ± SD) as a function of UV exposure time for the hydrogel base formation.

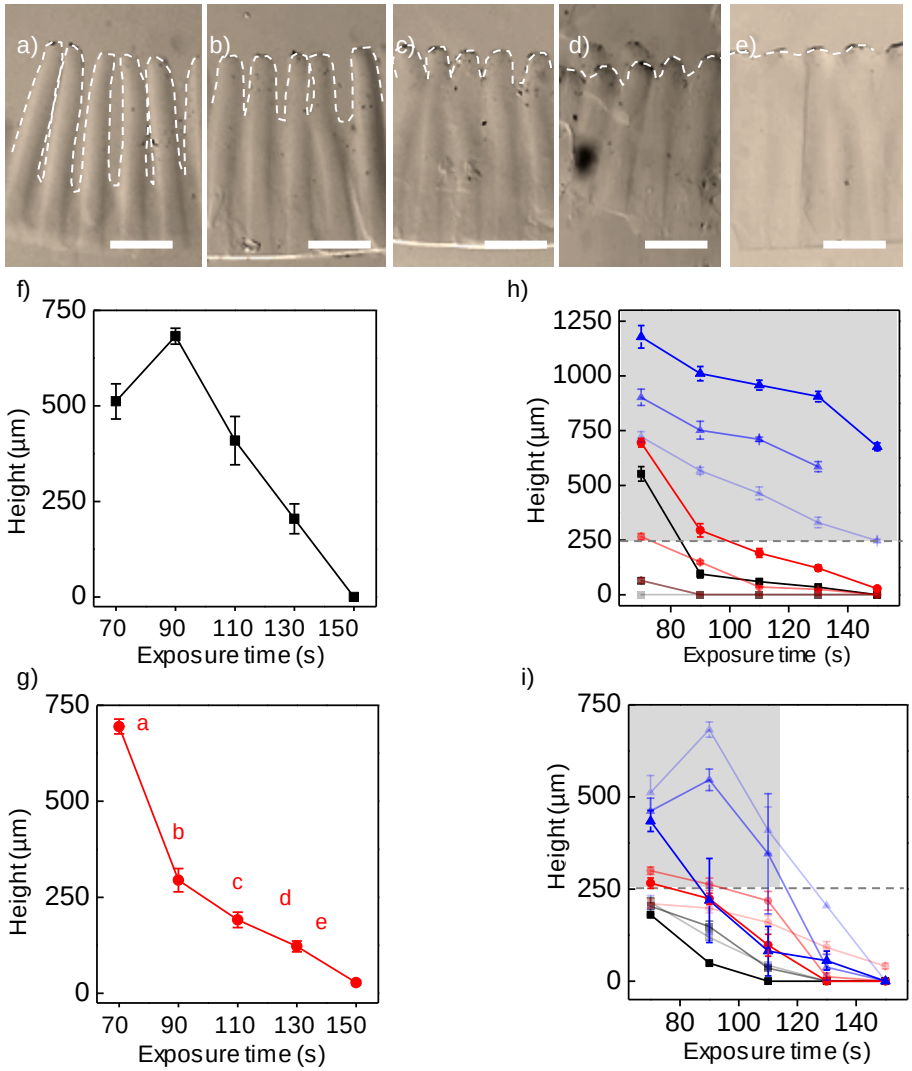

Figure 4.22: Effects of the UV exposure time on the hydrogel microstructures fabricated by UV exposure in two steps. a-e) Images of microstructures made of 7.5% $PEGDA_{6000}$, and exposed 5 s for the base and between 70 to 150 s for the microstructure. Scale bar = 300 µm. Plots of the microstructures height as a function of UV exposure time (mean ± SD): f) 5% w/v $PEGDA_{575}$, and g) 7.5% w/v $PEGDA_{6000}$. Plots of microstructures height as a function of UV exposure of all experimental conditions (see Table 3.1 in Materials & Methods) for $PEGDA_{575}$ (h), $PEGDA_{6000}$ (i). Regions of interest are represented in grey above the 250 µm in height. 5% w/v PEGDA in blue, 7.5% w/v PEGDA in red, and 10% w/v PEGDA, by using 5, 10 or 15 s for the formation of the hydrogel base (color gradient).

For a given value of base exposure, the effective height of the microstructures depended on the second UV exposure time. Interstitial polymerization was observed, and the effective heights showed a maximum before decreasing. (Fig. 4.22). Systematic studies allowed to establish optimal exposure times for each specific polymer solution (PEGDA molecular weight and polymer percentage). Because we want to mimic *in vitro* native intestinal villi, we are interested in microstructures with minimum heights of 250 µm.[9,10] With this in mind, the regions of interest were identified for $PEGDA_{575}$ and $PEGDA_{6000}$ (Fig. 4.22h and 4.22i) and experimental conditions within these regions will be further explored.

4.2.4 EFFECTS OF THE MOLECULAR WEIGHT AND POLYMER CONCENTRATION ON PEGDA MICROSTRUCTURES

When fabricated in optimal conditions, microstructures made of $PEGDA_{575}$ presented bullet-like shapes with sharp tips while microstructures of $PEGDA_{6000}$ showed columnar structures with rounded tips (Fig. 4.23). Their heights also differed: $PEGDA_{575}$ pillars were significantly shorter than $PEGDA_{6000}$ pillars within the range studied (Fig. 4.23c,d). These differences in height could be attributed to factors involved in the polymerization reaction. This might result in a material that is more absorbent to UV light, so intensity quickly decrease in z direction and polymerization is not effective. For the same polymer concentration (weight to volume ratio) the difference in the monomer size between $PEGDA_{575}$ and $PEGDA_{6000}$ means that we are comparing solutions of different molarities. This directly affects the chain propagation rate of the reaction, R_p (Eq. 11).

$$R_p = k_p \sqrt{\frac{2k_d f[PI]}{k_t}}[M] \qquad \text{Eq. 11}$$

Assuming that the photoinitiator concentration [PI], the photoinitiator efficiency (f), and the rates of decomposition (k_d), propagation (k_p) and termination (k_t) are the same for both molecular weights,[316] R_p depends on the monomer molarity [M]. For the same weight percentage, molar ratio ($PEGDA_{575}$:$PEGDA_{6000}$) is 10:1 so chain propagation rate would be ten times faster for $PEGDA_{575}$ than for $PEGDA_{6000}$, as more molecules with acrylated ends can interact. This implies that for the same exposure time, a higher degree of cross-linking is achieved for the smallest PEGDA molecular weight.[234] This higher cross-linking density results in higher values of the elastic modulus (30 kPa *vs*. 375

kPa)[236,351] and smaller pore size within the structure (~10 nm *vs.* 1 nm).[294,352] This denser material reduces the transmission of UV light, thus resulting in lower microstructures.

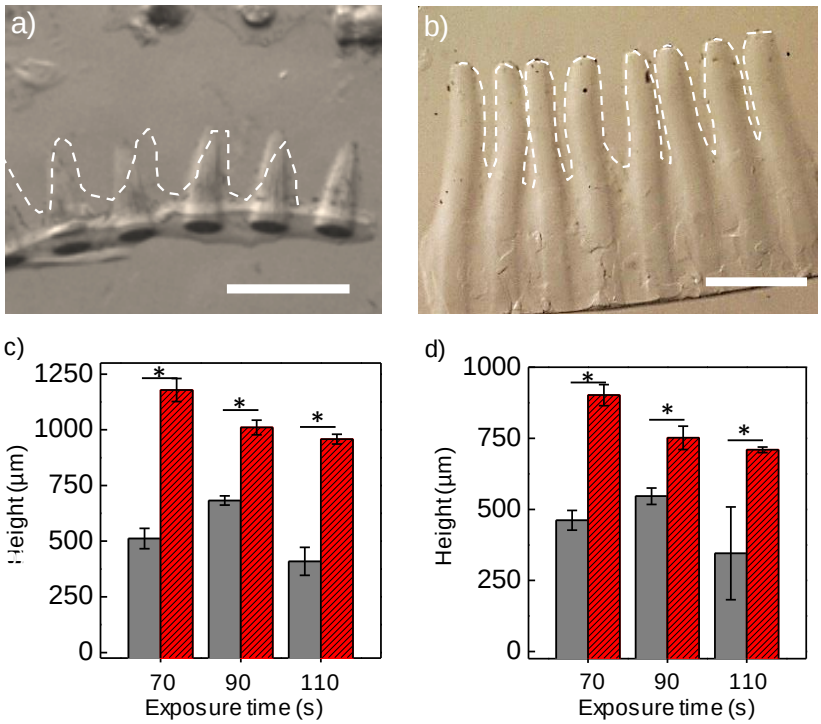

Figure 4.23: Effects of the PEGDA molecular weight on the microstructure morphology. Pictures of microstructures made of $PEGDA_{575}$ (a) and $PEGDA_{6000}$ (b) at 10% w/v fabricated by the UV exposure of 5 s (hydrogel base) and 70 s (microstructures). Scale bars = 400 µm. Plots of the microstructures height (mean ± SD) made of $PEGDA_{575}$ (grey) and $PEGDA_{6000}$ (red pattern) at 5% w/v, by the UV exposure of c) 5 s (base) and d) 10 s (base). * denotes p-value < 0.05 from Mann–Whitney U test.

We also studied the effect of the polymer concentration of polymer solutions on the microstructures. For each molecular weight three polymer concentrations were studied: 5%, 7.5% and 10% w/v. The main effect observed was the increase of polymerized hydrogel at unexposed regions when increasing polymer concentrations (Fig. 4.24). This results in a significant shortening on the effective height of the microstructures (Fig. 4.24g-i). This increasing in polymerized material between pillars can be also related to the effects in chain propagation rate described by Eq. 11. Because of proximity effects when UV transparent windows are too close, and the presence of light scattered from the photomask and the base, the space between microstructures might receive

enough UV light to polymerize. When propagation rate is higher due to increasing polymer concentration, the amount of polymerized material also increases.

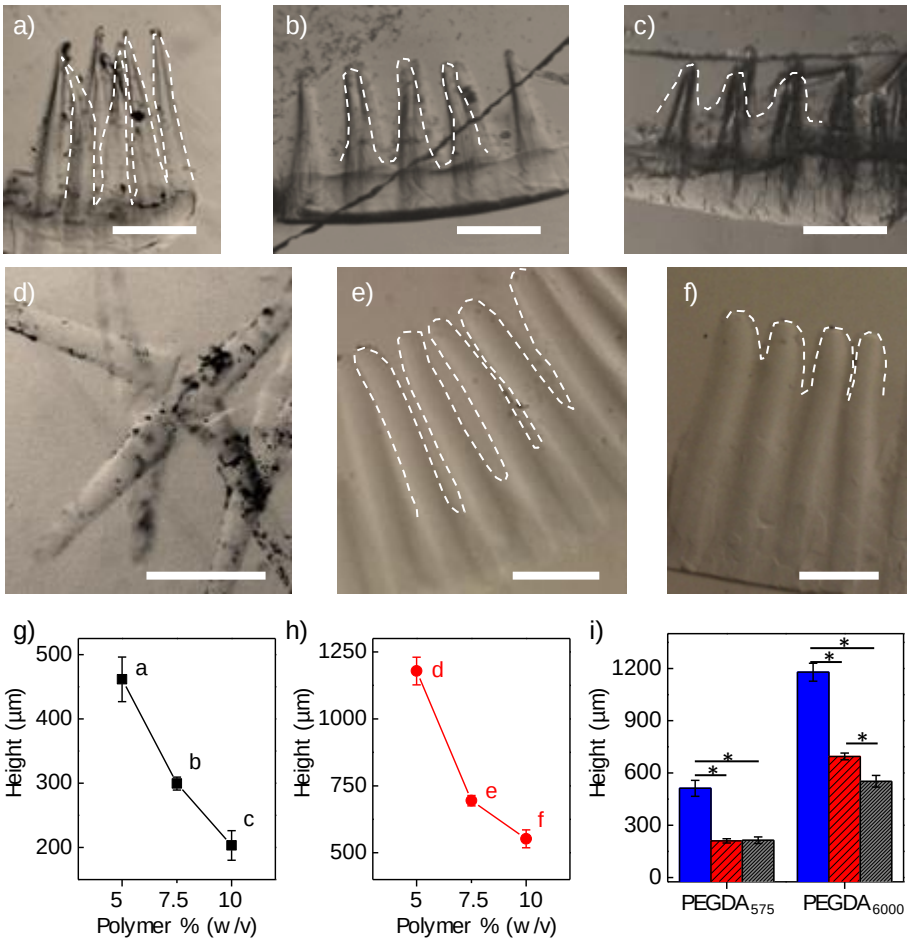

Figure 4.24: Effect of polymer concentration on the microstructure morphology. $PEGDA_{575}$ microstructures fabricated by UV exposure of 10 s (hydrogel base) and 70 s (microstructures) at a) 5%, b) 7.5%, and c) 10% w/v. $PEGDA_{6000}$ microstructures fabricated by UV exposure of 5 s (hydrogel base) and 70 s (microstructures) at d) 5%, e) 7.5%, and f) 10% w/v. The dash lines highlight the microstructure profile. Scale bar = 300 µm. Plots of the microstructure height, g) $PEGDA_{575}$, and h) $PEGDA_{6000}$. Plot of the microstructures height (mean ± SD) made of polymer concentrations of 10% w/v (grey), 7.5% w/v (red), and 5% w/v (blue) by the UV exposure of 5 s (base) and 70 s (microstructures). * denotes p-value < 0.05 from Mann–Whitney U test.

Thus, PEGDA molecular weight affected the morphology of the microstructures, making them shorter and sharper when using low molecular weight, instead the larger and rounded ones when using high molecular weight.

PEGDA concentration has also an intense effect on the amount of polymerized hydrogel on the unexposed regions, meaning that height of microstructures was dramatically reduced by increasing the PEGDA concentration. These changes in the polymerization, depending on the molecular weight and polymer concentration suggest different implications in the reaction of polymerization.[242] Indeed, both factors affect kinetics and lead high rates of propagation, which made the polymerization on unexposed regions faster and uncontrolled.[164] The low molecular weight and high concentration increase the viscosity of the polymer solution, which has been reported that reduce the oxygen diffusion, another factor that would make easier the extent of polymerization on the unexposed regions.[353]

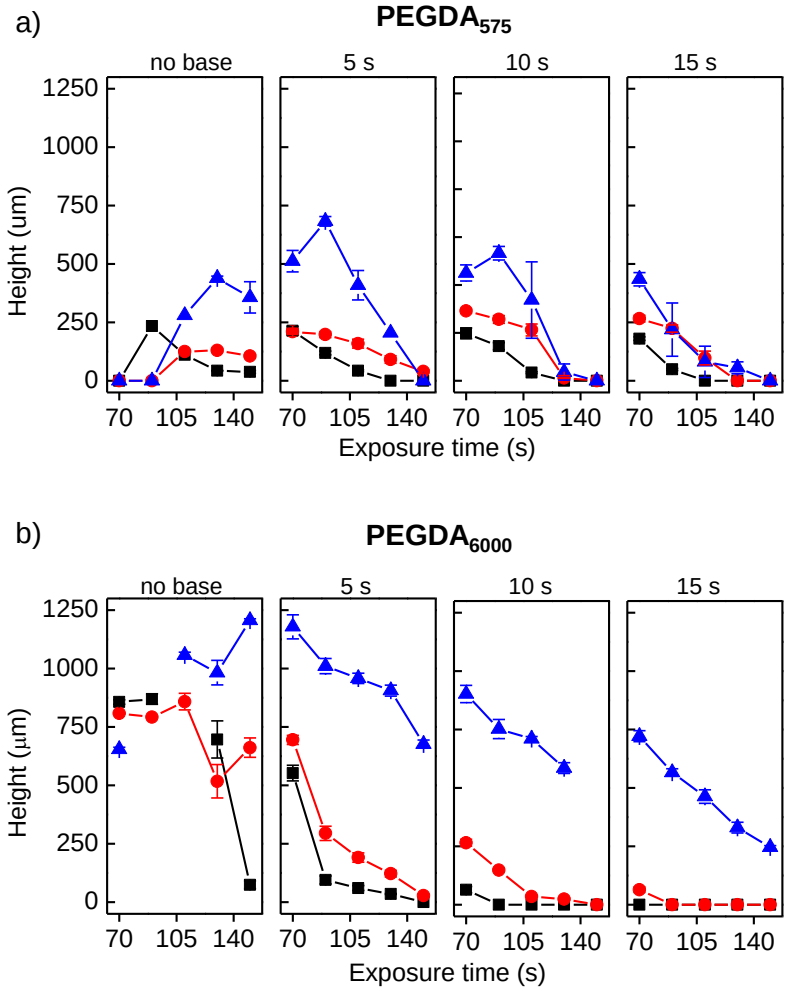

Figure 4.25: Combined plots of the heights of the microstructures (mean ± SD) as a function of the UV exposure time a) $PEGDA_{575}$ and b) $PEGDA_{6000}$. Polymer concentrations of 10% w/v (black), 7.5% w/v (red), and 5% w/v (blue).

As a summary of the influence of the fabrication parameters on the height of microstructures, all the assayed conditions are plotted in Figure 4.25. These plots were used as a reference to select the best fabrication conditions to obtain microstructures with high aspect ratios (> 5) that would be able to stand up, and predict their final height.

Therefore, $PEGDA_{6000}$ seems to be feasible material for developing large and rounded microstructures which mimic villi. Also, at 5% w/v microstructures acquired the highest height (up to 1200 µm) by the UV exposure ranging from 5 s to 10 s (base) and 70 s (microstructure). However, these microstructures eventually fallen, stacked and could be too soft. As an improvement, 6.5% w/v $PEGDA_{6000}$ was chosen between 5% and 7.5% w/v to avoid excessive polymerization on unexposed regions and to ensure that microstructures will stand up after fabrication.

4.3 EFFECTS OF ACRYLIC ACID IN THE FABRICATION OF MICROSTRUCTURED PEGDA HYDROGELS

4.3.1 CHARACTERIZATION OF THE COPOLYMERIZATION OF PEGDA AND ACRYLIC ACID

To make hydrogels bioactive we need to provide functional groups for the anchorage of peptides and proteins, which would promote cell adhesion and growth. For this reason, acrylic acid was added into the polymer recipe. The vinyl group of the acrylic acid allows its copolymerization with PEGDA by photopolymerization (Fig. 4.26). The carboxylic groups, now incorporated to the polymer chains, serve as functional sites to bind proteins by carbodiimide-mediated reaction (section 3.4).[297,298]

To determine the successful copolymerization of PEGDA and acrylic acid, infrared absorption spectra of PEGDA and PEGDA-acrylic acid hydrogels were analyzed by ATR-FTIR (Fig. 4.26). Two concentrations of acrylic acid were studied, low (0.3% w/v) and high (1.2% w/v). FTIR spectra displayed absorbance peaks centered at 1100, 1729, and 2880 cm^{-1}, which correspond to C-O symmetric stretching, CH_2 bending, and C=O stretching from ester bonds. These peaks correspond to main features found in the infrared spectrum of the PEGDA backbone (1100, 1730, 2880 cm^{-1}).[323,354] Therefore, the addition of acrylic acid at low or high concentrations did not disrupt the chemical structure of PEGDA hydrogels. FTIR spectra were then analyzed in detail to determine the successful copolymerization of PEGDA and acrylic acid (Fig. 4.27). Copolymerized hydrogels showed a strong absorbance peak at 1576 cm^{-1}, attributed to the asymmetric vibration of carboxyl groups, while the symmetric band of carboxylic groups

(~1400 cm^{-1}) increased its intensity (Fig. 4.27d,f). The appearance of these two peaks is characteristic of carboxylate groups in the PEGDA–acrylic acid hydrogel,[355] and prove the successful copolymerization of PEGDA and acrylic acid. Moreover, the C=O peak shifted to smaller wavenumbers and suffered a slightly broadening because of the carboxyl group (Fig. 4.27c,f). Finally, the band of -C-H stretching vibration, located at ~3500 cm^{-1}, also suffered a broadening by the appearance of a –OH related peak at 3276 cm^{-1} (Fig. 4.27b,e).

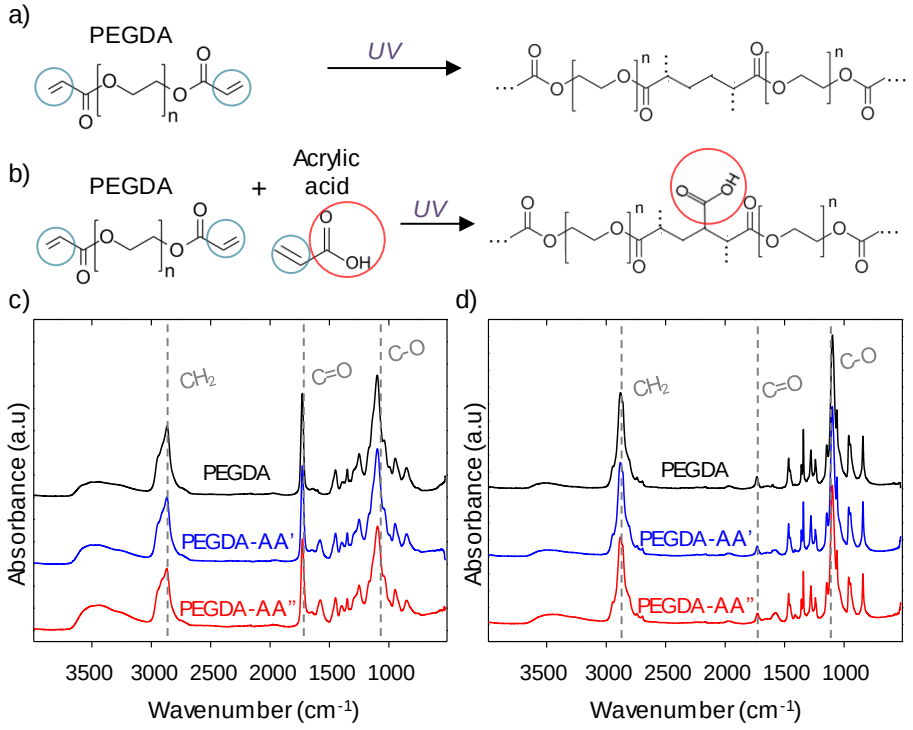

Figure 4.26: Chemical structure of a) PEGDA hydrogel and b) PEGDA–acrylic acid hydrogel. Blue circles are vinyl groups that take part in the polymerization, and red circle is the carboxyl group. FTIR spectra of 10% w/v PEGDA hydrogels (black), 10% w/v PEGDA-0.3% w/v acrylic acid (blue) and 10% w/v PEGDA-1.2% acrylic acid (red) copolymers, obtained from c) $PEGDA_{575}$ and d) $PEGDA_{6000}$.

Copolymerization between PEGDA and acrylic acid has been to increase their water absorbency,[354,356] or to tune their mechanical properties.[357] Also PEGDA has been used as cross-linker to fabricate a poly(acrylic acid) ionogels.[358] Furthermore, Wu *et al.* improved the control of load and release of antimicrobials adding electrostatic charges by blending poly (acrylic acid) (PAA) into PEGDA, to create an interpenetrating network[355]. Other works also used this interpenetrating network of PAA/PEGDA to enhance positive ions absorption.[359]

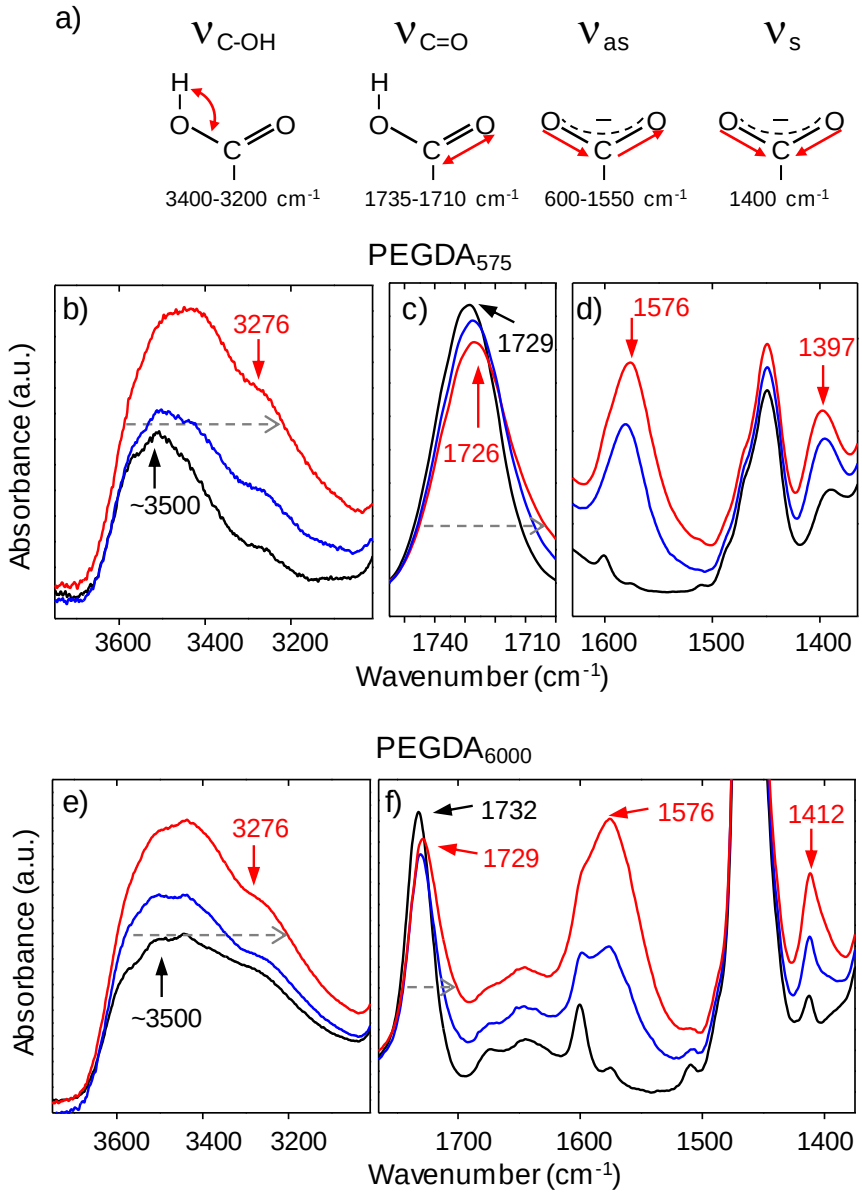

Figure 4.27: a) Schematics of the OH stretch (C-OH), carbonyl stretch (C=O), asymmetric (ν_{as}) and the symmetric vibrational modes (ν_s) of carboxylic the group. Detailed IR spectra of b) OH stretch, c) carbonyl stretch, and d) asymmetric and symmetric modes of 10% w/v $PEGDA_{575}$ (black), 10% w/v $PEGDA_{575}$–0.3% w/v acrylic acid (blue), and 10% w/v $PEGDA_{575}$-1.2%w/v acrylic acid (red) hydrogels; e) OH stretch, and f) carbonyl stretch, asymmetric and symmetric modes of 10% w/v $PEGDA_{6000}$ (black), 10% w/v $PEGDA_{6000}$–0.3% w/v acrylic acid (blue), and 10% w/v $PEGDA_{6000}$-1.2%w/v acrylic acid (red) hydrogels. The dashed arrows indicate broadening of the peaks.

After this qualitative evaluation of the copolymerization reaction, Toluidine blue (TBO) assay was used for a quantitative evaluation. Disc-shaped hydrogels made of $PEGDA_{575}$ and $PEGDA_{6000}$ at 5% w/v and 10% w/v were fabricated varying their acrylic acid content in a range from 0.06% w/v (8.3 mM) to 2.4% w/v (333 mM). After TBO incubation, hydrogels stained differently as a function of the amount of acrylic acid incorporated to their structure. Blue color was more intense when increasing the content of acrylic acid (Figure 4.28a-b). Therefore, the staining corroborates the presence of carboxyl groups and the successful copolymerization of PEGDA and acrylic acid.

The absorbance values of the solutions measured at 633 nm were converted in COOH moles using a calibration curve. The total amount of carboxylic groups in the hydrogels increased when increasing the acrylic acid amount present in the polymer solutions (Fig. 4.28c,d). This happens for both $PEGDA_{575}$ and $PEGDA_{6000}$ hydrogels. Therefore, the acrylic acid incorporation in the hydrogel occurred in a concentration-depend manner. On the other hand, the percentage of acrylic acid incorporation to the PEGDA backbone was low (10%) for acrylic acid solutions of up to 0.3% w/v. Then, it was increasing until saturation (60%) for acrylic acid concentrations higher than 0.12% w/v. No significant differences were found in the incorporation of carboxyl groups between hydrogels produced from solutions at 5% and 10% w/v concentrations, meaning that PEGDA concentration did not affect acrylic acid polymerization. In addition, absorbance values returned statistical significances when comparing $PEGDA_{575}$ and $PEGDA_{6000}$, for 0.3%, 0.6%, and 1.2% w/v acrylic acid concentrations (Table 4.3) being $PEGDA_{6000}$ which incorporated more acrylic acid. Molarity of PEGDA solutions changes one order of magnitude when comparing $PEGDA_{575}$ and $PEGDA_{6000}$. This difference in molarity could explain the significant differences found.

In summary, results show that PEGDA was successfully copolymerized with acrylic acid and that the number of carboxylic groups in the hydrogels depends on the concentration of acrylic acid in the polymer solution. They also showed that the efficiency of acrylic acid incorporation is maximal for acrylic acid concentrations higher than ~1.2% w/v. Poellmann *et al.*, copolymerized polyacrylamide and acrylic acid with the same intention of protein anchoring, and reported similar results than us respect to the TBO analysis. They found significant differences in the amount of released TBO increasing acrylic acid concentration, but the TBO levels did not show significant differences by increasing the amount of polymer (polymer concentration).[300]

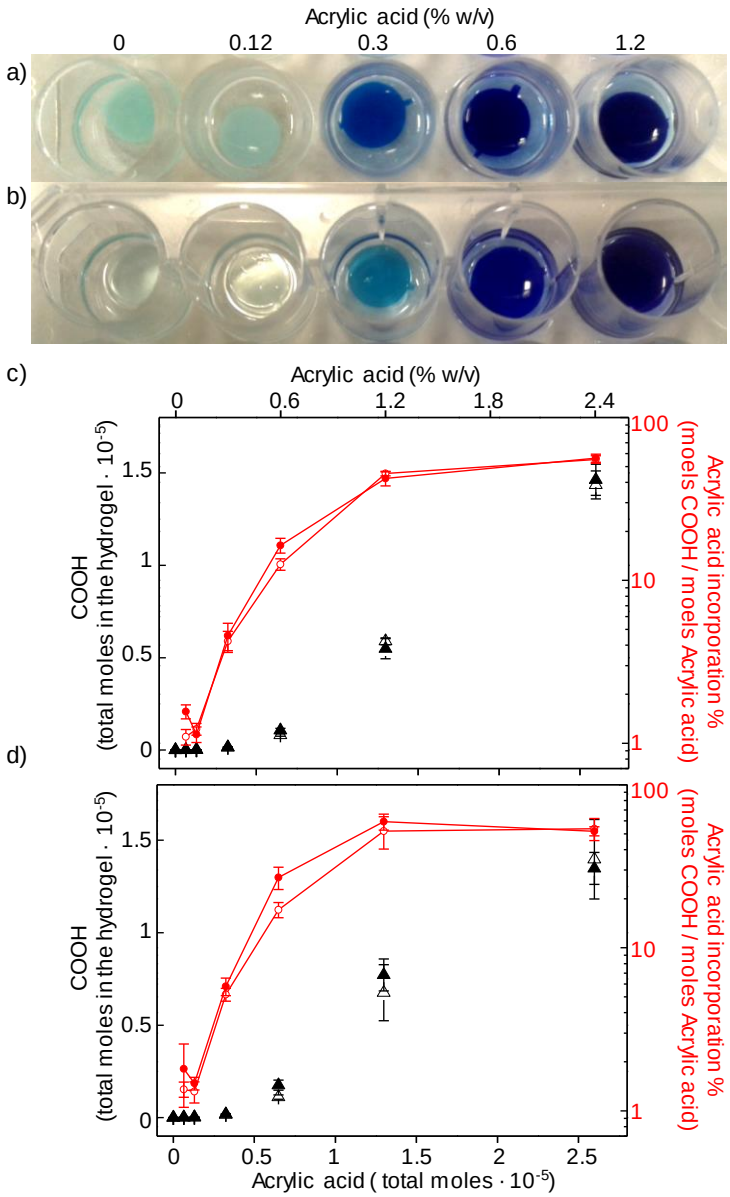

Figure 4.28: Toluidine blue assay. Pictures of a) $PEGDA_{575}$ and b) $PEGDA_{6000}$ containing different concentrations of acrylic acid. Graphs plotting the total moles of carboxyl groups (black triangles) measured in the hydrogels (mean ± SD) and the percentage of acrylic acid incorporated in the hydrogels with respect to the amount included the polymer solution (red circles) (mean ± SD) as a function of moles of acrylic acid in the polymer solutions: c) $PEGDA_{575}$ hydrogels and d) $PEGDA_{6000}$ hydrogels. Polymer solutions contained 5% w/v (hollow symbols) and 10% w/v (solid symbols).

	$PEGDA_{575}$ 5% vs 10%	$PEGDA_{6000}$ 5% vs 10%	$PEGDA_{575}$ vs $PEGDA_{6000}$
Acrylic acid (% w/v)	p-value	p-value	p-value
0.06	0.1	0.7	0.6
0.12	0.7	0.4	0.06
0.3	0.7	0.4	*0.03*
0.6	0.1	0.1	*0.02*
1.2	0.4	0.4	*0.04*
2.4	0.7	1	0.2

Table 4.3: Statistical analysis (Mann–Whitney U test) of measurements represented in Figure 4.28c and d.

4.3.2 EFFECTS OF ACRYLIC ACID ON THE MECHANICAL AND PHYSICOCHEMICAL PROPERTIES OF PEGDA–ACRYLIC ACID HYDROGELS

The effects of acrylic acid on the mechanical properties of PEGDA-acrylic acid hydrogels were studied by determining the Young's modulus in a compression assay. Disc-shaped hydrogels were made of 6.5% w/v $PEGDA_{6000}$ and acrylic acid in concentrations ranging from 0.06% w/v (8 mM) to 1.2% w/v (166.5 mM). Stress-strain curves measured are plotted in Figure 4.29.

Young's modulus values were extracted from the slope of the linear regions comprised between 7% and 10% strain and are plotted in Figure 4.29b. Young's modulus mean values increased for small amounts of acrylic acid in the solution, reached a maximum and decreased again. However, Young's modulus values showed only significant differences (by Kruskal-Wallis test (p = 0.014 > 0.05)) between 0.06% w/v and 0.6% w/v (Fig. 4.29b). Despite these differences when low concentrations of acrylic acid are employed for fabrication, elastic modulus values do not show significant differences with PEGDA when acrylic acid concentrations from 0.6 to 1.2% w/v are used. Young's modulus values remained within the physiological range reported for small intestine[360] for acrylic acid concentrations up to 1.2% w/v (Fig. 4.29c).

In addition, swelling ratio was calculated as the ratio between the difference in heights of a swollen hydrogel and hydrogel after fabrication, and the height after fabrication ($\Delta H/H_0$) and was plotted as a function of acrylic acid content (Fig. 4.30). By statistical comparisons, significant differences between swelling ratios of 6.5% w/v $PEGDA_{6000}$ hydrogel and 6.5% w/v $PEGDA_{6000}$–1.2% w/v acrylic acid hydrogel were found (Kruskal-Wallis test, $p < 0.05$).

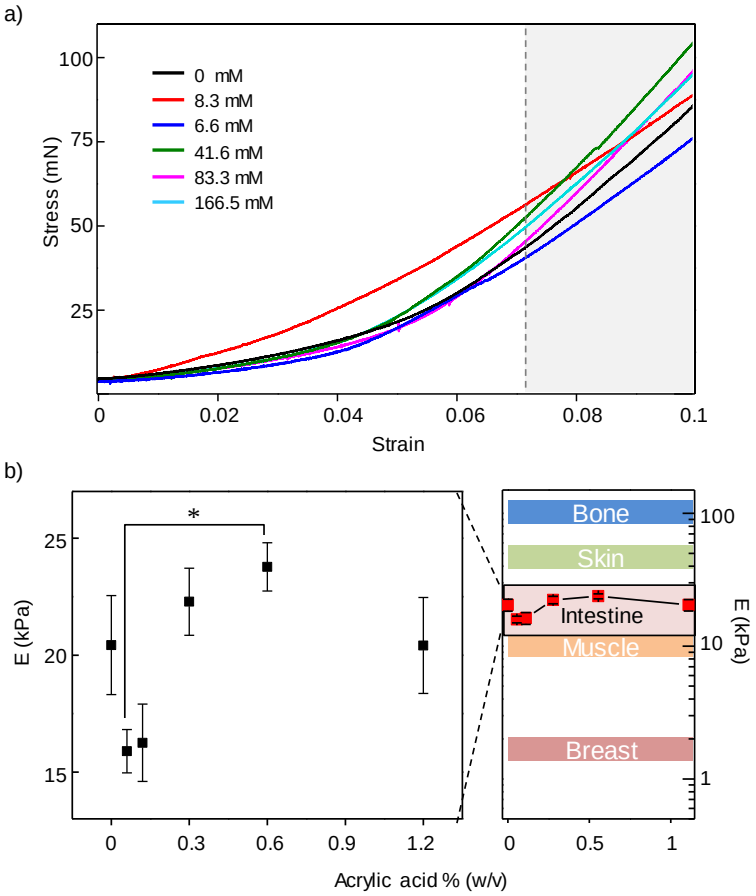

Figure 4.29: Mechanical properties of PEGDA hydrogels. a) Stress-strain curves of 6.5% w/v PEGDA$_{6000}$ hydrogels varying acrylic acid content. b) Young's modulus as a function of the acrylic acid content (mean ± SD, * $p<0.05$). Comparative to the stiffness of soft tissues that range from 0.1 to 100 kPa.[360,361]

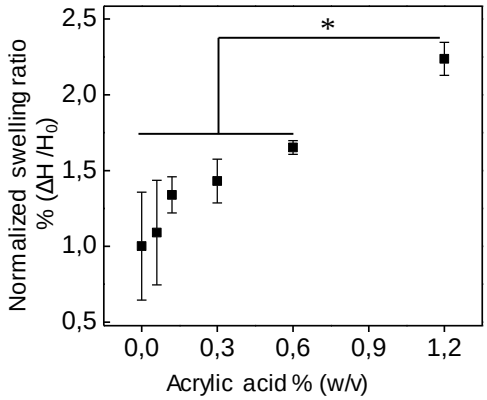

Figure 4.30: Swelling ratios of PEGDA$_{6000}$ 6.5% w/v hydrogels varying acrylic acid, normalized to PEGDA control (0% w/v acrylic acid) (mean ± SD, * $p<0.05$).

Swelling ratio increases, indicating a looser polymeric cross-linked network formed in the PEGDA–acrylic hydrogels. These changes may be attributed to changes in the polymerization. Acrylic acid competes with PEGDA molecules to graft onto PEGDA acrylate groups. As the grafted acrylic acid increased, the availability of vinyl groups of PEGDA decreased. Since such groups also serve as the cross-linking site for PEGDA, this reaction unavoidably lowers the cross-linking density of the PEGDA–acrylic acid hydrogels.[171] Taking into account that the total polymer concentration increases considerably, 20%, when adding acrylic acid at 1.2% w/v, the stiffness did increase significantly.

4.3.3 EFFECTS OF ACRYLIC ACID ON THE SHAPE OF THE MICROSTRUCTURES

The effects of the acrylic acid on hydrogel microstructuring were studied on 6.5% $PEGDA_{6000}$ hydrogels containing acrylic acid concentrations ranging from 0.06% to 1.2% w/v. The microstructured hydrogels were fabricated by UV exposure in two steps, 10 s (hydrogel base) and 70 s (microstructures). The addition of acrylic acid in the polymer solution had a dramatic effect on the morphology of the microstructures (Fig. 4.31).

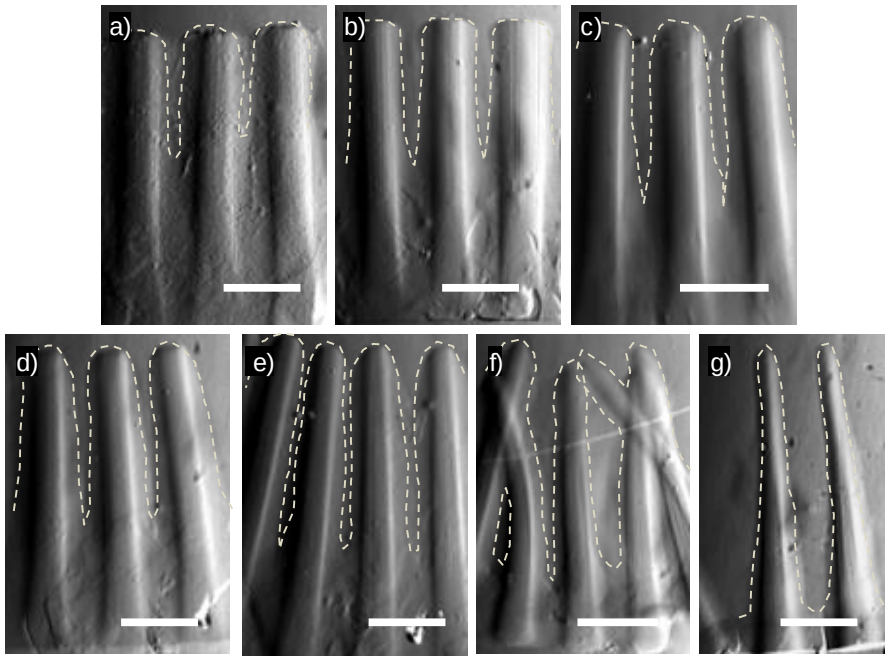

Figure 4.31: Effects of acrylic acid on the morphology of the microstructures. Images of the microstructure profiles highlighting their contours (dash line), corresponding to acrylic acid percentages of a) 0%, b) 0.06%, c) 0.12%, d) 0.3%, e) 0.6%, f) 0.9% and f) 1.2% w/v. Scale bar = 250 μm.

It was observed a substantial reduction in the diameter of the pillars, leading the progressive sharpening of their tips when increasing the acrylic acid concentration. The samples with the highest amount of acrylic acid (0.9% and 1.2% w/v) were so strongly affected that some of them start bending (Fig. 4.31f). The reduction in diameter was also accompanied with a significant reduction of the interstitial material between pillars within the unexposed areas. As a consequence, the effective height of the microstructures increased when increasing acrylic acid content. Contrary, their diameter decreased when increasing the acrylic acid content (Fig. 4.32). The increase in the acrylic acid concentration allowed obtaining microstructures with high aspect ratios, pf about ten height:width. Samples fabricated with acrylic acid concentrations above 0.3% w/v showed diameters below 100 µm, which compromises the objectives of mimicking native villi dimensions (125 µm in diameter).[9,10] Therefore, 0.3% w/v concentration of acrylic acid was selected as the most beneficial for fabricating villi-like microstructures.

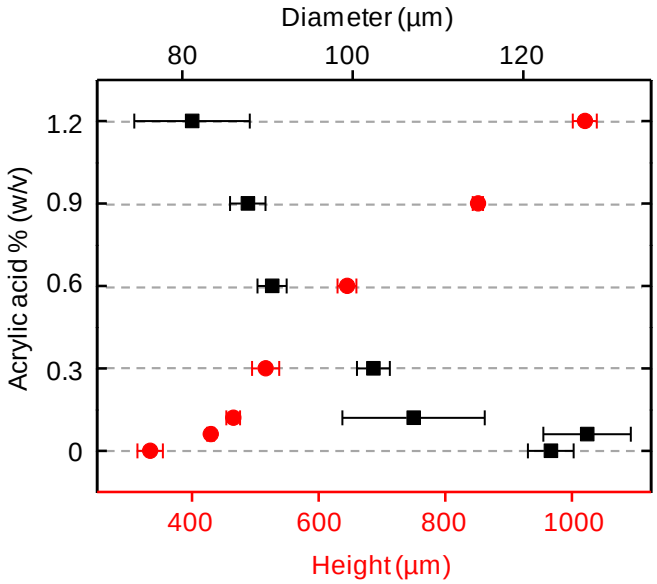

Figure 4.32: Plot of the diameter (black) and the height (red) of the microstructures as a function of acrylic acid concentration (mean ± SD).

Thus, for the fabrication parameters tested, acrylic acid reduced polymerization on unexposed regions and even the dimeter of the microstructures close to the bottom of the container (z~1 mm). To determine the influence of UV exposure times on the PEGDA-acrylic acid microstructuring process, samples were exposed for 10 s for the hydrogel base formation and 50 s, 70 s, and 90 s for the fabrication of microstructures. The resulting microstructure

profiles are shown in Figure 4.33. It can be seen that, similar to PEGDA, the height of PEGDA–acrylic acid microstructures is sensitive to UV exposure time. Combining 10 s and 50 s was not enough produce long microstructures (Fig. 4.33a). However, the combination of 10 s and 90 s over-polymerized the space between microstructures, reducing the effective pillar height below 150 μm (Fig 4.33c). Thus, the combination of 10 s and 70 s was the most appropriate for the fabrication of microstructures with the target dimensions. These combination of exposure times developed shorter microstructures by using PEGDA (without acrylic acid), due to the polymerization on exposed regions. Thus, shorter exposure times would be required for avoid the uncontrolled polymerization, returning, may be, microstructures no longer enough (Fig. 4.25 and Fig. 4.32).

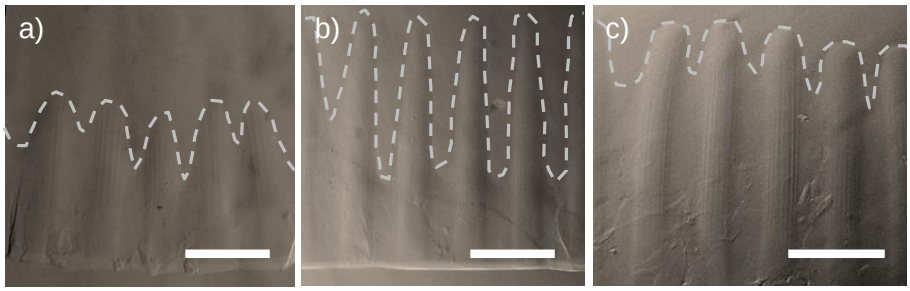

Figure 4.33: Images of the microstructure profiles made of 6.5% w/v $PEGDA_{6000}$ and 0.3% w/v acrylic acid exposed 10 s (hydrogel base) and a) 50 s (microstructures), b) 70 s (microstructures), and c) 90 s (microstructures). The dashed lines highlight the contours of the microstructures. Scale bar = 300 μm.

Overall, high acrylic acid concentrations would be desirable to produce a high density of anchoring points for the functionalization of the material with peptides or proteins. Moreover, for hydrogel surfaces it has been shown, that there is a minimal ligand density needed for an efficient cell adhesion.[140,149,362] However, and even though high acrylic acid concentrations reduce the hydrogel polymerization on unexposed regions and increase microstructures height, concentrations higher than 0.3% w/v produced a considerable reduction in the diameter of the microstructures. For acrylic acid concentrations, up to 0.3% w/v the Young's modulus of the resulting material and its swelling ratio did not differ significantly from those corresponding to PEGDA. Experiments performed with different UV exposure times proved that 10 s for the formation of the base and 70 s for the formation of microstructures were the most appropriate conditions to obtain pillar structures with dimensions close to the native intestinal villi.

4.4 BIOACTIVATION OF PEGDA - ACRYLIC ACID HYDROGELS

4.4.1 CHARACTERIZATION OF FUNCTIONALIZATION PROCESS BY ATR-FTIR

PEGDA – acrylic acid hydrogels show carboxylic groups that can be used to bind cell adhesive molecules, such as extracellular matrix proteins or peptides.

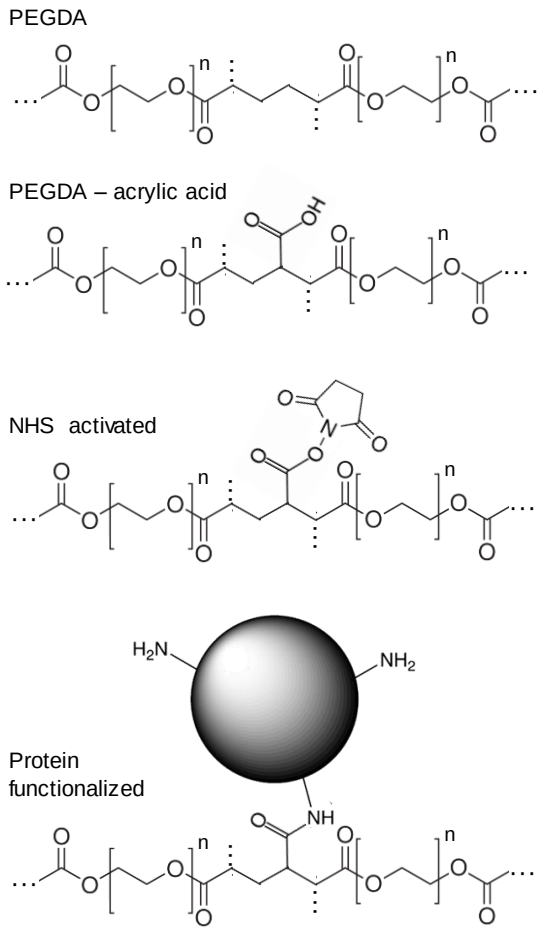

Figure 4.34: Chemical structure and of PEGDA–acrylic acid hydrogels, activation with EDC/NHS and protein conjugation. After activation, PEGDA–acrylic hydrogels contain instable NHS that enhances the covalent conjugation of the amine group of the protein.

Carbodiimide-mediated reaction targets amino group bearing molecules. Functionalization process was based on the copolymerization of PEGDA and acrylic acid, the activation of the carboxylic groups of the acrylic acid by EDC/NHS reaction, and the incorporation of the functional biomolecules (Fig. 4.34). Disc-shaped hydrogels made of 10% w/v $PEGDA_{6000}$ and 1.2% w/v acrylic acid were

used for the qualitative analysis of each functionalization step by ATR-FTIR. Samples with high contents of acrylic acid was selected for this experiment to improve signal to noise ratio and facilitate data analysis.

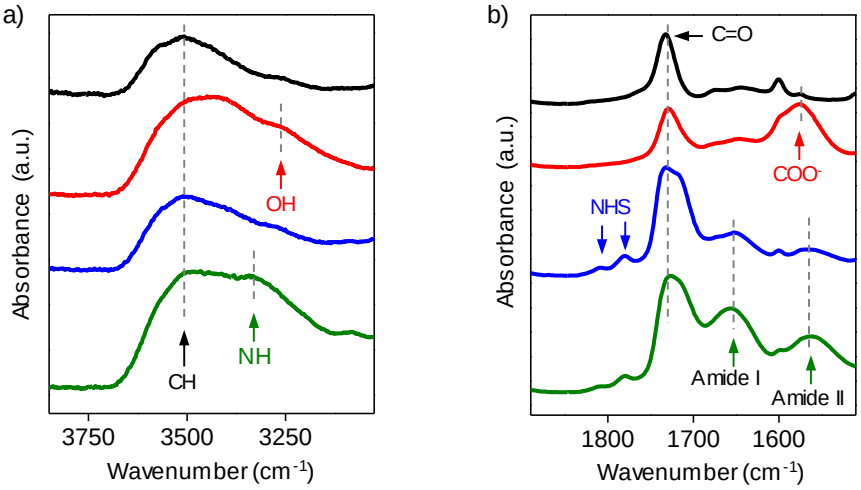

Figure 4.35: FTIR spectra acquired after each step of the functionalization process. a) Detailed spectra of the region of interest between 4000 and 3000 cm^{-1}. b) Detailed spectra of region of interest between 1900 and 1500 cm^{-1}. PEGDA hydrogels in black, PEGDA–acrylic acid hydrogels in red, EDC/NHS activated hydrogels in blue, and hydrogels functionalized with collagen in green.

After activating the hydrogels in the EDC/HNS solution, the carboxylate peak of the acrylic acid, located at 1576 cm^{-1}, disappeared due to the incorporation of NHS molecules through amide bounds (Fig. 4.35b). Two characteristic peaks of NHS appeared around 1800 cm^{-1}, and a weak band related to amide I and amide II bounds around 1550 to 1650 cm^{-1}. After protein incubation, amide peaks became much stronger and NHS peaks showed a decrease in their absorbance. C=O peaks also suffered a broadening and shifted to lower wavenumbers due to the amide bounds present in NHS and proteins. In addition, when binding the protein (Collagen I) the band located around 3500 cm^{-1} broadened due to the contribution of the –NH stretch mode (Fig. 4.35a). All main peaks of the different spectra with their attributed vibrational modes are detailed in Table 4.4. These results demonstrate the success of our strategy for the functionalization of PEGDA-acrylic acid hydrogels.

To optimize the functionalization protocol to maximize the amount of protein incorporated, the activation step was studied for two different concentrations of EDC/NHS (6 mM/5 mM and 50 mM/30 mM). Also, protein incubation was performed with two different concentrations of collagen I (0.04 and 0.4 mg/mL). The increasing on EDC/NHS concentration enhanced the

absorbance of the NHS and amide peaks, and produced higher absorbance and broadening of the C=O peak (Fig. 4.36a). After protein incubation, the relative intensity of the amide peaks correlated witht their concentrations. (Fig. 4.36b,c).

Assigned bond	PEGDA-Acrylic acid	NHS activation	Collagen functionalization	Tabulated value
-C-H stretch vibration	3508	3508	3508	3445[322]
$-CH_2$ stretch	2880	2880	2880	2882[322]
-C=O stretch	1729	1726	1726	1730[323]
C = C stretch	1600	1600	1600	1600[324]
C-O	1100	1100	1100	1098[325]
-OH	3276	–	–	3100-3650[363]
COO^- asym. vibration	1576	–	–	1590[363]
NHS_1	–	1807	1807	1825[363]
NHS_2	–	1780	1780	1793[363]
-NH	–	–	3299	3295[364]
Amide I	–	1652	1656	1650[364]
Amide II	–	1567	1564	1560[364]

Table 4.4: Peak wavenumbers (cm^{-1}) identified in the experimental spectra of PEGDA-acrylic acid hydrogels during the functionalization. And their assignments.

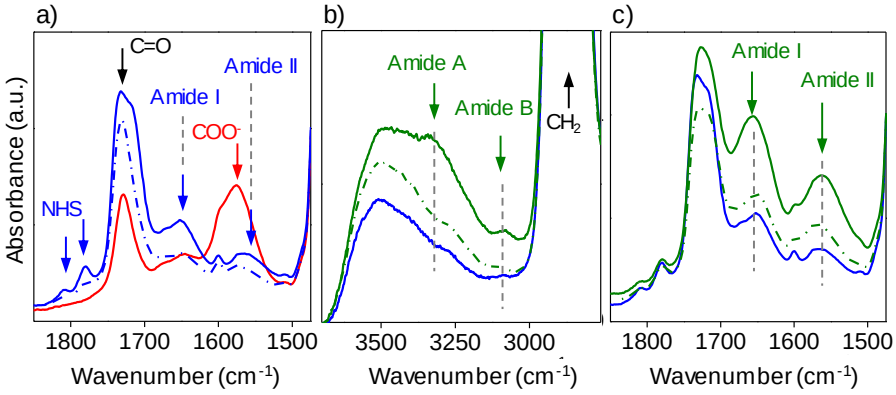

Figure 4.36: Detailed FTIR spectra of a) PEGDA–acrylic acid hydrogels (red), after activation by EDC/NHS (6 mM/5mM dashed blue, 50 mM/30mM blue), and b,c) samples activated with 50 mM/30mM after incubation with Collagen type I (0.04 mg/mL dashed green, 0.4 mg/mL green).

The functionalization protocol proved to be sensitive to activation agent and protein concentrations. Even collagen footprint was already found at 0.04 mg/mL, the increasing of collagen concentration up to 0.4 mg/mL increased the amount of protein incorporated. Considering these results, EDC/NHS concentrations of 50 mM/30mM was stablished as satisfactory for the functionalization process.

4.4.2 STUDY OF THE STABILITY OF THE FUNCTIONALIZATION PROTOCOL

After the characterization of the functionalization process, protein binding was checked by fluorescence microscopy to verify that the proteins remain anchored to the hydrogel, as it would be expected for covalent bounds. In a preliminary test, the fluorescence intensity was qualitatively evaluated after incubating microstructured hydrogels made of 5% w/v $PEGDA_{575}$ and 0.6% w/v acrylic acid with Streptavidin Texas Red® (SAV-TR). Figure 4.37 shows z-stack images of microstructured PEGDA and PEGDA–acrylic acid hydrogels after activation and functionalization, and the fluorescence intensity of several microstructures.

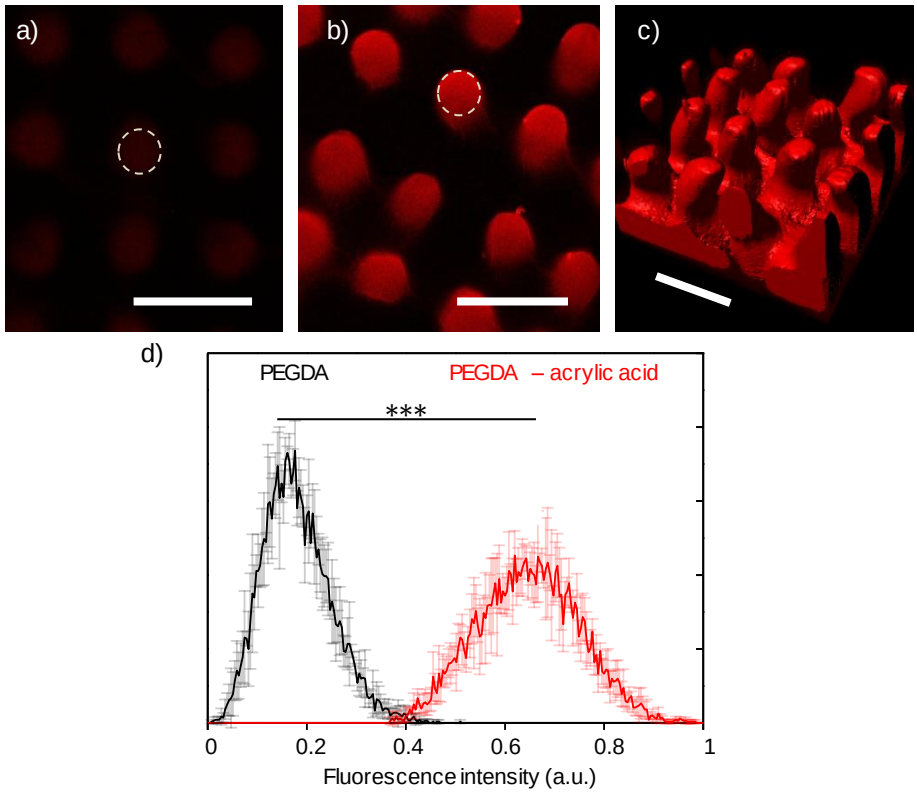

Figure 4.37: Fluorescence intensity of the microstructured a) PEGDA and b) PEGDA-acrylic acid hydrogels, incubated with Streptavidin Texas Red®. c) 3D reconstruction of the PEGDA–acrylic hydrogel. d) Histograms of the fluorescence intensity of PEGDA (black) and PEGDA-acrylic acid (red) hydrogels incubated in SAV-TR. Averaged intensities (mean±SD) showed significant differences between the two samples (T-student test, ***$p<0.001$). Scale bars = 250 µm.

The fluorescence intensity of the hydrogels containing acrylic acid was found to be significantly higher ($p<0.001$) than for those without acrylic acid. The fluorescence signal in the hydrogels without acrylic acid could be due to the unspecific adsorption or trapping of some SAV-TR molecules inside the hydrogel. As controls, PEGDA and PEGDA–acrylic acid hydrogels without EDC/NHS activation were also incubated with the SAV-TR solution and no fluorescence signal was detected. This result proves the need of EDC/NHS activation step for the successful covalently protein binding.

To study the stability of the protein covalently bound to rinsing and storage time, the fluorescence intensity of disc-shaped hydrogels functionalized with SAV-TR was employed. Comparing the fluorescence intensity after increasing storage time (Fig. 4.38a) and number of rinses (Fig. 4.38b), significant differences were found by one way ANOVA test ($p<0.05$) only between 1 and 7 days, and between 3 and 10 rinses. However, as a general trend, increasing rinse number and storage time did not monotonously diminish the fluorescence intensity. Moreover, all intensity values were kept within a narrow range, meaning that the protein binding achieved is stable enough. This has implications in the application of this material to cell culture, the results guarantee that proteins remain non-degraded for long-term culture periods..

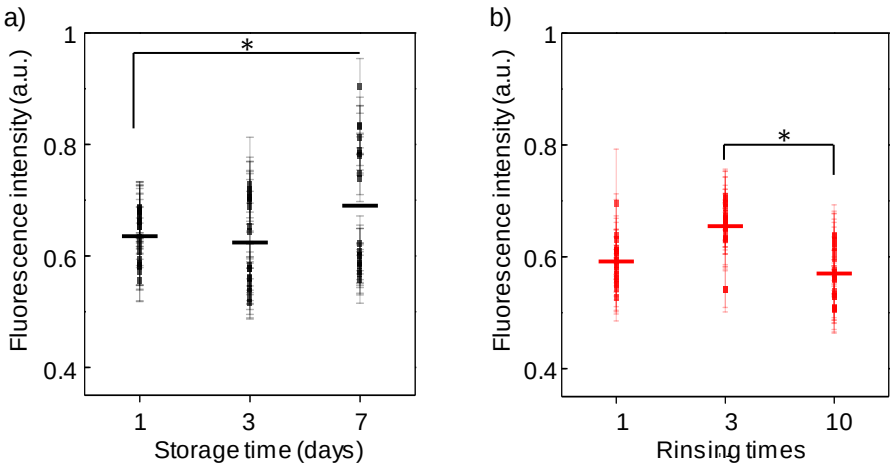

Figure 4.38: Plots of the fluorescence intensity (mean ± SD) of SAV-TR functionalized hydrogels as a function of a) storage time (black) and b) rinsing number (red). The means and SD plotted correspond to each imaged analyzed.

The acrylic acid content in the hydrogels determined the amount of exposed carboxylic groups and, therefore, it is expected to quantitatively correlate such value with the amount of protein bound. To asses this dependence, disc-shaped hydrogels with different acrylic acid content were incubated with

SAV-TR and their fluorescence intensity was evaluated (Fig. 4.39). The solution of SAV-TR protein was highly concentrated (500 µg/mL) to ensure that amino groups exposed by proteins (~10^{-4} moles, considering each protein has ~30 exposed amino groups) will be in excess for the number of carboxylic groups available (~10^{-5} moles).

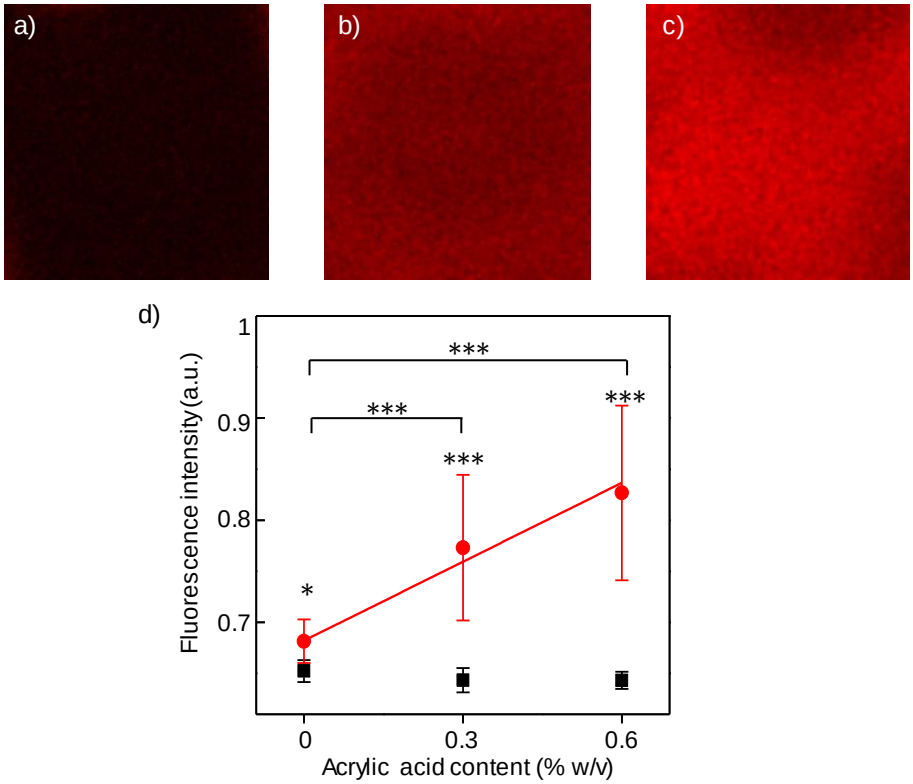

Figure 4.39: Effect of acrylic acid content in the protein binding. Fluorescence images of a) PEGDA, b) PEGDA–acrylic acid (0.3% w/v), and c) PEGDA–acrylic acid (0.6% w/v) hydrogels functionalized with SAV-TR. d) Plot of the fluorescence intensity (mean ± SD) as a function of the acrylic acid content of the polymer solutions after EDC/NHS activation (red circles). Non-activated hydrogels were used as controls (black squares) The line is an eye guide. (*** $p < 0.001$, * $p < 0.05$).

Increasing the acrylic acid concentration in the polymer solution significantly increased ($p<0.001$) the fluorescence intensity of the samples in a concentration dependent manner for the range of concentrations assayed. Non-activated hydrogels (control) showed similar low values of fluorescence intensity for all the different acrylic acid contents. These results proved the need of the EDC/NHS activation for the success of the functionalization. Thus, acrylic acid

concentrations ranging from 0.3% to 0.6% w/v, established as optimal for the fabrication of anatomically biomimetic villi-like microstructures in the previous section, provide enough number of carboxylic groups in the hydrogels for their successful functionalization using protein solutions with concentrations > 50 µg/mL.

Overall, *in situ* copolymerization of PEGDA and acrylic acid is an efficient strategy to anchor proteins that remain stable for long periods. This strategy of copolymerize acrylic acid with PEGDA to make PEGDA hydrogels with carboxyl groups and follow EDC/NHS coupling chemistry for conjugation of proteins, was been published firstly by Drumheller *et al.* in 1994.[365] Since then, few reports have followed similar strategies. First, PEGDA has been photopolymerized and post-grafted by acrylic acid. PAA and PEG formed a superficial interpenetrating network and a thin layer of PAA above the PEG hydrogel surface.[366] Carboxylic groups of the PAA were used to anchor collagen and enhance cell adhesion. On the other hand, the copolymerization of acrylic acid and PEGDA has been used to control specific adsorption of antibodies onto photonic crystals. [367]

4.4.3 PEGDA – ACRYLIC ACID HYDROGELS SUPPORT NIH 3T3 CELLS GROWTH

To ensure that functionalized PEGDA–acrylic acid hydrogels support cell attachment, cell culture experiments with NIH-3T3 fibroblasts were carried out. For this purpose, $PEGDA_{575}$, which has been previously used to encapsulate and culture cells successfully, was selected.[173,190,368] Fibroblast attachment and spreading require substrates with enough rigidity,[369,370] so $PEGDA_{575}$ was used at 20% w/v concentration.[170,234] To ensure enough amount of protein anchored, 2.5% w/v of acrylic acid (0.35 M) was added to the polymer solution, and flat hydrogels were fabricated by 200 s of UV exposure. Hydrogels without acrylic acid were used as controls. After 3 days of swelling, hydrogels were functionalized with 500 µL of 100 µg/mL fibronectin solution (section 3.4). Then, NIH-3T3 fibroblasts were seeded at a density of 10^5 cells/cm^2 and cultured during 4 hours. After this time, few cells were found on $PEGDA_{575}$ hydrogels (9% of seeded cells) (Fig. 4.40a). Moreover, they had an extremely rounded morphology (Fig. 4.40b). This is as expected, due to PEG resistance to protein adsorption, which inhibits cell adhesion.[371] On the contrary, $PEGDA_{575}$-acrylic acid hydrogels displayed a lot of nuclei (Fig. 4.40c) equivalent to 70% of cell attachment. Also, already at 4 h cells showed a spread morphology (Fig. 4.40d). These huge differences in cell adhesion (Fig. 4.40e) demonstrated the improvement on the PEGDA bioactivity due to the successful co-polymerization with acrylic acid.

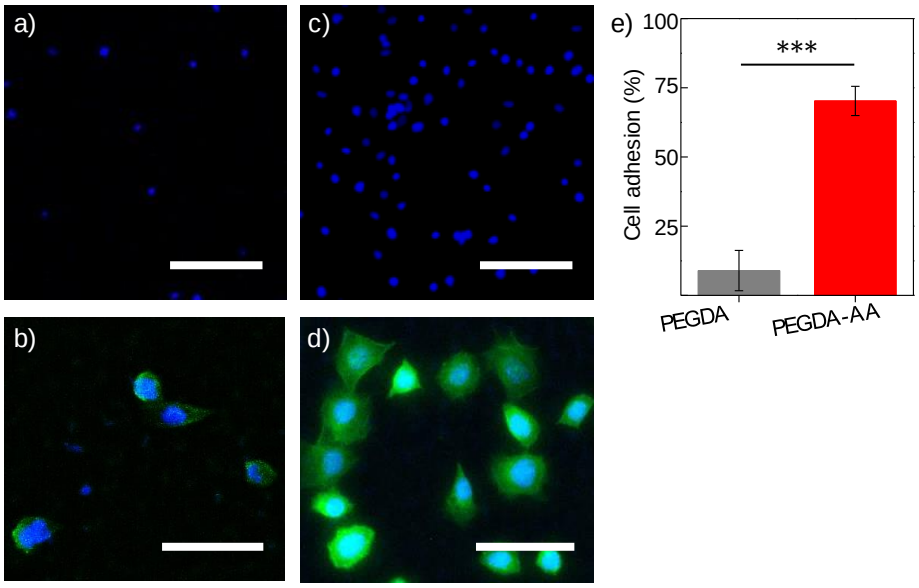

Figure 4.40: Representative pictures of NIH-3T3 fibroblasts cultured on a,b) 20% w/v $PEGDA_{575}$, and c,d) 20% w/v $PEGDA_{575}$–2.5% w/v acrylic acid functionalized with fibronectin. Nuclei are stained in blue and F-actin in green. e) Cell adhesion percentage (mean±SD) for PEGDA and PEGDA–acrylic acid (PEGDA – AA) hydrogels. Three replicas (N = 3) were used and three images were taken at 10X magnification for each hydrogel. Cell adhesion was calculated as an average of the nine pictures. *** denotes p-value < 0.001 from Mann–Whitney U test. Scale bars: a,c = 50 µm, b,d = 25 µm.

These experiments showed that fibroblast successfully adhered on hydrogels fabricated using 20% w/v $PEGDA_{575}$–acrylic acid solutions. However, 20% w/v $PEGDA_{575}$ hydrogels have very small mesh sizes, between 1.3 and 3.7 nm,[372] which may comprise the diffusion of nutrients and waste metabolites at the basal part of the cells.[373]. In addition, their Young's modulus has been reported to be higher than 500 kPa,[173] which is out of the physiological range reported for the small intestine mucosa.[374] Therefore, fibroblast growth was also tested in hydrogels fabricated from 10% w/v $PEGDA_{575}$ and 1.25% w/v acrylic acid solutions. In these experiments, we also decided to evaluate the influence of the microstructuring. Microstructures were fabricated by a single UV exposure of 170 s through a photomask with windows 300 µm in diameter. By this process, pillars of 461 ± 9 µm in height were obtained (Fig. 4.41). As no base exposure was used, pillars were formed directly on top of the glass coverslip, leaving some areas non-covered by hydrogel. The microstructured hydrogels were then functionalized with 50 µg/mL fibronectin solution, and fibroblasts were seeded at $2.5 \cdot 10^4$

cells/cm^2. Cell culture was stopped after 7 days, when cells were fixed. Cell nuclei and actin cytoskeleton were stained and imaged.

A top view picture of a sample showing the autofluorescent signal of the microstructures and the cell nuclei is shown in Figure 4.41a. The microstructures were fallen due to the sample mounting. Cell-empty round areas refer to the places that microstructures occupied before falling, and arrows indicate cells grown on coverslip regions between pillars. After seeding, cells were homogenously distributed between the pillars. After 7 days, the fibroblasts adhered and proliferated on both the hydrogel microstructures and the coverslip areas surrounding them. In terms of cell density, significant differences were not found between the coverslip areas and the microstructures of the same sample (Fig. 4.41b). However, cell density on microstructures was highly variable (68%) in the same sample as the standard deviation in Figure 4.41b shows. Regarding the position adopted by the cells along the microstructure, cell density was significantly higher at the upper half of the microstructures from that found at the bottom half ($p<0.01$). Statistically significant differences ($p<0.05$) were also found comparing cell densities at the upper half of the microstructures and on the coverslip, being higher again at the tip of the microstructures (Fig. 4.41c). These differences in cell density also could be observed in higher magnification images where the tip (Fig. 4.41e) shows a full coverage of spread cells, but not the base (Fig. 4.41f). In both cases, the cells displayed a well-formed F-actin cytoskeleton and radial projections or filopodia.

We found that fibroblasts did not create a cell monolayer on the whole microstructure, but some empty areas were found at the tip and more at the base. We attribute this to the fact that cells might not had enough time in culture. Overall, these results showed successful fibroblast proliferation and migration on microstructured hydrogels.

Considering the results on cell positioning, cells may migrate from the coverslip to the microstructures. It is extensively reported the preferentially migration of fibroblasts toward stiffer substrates,[369,370,375] but in our case it seems that cells migrate to the softer hydrogel. Chemical and mechanical stimuli play significant roles in guiding the direction of fibroblast migration, and Hale *et al.* reported similar results when culturing fibroblasts in substrates with dual chemical-mechanical gradients. Fibroblasts chose as a primary direction of motion high collagen-low Young's modulus substrates, instead the low collagen-high Young's modulus subtrates.[376]

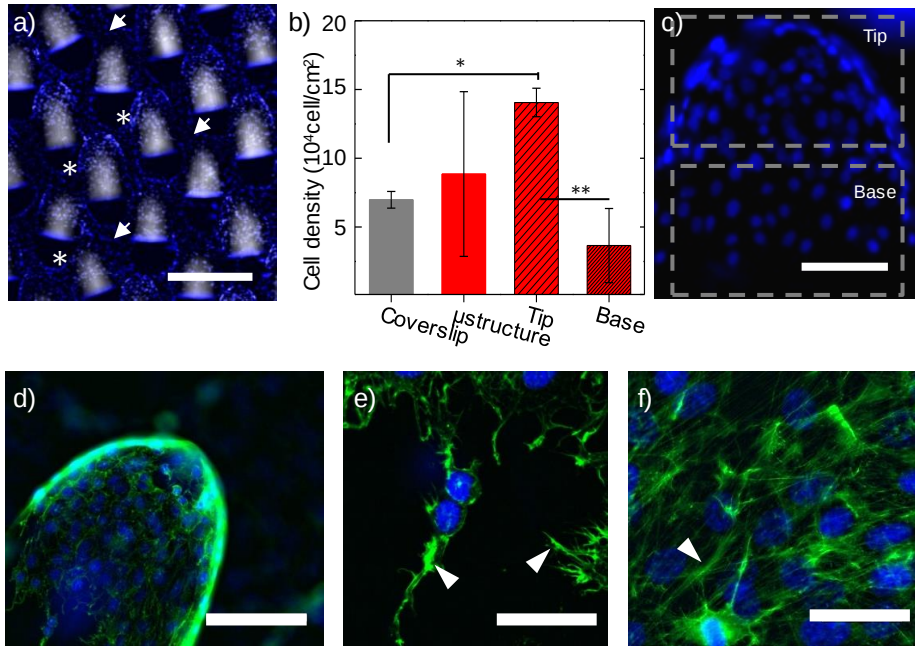

Figure 4.41: NIH-3T3 fibroblasts on PEGDA-acrylic acid microstructures at day 7 of cell culture. a) Top view image of fibroblasts cultured on microstructures. Empty holes are the places that microstructures occupied before falling (asterisk), and arrows indicate cells on coverslip. b) Plot of cell density (mean ± SD). Three replicas per condition were used. ** and * denotes p-value < 0.01 and < 0.05 from Mann–Whitney U test. c) Detail of a microstructure where it can be seen the different cell density between the tip and the base. d) Fluorescence microscopy image of a microstructure covered by spread fibroblasts. Detailed images of the base e) and the f) tip of a microstructure, and filopodia (arrowhead). Nuclei in blue, F-actin in green. Scale bar: a= 750 μm, c = 100 μm, d = 125 μm, e, f = 25 μm.

4.5 FABRICATION OF MICROSTRUCTURED PEGDA-ACRYLIC ACID HYDROGELS SUPPORT EPITHELIAL-LIKE CELL MORPHOLOGY

4.5.1 LAMININ FUNCTIONALIZED HYDROGELS PROMOTE THE ADHESION OF MDCK CELLS

Once we saw that the microstructured PEGDA-acrylic acid hydrogels allowed the proliferation and migration of fibroblasts, Madin-Darby canine kidney (MDCK) cell line was chosen as a model to study the effects of PEGDA-acrylic acid hydrogels on their epithelial morphology. MDCK cell line is widely used as a epithelial cell model because it shows a marked apico-basolateral polarity, well defined tight junctions, and rapid growth rate.[377,378]

To promote epithelial cell morphology, laminin was chosen as the protein to functionalize hydrogels. Laminin is the major non-collagenous component of the basement membrane of epithelial tissues.[14] To determine the minimum amount of laminin that enable MDCK adhesion, disc-shaped hydrogels made of 10% w/v $PEGDA_{575}$ and 1.25% w/v acrylic acid were functionalized with several concentrations of laminin (0, 10, 50 and 100 μg/mL). Then, MDCK cells were seeded at a density of $2 \cdot 10^5$ cells/cm^2 and cultured during 24 h.

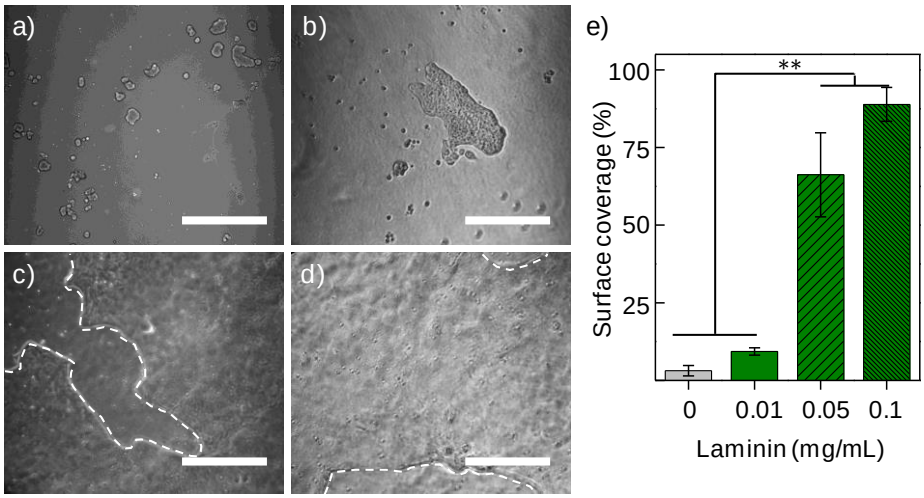

Figure 4.42: Effects of laminin concentration on MDCK adhesion and spreading. Bright field microscopy images of MDCK cells cultured on 10% w/v $PEGDA_{575}$–1.25% w/v acrylic acid, functionalized with laminin at a) 0, b) 10, c) 50, d) 100 μg/mL. Scale bar = 500 μm. e) Plot of MDCK surface coverage (mean ± SD) as a function of laminin concentration. Tree images of randomly selected areas were taken of three replicas. ** denotes p-value < 0.01 from Mann–Whitney U test.

No significant cell adhesion and spreading was found on the hydrogels without laminin (Fig. 4.42a). For the samples with laminin, the extent of cell adhesion and spreading was dependent on the laminin concentration. Increasing laminin concentrations produced better cell adhesion and greater coverage of the hydrogel surfaces (Fig. 4.42b-d). Quantitative measurements of the cell surface coverage showed that by using 10 μg/mL laminin solutions no significant improvement was found with respect to the control (Fig. 4.42b), while laminin concentrations higher than 50 μg /mL allowed MDCK surface coverage with a statistical relevance ($p < 0.01$), with respect to the control. No significant differences were found when employing laminin concentrations of 50 and 100 μg/mL, but the average value was higher for 100 μg/mL (Fig. 4.42e). Therefore, 100 μg/mL laminin was chosen as the minimum concentration to be used in the functionalization of the hydrogels for the culture of epithelial cells.

4.5.2 MICROSTRUCTURED PEGDA-ACRYLIC ACID HYDROGELS ALLOW MDCK PROLIFERATION AND PROMOTE EPITHELIAL MORPHOLOGY

To evaluate the effects of our engineered PEGDA–acrylic acid hydrogels on the polarization of MDCK cells, microstructures made of 10% w/v $PEGDA_{575}$ and 1.25% acrylic acid (the same tested with fibroblasts) and 5% w/v $PEGDA_{575}$ and 0.6% acrylic acid were used. The 5% w/v solution was studied because it is reported that epithelial tissues are indeed softer than the elastic modulus provided by the 10% w/v $PEGDA_{575}$.[173,360] The microstructures were fabricated by a single UV light exposure 170 s. By this process, pillars of 461 ± 9 µm in height were obtained. As no base exposure was used, pillars were formed directly on top of the glass coverslip, leaving some areas non-covered by hydrogel. Microstructures were functionalized with 100 µg/mL laminin solution.

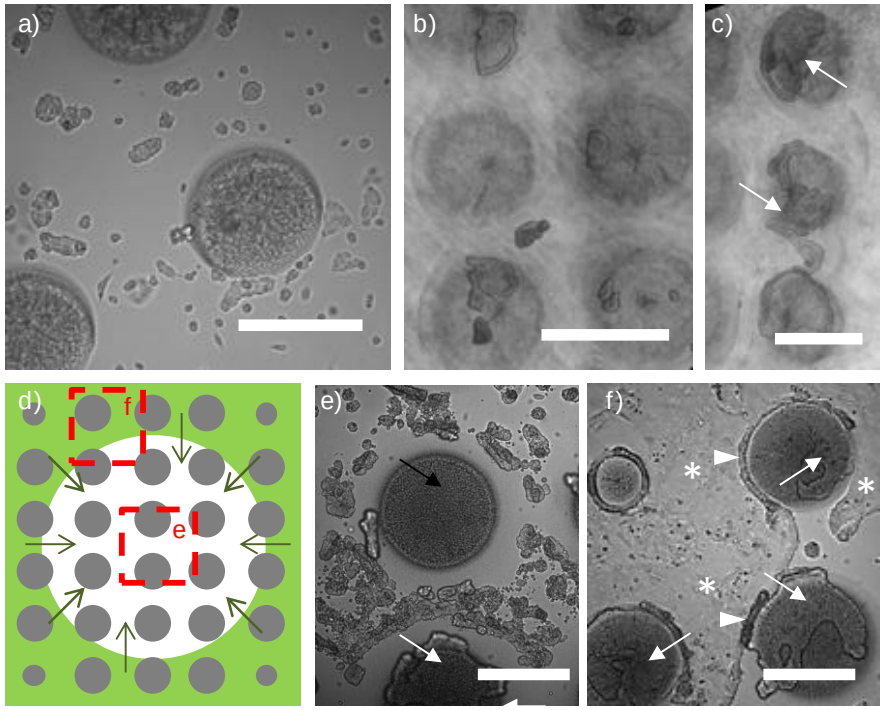

Figure 4.43: MDCK cells cultured on the hydrogel microstructures. Top view images of hydrogels taken by bright field microscopy after a) 4 hours of seeding on 10% w/v $PEGDA_{575}$–1.25% w/v acrylic acid microstructures, and b-c) 7 days on 5% w/v $PEGDA_{6000}$–0.6% w/v acrylic acid microstructures. d) Scheme of the microstructured area (grey circles) depicting the areas covered by MDCK cells (green) and not covered (white). Red squares show the approximated position for images e) and f). e,f) Top view images of MDCK cells after 7 days on 10% w/v $PEGDA_{575}$–1.25% w/v acrylic acid microstructures. White arrows denote cell aggregates on top of microstructures, black arrow denote a microstructure with no cells, asterisks cell covered surfaces, and arrowheads cell edges. Scale bars: a,e,f = 300 µm, b= 500 µm, c = 400 µm.

MDCK cells were seeded at a density of $2.5 \cdot 10^4$ cells/cm^2, the same as fibroblasts, and were cultured for 7 and 14 days. After 4 hours of seeding cells were distributed at the base of the hydrogels, between microstructures (Fig. 4.43a). At day 7, on the 5% w/v $PEGDA_{575}$ microstructures, some cells were on the tip of the microstructures, covering small areas forming clusters. Almost no cells were at the base of the pillars (Fig. 4.43b,c). For 10% w/v $PEGDA_{575}$, the culture was not homogeneous over all the microstructured surface. At the center of the microstructured area, cells started to form aggregates, covered the glass space between microstructures (Fig. 4.43e), and some cell patches were found on top of microstructures. The base areas close to the edges of the microstructured area were fully covered by MDCK cells, while at the center cells partially covered few microstructures (Fig. 4.43f). To be noticed, cell dense areas appeared around the microstructures. These bulges seem to be composed by fronts of migrating cells, which were climbing up the pillar walls.

After 14 days, the cell culture on 5% w/v $PEGDA_{575}$ microstructures did not improve, the mass of cells on the top of the microstructures remained with no significant changes (Fig. 4.44a-c). On the other hand, cells on 10 % w/v $PEGDA_{575}$ microstructures covered more surface between the microstructures (Fig. 4.44d), but the surface coverage was not complete. The microstructures were still surrounded by cell masses and there were also differences in cell coverage depending on the position within the array. At the center of the microstructured area almost the 60% of the microstructures had cells on the top. However, they were only partially covered, from 4 to 60% (30% ± 20%) of their areas (Fig. 4.44e,f). On the boundaries of the microstructured area, where the microstructures were shorter, MDCK cells fully covered the microstructures and the space between them forming a full packed monolayer (Fig. 4.44f).

Thus, from these experiments we conclude that MDCK cells attached to PEGDA–acrylic acid hydrogels and proliferate for 14 days. On microstructures of 300 μm in diameter, migrating cell fronts were observed, which in most cases stopped at the lowest parts of the pillars. Cell spreading and migration over the surface was more effective on the microstructures fabricated from polymer solutions at 10% w/v of $PEGDA_{575}$. It has been reported that stiffness of the substrate is an important factor for cell spreading and migration.[375] During the time of cell culture tested (14 days), cells on 10% w/v were increasing their surface coverage progressively. At day 14, the lowest part of the microstructures showed cell layers around their bases, and a partial coverage on the pillars while most of the surface between microstructures (coverslip) was covered. This progression of the cell culture together with the fact that shorter pillars on the edges of the microstructured area were fully covered indicates that maybe increasing cell culture time may lead the formation of a complete monolayer.

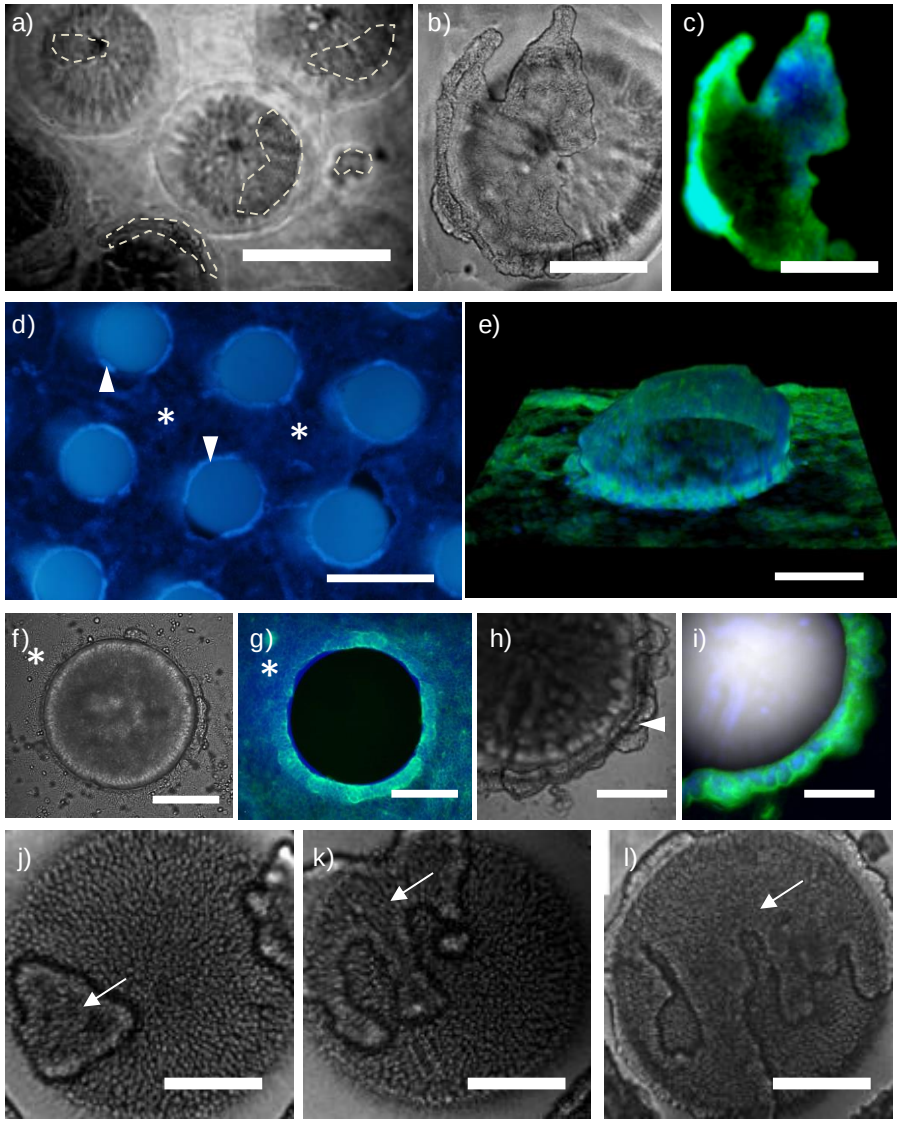

Figure 4.44: MDCK cells cultured on the hydrogel microstructures at day 14. a) Top view image of 5% w/v PEGDA$_{6000}$–0.6% w/v acrylic acid microstructures. The dash line highlights where cells are. Detail of the tip of a microstructure on b) bright field and c) fluorescence microscopy. d-l) 10% w/v PEGDA$_{575}$–1.25% w/v acrylic acid microstructures. d) Fluorescence microscopy image that show high degree of surface coverage (asterisk). Arrowheads indicate cell masses at the edges of microstructures. e) Microstructure located at the boundary of the UV exposed area showing full cell coverage. f,g) Microstructure located at the center of exposed area showing no cells on its tip. h,i) Detail of the edge of a microstructure showing an accumulation of cells forming a ring. j-l) Different microstructures partially covered (arrows) by cells. Nuclei in blue and F-actin in green. Scale bars: a,d = 500 µm, b,c,f,g= 150 µm, e = 50 µm, h-l = 100 µm.

At this stage, not only surface coverage was relevant but also it was important to get information of the polarization stage of cells at the end of the culture time. Therefore, polarization indicators such as cell morphology, position of the nuclei and accumulation of actin at the apical side were investigated by high magnification confocal microscopy. Figure 4.45a shows how the cells formed a monolayer at the base of the hydrogels, which continued up along the wall of microstructure. A cross-section of this monolayer showed that, although it did not reach the tip of the microstructures, cells showed the typical apico-basal morphology of the epithelial cells (Fig. 4.45b). This morphology is characterized by a palisade disposition of the cells with a columnar shape and the nuclei positioned close to the basal side. Interestingly, cells also showed an elongated cell shape with the presence of a brush border (an accumulation of actin signal) at the apical side of the cells (Fig. 4.45b,c). The immunostaining of two specific epithelial cell markers, ZO-1, found in the tight junctions foci at the apical cell region, and β-catenin, found at the basolateral membrane, was also performed. Fig. 4.45d shows that MDCK cells cultured for 14 days on the 10%w/v $PEGDA_{575}$ microstructures expressed these epithelial markers properly located: ZO-1 as dots between adjacent cells at the upper part of the cell, and β-catenin distributed along the basolateral cell domain.

Overall, microstructures of 300 μm in diameter allowed MCDK adhesion and proliferation, preferentially on hydrogels made of 10% w/v $PEGDA_{575}$–1.25% w/v acrylic acid than on the softer (5% w/v $PEGDA_{575}$- 0.6% acrylic). The Low cell attachment, spreading, motility and proliferation on compliant substrates has been reported previously by several authors[379–381]

Despite MDCK cells showed columnar polarization and properly located epithelial markers, almost 50% of the microstructures did not show full cell coverage. Cells cultured on porous membranes usually reach cell confluence after 3-5 days of seeding when starting with similar cell densities.[382] However, one must consider that the total surface area of our microstructures, due to their 3D topography is much larger than 2D area (up to 5 times for structures 400 μm in height). Therefore, it is expected for the cells to take longer periods of time for a full coverage. This is supported by the fact that shorter microstructures (<100 μm in height), which have less total surface, are fully covered by cells. To further investigate this hypothesis, shorter microstructures were fabricated. In addition, the diameter of the pillars was reduced to 100 μm. This aimed also to make the microstructure dimensions closer to those reported for native villi.

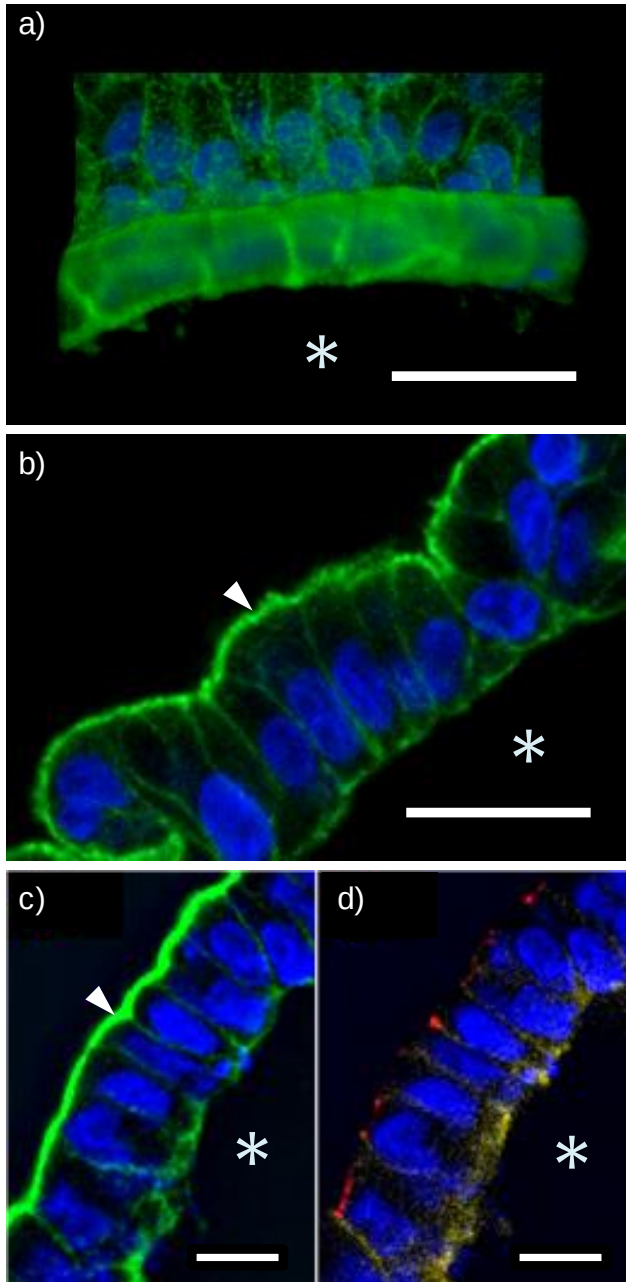

Figure 4.45: Confocal images of MDCK cells cultured on hydrogels after 14 days. a) Top view, and b) transversal cross-section of the MDCK cells cultured of a microstructure, demonstrating the high apico-basal polarization and the brush border formation (arrowhead). c,d) Cross-section of the hydrogel, which shows the brush border formation and the properly located polarization markers. Nuclei are stained in blue, F-actin is stained in green, ZO-1 in red, and β-catenin in yellow. Asterisks refers to the place where hydrogel is located. Scale bars: a = 50 μm, b = 25 μm, c,d = 15 μm.

To study the effects of the microstructure size on MDCK cell coverage, polymer solutions of 10% w/v $PEGDA_{575}$-1.25% acrylic acid, and 5% w/v $PEGDA_{575}$-0.6% acrylic acid were exposed 170 s using the photomask with windows 100 μm in diameter. With these fabrication parameters, no pillars were obtained using 10% w/v solutions due to polymerization of unexposed regions. For 5% w/v solutions, pillars of 213 ± 7 μm in height and 109 ± 8 μm in diameter were obtained. These sizes represent a reduction of up to 2 times in height, and 3 times diameter (20 in total surface area) with respect of microstructures used in the previous experiment. The hydrogels were functionalized with 100 μg/mL laminin solution and MDCK cells were seeded at a density of $2.5 \cdot 10^4$ cells/cm^2 and cultured for 21 days. Figure 4.46 shows the evolution of MDCK cells over the period of time in culture. Despite MDCK cells showed a poor evolution on microstructures of 300 μm in diameter and 400 μm in height, it was found that on pillars of 100 in diameter and 200 in height MDCK cells covered all the surface of microstructures at day 14. However, the microstructures were very soft (36 kPa),[383] so they bended and stacked at their tips, forming cell aggregations (Fig. 4.46d). In addition, a lot of microstructures detached from the coverslip (Fig. 4.46e), resulting in a mixture of clustered cells and microstructures (Fig. 4.46f).

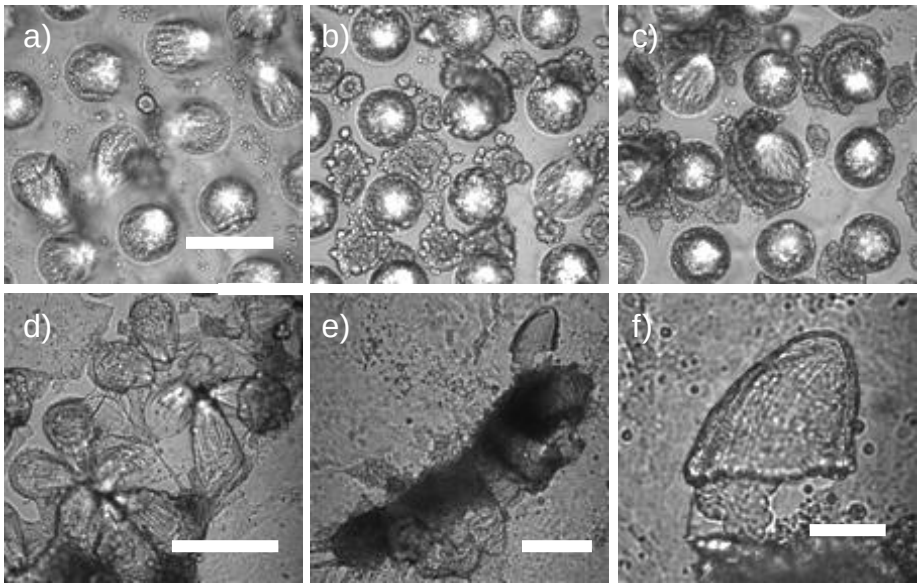

Figure 4.46: Spatiotemporal distribution of MDCK cells cultured on 5% w/v $PEGDA_{575}$-0.6% acrylic acid microstructures of 100 μm in diameter. Top view images a) after seeding, b,c) 7 days, d) 14 days, and e,f) 21 days. e) Group of detached microstructures. f) Detail of an isolated microstructure covered by cells. Scale bars: a-c = 200 μm; d = 300 mm; e = 200 μm; f = 50 μm.

With these promising results, we decided to test microstructures fabricated with a hydrogel base, which might be useful to avoid the detachment of the microstructures. To include a base, a set of experiments were designed where microstructures were fabricated by UV exposure in two steps.

Two polymer solutions were used: 5% w/v $PEGDA_{575}$-0.15% w/v acrylic acid, and 10% w/v $PEGDA_{575}$ - 0.3% w/v acrylic acid. The hydrogels were fabricated by an exposure of 10 s to form the hydrogel base, and 150 s to grow the microstructures. With respect to the samples described in the previous experiments, the amount of acrylic acid was reduced to adjust its concentration to the ranged described previously. Despite of decreasing acrylic acid concentrations, the fabrication of microstructures from 10% w/v $PEGDA_{575}$-0.3% w/v acrylic acid solutions was unsuccessful, due to polymerization in unexposed areas. On the other hand, the functionalization of the microstructures fabricated from 5% w/v polymer solutions was carried out by placing a 50 µL drop of 500 µg/mL laminin solution onto the hydrogels. MDCK cells were seeded at $2.5 \cdot 10^4$ cells/cm^2 and cultured for 14 and 21 days. At day 14 a set of samples were fixed, and nuclei and F-actin were stained.

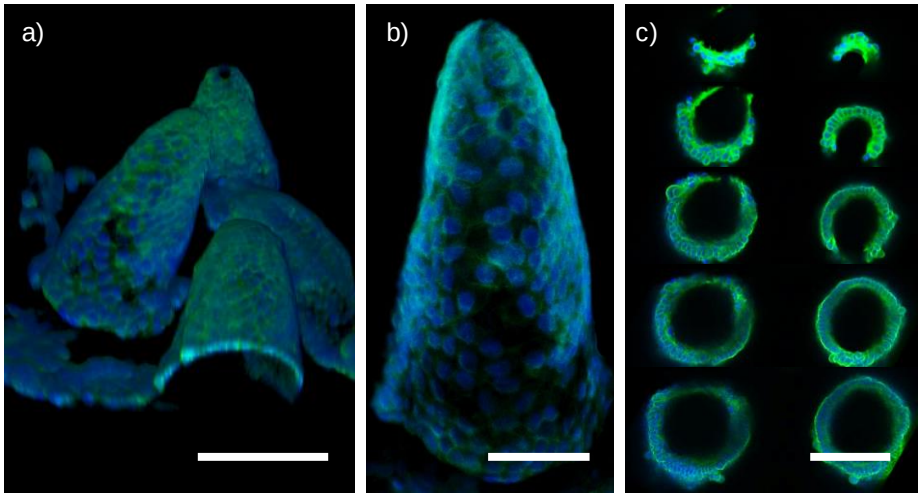

Figure 4.47: Confocal images of MDCK cells cultured on microstructures of 100 µm in diameter fabricated from 5% w/v $PEGDA_{575}$-0.15% w/v acrylic acid polymer solution at day 14 of culture. a) 3D reconstruction of a z-stack of tilted microstructures. b) 3D reconstruction of a z-stack of a vertical microstructure. c) Sequential z-stacks from two microstructures showing their cross-sections from the base to the tip of the microstructures. Nuclei in blue and F-actin in green. Scale bars: a,c = 100 µm, b = 50 µm.

Figure 4.47 shows a 3D reconstruction of z-stacks of some of the microstructures at day 14 of culture. The microstructures were almost fully covered by cells, leaving few cell-free areas. To see in detail the cell morphology

along the z axis of these microstructures, serial cross-sections from the base to the tip were imaged. It was observed that MDCK cells acquired a columnar shape and were organized in a palisade disposition around the microstructure.

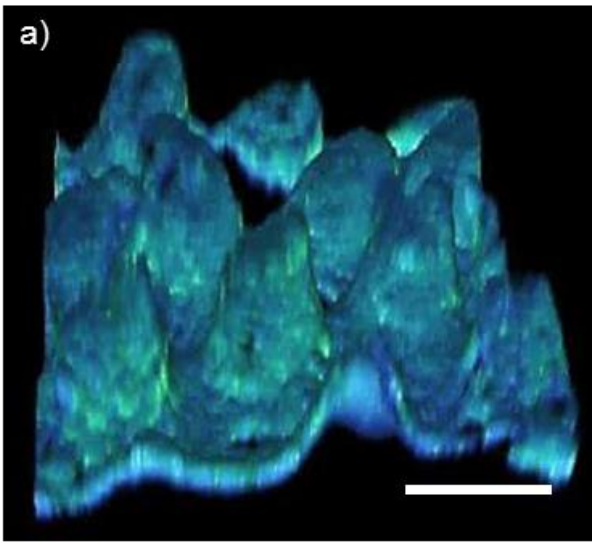

Figure 4.48: 3D reconstruction of z-stack from confocal images of MDCK cells cultured on $PEGDA_{575}$ microstructures of 100 μm in diameter made of 5% w/v $PEGDA_{575}$-0.15% w/v acrylic acid microstructures. Nuclei in blue and F-actin in green. Scale bars = 200 μm.

At day 21, the microstructured hydrogels made of 5% w/v $PEGDA_{575}$-0.15% w/v acrylic acid were still fully covered by the MDCK cells (Fig. 4.48a,b) and cells show a polarized morphology typical of epithelial monolayers. Therefore, the use of 5% w/v $PEGDA_{575}$-0.15% w/v acrylic acid in a two-step fabrication process produced microstructures that promoted the polarization of MDCK cells. However, due to the softness of the material produced, it was easy to find the microstructures partially tilted, fallen, and stacked to their tip.

Therefore, potential improvements on the system were investigated by using PEGDA solutions of higher molecular weight. As shown in Figure 4.23, microstructures made of PEGDA6000 develop longer structures with rounded tips, instead the shorter bullet-like shapes with sharp when using $PEGDA_{575}$. Polymer solutions of 10% w/v $PEGDA_{6000}$ and 0.6% w/v acrylic acid were used to fabricate microstructured hydrogels using photomasks with windows 100 μm in diameter. UV exposure took place in two steps: 10 s to form the hydrogel base and 150 s to grow the microstructures. Despite the presence of polymerized hydrogel on unexposed regions (Fig. 4.49), microstructures of almost 300 μm in height were obtained (Fig. 4.49b).

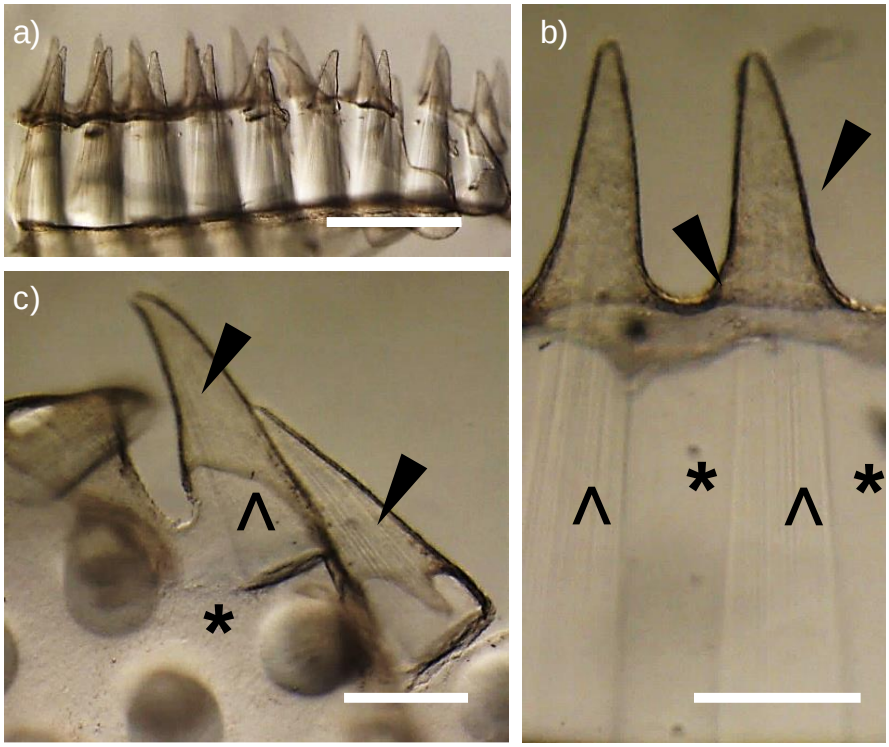

Figure 4.49: Stereoscope images of microstructures fabricated from 10% w/v $PEGDA_{6000}$ and 0.6% w/v acrylic acid solution after 14 days of MDCK culture. a) Frontal view of the sample. Detail of microstructures b) at the center of microstructured area, and c) at boundaries of the exposed areas (∧) showing polymerized hydrogel on unexposed areas (asterisk), and cells covering the hydrogel (arrowhead). Scale bars: a = 500 µm; b, c = 150 µm.

Hydrogels were functionalized with a 20 µL drop of 500 µg/mL laminin solution, and MDCK cells were seeded at $1.5 \cdot 10^4$ cells/cm^2. After 14 days of culture, MDCK cells grew lining the whole surface, forming a monolayer effectively covering both the base and the microstructures (Fig. 4.49b, Fig. 4.50a). The cells forming the monolayer displayed a polygonal morphology typical of epithelial cell layers (Fig. 4.50b). However, a cross-section of cells on microstructures showed that cells are horizontally elongated, lining on the microstructure, and showed a high spread morphology instead of the desired apico-basal columnar elongation (Fig. 4.50c). This fact could be attributed to the stiffness of the material or that MDCK cells required more time to arrange in a columnar morphology. It has been well established that MDCK cells become spherical and even detach, form cell clusters or cysts when culture on soft substrates, instead the flattened cohesive epithelial monolayers on rigid surfaces, because of their strong cell-cell adhesion.[380,384–386]

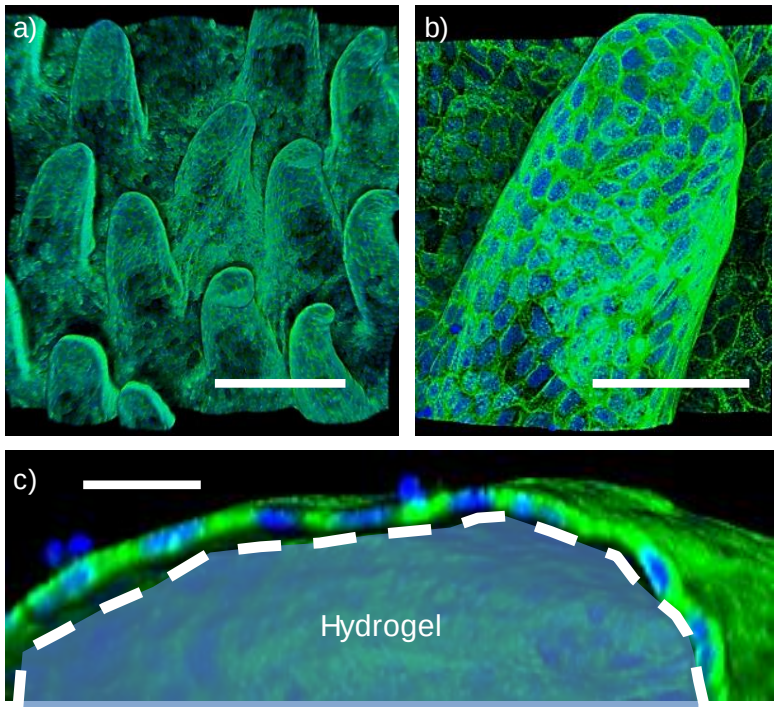

Figure 4.50: Confocal images of microstructures fabricated from 10% w/v $PEGDA_{6000}$ and 0.6% w/v acrylic acid after 14 days of MDCK culture. a) 3D reconstruction of z-stacks. b) Microstructure showing the polygonal cell morphology. c) Cross-section of a microstructure. Nuclei in blue, F-actin in green. Dash line limits the hydrogel. Scale bars: a = 200 µm; b = 75 µm, c = 25 µm.

4.6 PEGDA-ACRYLIC ACID MICROSTRUCTURED HYDROGELS AS A BIOMIMETIC MODEL OF THE SMALL INTESTINAL EPITHELIUM. A PROOF-OF-CONCEPT STUDY

4.6.1 GROWTH OF HUMAN EPITHELIAL COLORECTAL ADENOCARCINOMA (CACO-2) CELLS ON MICROSTRUCTURED PEGDA-ACRYLIC ACID HYDROGELS

Experiments with NIH-3T3 fibroblasts and MDCK epithelial cells showed that microstructured PEGDA–acrylic acid hydrogels support cell coverage. To validate them as synthetic models of the small intestinal epithelium, Caco-2 cell line was chosen. Caco-2 cells are widely used to model the intestinal barrier.[117] Taking into account the results from morphometric analysis (section 4.4.3), and those obtained with MDCK cells, solutions of 6.5% w/v $PEGDA_{6000}$-0.3% w/v acrylic acid were selected to produce the microstructures. Double UV exposure was used: 10 s to form the l base and 70 s to grow the microstructures. By this

process, microstructures of ~550 µm in height and ~100 µm in diameter were obtained (Fig. 4.32) surrounded by a hydrogel base. After functionalizing the hydrogels with laminin, Caco-2 cells were seeded at a density of $2.5 \cdot 10^4$ cells/cm^2 (the one used for the fibroblasts and MDCK cells).

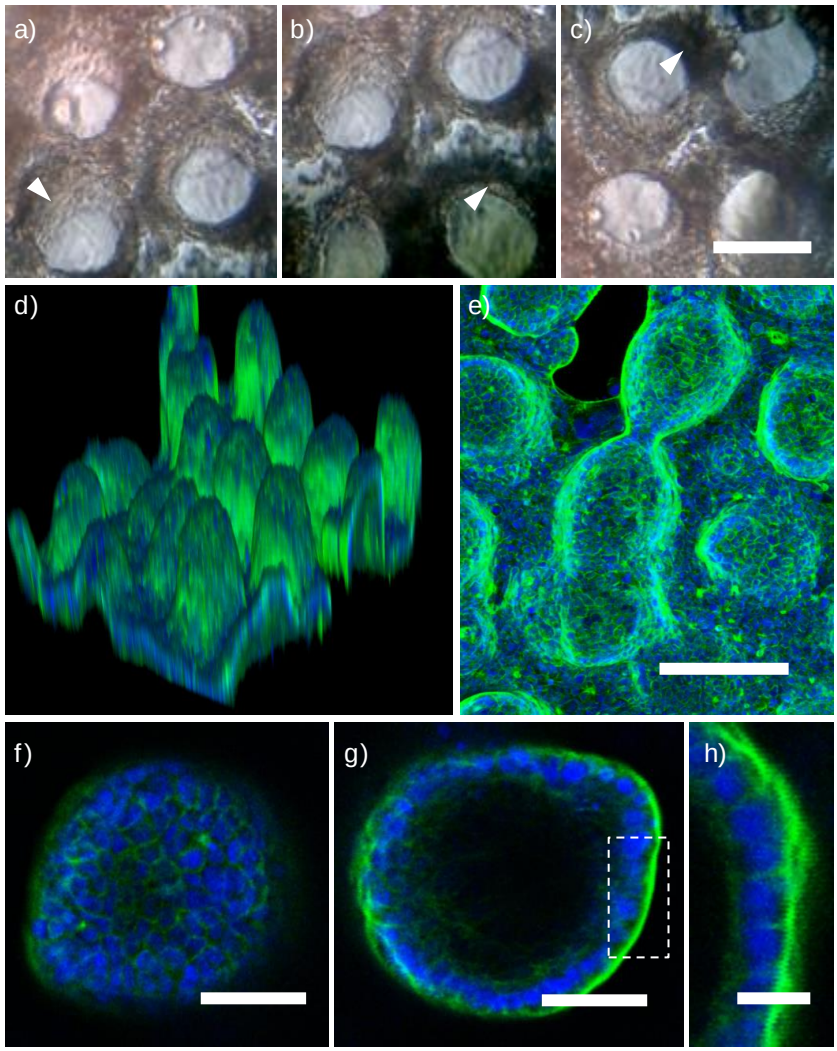

Figure 4.51: Caco-2 cells cultured on microstructures fabricated from 6.5% w/v $PEGDA_{6000}$ and 0.3% w/v acrylic acid solution after 7 days. a-c) Top view bright field images of microstructures. d) 3D reconstruction of z-stacks obtained by confocal microscopy and e) top view of a cell covered area. Details of f) tip cross-section and g) cross-section at half-height of a microstructure. g) showing magnification pictures of nuclei and cytoskeleton. h) Inset of image g). Nuclei are shown in blue and F-actin is shown in green. Arrowheads indicate cell aggregates at the base of the microstructures. Scale bars: a,b,c,e=150 µm, f,g=50 µm, h=5 µm.

After 2 weeks of culture, no relevant cell coverage occurred nor at the microstructures neither at the base of hydrogel. Therefore, and in agreement with literature,[287,288,387] cells were seeded at a higher density, $5 \cdot 10^5$ cells/cm^2. At day 7, Caco-2 cells adhered and proliferated at the bottom of the hydrogel, between the microstructures, in granulate aggregates and surrounding the microstructures. (Fig. 4.51). Microstructures looked translucent at the bright field microscope, meaning they were not fully cell covered yet (Fig. 4.51a-c). It was possible to find small areas where Caco-2 cells already formed a monolayer on the microstructures (Fig. 4.51d-e). However, although cells showed apparent brush borders (Fig. 4.51g), cells did not show a columnar morphology. Both cells and nuclei were spread onto the hydrogel surface with low apico-basal elongation regardless their position on the microstructures (Fig. 4.51g,h).

After 14 days of culture, it was possible to find samples where cells extended and covered the whole hydrogel surface (Fig. 4.52a). Now point, Caco-2 cells showed apico-basal polarity, with an elongated cytoplasm and elongated nuclei. Z-stacks from confocal imaging show the columnar morphology of Caco-2 cells at different heights of the microstructures (Fig. 4.52b-e). After 21 days of cell culture, cells still fully covered the microstructures.

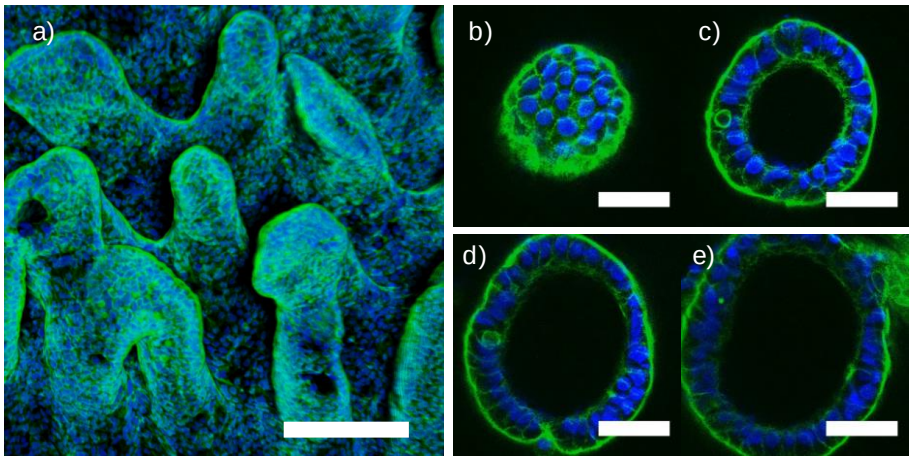

Figure 4.52: Caco-2 cells cultured on microstructures fabricated from 6.5% w/v $PEGDA_{6000}$ and 0.3% w/v acrylic acid solution after 14 days. a) 3D reconstruction of z-stacks obtained by confocal microscopy of a fully cell covered area. Detailed cross sections of a microstructure going sequentially in z from b) the tip to e) the base. Nuclei are shown in blue and F-actin is shown in green. Scale bars: a = 200 µm, b-e = 50 µm.

By checking the evolution of the cell culture from the seeding time, where cells are located mostly at the base of the hydrogels, between the microstructures, it can be assumed that cells proliferate and migrate from the bases to the tip of

the microstructures, covering most of them. Thus, this event seems to happen like in the native mucosa, where cells move from the crypts to the tips of villi.

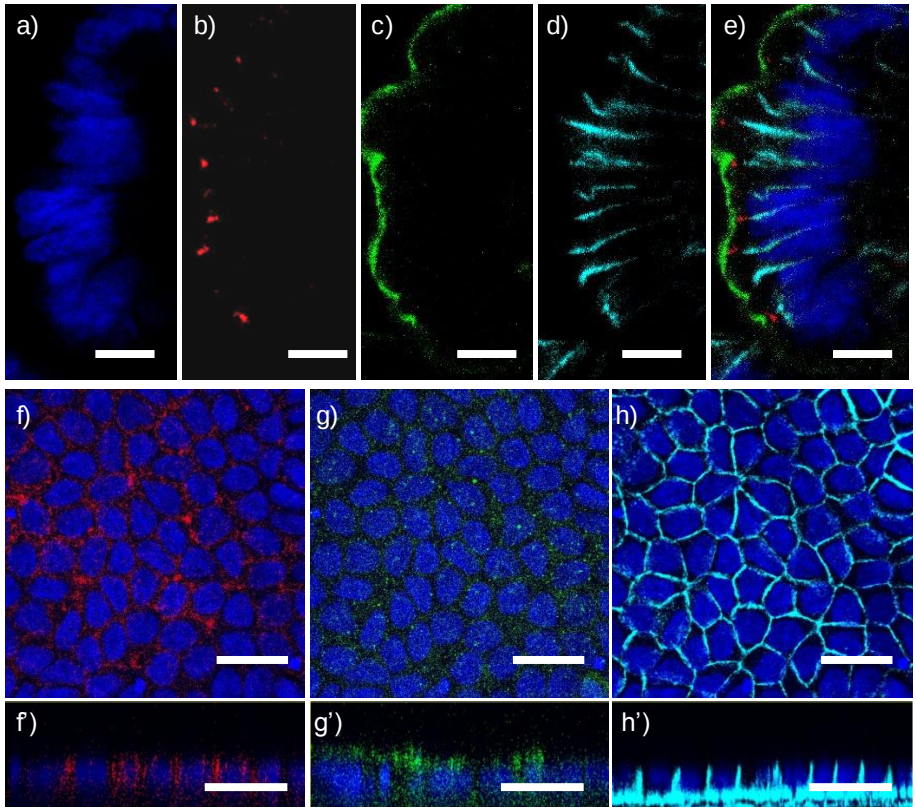

Figure 4.53: Detailed cross section of a microstructure after 21 days of Caco-2 cell culture. a) Nuclei in blue, b) ZO-1 in red, c) villin in green, d) β-catenin in cyan and e) merged. Top view and cross section of Caco-2 cells cultured on Transwell® after 21 days. f) ZO-1 in red, g) villin in green, and h) β-catenin in cyan. Nuclei in blue. Scale bar: a-d=10, e-g= 25 μm.

It must be acknowledged that some replicas were not fully covered and sometimes they displayed microstructures that were tilted or stuck by cell aggregates. We estimated the success ratio in about 60%. Successful samples were fixed at day 21 to determine the expression of polarization markers. Epithelial cell markers such as villin, characteristic protein of microvilli, ZO-1, found in tight junctions, and β-catenin found at the basolateral membrane, were expressed and located at the proper regions. In most of z-stacks nuclei were highly elongated, villin was brightly and located at the apical side of cells, ZO-1 appeared as dots between cells, and β-catenin contoured the basolateral domain of cells similarly to a honeycomb (Fig. 4.53a-e). These results were compared

with Caco-2 cells cultured on Transwell,® which is the standard cell culture platform (Fig. 4.53f-g). In both cases cells are elongated and expressed the epithelial cell markers properly located. However, Caco-2 cells cultured on the microstructured hydrogels seem to have more elongated cytoplasm and nuclei. Polarization and epithelial markers were consistently expressed on all the cells located along the tip-base vertical axis of the microstructures (Fig. 4.54).

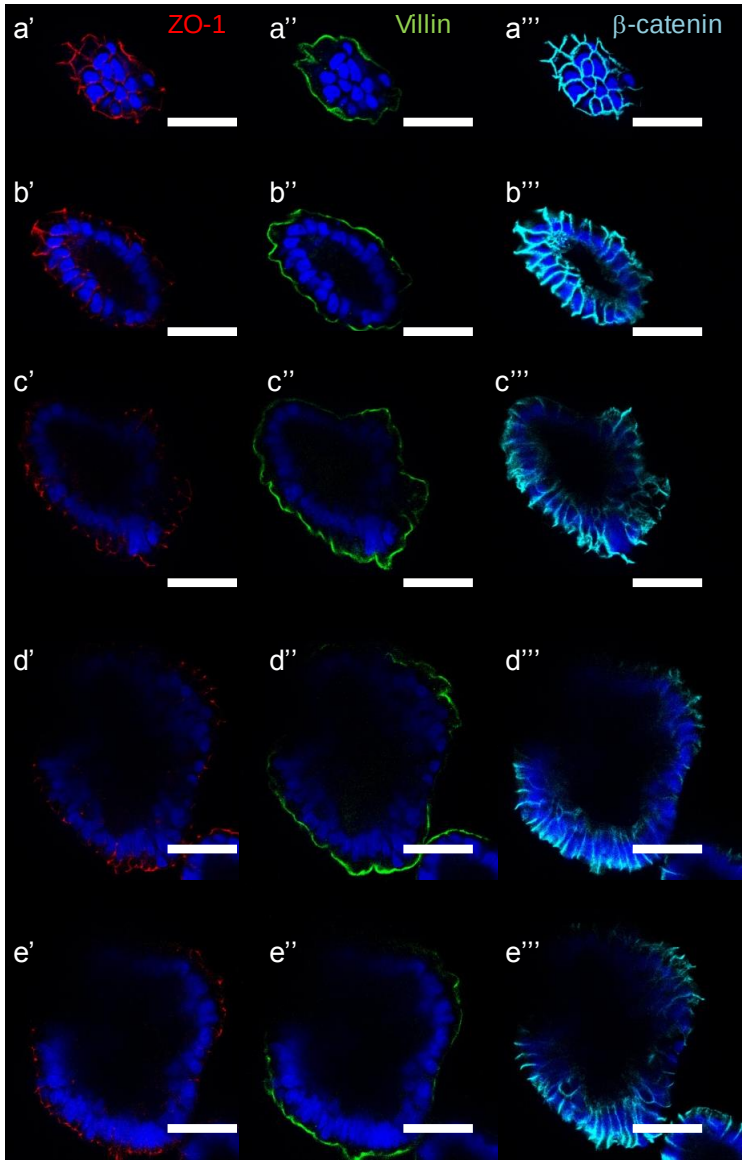

Figure 4.54: Sequential cross-sections from the a) tip to the e) base of a microstructure after 21 days of Caco-2 cell culture. ZO-1 in red (left), villin in green (center), and β-catenin in cyan (right). Nuclei are shown in blue. Scale bars = 50 μm.

Polarization was also assessed by the analysis of nuclei morphology and orientation with respect to the surface of the microstructures. Images taken by confocal microscopy from Transwell® at day 21, and from microstructured hydrogels at days 14 and 21, were processed by ImageJ software to obtain well defined nuclei of each stack. In addition, histochemical images from human villi were used as controls (Fig. 4.55a-f). Then, shape descriptors of nuclei were calculated: major and minor axis, and angle with respect to the surface. For the morphology analysis, aspect ratio between the major and the minor axis of nuclei was used as an elongation or polarization marker. At first sight, Figure 4.55 shows native villi with highly elongated nuclei in comparison with confocal images of Transwell® at day 21, and microstructured hydrogels. This agrees with the results plotted in the Figure 4.56a, where aspect ratio of nuclei on native villi showed significant higher values than the other two conditions ($p<0.001$). Aspect ratio of nuclei on Transwell® after 21 days and on hydrogels after 14 days did not show significant differences. However, the aspect ratio of nuclei on hydrogels after 21 days was significantly higher than that measured for the hydrogel after 14 days and Transwell® after 21 days ($p < 0.001$) and showed a distribution closer to that found on the native villi.

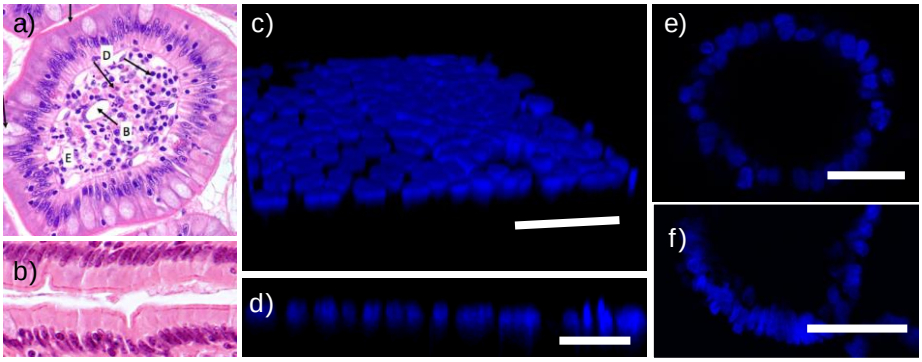

Figure 4.55: a) Cross section at the middle and b) longitudinal cross section of villi (http://medcell.med.yale.edu/systems_cell_biology/gi_tract_lab.php). c) 3D rendering and d) cross section from confocal images of Caco-2 cells on a Transwell® after 21 days of cell culture. e) Cross section of a microstructured hydrogel after 14 days and f) after 21 days of Caco-2 cell culture. Scale bar: c,e,f = 50 µm, d=25 µm.

Orientation analysis was performed by comparing nuclei orientation with respect to the surface. First, angles described by the nuclei were estimated following the procedure described in section 3.5.9, and plotted in a wind rose graph (Fig. 4.56b). In the case of native villi, most of nuclei kept positioned above 60° to the surface, basically perpendicular to the surface. However, in the case of nuclei on Transwell® more than 40% of nuclei were positioned almost parallel to

the surface, and about 25% of cells were perpendicular to the surface. On the other hand, cells cultured on the hydrogels covered the entire range of orientations with a predominant perpendicularity in the case of hydrogels after 21 days.

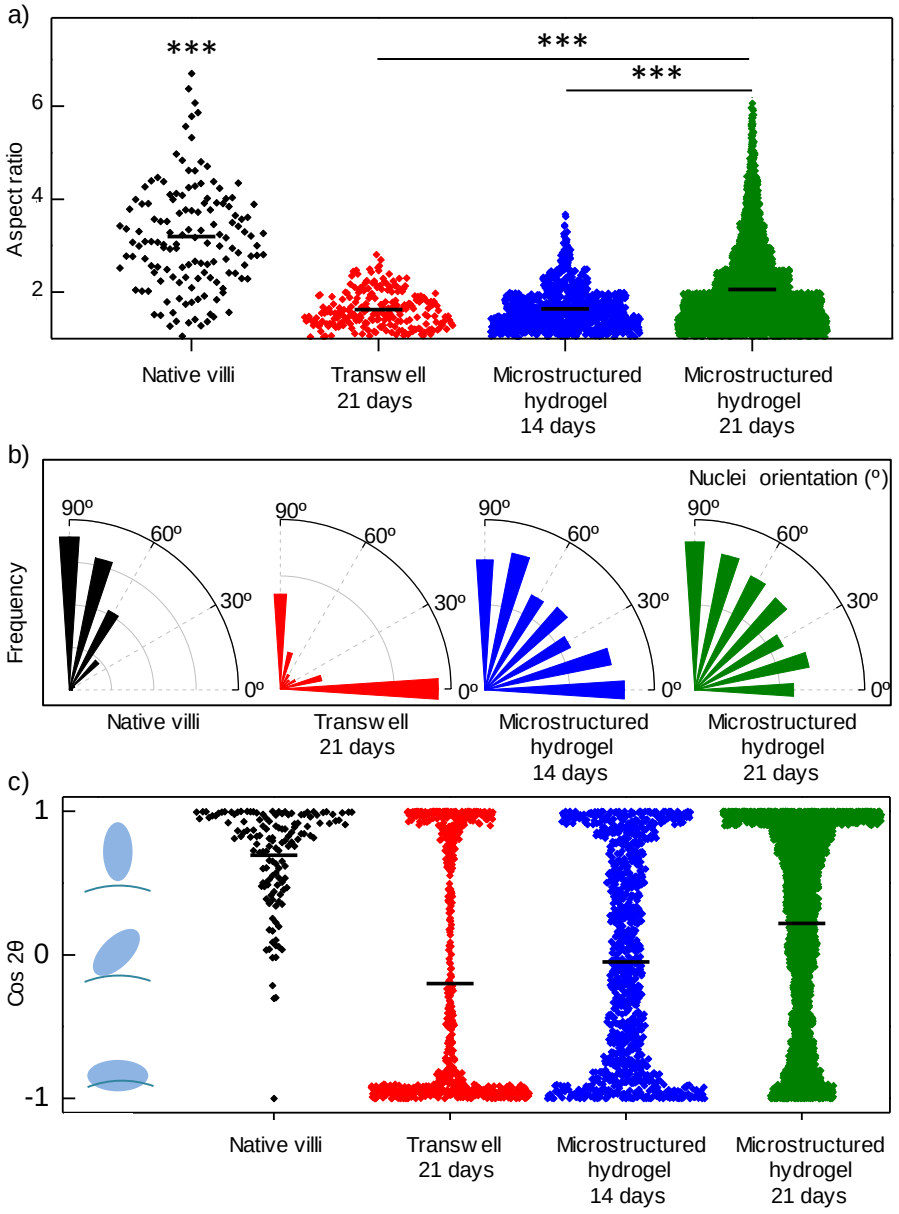

Figure 4.56: Nuclei elongation and orientation analysis. Plots of a) nuclei aspect ratio, b) angle distribution of nuclei orientation, and c) cos2θ. *** denotes p-value < 0.001 from Mann–Whitney U test.

These results are supported by the cos 2θ graph (Fig. 4.56c), which returns values close to 1 if nuclei are perpendicular to the surface, and values close to -1 if nuclei are parallel to the surface. In the case of the microstructured hydrogels at 21 days, even if all orientations are represented, nuclei positioned in a perpendicular orientation are predominant. This situation is related to cell confluence, if cells have enough space they will spread as much as possible; consequently, nuclei will be positioned in a parallel disposition. On the other hand, after the cells become confluent they start to compact, positioning their nuclei perpendicular to the substrate.

Despite Caco-2 cells cultured on Transwell® developed apico-basal polarization, demonstrated by the expression of epithelial markers (Fig. 4.54), and show a lot of nuclei perpendicularly positioned (Fig. 4.56), it was also found a relevant percentage of nuclei that tend to be positioned in a parallel manner onto the surface. Meanwhile, cells on the hydrogels also showed nuclei positioned in a wide range of orientations, but after 21 days it was found a tendency to keep them perpendicular to the surface. Considering that polycarbonate membranes are stiffer (2 GPa) than the hydrogels (22 kPa), this fact could affect the cell and nuclei disposition. It was reported that substrate rigidity modulates nuclei shape, and stiffer substrates promote flattened nuclei compared to more compliant substrates, which enhance rounded nuclei.[388] In addition, DiMarco *et al.* recently showed that Caco-2 monolayers cultured on matrices mimicking the low mechanical stiffness of the small intestinal submucosa (~150 kPa),[389] resulted in more apico-basal elongated cells than those culture on conventional hard substrates. They attributed this behavior to the modification of cell-cell junctions through the control of cell-matrix adhesions.[390] This supports our hypothesis that the softness of the hydrogel can influence the morphology of the Caco-2 cells, and promote a more reliable morphology of the epithelial monolayers.

Overall, we have developed a material and a fabrication method that allows obtaining substrates that recapitulate the 3D architecture of the intestinal mucosa. In addition, these synthetic villi promote the formation of Caco-2 cell monolayers, which show morphologies comparable to the intestinal epithelial cells, and express specific epithelial markers properly located.

4.7 TRANSEPITHELIAL ELECTRICAL RESISTANCE (TEER) MEASUREMENTS OF CACO-2 MONOLAYERS ON THE MICROSTRUCTURED HYDROGELS

Transepithelial electrical resistance (TEER) measurement is a widely used method to assess the barrier function of Caco-2 cells.[43] In order to perform

TEER measurements of the Caco-2 cell monolayers on the microstructured hydrogels two methods have been used: the conventional method using a Voltohmmeter and a more novel approach based on impedance spectroscopy measurements.

4.7.1 TEER MEASUREMENTS BY A VOLTOHMMETER

Conventional TEER measurements of epithelial monolayers are performed using Transwell® inserts. This allows forming two compartments that, once the cell monolayer is formed, are separated by the cell barrier (section 1.2.3).[92] The two compartments are initially separated by a polymeric semipermeable membrane. The microstructured hydrogels made by the experimental set-up described in section 3.2.1, cannot be placed directly inside Transwell® inserts, because they are adhered on glass coverslips. To solve this issue, two experimental approaches were tried: 1) hydrogel polymerization *in situ*, or 2) outside polymerization and posterior sealing (Fig. 4.57).

The First approach, *in situ* polymerization, was tried filling the insert with the polymer solution and placing the photomask and UV light source below. Unfortunately, several experimental issues hampered the success of this approach. First, polymer solution leaked through the porous membrane and polymerized between the outer part of porous membrane and the coverslip. Second, inside the Transwell®, the polymerization happened in a non-homogeneous way, microstructuring was not visible and the heterogeneous mass of hydrogel detached from porous membrane. Thus, this method was discarded.

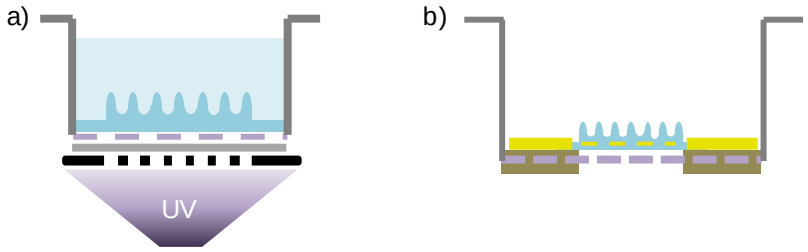

Figure 4.57: Illustration of the two approaches to adapt the fabrication set-up to Transwell®, a) *in situ* polymerization and b) Transwell® sealing.

The second approach was based on placing the microstructured hydrogels inside Transwell® inserts, which were outerly sealed using a PDMS layer, and innerly sealed with an adhesive tape (section 3.6.1). Through the sealing, the electrical current was forced to pass across hydrogels and cells, and

leakage current was avoided. Proper sealed was not always achieved for all samples, but at least three samples for each condition had a suitable progress and were used for TEER measurements using a chopstick electrode. The resistance measurements as a function of the cell culture time are plotted in Figure 4.58. The resistance of the Transwell® with hydrogel were higher than Transwell® controls at each time point for samples with and without cells. Because of the sealing, the surface of the porous membrane was effectively reduced from 4.5 cm^2 to 0.785 cm^2, therefore increasing its electrical resistance, R (Eq. 28).

$$R = \frac{\rho \times l}{Area} \qquad \text{Eq. 28}$$

where ρ is the resistivity of the membrane, l its thickness and A its area. The resistance will increase up to 5-fold, from 39 Ω (Fig. 58a) to 223.6 Ω.

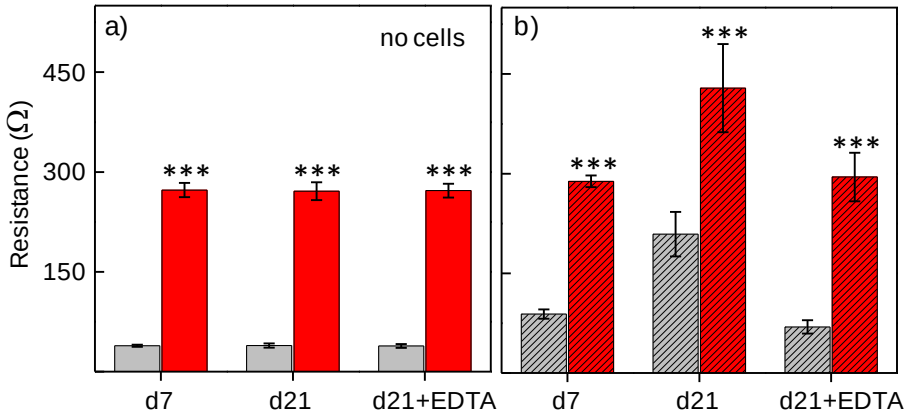

Figure 4.58: Measured resistance (mean ± SD) on unmodified Transwell® (gray) and on Transwell® with hydrogels (red). a) Control samples without cells, and b) with cells. *** denotes p-value < 0.001 from Mann–Whitney U test.

In addition, hydrogels also contributed to increase the resistance. Transwell® with hydrogels showed resistance values up to 270.9 ± 5.2 Ω, which result in hydrogel resistances of ~ 47.3 Ω. This low value makes sense because hydrogels contain a high proportion of water, which will easily allow the pass of electrical current. On other hand, the resistance measured on samples with cells was much higher for Transwell® with hydrogels than on Transwell® controls (Fig. 58b), again due to the reduction in the surface area.

Once measured the total resistance values, the resistance of the cell monolayer was calculated the total resistance from the corresponding cell-free sample. Then, TEER, expressed in Ω · cm^2, was calculated by multiplying $R_{monolayer}$

and surface area of the Transwell® or the microstructured hydrogels. For Transwell®, surface area is 4.5 cm^2. For the hydrogels, the area was 0.78 cm^2 containing a 0.5 cm x 0.5 cm square of microstructures. This microstructured hydrogels were fabricated from solutions of 6.5% w/v PEGDA6000-0.3% w/v acrylic acid by the double UV exposure of 10 s to form the hydrogel base and 70 s to grow the microstructures. By this process, microstructures of ~550 µm in height and ~100 µm in diameter were obtained.

Confocal microscopy was used to measure the total surface area of PEGDA-acrylic acid microstructured hydrogels. Hydrogels were functionalized with SAV-TR to obtain z-stacked images and 3D reconstructions (Fig. 4.59). These reconstructions were used to calculate surface correction factor, which relates the 3D total surface area of the microstructured hydrogels to their 2D area using IMARIS software using their surface tools (Eq. 15).

$$\text{SCF} = \frac{\text{3D total Surface area}}{\text{2D Surface area}} \qquad \text{Eq. 22}$$

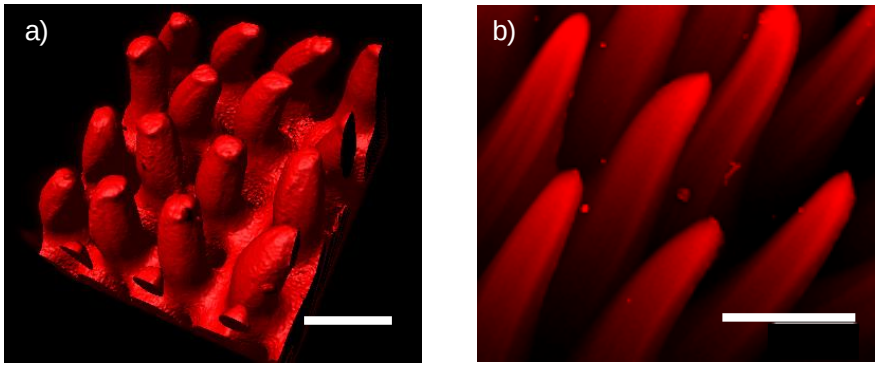

Figure 4.59: 3D reconstruction of microstructured hydrogels of a) $PEGDA_{575}$ and c) $PEGDA_{6000}$. Scale bars = 200 µm. At least five different regions, containing different number of microstructures, were analyzed to obtain an averaged ratio between the 3D total surface area and the 2D surface area.

For microstructures with heights ranging between 350 and 550 µm, SCF values were 4.9 ± 0.5 to 8.1 ± 0.9. This procedure was individually employed for each type of microstructure due to the morphological sensitivity of microstructures to fabrication conditions.

As shown in Figure 4.60, TEER of Caco-2 cell monolayers on both Transwell® and hydrogels increased from day 7 to day 21 of cell culture, which is consistent with the formation of a monolayer that progressively covers the surface. After 7 days, cells on Transwell® already show a significant increment in

TEER values with respect to the control. On the contrary, at this time point TEER on hydrogels was basically inexistent. These results could be attributed to a slower progress in cell proliferation and covering on the microstructured hydrogels with respect to Transwell®. After 21 days, TEER increased significantly in both hydrogels and Transwell®, meaning that cells function as an epithelial cell barrier. TEER values were statistically significantly lower ($p < 0.001$) on the microstructured hydrogels than on Transwell®. To prove the response of the cell barrier formed, EDTA treatment was performed after 21 days on samples grown in Transwell® and on hydrogels. EDTA is a chelating agent that prevents joining of cadherins between cells, and produce cell-cell detachment, and the disruption of cell barriers. EDTA treatment made TEER decrease in all the cell containing samples, demonstrating that TEER increase at 21 days was due to the formation of an epithelial cell barrier. These results denote that Caco-2 monolayer on unmodified Transwell® achieved higher degree of impermeability at the time points assayed than on our microstructured hydrogel. The reduction on the TEER values of Caco-2 monolayers cultured on 3D architectures has been already reported, [286,197] and the values found similar to the *in vivo* readings are in agreement that the three-dimensionality of the constructs affect the epithelial barrier formation in a manner close to native intestinal epithelium.

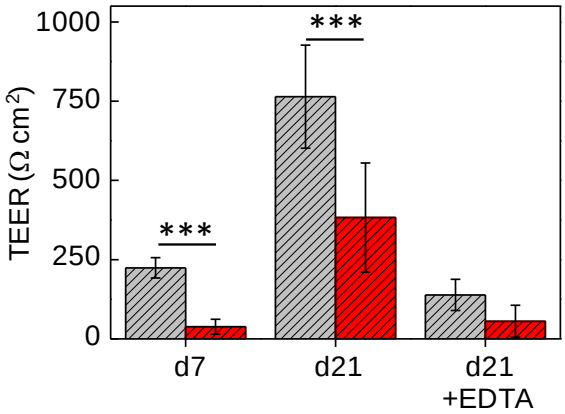

Figure 4.60: TEER of cell monolayers (mean ± SD) on unmodified Transwell® (gray) and on Transwell® with microstructured hydrogels (red) after 7 and 21 days, and after the EDTA treatment. *** denotes p-value < 0.001 from Mann–Whitney U test.

Thus, by the incorporation of hydrogels on Transwell®, TEER of Caco-2 cell monolayers cultured on the microstructured hydrogels was successfully measured using Voltohmmeter and a chopstick electrode. In addition, Caco-2 cells formed a cell barrier, as demonstrated by the TEER measurements at day 21.

These results support the expression of polarization markers, such as ZO-1 that prove the well-formed tight junctions, which are responsible of the TEER resistance.

On the other hand, TEER readings were maybe affected by the distance of electrodes to the area measured (6.5 mm), because are highly dependent on the electrode position.[94] Yeste *et al.* evidenced that some TEER measurements resulted in errors when using Transwell® inserts from 6.5 mm, due to the very low sensitivity.[391] They also found that using interdigitated electrodes configuration the entire cell culture area contributes equally to the measurement.

4.7.2 ELECTRICAL IMPEDANCE SPECTROSCOPY

The second approach to obtain TEER values was performed in collaboration with the Biomedical Applications Group of the Institut de Microelectrònica de Barcelona, IMB-CNM (CSIC). This group has developed a bioreactor chamber with integrated interdigitated electrodes and the electronics for monitoring the impedance of cell barriers along the time and within a range of frequencies.[308,391,392] The equipment is portable, so it can be transported to cell culture room. Circular substrates containing three channels with polycarbonate porous membranes were used to culture Caco-2 cells (Fig. 4.61). These circular substrates were placed in the bioreactor as the inserts of Transwell® and create two separated compartments that can be used to perform electrical impedance spectroscopy measurements.

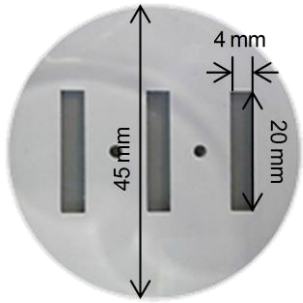

Figure 4.61: Circular insert containing three channels of polycarbonate membrane, used for cell culture. The insert is placed between two chambers that have integrated electrodes to perform electrical impedance measurements.

To use this system, we adapted the fabrication process to perform an *in situ* polymerization of our hydrogels on top of the porous membranes (section 3.6.3). Two types of membranes were chosen: a nylon mesh and porous

membranes. The nylon mesh has the advantage that its huge pores allow the pass of UV light, therefore, is not affecting significantly the polymerization process. The first attempt consisted on fabricating flat hydrogels from 6.5% w/v $PEGDA_{6000}$ and 0.3% w/v acrylic acid on top of the nylon mesh (Fig. 4.62).

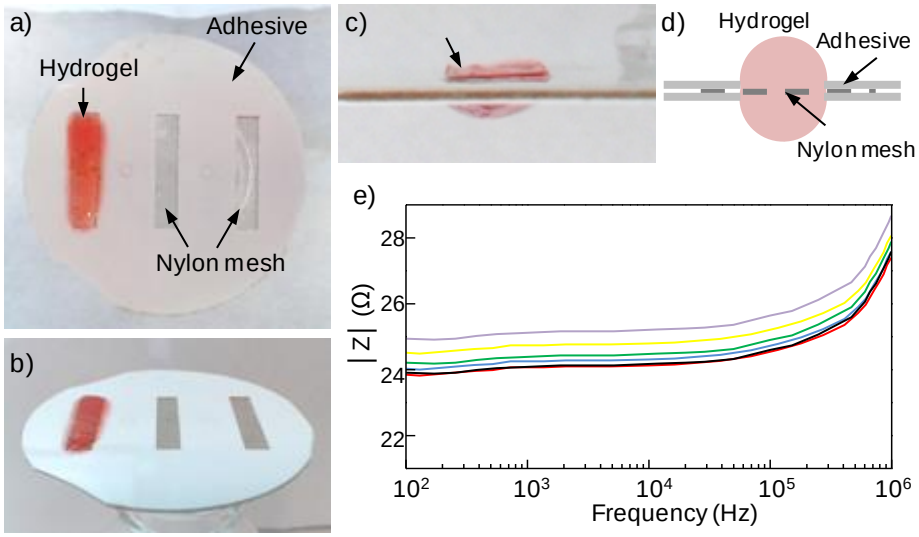

Figure 4.62: a-c) Photographs of nylon mesh adapted on a circular device, and the attached hydrogel (red) after swelling hydrogel. d) Schematics of the set-up. e) Impedance measurements across hydrogels mounted in a nylon mesh.

After polymerization, hydrogels kept attached because the polymer solution wet the nylon mesh before polymerization, and thus hydrogel was embedded after UV exposure. Figure 4.62 shows how the hydrogels protruding from the two sides of the nylon mesh after reaching equilibrium swelling (Fig. 4.62c,d). Impedance spectroscopy measurements were performed on two of these circular insets (6 channels in total) modified with flat hydrogels on the nylon mesh. Figure 4.62 shows that the measurements were reproducible within a narrow range of values. The impedance obtained is compatible with pure resistor for frequencies in the range of 10^2 – 10^5 Hz. The channels are fabricated to determine the same surface area of a Transwell® insert of 12 mm (~ $1cm^2$) In addition, resistance values are very small compared to values for Transwell® inserts, so presumably the hydrogel inserts will not hamper the pass of current significantly. Even though nylon meshes allowed the adhesion and fabrication of hydrogels, their preparation was too laborious. In addition, because of swelling to control the leakage current was not easy. For this reason, an alternative approach was attempted.

As an alternative to nylon meshes, *in situ* hydrogel polymerization was

attempted on polycarbonate porous membranes, which are commonly used in Transwell® for TEER measurements.[43] For this purpose, our established fabrication set-up was used, adding porous membranes of 1 μm in pore size between the PDMS stencil and the glass coverslip. A photomask with windows 100 μm in diameter and a polymer solution containing 6.5% w/v $PEGDA_{6000}$ and 0.3% w/v acrylic acid were used to test the fabrication of microstructures. UV exposure was performed in two steps 10 s to form the hydrogel base and 70 s to grow the microstructures. Two types of materials, polycarbonate and PFTE were selected to study the polymerization and hydrogel attachment on the porous membranes. Circular devices containing porous membranes were used to fabricate flat hydrogels made of 6.5% w/v $PEGDA_{6000}$ and 0.3% w/v acrylic acid, by a single UV exposure of 150 s. After fabrication, circular devices were kept for 1 week in a PBS solution at 4°C to allow for equilibrium swelling. In the case of PFTE membranes, although hydrogels polymerized, they detached from PTFE just after fabrication. On the polycarbonate membranes, the hydrogels kept attached after polymerization but they detached after some hours. Therefore, two silanization protocols were assayed to avoid hydrogel detachment during the swelling procedure (section 3.6.3). Silanization protocol was further optimized, and ensured hydrogel attachment for long periods of time (more than 7 days).

As polycarbonate membranes, those of 1 μm and 0.4 μm pore size were tested. Hydrogels fabricated on 0.4 μm pore size looked like a thin layer, while the ones fabricated on 1 μm pore size showed a thicker layer (Fig. 4.63a,b). To understand the role played by the pore size of the membranes on the hydrogel fabrication, the transmittance through the two membranes was measured. Figure 4.63c shows that, at the wavelength range used for the fabrication, the transmittance (260 – 600 nm) through 0.4 μm pore size membranes was 2%. In contrast, the transmittance through 1 μm pore size membranes achieved nearly 60%. This translated in a measured transmitted intensity of 80% for the 1 μm pore size membranes (Fig. 4.63d). Light intensity was also measured through the polycarbonate membranes including the photomask. Lambert-Beer (Eq. 25) may explain why hydrogels fabricated on 0.4 μm pore size membranes were much thinner than ones fabricated from 1 μm pore size membranes (Fig. 4.63a,b). Attenuation is directly related to the light absorbance of the material, and as has been in previous sections light attenuation cause the shortening of hydrogels. Therefore, 1 μm pore size polycarbonate membranes allowed the photopolymerization of the PEGDA solutions and their microstructuring (Fig. 4.64) and were chosen to perform TEER measurements.

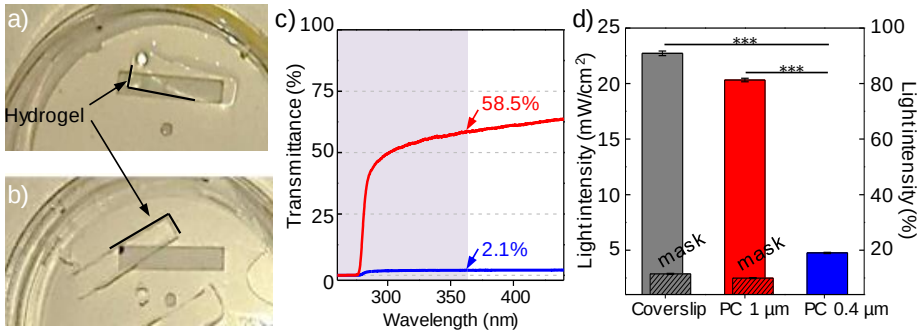

Figure 4.63: Effects of the pore size of polycarbonate membranes on the hydrogel polymerization. Photographs of hydrogels fabricated through polycarbonate membrane of a) 1 µm or b) 0.4 µm pore size. c) Transmittance through polycarbonate porous membrane (red 1 µm or blue 0.4 µm pore size). d) Light intensity measured under polycarbonate membranes with and without photomasks. *** denotes p-value < 0.001 from Mann–Whitney U test.

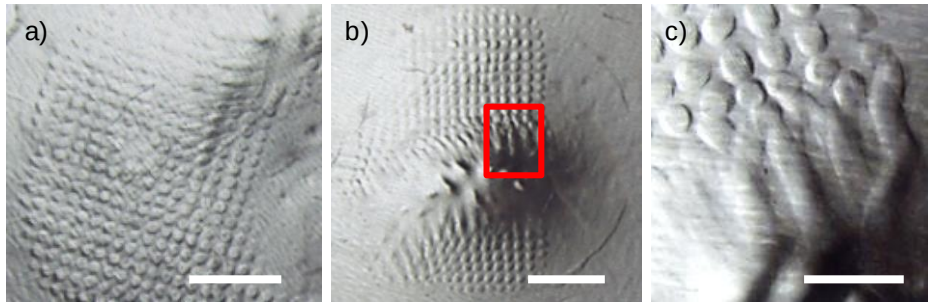

Figure 4.64: a,b) Top view images of microstructured hydrogels on polycarbonate porous membranes of 1 µm pore size and c) detail from b. Scale bars: a,b= 1.5 mm, c= 500 µm.

A circular insert with these membranes in each channel was used to fabricate hydrogel microstructures made from polymer solutions containing 6.5% w/v $PEGDA_{6000}$-0.3% w/v acrylic acid, and 1% I2959. The photomask had windows 100 µm in diameter and it was exposed to UV light for 10 s to create the hydrogel base and 70 s to create the microstructures. With these conditions, microstructures of 297 ± 8 µm in height were obtained on the porous membrane (Fig. 4.65). There was a significant reduction on the microstructure heights due to the light absorption of the membrane (without the membrane these fabrication conditions resulted in pillars 550 µm in height). However, the resulting microstructures were considered to be high enough to be representative of the dimensions of villi in native tissues.

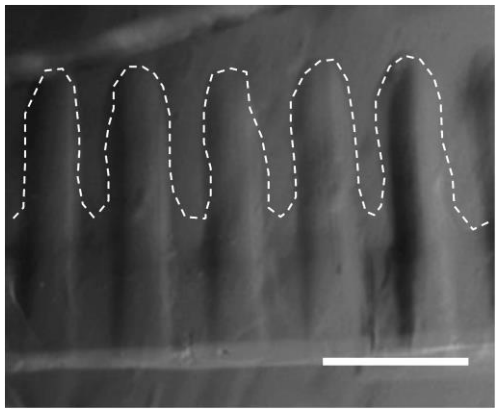

Figure 4.65: Image of the 6.5% w/v $PEGDA_{6000}$-0.3% w/v acrylic acid microstructure profile fabricated using a 1 μm pore size polycarbonate membrane. The dash line highlights the microstructure contour. Scale bar = 300 μm.

The microstructured hydrogels were functionalized with a laminin solution of 50 μg/mL and Caco-2 cells were seeded at a density of $5 \cdot 10^5$ cells/cm^2. After 14 days of cell culture, the insert was placed on the bioreactor chamber to carry out impedance spectroscopy measurements. The measurements were done in parallel at the three channels of the device (Fig. 4.66). The first channel showed high impedance values at all frequencies, whereas channel 3 showed very low values of impedance. These spectra could be attributed to the mounting and the current leakage, respectively. Channel 2 was the only showing the typical sigmoid curve of epithelial barriers, characterized by high impedances at mid-range frequencies that decrease at high frequencies. This channel was selected to determine the TEER of the monolayer (Fig. 4.66b). After measuring the impedance values of channel 2 ($Z_{measured}$), the hydrogel with cells on top was removed to measure the impedance related to that particular silanized membrane (Z_{sm}). A non-modified inset (polycarbonate membrane) was used as a control to avoid influences of the mounting into the bioreactor. To calculate TEER, Zsm was subtracted from $Z_{measured}$ and fitted to an equivalent electric circuit that describes the impedance spectrum of a cell barrier. The plot of Figure 4.66c shows the typical silhouette of impedance spectrum of a cell monolayer at different frequencies, where at mid-range frequencies impedance from cell monolayer are predominant, and at high frequencies the total impedance converges to the resistance of the medium.[43] TEER was obtained by multiplying impedance at 100 Hz and total surface area of the microstructured hydrogel. The microstructures fully occupied the porous membrane area (0.8 cm^2), and the microstructures fabricated had a total surface area of 3.68 cm^2. Therefore, TEER value obtained was 73.6 $\Omega \cdot cm^2$.

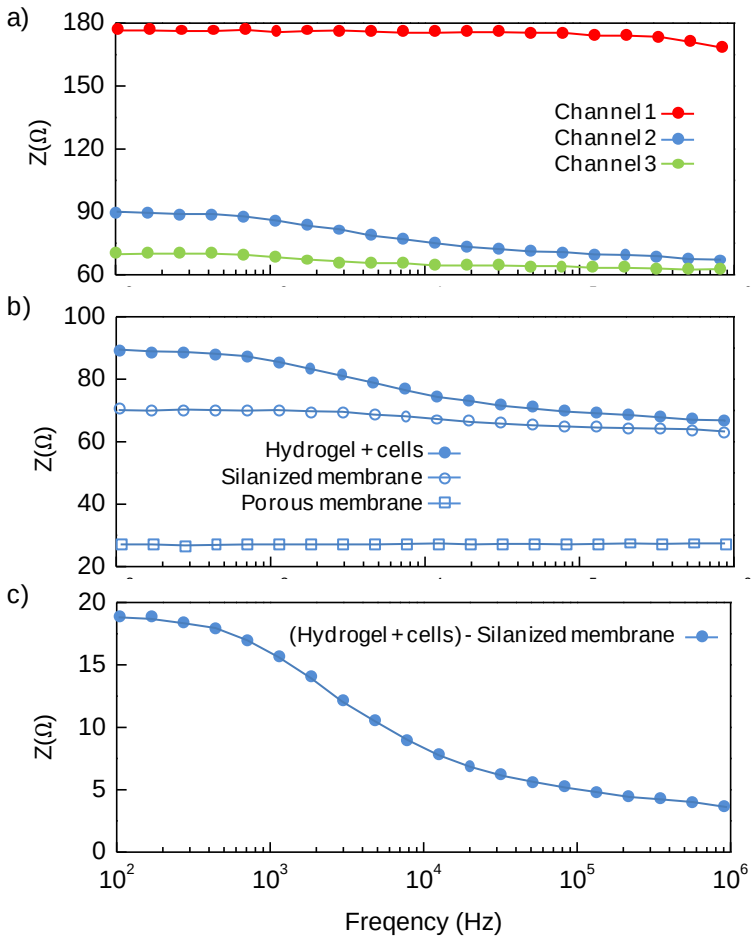

Figure 4.66: Impedance spectroscopy data of cell cultured on hydrogels of a) the tree channels after14 days of Caco-2 culture. Experimental data (symbols) were fitted (lines) according to equivalent electric circuits including TEER, intracellular resistance (Ri), a CPE, and the media resistance. b) Comparison of impedances on channel 2 of hydrogel, silanized membrane and porous membrane. c) Cell monolayer impedance described the typical spectrum of epithelial cell monolayers with high impedances at mid frequencies (10^2 Hz) and low impedances at high frequencies (10^6 Hz).

TEER reading by EIS are about ten times lower than the obtained on the Transwell®. Unfortunately, we do not have enough good experimental data to assess the consistency of EIS values. At this point, we can only speculate with the influence of the position of the electrodes on the measurement, which was significantly different in both experimental approaches.

In any case, TEER values of Caco-2 monolayers grown on the microstructured hydrogels were significantly lower, on both the Transwell® and the EIS chamber, than those obtained for Caco-2 monolayers grown on 2D

polymer membranes. It has been reported that TEER of Caco2 monolayers grown in Transwell® is far too high when compared to TEER of the native tissue.[286] These facts have been related to the leakiness of the tight junctions at the tip of villi.[36,95,393] In addition, it has also been reported that cell phenotype (also the tight junctions) is affected by the physicochemical properties of the substrate.[390] Taken all these information together, one can infer that our system, which replicates 3D villi features on soft materials might provide a model of the intestinal epithelial monolayer that represents better the *in vivo* functionality.

5 Discussion

The functionality of small intestinal epithelium is related with the crypt-villus unit. First, villi increase the absorptive surface area due to their high aspect ratio, from 2 to 10 height to width.[4,9,10] The 3D architecture of villi is also important in the spatial distribution of specialized cells along the crypt-villus axis. Proliferative cells are confined to the crypt domains while differentiated cells migrate along the villi to the tip, where they shed to the lumen. Cell proliferation, differentiation and migration are regulated by biochemical gradients generated along the crypt-villus axis.[394] These findings correlate with the gradual decreasing of the paracellular pore size,[395] and the distribution of patterns of laminin isomorfs[396] along the crypt–villus axis. In addition, not only the cell composition of the epithelium varies, but the lamina propria also show different immune cell populations along of this axis.[397] Thus, mimicking the natural tissue 3D structure is expected to be crucial for the modelling of intestinal epithelial barrier.

Conventional 2D *in vitro* models of the intestinal epithelium, based on the culture of Caco-2 cells on Transwell® inserts, fail to represent small intestinal microenvironment and lack physiological relevance in some applications.[278] Even if the porous membranes of Transwell® inserts can be coated with various extracellular matrix proteins, their mechanical properties (2 GPa)[398] do not resemble those of the epithelial basement membrane (3-30 kPa).[360,399] In addition, the flat surface of porous membranes completely lacks 3D villi-like features. These restrictions have negative effects on the Caco-2 cells phenotype when compared with the native intestinal tissue: Caco-2 cells show less apico-basal elongation,[390] and form stiffer tight junctions than those found *in vivo*[117] due to smaller paracellular pores.[400] Such characteristics lead to the underestimation of paracellular absorption.[401] TEER readings are also affected and show values 5 -30 fold higher values compared to *in vivo*.[402,403] To address these issues, several studies have recently reported different strategies and materials to mimic the three-dimensional architecture of crypt-villus units to improve the *in vitro* models of small intestinal epithelium.[183,286,197,68,279,284,285,287,288] TEER and permeability improvements have been reported by culturing Caco-2 cells on the synthetic villi,[286] which also enhanced epithelial cell morphology and differentiation.[197,279] Even though these reports have shown valuable progress towards improving the accuracy of the *in vitro* models, complex fabrication methods, sophisticated or non-tunable materials and experimental set ups not adapted to the conventional measurements are still hampering the use of these new systems in standard testing.

The first challenge in the development of biomimetic *in vitro* epithelial models is the use of materials that mimic the structure, mechanical properties and chemical composition of the basement membrane. ECM proteins found in the

basement membrane, such as laminin or collagen, should be incorporated. To provide enough ligand density for the cell-substrate interactions, the material should allow the control over its physicochemical properties. In addition, it would be desirable a porous matrix, which will allow the diffusion of oxygen and nutrients and at the same time does not hamper permeability and TEER measurements. As the intestinal mucosa is a soft tissue, a material with high-water content, and mechanical properties within the range of 3-30 kPa is desirable.

We are not only interested in mimicking the *in vivo* cell-substrate interactions, but also in adding the 3D architecture of the *in vivo* intestinal tissue. Therefore, it is crucial that the chosen material can be microstructured, giving rise to high aspect ratio microstructures with dimensions of a few hundreds of microns in a simple, reliable and reproducible way. In addition, the degradability of these structures has to be taken into account, because of Caco-2 culturing takes place for at least 21 days. The constructs also have to be suitable to integrate them in conventional tests of the epithelial integrity (TEER, permeability) to expand their applicability in drug absorption tests.

As a widely-used biomaterial, PEGDA hydrogels were chosen as the material to support the growth on intestinal epithelial cells. PEGDA is highly hydrophilic, its physicochemical properties can be tuned in a controllable manner, it is non-biodegradable and it can be easily produced by photocross-linking.[153,236] However, PEGDA hydrogels show low bioactivity, which results in a non-fouling material. To overcome its low bioactivity, in the present study acrylic acid is introduced into the material recipe to improve the cell attachment capacity of PEGDA hydrogels. PEGDA and acrylic acid were copolymerized by photopolymerization. Acrylic acid not only has a vinyl group to react in the free radical polymerization but also a carboxyl group, which can be functionalized with many proteins. This method allowed to obtain hydrogels with controlled amounts of exposed carboxyl groups, which support their functionalization with ECM proteins. The strategy of copolymerizing acrylic acid with PEGDA for the anchoring of proteins was published first by Drumheller *et al.* in 1994.[365] Since then, few reports have followed similar strategies. Conversely, acrylic acid has been post-grafted on PEGDA surfaces creating a polyacrylate layer that was functionalized with collagen to enhance cell adhesion.[366] On the other hand, the copolymerization of acrylic acid and PEGDA has been used to create photonic crystals and control the specific adsorption of antibodies.[367] In this sense, it has been shown that ligand density plays an important role for cell adhesion on hydrogel surfaces,[140,149,362] and our fabrication method allows to tune the ligand density in the hydrogels by changing their acrylic acid concentration (Fig. 4.39). On the contrary, the post-grafting methods do not allow for the fine control over

the number of carboxylic groups. In addition, our strategy results advantageous over other alternatives to improve bioactivity of PEGDA such as the incorporation of gelatin methacrylate[258] or methacrylated hyaluronic acid,[404] because of the specific and controlled targeting of the functional carboxyl groups of the hydrogel.

An appropriate material to develop epithelial barriers requires physicochemical properties that enable the formation of cell monolayers. Considering the relevance of the substrate stiffness on the epithelial cell behaviour,[405] it is noticeable that the mechanical properties of PEGDA-acrylic acid hydrogels can be easily tailored by changing PEGDA concentration.[234,236] In our case, PEGDA-acrylic acid hydrogels were formulated to present mechanical properties within the physiological range of small intestine. On natural-derived hydrogels such as Matrigel,™ the control over the mechanical properties is often not straightforward. Despite Matrigel™ possesses inherent biochemical factors that enhance cell adhesion and it is widely used for the culture of Caco-2 and human intestinal cells, its low stiffness (from tens to hundreds of Pa)[406] promotes the formation of cysts instead of monolayers. On the other hand, stiffer synthetic substrates such as the conventional polycarbonate porous membranes, induced undesirable changes in the cell phenotype.[117,390] Unlike of using collagen or PLGA,[183,197] on our hydrogels the ligand density can be controlled without changing significantly the mechanical properties of the hydrogels in the range of the fabrication parameters considered (0.06% - 1.2 % w/v acrylic acid) (Fig. 4.29). To modify the ligand density on collagen or other pure substrates, the quantity of the material, or they concentration in the pre-gel form, must be changed. Because of changing the amount of collagen implies changes the mechanical properties, the chemical and the mechanical contributions cannot be independently studied.[390,407,408] On the contrary, our system allows to decouple the effects of both parameters and study and optimize their contributions in an independent way.

A crucial factor when mimicking the basement membrane is the diffusion within the material as some molecules must be able to go across the basement membrane synthetic constructs. PEGDA–acrylic acid hydrogels contain a high amount of water and their mesh size and diffusivity can be tuned by changing the PEGDA concentrations.[294,409] Here, we achieved porosities between 9 and 12 nm,[294] which are in the range of those of the basement membrane and allow the diffusion of metabolites and other biomolecules with hydrodynamic radius below 5 nm.[410,411] This is a relevant issue when trying to mimic the *in vivo* environment, because the native basement membrane show an important traffic of nutrients from the digestion to the bloodstream. When considering small intestinal epithelium *in vitro* models because, porosity is a key factor, as permeability and

TEER measurements should be performed without the interference of the substrate. Therefore, even though villi-like microstructures that support the growth of epithelial cell monolayers can be obtained in materials such as PDMS or dense collagen, these materials do not allow molecule diffusion. For this reason, alternative materials such as porous PLGA have been proposed..[197,288] In our case, PEGDA-acrylic acid hydrogels fabricated at the polymer concentrations reported here have a porosity large enough to avoid the hydrogel interfering in permeability tests or TEER measurements.[410,411]

Another relevant factor to choose the material for *in vitro* models of epithelial tissues is the degradability. Considering that Caco-2 cell cultures take place for at least 21 days after seeding biomimetic constructs should keep their integrity for at least 3 weeks. In this regard, although collagen 3D villi-like scaffolds have shown to promote cell adhesion and proliferation, collagen degradation hampered the use of the structures for more than two weeks. [197,279,286]. PLGA and chemically cross-linked collagen have been investigated as alternative materials..[197,279] In contrast, our approach relies in a non-biodegradable material that will withstand long term cultures,[132,412]

Mimicking the 3D architecture of the small intestinal epithelium requires the fabrication of soft microstructures relatively large (hundreds of microns) and with high aspect ratios. The development of soft materials with these aspect ratios imply some technical shortcomings because of the mechanical stability of these soft hydrogels. The main problem when using molding with hydrogels is demolding, as they might be sticky or very soft, so microstructures can be deformed or even broken in this procedure. To overcome this restriction, Yu *et al.* fabricated high aspect ratio synthetic villi made of collagen by using sequential molding-demolding steps, passing through a hard mold, PDMS and agarose as sacrificial layer.[286] Other methods, such as stereolithography and two-photon polymerization have also been used to create high aspect ratio hydrogels, or complex scaffolds.[222,413] Also, another possible method is 3D bioprinting, which applies rapid prototyping techniques to model complex living tissues, such as an arterial bifurcation.[414]

Here, we take profit of the photocross-linking method used to fabricate our PEGDA-acrylic acid hydrogels, to create microstructures. Photolithography is a very simple and low-cost process for the fabrication of microstructures over large surface areas in a single step. Demolding steps are avoided, and considering the dimensions to mimic (> 100 μm), high resolution photomasks are not needed, which in addition reduces the costs. Another advantage of this technique is that the biomimetic construct can be photopolymerized *in-situ* in the Transwell®, for the functional assays, or adapted to non-conventional systems such as bioreactors or lab-on-chip devices. Following the photolithographic process, we

have succeeded in fabricating PEGDA-acrylic acid microstructures that mimic the 3D architecture and the anatomic dimensions of the small intestinal epithelium. Moreover, adjusting the fabrication parameters (polymer concentration, molecular weight, photoinitiator concentration and exposure time) allowed us to control the dimensions of the microstructures. Also, the physicochemical properties of the microstructured substrates, such as the elastic modulus, the pore size and the swelling ratio, can be tuned by changing the PEGDA concentration.[409] Several reports used pure or highly concentrated PEGDA solutions,[335] to produce high aspect ratio pillar microstructures by photolithography.[222,263–265] These studies lead to stiff constructs, with elastic modulus values in the range of ~ MPa. In contrast, in the present study villi-like microstructured hydrogels have been fabricated from low concentrated solutions, obtaining in a successful way very soft (3 kPa)[415] high aspect ratio microstructures that are mechanically stable for the intended applications.

Because of the urgency in improving conventional *in vitro* models of small intestinal epithelium by incorporating 3D features, quite a lot reports have addressed this challenge with variable degree of success.[68,183,197,279,284–288] A lot of these studies focused on the microfabrication method used to produce the 3D architecture. For example, Salomon *et al.* mimicked the villi architecture fabricating PDMS pillars through molding. This has the advantage of using a simple fabrication technique, but t the material is not the most appropriate, as it lacks crucial features such as porosity.[284] Other works developed synthetic villi using sequential molding, employing rigid materials such as PLGA (1-2 GPa),[197] and PLA (3.4 GPa)[285] or soluble materials as sacrificial layers.[279,286] In contrast with this multistep methodology, we produce microstructures by a single-step photolithography technique.

We designed a protocol to produce hydrogel microstructures by a double UV exposure: first, the hydrogel is exposed without the photomask to create a thin hydrogel base, and a second exposure with the photomask, which contains circular UV transparent windows, produces the microstructures. The hydrogel microstructures acquired bullet-like or pillar-like shapes with a rounded cap and wider base, and soft boundaries. Interestingly, hydrogel height could be regulated by changing both the photoinitiator concentration and the UV exposure time (energy dosage).[321] Increasing photoinitiator concentration enhances the monomer cross-linking at a given energy dosage, and, thus polymer gelation, in agreement with previous works.[316] Taking into account the Beer Lambert law, at high photoinitiator concentrations light intensity is prominently attenuated across the light propagation direction. Therefore, in our study, hydrogel height can be precisely controlled by the exposure time, which limits the formation of

radicals down to a certain distance from the UV source. A similar behavior has been previously reported and modelled in multifunctional acrylate molecules.[166]

However, with increasing UV exposure time, the height of the microstructures does not increase in a monotonous trend. On the contrary, it increases for short exposure times but at certain point it starts decreasing and might be zero (flat hydrogels) for prolonged exposure times. This is due to the hydrogel polymerization on the unexposed regions and it has already been described in the fabrication of PHEMA epidermal topographical features by photolithography.[416] The polymerization on the unexposed regions and the soft boundaries of the microstructures produced may be attributed to the high diffusion rates of the radicals into unexposed regions,[346,347] leading to the cross-linking between microstructures. This effect is convoluted with the diffusion of the PEGDA monomers toward the hydrogel boundaries, where they are depleted. These effects are attenuated far away from the photomask (1 mm) where the height of the microstructures and the polymerization on unexposed regions is limited. At these distances, light intensity is attenuated following the Beer-Lambert law, implying less radicals to initiate the polymerization, and also more effect of the oxygen inhibition of the polymerization reaction.[316,333] According to Shim *et al.*,[265] the chemical gradients of radicals and O_2 generated along the propagation direction of light, make possible the fabrication of rigid PEGDA microstructures (~ MPa)[335] with complex shapes that cannot be obtained by any other fabrication method. We have extended this concept for soft hydrogels and we have taken advantage of the complex, roundish shapes to produce biomimetic 3D microstructures that faithfully reproduce the geometry and dimensions of intestinal villi in a single fabrication step.

The use of photolithography to produce microstructures while copolymerizing PEGDA-acrylic acid to form hydrogels had not been reported previously to the best of our knowledge. When exploring the effects of adding acrylic acid to the photolithography cross-linking process, we found out that the addition of acrylic acid to the polymer solution improves the shape of the microstructures, diminishing the hydrogel polymerization on unexposed regions (Fig. 4.31). These changes in morphology may be attributed to changes in the reaction of polymerization. Acrylic acid competes with other PEGDA molecules to graft onto the acrylate group of PEGDA. As the grafted acrylic acid increased, the availability of vinyl groups of PEGDA decreased. Since the vinyl group of PEGDA also serve as the cross-linking site for PEGDA macromolecules, this reaction lowers the cross-linking degree of the PEGDA–acrylic acid hydrogels. We are increasing polymer total concentration (up to 20%) when adding acrylic acid, however stiffness values of the hydrogels did not show any significant changes. These results support this theory and the inhibition effect on the unexposed

regions, where the polymerization is avoided.[171,295] Moreover, the addition of acrylic acid in the polymer solutions dramatically decreases their viscosity, which benefits the O_2 inhibition.[330]

PEGDA-acrylic acid hydrogels proved to be suitable for the development of epithelial monolayers, as evidenced by the culture of MDCK cells. MDCK cells acquired epithelial-like morphology, and showed polarization markers properly located. MDCK surface coverage and phenotype was sensitive to the substrate rigidity (here controlled by the polymer concentration of the initial solution) and the dimensions of the microstructures, in particular, of their diameter. MDCK cells attached and proliferated on the most rigid hydrogels (10% w/v, leading to elastic modulus values of ~ 30 kPa). In contrast, on the more compliant hydrogels (5% w/v, elastic modulus of ~ 3 kPa) cells tend to show roundish morphologies, low attachment and proliferation, and form cell aggregates. The fact that mechanical properties of the substrate can regulate the cell behavior is very well documented.[369,417] It has been well established that MDCK cells become spherical and even detach, and form cell clusters or cysts when cultured on soft substrates. MDCK cells cultured on Matrigel™ form cysts with an empty lumen of about 50 μm in diameter after 2-7 days, and reach more than 100 μm after 10 days [418,419] Instead, on rigid surfaces flattened cohesive epithelial monolayers are obtained, this being attributed to their cell-cell adhesion.[380,384–386] Our samples, that differ one order of magnitude in their mechanical properties, exemplified this behavior. Regarding the effects of microstructure dimensions, even though MDCK cells showed notable apico-basal polarization at the base of large microstructures (300 μm in diameter), they just partially covered them. In contrast, smaller microstructures (100 μm in diameter) were fully covered after 14 days. These dramatic differences in behavior resulting from changes in the microstructure diameter is particularly surprising. It might be possible that the 100 μm microstructures may keep the cells close enough to promote their mechanical contact from early time points and allow the progression of the cell culture. Recently, Yevick *et al.* studied the monolayer organization on wires of various diameters. They found that on smaller wires (80 μm in diameter) actin fibers were highly oriented perpendicular to the wire longitudinal axis, while on larger wires (170 μm in diameter) actin fibers were randomly oriented.[420] These results may support the hypothesis that microstructures of 100 μm in diameter promote the formation cell-cell adhesions that keep the cells mechanically connected and covering the hydrogel.

Caco-2 cells were successfully grown on the hydrogels mimicking the 3D architecture of villi. We identified PEGDA-acrylic acid formulations suitable for the fabrication of microstructured hydrogels that, once laminin functionalized, supported the formation of polarized epithelial Caco-2 monolayers. Caco-2 cells

were cultured onto the hydrogels for up to 21 days and they colonized and covered the microstructures. The overall morphology of the cell-covered microstructured hydrogels showed a great similarity to the *in vivo* human villi. Meanwhile, Caco-2 cells developed apico-basal polarization with elongated nuclei and well located characteristic epithelial-like markers. We found that nuclei orientation was more perpendicular on hydrogels than on Transwell®. This may be related to the mechanical properties of the substrate, as it has been reported that substrate rigidity modulates nuclei shape and nuclei appear more flattened on stiffer substrates.[388] In addition, force balance between cell–cell and cell–substrate adhesions regulates cell shape and, therefore, nuclei orientation.[421] Thus, the compliance of the hydrogels, in the range of the intestinal epithelium, shift the balance to a larger contribution of the cell-cell adhesions, which promotes nuclei elongation and perpendicular orientation with respect to the surface, in a morphology close to that found in native villi. These considerations are in agreement with the recent findings of DiMarco *et al.* who reported cell phenotype and permeability values closer to *in vivo* situation when culturing Caco-2 monolayers in compliant matrices.[390]

As a proof-of-concept of the functionality of the Caco2 cell monolayers as actual epithelial barriers, TEER measurements were performed on the cell monolayers grown on the villi-like microstructures. TEER measurements performed on modified Transwell® demonstrated the formation of an epithelial barrier. TEER values obtained were significantly lower than those corresponding to the monolayers grown on porous membranes. This may be due to the effects produced by the three dimensional architecture, as it has been reported that cell tight junctions are weaker at the tips of the villi.[36,95,393] It is well known the poor correlation between TEER values from conventional *in vitro* intestinal models and *in vivo* measurements, that can reach readings 5 -30 fold lower.[402,403] The weak tight junctions at the tip is believed to be the reason behind TEER values reported *in vivo* are significantly smaller than those reported for monolayers. In addition to the architecture, the softness of the material can also affect the formation of the epithelial barrier. In fact, TEER measurements carried out on Caco-2 monolayers grown on collagen or PLGA villous scaffolds also shown lower values than on Transwell® and 2D scaffolds, and were similar to *in vivo* intestinal values.[286,197] In the present study TEER values of Caco-2 monolayer grown in the microstructured hydrogels were even closer to *in vivo* than the ones previously reported.[286,197]

Our results are supported by the hypothesis that villous geometry improves cell physiology and, therefore, barrier function, driving it closer to the *in vivo* situation.[402] At this point, further efforts are required to engineer a robust set up compatible with standard Transwell® inserts to perform systematic

measurements of permeability and transport. Due to the simplicity and versatility of the fabrication method designed, microstructured PEGDA-acrylic acid hydrogels might find uncountable applications. The method can be used to design more complex models of intestinal mucosa, by incorporating other cell types such as goblet cells, intestinal stem cells, immune cells and even commensal or pathogenic bacteria. In addition, because of the PEGDA-acrylic acid tunable properties, the methodology can be extended to other epithelial tissues presenting 3D architectures relevant for their functionality such as the cornea, the esophagus or the skin.

6 Conclusions

- We have described a simple and cost-effective method to produce microstructures in soft hydrogels using PEGDA-acrylic acid polymer solutions and conventional photolithography. The process parameters affecting the microfabrication (UV exposure time, photoinitiator concentration, and PEGDA molecular weight and concentration) have been identified and studied. By properly selecting these parameters, microstructures with the shape and dimensions of native villi have been obtained. The particular characteristics of the polymerization reaction in the experimental set-up designed produced high aspect ratio microstructures on soft materials with bullet-like shapes and roundish contours, faithfully resembling the anatomy of villi structures found *in vivo.*

- We have demonstrated that PEGDA-acrylic acid can be copolymerized to form microstructured hydrogels and can be easily further functionalized with several extracellular matrix proteins. Acrylic acid incorporation provides control over the ligand density on the hydrogels. In addition, within the range of experimental conditions tested here, ligand density can be optimized without a significant modification of the mechanical properties of the hydrogel. Optimized conditions for the fabrication and functionalization of villi-like microstructured hydrogels supporting epithelial cell growth have been established.

- We have proved that functional epithelial cell monolayers are formed on the villi-like microstructured PEGDA-acrylic acid hydrogels. This has been tested successfully with two epithelial cell lines, which could adhere, proliferate forming a monolayer of cells that display cellular and nuclei epithelial morphology and express epithelial markers (villin, ZO-1, β catenin) at the proper locations. We have determined that the stiffness of the produced microstructures (here tuned by the polymer concentration and polymer molecular weight) is a crucial parameter for the formation of epithelial monolayers. Substrate stiffness and ligands density determine the balance between the strength of cell-matrix and cell-cell contacts, which will result in the formation of monolayers or 3D cysts structures.

- We have successfully adapted our substrates to standard cell culture platforms for the measurement of transepithelial electrical resistance (TEER) of the resulting monolayers. TEER measurements confirmed the formation of functional epithelial cell barriers displaying TEER values

closer to *in vivo* situation than those measured for conventional monolayers. Therefore, we have engineered a 3D biomimetic model of the small intestinal epithelium that, as evidenced the promising results reported, sets the foundations of a novel *in vitro* platform to be applied in drug absorption and toxicity tests, was well as biological studies and disease modelling.

7

References

1. Hall, J. E. & Guyton, A. C. *Guyton and Hall Textbook of Medical Physiology*. *Journal of Chemical Information and Modeling* **53,** (2011).
2. Peterson, L. W. & Artis, D. Intestinal epithelial cells: regulators of barrier function and immune homeostasis. *Nat. Rev. Immunol.* **14,** 141–53 (2014).
3. Barrett, K., Barman, S., Boitano, S. & Brooks, H. Ganong's Review of Medical Physiology, 25e. *New York, NY McGraw-Hill* 1–32 (2016).
4. Tortora, G. J. & Derrickson, B. Principles of Anatomy and Physiology. *Wiley* **15,** 1127 (2014).
5. Marchiando, A. M., Graham, W. V. & Turner, J. R. Epithelial barriers in homeostasis and disease. *Annu. Rev. Pathol.* **5,** 119–144 (2010).
6. Encyclopedia Britannica. Britannica Online Encyclopedia. *Encycl. Br.* 1–73 (2014).
7. Viswanathan, V. K., Hodges, K. & Hecht, G. Enteric infection meets intestinal function: how bacterial pathogens cause diarrhoea. *Nat. Rev. Microbiol.* **7,** 110–119 (2008).
8. Alberts, B. *et al. Molecular Biology of the Cell. 4th Edition, New York* (2002).
9. Louis-Auguste, J. *et al.* High dose multiple micronutrient supplementation improves villous morphology in environmental enteropathy without HIV enteropathy: results from a double-blind randomised placebo controlled trial in Zambian adults. *BMC Gastroenterol.* **14,** 15 (2014).
10. Kelly, P. *et al.* Responses of small intestinal architecture and function over time to environmental factors in a tropical population. *Am. J. Trop. Med. Hyg.* **70,** 412–419 (2004).
11. Marsh, M. N. & Swift, J. A. A study of the small intestinal mucosa using the scanning electron microscope. *Gut* **10,** 940–949 (1969).
12. Muñoz-Pinto, D., Whittaker, P. & Hahn, M. S. Lamina Propria Cellularity and Collagen Composition: An Integrated Assessment of Structure in Humans. *Ann. Otol. Rhinol. Laryngol.* **118,** 299–306 (2009).
13. Sun, M., He, C., Cong, Y. & Liu, Z. Regulatory immune cells in regulation of intestinal inflammatory response to microbiota. *Mucosal Immunol.* **8,** 969–978 (2015).
14. Li, A. C. Y. Basement membrane components. *J. Clin. Pathol.* **56,** 885–887 (2003).
15. Atuma, C., Strugala, V., Allen, a & Holm, L. The adherent gastrointestinal mucus gel layer: thickness and physical state in vivo. *Am. J. Physiol. Gastrointest. Liver Physiol.* **280,** G922-9 (2001).
16. Linden, S. K., Sutton, P., Karlsson, N. G., Korolik, V. & McGuckin, M. A. Mucins in the mucosal barrier to infection. *Mucosal Immunol.* **1,** 183–197 (2008).

17. Soler, M. *et al.* Adhesion-related glycocalyx study: quantitative approach with imaging-spectrum in the energy filtering transmission electron microscope (EFTEM). *FEBS Lett.* **429,** 89–94 (1998).

18. Kim, Y. S. & Ho, S. B. Intestinal Goblet Cells and Mucins in Health and Disease: Recent Insights and Progress. *Curr. Gastroenterol. Rep.* **12,** 319–330 (2010).

19. Rescigno, M. The intestinal epithelial barrier in the control of homeostasis and immunity. *Trends Immunol.* **32,** 256–264 (2011).

20. Liu, L. & Talmon, G. Quantification of intraepithelial lymphocytes in normal pediatric small intestinal allograft and native ilea. *Transplant. Proc.* **43,** 1831–1835 (2011).

21. Mowat, A. M. & Agace, W. W. Regional specialization within the intestinal immune system. *Nat Rev Immunol* **14,** 667–685 (2014).

22. Round, J. L. & Mazmanian, S. K. The gut microbiota shapes intestinal immune responses during health and disease. *Nat. Rev. Immunol.* **9,** 313–23 (2009).

23. McGuckin, M. A., Lindén, S. K., Sutton, P. & Florin, T. H. Mucin dynamics and enteric pathogens. *Nat. Rev. Microbiol.* **9,** 265–278 (2011).

24. Goodell, M. a, Nguyen, H. & Shroyer, N. Somatic stem cell heterogeneity: diversity in the blood, skin and intestinal stem cell compartments. *Nat. Rev. Mol. Cell Biol.* **16,** 299–309 (2015).

25. Crosnier, C., Stamataki, D. & Lewis, J. Organizing cell renewal in the intestine: stem cells, signals and combinatorial control. *Nat. Rev. Genet.* **7,** 349–359 (2006).

26. Gregorieff, A. Wnt signaling in the intestinal epithelium: from endoderm to cancer. *Genes Dev.* **19,** 877–890 (2005).

27. Barker, N. Adult intestinal stem cells: critical drivers of epithelial homeostasis and regeneration. *Nat. Rev. Mol. Cell Biol.* **15,** 19–33 (2014).

28. Mayhew, T. M. Epithelial integrity, cell death and cell loss in mammalian small intestine. *Histology and Histopathology* **14,** 257–267 (1999).

29. Williams, J. M. *et al.* Epithelial cell shedding and barrier function: a matter of life and death at the small intestinal villus tip. *Vet. Pathol.* **52,** 445–55 (2015).

30. Barker, N. *et al.* Identification of stem cells in small intestine and colon by marker gene Lgr5. *Nature* **449,** 1003–1007 (2007).

31. Sato, T. *et al.* Single Lgr5 stem cells build crypt-villus structures in vitro without a mesenchymal niche. *Nature* **459,** 262–5 (2009).

32. Sato, T. *et al.* Paneth cells constitute the niche for Lgr5 stem cells in intestinal crypts. *Nature* **469,** 415–8 (2011).

33. Umar, S. Intestinal Stem Cells. *Curr. Gastroenterol. Rep.* **12,** 340–348 (2010).

34. Carulli, A. J., Samuelson, L. C. & Schnell, S. Unraveling intestinal stem cell behavior with models of crypt dynamics. *Integr. Biol.* **6,** 243 (2014).

35. Standring, S. *Gray's Anatomy: The Anatomical Basis of Clinical Practice*. *Development* **2,** (2008).

36. Yu, Q. H. & Yang, Q. Diversity of tight junctions (TJs) between gastrointestinal epithelial cells and their function in maintaining the mucosal barrier. *Cell Biol. Int.* **33,** 78–82 (2009).

37. Anderson, J. M. Molecular structure of tight junctions and their role in epithelial transport. *News Physiol. Sci.* **16,** 126–30 (2001).

38. Tortora, G. J. *et al. PRINCIPLES OF ANATOMY AND Br yan Derrickson*. (2010).

39. Camilleri, M. Integrated Upper Gastrointestinal Response to Food Intake. *Gastroenterology* **131,** 640–658 (2006).

40. Delacour, D., Salomon, J., Robine, S. & Louvard, D. Plasticity of the brush border — the yin and yang of intestinal homeostasis. *Nat. Rev. Gastroenterol. Hepatol.* **13,** 161–174 (2016).

41. Lozovatsky, L., Abayasekara, N., Piawah, S. & Walther, Z. CASK Deletion in Intestinal Epithelia Causes Mislocalization of LIN7C and the DLG1/Scrib Polarity Complex without Affecting Cell Polarity. *Mol. Biol. Cell* **20,** 4489–4499 (2009).

42. Neunlist, M. *et al.* The digestive neuronal–glial–epithelial unit: a new actor in gut health and disease. *Nat. Rev. Gastroenterol. Hepatol.* **10,** 90–100 (2012).

43. Benson, K., Cramer, S. & Galla, H.-J. Impedance-based cell monitoring: barrier properties and beyond. *Fluids Barriers CNS* **10,** 5 (2013).

44. Griffin, B. & Driscoll, C. O. Diseases of the Small Intestine. 34–76 (2007). Available at: http://www.ddc.musc.edu/public/diseases/small-intestine/.

45. Prevalence of enteric pathogen-associated community gastroenteritis among kindergarten children in Gaza. *J. Biomed. Res.* 61–68 (2015). doi:10.7555/JBR.29.20130108

46. Kirk, M. D. *et al.* World Health Organization Estimates of the Global and Regional Disease Burden of 22 Foodborne Bacterial, Protozoal, and Viral Diseases, 2010: A Data Synthesis. *PLOS Med.* **12,** e1001921 (2015).

47. Kolling, G., Wu, M. & Guerrant, R. L. Enteric pathogens through life stages. *Front. Cell. Infect. Microbiol.* **2,** 114 (2012).

48. Fasina, Y. O., Hoerr, F. J., McKee, S. R. & Conner, D. E. Influence of Salmonella enterica Serovar Typhimurium Infection on Intestinal Goblet Cells and Villous Morphology in Broiler Chicks. *Avian Dis.* **54,** 841–847 (2010).

49. Benjamin, M. A., Lu, J., Donnelly, G., Dureja, P. & McKay, D. M. Changes in murine jejunal morphology evoked by the bacterial superantigen Staphylococcus aureus enterotoxin B are mediated by CD4+ T cells. *Infect. Immun.* **66,** 2193–2199 (1998).

50. Danielsen, E. M., Hansen, G. H. & Karlsdóttir, E. Staphylococcus aureus enterotoxins A- and B: Binding to the enterocyte brush border and uptake by perturbation of the apical endocytic membrane traffic. *Histochem. Cell Biol.* **139,** 513–524 (2013).

51. Wang, Q. *et al.* The Bacteriocin Sublancin Attenuates Intestinal Injury in Young Mice Infected With Staphylococcus aureus. *Anat. Rec. (Hoboken).* **0,** 1–8 (2014).

52. Nataro, J. Enteroaggregative Escherichia coli. *Emerg. Infect. Dis.* **4,** 251–261 (1998).

53. Hicks, S., Candy, D. C. A. & Phillips, A. D. Adhesion of enteroaggregative Escherichia coli to pediatric intestinal mucosa in vitro. *Infect. Immun.* **64,** 4751–4760 (1996).

54. Reiter, K., Eggebrecht, S., Drewes, B., Riess, M. & Weyrauch, K. D. Effects of Enterococcus faecium and Bacillus cereus var. toyoi on the morphology of the intestinal mucous membrane in piglets*. *Sect. Cell. Mol. Biol.* **616,** 803–809 (2006).

55. Catassi, C., Gatti, S. & Fasano, A. The new epidemiology of celiac disease. *J. Pediatr. Gastroenterol. Nutr.* **59 Suppl 1,** S7-9 (2014).

56. Agarwal, S., Kovilam, O., Zach, T. L. & Agrawal, D. K. Immunopathogenesis and therapeutic approaches in pediatric celiac disease. *Expert Rev. Clin. Immunol.* **12,** 857–869 (2016).

57. Gujral, N. Celiac disease: Prevalence, diagnosis, pathogenesis and treatment. *World J. Gastroenterol.* **18,** 6036 (2012).

58. Ediger, T. R. & Hill, I. D. Celiac Disease. *Pediatr. Rev.* **35,** 409–416 (2014).

59. Naganuma, M. *et al.* Characterization of structures with T-lymphocyte aggregates in ileal villi of Crohn's disease. *Am. J. Gastroenterol.* **97,** 1741–1747 (2002).

60. Molodecky, N. A. *et al.* Increasing Incidence and Prevalence of the Inflammatory Bowel Diseases With Time, Based on Systematic Review. *Gastroenterology* **142,** 46–54.e42 (2012).

61. World Cancer Research Fundation. Available at: http://www.wcrf.org/.

62. Torre, L. A. *et al.* Global cancer statistics, 2012. *CA. Cancer J. Clin.* **65,** 87–108 (2015).

63. Ohmiya, N. *et al.* Classification of Intestinal Lymphangiectasia with Protein-Losing

Enteropathy: White Villi Type and Non-White Villi Type. *Digestion* **90,** 155–166 (2014).

64. Ebert, E. C. & Nagar, M. Gastrointestinal manifestations of amyloidosis. *American Journal of Gastroenterology* **103,** 776–787 (2008).

65. Gerson, L. B. & Triadafilopoulos, G. Palliative care in inflammatory bowel disease: An evidence-based approach. *Inflamm. Bowel Dis.* **6,** 228–243 (2007).

66. Wales, P. W. *et al.* Neonatal Short Bowel Syndrome: Population-Based Estimates of Incidence and Mortality Rates. in *Journal of Pediatric Surgery* **39,** 690–695 (2004).

67. Spurrier, R. G. & Grikscheit, T. C. Tissue Engineering the Small Intestine. *Clin. Gastroenterol. Hepatol.* **11,** 354–358 (2013).

68. Ladd, M. R., Niño, D. F., March, J. C., Sodhi, C. P. & Hackam, D. J. Generation of an artificial intestine for the management of short bowel syndrome. *Curr. Opin. Organ Transplant.* **21,** 1 (2016).

69. Ferrec, E. *et al.* In Vitro Models of the Intestinal Barrier. *Atla* **29,** 649–668 (2001).

70. Meunier, V., Bourrie, M., Berger, Y. & Fabre, G. The human intestinal epithelial cell line Caco-2; pharmacological and pharmacokinetic applications. *Cell Biol. Toxicol.* **11,** 187–194 (1995).

71. Goyal, N., Rana, A., Ahlawat, A., Bijjem, K. R. V. & Kumar, P. Animal models of inflammatory bowel disease: a review. *Inflammopharmacology* **22,** 219–233 (2014).

72. Alderuccio, F., Sentry, J. W., Marshall, A. C. J., Biondo, M. & Toh, B. H. Animal Models of Human Disease: Experimental Autoimmune Gastritis—A Model for Autoimmune Gastritis and Pernicious Anemia. *Clin. Immunol.* **102,** 48–58 (2002).

73. Jiminez, J. A., Uwiera, T. C., Douglas Inglis, G. & Uwiera, R. R. E. Animal models to study acute and chronic intestinal inflammation in mammals. *Gut Pathog.* **7,** 29 (2015).

74. Johnson, R. L. & Fleet, J. C. Animal models of colorectal cancer. *Cancer Metastasis Rev.* **32,** 39–61 (2013).

75. Jackstadt, R. & Sansom, O. J. Mouse models of intestinal cancer. *J. Pathol.* **238,** 141–151 (2016).

76. Marietta, E. V., David, C. S. & Murray, J. A. Important Lessons Derived from Animal Models of Celiac Disease. *Int. Rev. Immunol.* **30,** 197–206 (2011).

77. Stahl, M. *et al.* A Novel Mouse Model of Campylobacter jejuni Gastroenteritis Reveals Key Pro-inflammatory and Tissue Protective Roles for Toll-like Receptor Signaling during Infection. *PLoS Pathog.* **10,** e1004264 (2014).

78. Glaeser, H. & Fromm, M. F. Animal models and intestinal drug transport. *Expert Opin. Drug Metab. Toxicol.* **4,** 347–361 (2008).

79. Billat, P.-A., Roger, E., Faure, S. & Lagarce, F. Models for drug absorption from the small intestine: where are we and where are we going? *Drug Discov. Today* (2017). doi:10.1016/j.drudis.2017.01.007

80. Singh, M., Mensah, G. A. & Bakris, G. Pathogenesis and Clinical Physiology of Hypertension. *Cardiol. Clin.* **28,** 545–559 (2010).

81. Li, M. *et al.* Excipients enhance intestinal absorption of ganciclovir by P-gp inhibition: Assessed in vitro by everted gut sac and in situ by improved intestinal perfusion. *Int. J. Pharm.* **403,** 37–45 (2011).

82. Randall, K. J., Turton, J. & Foster, J. R. Explant culture of gastrointestinal tissue: A review of methods and applications. *Cell Biol. Toxicol.* **27,** 267–284 (2011).

83. Carvalho, F. C., Bruschi, M. L., Evangelista, R. C. & Gremião, M. P. D. Mucoadhesive drug delivery systems. *Brazilian J. Pharm. Sci.* **46,** 1–17 (2010).

84. Alam, M. A., Al-Jenoobi, F. I. & Al-Mohizea, A. M. Everted gut sac model as a tool in pharmaceutical research: Limitations and applications. *J. Pharm. Pharmacol.* **64,** 326–336 (2012).

85. Liu, W. *et al.* Developments in Methods for Measuring the Intestinal Absorption of Nanoparticle-Bound Drugs. *Int. J. Mol. Sci.* **17,** 1171 (2016).

86. Van De Kerkhof, E. G. *et al.* Innovative methods to study human intestinal drug metabolism in vitro: Precision-cut slices compared with Ussing chamber preparations. *Drug Metab. Dispos.* **34,** 1893–1902 (2006).

87. De Kanter, R. *et al.* A new technique for preparing precision-cut slices from small intestine and colon for drug biotransformation studies. *J. Pharmacol. Toxicol. Methods* **51,** 65–72 (2005).

88. Li, M., de Graaf, I. A. M. & Groothuis, G. M. M. Precision-cut intestinal slices: alternative model for drug transport, metabolism, and toxicology research. *Expert Opin. Drug Metab. Toxicol.* **12,** 175–190 (2016).

89. Clarke, L. L. A guide to Ussing chamber studies of mouse intestine. *AJP Gastrointest. Liver Physiol.* **296,** G1151–G1166 (2009).

90. He, L. *et al.* Use of the Ussing chamber technique to study nutrient transport by epithelial tissues. *Front. Biosci. (Landmark Ed.* **18,** 1266–74 (2013).

91. Membrane, R. T. *et al.* Transwell ® Permeable Supports Selection and Use Guide. (2007).

92. Grajek, W. & Olejnik, A. EPITHELIAL CELL CULTURES IN VITRO AS A MODEL TO STUDY FUNCTIONAL PROPERTIES OF FOOD. *Polish J. Food Nutr. Sci.* **13,** 5–24 (2004).

93. Benam, K. H. *et al.* Engineered In Vitro Disease Models. *Annu. Rev. Pathol.* **10,** 195–262 (2015).

94. Srinivasan, B. *et al.* TEER Measurement Techniques for In Vitro Barrier Model Systems. *J. Lab. Autom.* **20,** 107–126 (2015).

95. Steed, E., Balda, M. S. & Matter, K. Dynamics and functions of tight junctions. *Trends Cell Biol.* **20,** 142–149 (2010).

96. Anderson, J. M. & Van Itallie, C. M. Physiology and Function of the Tight Junction. *Cold Spring Harb. Perspect. Biol.* **1,** a002584–a002584 (2009).

97. Wang, X., Becker, F. F. & Gascoyne, P. R. C. The fractal dimension of cell membrane correlates with its capacitance: A new fractal single-shell model. *Chaos An Interdiscip. J. Nonlinear Sci.* **20,** 43133 (2010).

98. Quaroni, A. Epithelioid cell cultures from rat small intestine. Characterization by morphologic and immunologic criteria. *J. Cell Biol.* **80,** 248–265 (1979).

99. Kaeffer, B. Mammalian intestinal epithelial cells in primary culture: a mini-review. *In Vitro Cell. Dev. Biol. Anim.* **38,** 123–134 (2002).

100. Schwerk, J. *et al.* Generation of Mouse Small Intestinal Epithelial Cell Lines That Allow the Analysis of Specific Innate Immune Functions. *PLoS One* **8,** (2013).

101. Sambuy, Y. *et al.* The Caco-2 cell line as a model of the intestinal barrier: Influence of cell and culture-related factors on Caco-2 cell functional characteristics. *Cell Biol. Toxicol.* **21,** 1–26 (2005).

102. Hidalgo, I. J., Raub, T. J. & Borchardt, R. T. Characterization of the human colon carcinoma cell line (Caco-2) as a model system for intestinal epithelial permeability. *Gastroenterology* **96,** 736–749 (1989).

103. Press, B. in 139–154 (2011). doi:10.1007/978-1-61779-191-8_9

104. Artursson, P., Palm, K., Luthmanb, K. & Luthman, K. Caco-2 monolayers in experimental and theoretical predictions of drug transport. *Adv. Drug Deliv. Rev.* **64,** 280–289 (2012).

105. Brück, S., Strohmeier, J., Busch, D., Drozdzik, M. & Oswald, S. Caco-2 cells - expression, regulation and function of drug transporters compared with human jejunal tissue. *Biopharm. Drug Dispos.* (2016). doi:10.1002/bdd.2025

106. Kang, T. *et al.* In vitro toxicity of different-sized ZnO nanoparticles in Caco-2 cells. *Nanoscale Res. Lett.* **8,** 496 (2013).

107. Lennernäs, H. Human jejunal effective permeability and its correlation with preclinical drug absorption models. *J. Pharm. Pharmacol.* **49,** 627–638 (1997).

108. Martínez-Maqueda, D., Miralles, B. & Recio, I. in *The Impact of Food Bioactives on Health* 113–124 (Springer International Publishing, 2015). doi:10.1007/978-3-319-16104-4_11

109. Pan, F., Han, L., Zhang, Y., Yu, Y. & Liu, J. Optimization of Caco-2 and HT29 co-culture in vitro cell models for permeability studies. *Int. J. Food Sci. Nutr.* **66,** 680–685 (2015).

110. Leonard, F., Collnot, E. M. & Lehr, C. M. A three-dimensional coculture of enterocytes, monocytes and dendritic cells to model inflamed intestinal mucosa in vitro. *Mol. Pharm.* **7,** 2103–2119 (2010).

111. Bermudez-Brito, M., Faas, M. M. & de Vos, P. Modulation of Dendritic-Epithelial Cell Responses against Sphingomonas Paucimobilis by Dietary Fibers. *Sci. Rep.* **6,** 30277 (2016).

112. Moyes, S. M., Morris, J. F. & Carr, K. E. Macrophages increase microparticle uptake by enterocyte-like Caco-2 cell monolayers. *J. Anat.* **217,** 740–754 (2010).

113. Kuntz, S. *et al.* Inhibition of low-grade inflammation by anthocyanins from grape extract in an in vitro epithelial-endothelial co-culture model. *Food Funct.* **6,** 1136–1149 (2015).

114. Kleiveland, C. R. in *The Impact of Food Bioactives on Health* 197–205 (Springer International Publishing, 2015). doi:10.1007/978-3-319-16104-4_18

115. Parlesak, A., Haller, D., Brinz, S., Baeuerlein, A. & Bode, C. Modulation of Cytokine Release by Differentiated CACO-2 Cells in a Compartmentalized Coculture Model with Mononuclear Leucocytes and Nonpathogenic Bacteria. *Scand. J. Immunol.* **60,** 477–485 (2004).

116. Shen, C., Meng, Q. & Zhang, G. Design of 3D printed insert for hanging culture of Caco-2 cells. *Biofabrication* **7,** 15003 (2015).

117. Sun, H., Chow, E. C., Liu, S., Du, Y. & Pang, K. S. The Caco-2 cell monolayer: usefulness and limitations. *Expert Opin. Drug Metab. Toxicol.* **4,** 395–411 (2008).

118. Sjöberg, V. *Immune response of the small intestinal mucosa in children with celiac disease - Impact of two environmental factors , resident microbiota and oats*. (2013).

119. Takenaka, T. *et al.* Human Small Intestinal Epithelial Cells Differentiated from Adult Intestinal Stem Cells as a Novel System for Predicting Oral Drug Absorption in Humans. *Drug Metab. Dispos.* **42,** 1947–1954 (2014).

120. Gattazzo, F., Urciuolo, A. & Bonaldo, P. Extracellular matrix: a dynamic microenvironment for stem cell niche. *Biochim. Biophys. Acta* **1840,** 2506–19 (2014).

121. Takeuchi, T. & Gonda, T. Distribution of the pores of epithelial basement membrane in the rat small intestine. *J. Vet. Med. Sci.* **66,** 695–700 (2004).

122. Glentis, A., Gurchenkov, V. & Vignjevic, D. M. Assembly, heterogeneity, and breaching of the basement membranes. *Cell Adh. Migr.* **8,** 236–245 (2014).

123. Verbeke, S. *et al.* Basement membrane and connective tissue proteins in intestinal mucosa of patients with coeliac disease. *J. Clin. Pathol.* **55,** 440–5 (2002).

124. Mahoney, Z. X., Stappenbeck, T. S. & Miner, J. H. Laminin 5 influences the architecture of the mouse small intestine mucosa. *J. Cell Sci.* **121,** 2493–2502 (2008).

125. Teller, I. C. *et al.* Laminins in the developing and adult human small intestine: Relation with the functional absorptive unit. *Dev. Dyn.* **236,** 1980–1990 (2007).

126. Kalluri, R. Angiogenesis: Basement membranes: structure, assembly and role in tumour angiogenesis. *Nat. Rev. Cancer* **3,** 422–433 (2003).

127. Gerlach, G. & Arndt, K.-F. Hydrogel Sensors and Actuators. *Springer Ser. Chem. Sensors Biosens.* **6,** 1–15 (2009).

128. Ganji, F., Vasheghani-Farahani, S. & Vasheghani-Farahani, E. Theoretical Description of Hydrogel Swelling: A Review. *Iran. Polym. J.* **19,** 375–398 (2010).

129. Tibbitt, M. W. & Anseth, K. S. Hydrogels as extracellular matrix mimics for 3D cell culture.

Biotechnol. Bioeng. **103,** 655–663 (2009).

130. Lee, K. Y. & Mooney, D. J. Hydrogels for tissue engineering. *Chem. Rev.* **101,** 1869–1879 (2001).

131. Peppas, N. A. N. a., Hilt, J. Z. Z., Khademhosseini, A. & Langer, R. Hydrogels in biology and medicine: From molecular principles to bionanotechnology. *Adv. Mater.* **18,** 1345–1360 (2006).

132. Hoffman, A. S. Hydrogels for biomedical applications. *Adv. Drug Deliv. Rev.* **64,** 18–23 (2012).

133. Jabaji, Z. *et al.* Type I Collagen as an Extracellular Matrix for the In Vitro Growth of Human Small Intestinal Epithelium. *PLoS One* **9,** e107814 (2014).

134. Hughes, C. S., Postovit, L. M. & Lajoie, G. A. Matrigel: a complex protein mixture required for optimal growth of cell culture. *Proteomics* **10,** 1886–1890 (2010).

135. Serban, M. A., Liu, Y. & Prestwich, G. D. Effects of extracellular matrix analogues on primary human fibroblast behavior. *Acta Biomater.* **4,** 67–75 (2008).

136. Esposito, A. *et al.* Hyaluronic acid based materials for intestine tissue engineering: A morphological and biochemical study of cell-material interaction. *J. Mater. Sci. Mater. Med.* **17,** 1365–1372 (2006).

137. Zakhem, E., Raghavan, S., Gilmont, R. R. & Bitar, K. N. Chitosan-based scaffolds for the support of smooth muscle constructs in intestinal tissue engineering. *Biomaterials* **33,** 4810–4817 (2012).

138. Gjorevski, N. *et al.* Designer matrices for intestinal stem cell and organoid culture. *Nat. Publ. Gr.* **539,** 560–564 (2016).

139. Lutolf, M. P. & Hubbell, J. a. Synthetic biomaterials as instructive extracellular microenvironments for morphogenesis in tissue engineering. *Nat. Biotechnol.* **23,** 47–55 (2005).

140. Zhu, J. & Marchant, R. E. Design properties of hydrogel tissue-engineering scaffolds. *Expert Rev. Med. Devices* **8,** 607–26 (2011).

141. DeForest, C. A. & Anseth, K. S. Advances in bioactive hydrogels to probe and direct cell fate. *Annu. Rev. Chem. Biomol. Eng.* **3,** 421–44 (2012).

142. Kharkar, P. M., Kiick, K. L. & Kloxin, A. M. Designing degradable hydrogels for orthogonal control of cell microenvironments. *Chem. Soc. Rev.* **42,** 7335–72 (2013).

143. Liu, S. Q. *et al.* Synthetic hydrogels for controlled stem cell differentiation. *Soft Matter* **6,** 67 (2010).

144. Seliktar, D. Designing Cell-Compatible Hydrogels for Biomedical Applications. *Science (80-.).* **336,** 1124–1128 (2012).

145. Nicodemus, G. D. & Bryant, S. J. Cell {Encapsulation} in {Biodegradable} {Hydrogels} for {Tissue} {Engineering} {Applications}. *Tissue Eng. Part B. Rev.* **14,** 149–165 (2008).

146. Huglin, M. R. Hydrogels in medicine and pharmacy Edited by N. A. Peppas, CRC Press Inc., Boca Raton, Florida, 1986 (Vol. l), 1987 (Vols 2 and 3). Vol. 1 Fundamentals, pp. vii + 180, £72.00, ISBN 0-8493-5546-X; Vol. 2 Polymers, pp. vii + 171, £72.00, ISBN 0-8493-5547-8; *Br. Polym. J.* **21,** 184–184 (1989).

147. Slaughter, B. V., Khurshid, S. S., Fisher, O. Z., Khademhosseini, A. & Peppas, N. A. Hydrogels in Regenerative Medicine. *Adv. Mater.* **21,** 3307–3329 (2009).

148. Flory, P. J. & Rehner, J. Statistical Mechanics of Cross-Linked Polymer Networks II. Swelling. *J. Chem. Phys.* **11,** 521 (1943).

149. Vats, K. & Benoit, D. S. W. W. Dynamic Manipulation of Hydrogels to Control Cell Behavior: A Review. *Tissue Eng. Part B Rev.* **19,** 455–469 (2013).

150. Hutanu, D. Recent Applications of Polyethylene Glycols (PEGs) and PEG Derivatives. *Mod. Chem. Appl.* **2,** (2014).

151. Del Bufalo, F. *et al.* 3D modeling of human cancer: A PEG-fibrin hydrogel system to study the role of tumor microenvironment and recapitulate the in vivo effect of oncolytic adenovirus. *Biomaterials* **84,** 76–85 (2016).

152. Kloxin, A. M., Benton, J. A. & Anseth, K. S. In situ elasticity modulation with dynamic substrates to direct cell phenotype. *Biomaterials* **31,** 1–8 (2010).

153. Zhu, J. Bioactive modification of poly(ethylene glycol) hydrogels for tissue engineering. *Biomaterials* **31,** 4639–4656 (2010).

154. Gonen-Wadmany, M., Goldshmid, R. & Seliktar, D. Biological and mechanical implications of PEGylating proteins into hydrogel biomaterials. *Biomaterials* **32,** 6025–6033 (2011).

155. Tsou, Y.-H., Khoneisser, J., Huang, P.-C. & Xu, X. Hydrogel as a bioactive material to regulate stem cell fate. *Bioact. Mater.* **1,** 39–55 (2016).

156. Lin, L., Zhu, J., Kottke-Marchant, K. & Marchant, R. E. Biomimetic-Engineered Poly (Ethylene Glycol) Hydrogel for Smooth Muscle Cell Migration. *Tissue Eng. Part A* **20,** 140109062102007 (2014).

157. Missirlis, D. & Spatz, J. P. Combined effects of PEG hydrogel elasticity and cell-adhesive coating on fibroblast adhesion and persistent migration. *Biomacromolecules* **15,** 195–205 (2014).

158. Garland, S. P. *et al.* A Cell Culture Substrate with Biologically Relevant Size-Scale Topography and Compliance of the Basement Membrane. *Langmuir* **30,** 2101–2108 (2014).

159. Lauridsen, H. M. & Gonzalez, A. L. Biomimetic, ultrathin and elastic hydrogels regulate human neutrophil extravasation across endothelial-pericyte bilayers. *PLoS One* **12,** e0171386 (2017).

160. Nishiguchi, A., Singh, S., Wessling, M., Kirkpatrick, C. J. & Möller, M. Basement Membrane Mimics of Biofunctionalized Nanofibers for a Bipolar-Cultured Human Primary Alveolar-Capillary Barrier Model. *Biomacromolecules* **18,** 719–727 (2017).

161. Enemchukwu, N. O. *et al.* Synthetic matrices reveal contributions of ECM biophysical and biochemical properties to epithelial morphogenesis. *J. Cell Biol.* **212,** 113–124 (2016).

162. Victor, H.-G., Gi Hun, C., Mollie, S., Rebecca, C. & Linda, G. Engineering the intestinal basement membrane microenvironment using PEG-based hydrogels. *Front. Bioeng. Biotechnol.* **4,** (2016).

163. Bowman, C. N. & Kloxin, C. J. Toward an enhanced understanding and implementation of photopolymerization reactions. *AIChE J.* **54,** 275–2795 (2008).

164. Korolev, G. V. & Mogilevich, M. M. *Three-dimensional free-radical polymerization: Cross-linked and hyper-branched polymers. Three-Dimensional Free-Radical Polymerization: Cross-Linked and Hyper-Branched Polymers* (Springer Berlin Heidelberg, 2009). doi:10.1007/978-3-540-87567-3

165. Su, W.-F. in 137–183 (2013). doi:10.1007/978-3-642-38730-2_7

166. Boddapati, A. Modeling Cure Depth During Photopolymerization of Multifunctional Acrylates. (2010).

167. University of Michigan. Polymerization. 354–383 (2014).

168. Zhao, T. *et al.* Water soluble hyperbranched polymers from controlled radical homopolymerization of PEG diacrylate. *RSC Adv.* **5,** 33823–33830 (2015).

169. Gunn, J. W., Turner, S. D. & Mann, B. K. Adhesive and mechanical properties of hydrogels influence neurite extension. *J. Biomed. Mater. Res. - Part A* **72,** 91–97 (2005).

170. Yañez-Soto, B., Liliensiek, S. J., Murphy, C. J. & Nealey, P. F. Biochemically and topographically engineered poly(ethylene glycol) diacrylate hydrogels with biomimetic characteristics as substrates for human corneal epithelial cells. *J. Biomed. Mater. Res. - Part A* **101 A,** 1184–1194 (2013).

171. Tan, F. *et al.* Fabrication of positively charged poly(ethylene glycol)-diacrylate hydrogel as a bone tissue engineering scaffold. *Biomed. Mater.* **7,** 55009 (2012).

172. Nguyen, Q. T., Hwang, Y., Chen, A. C., Varghese, S. & Sah, R. L. Cartilage-like mechanical properties of poly (ethylene glycol)-diacrylate hydrogels. *Biomaterials* **33,** 6682–6690 (2012).

173. Pan, J. & Chan, S. Y. Fabrication of a 3D hair follicle-like hydrogel by soft lithography. *… Res. Part A* **101,** 3159–69 (2013).

174. Fouassier, J.-P., Burr, D. & Wieder, F. Water-soluble photoinitiators: Primary processes in hydroxy alkyl phenyl ketones. *J. Polym. Sci. Part A Polym. Chem.* **29,** 1319–1327 (1991).

175. Bryant, S. J., Nuttelman, C. R. & Anseth, K. S. Cytocompatibility of UV and visible light photoinitiating systems on cultured NIH/3T3 fibroblasts in vitro. *J. Biomater. Sci. Polym. Ed.* **11,** 439–457 (2000).

176. Kappes, U. P., Luo, D., Potter, M., Schulmeister, K. & Rünger, T. M. Short- and long-wave UV light (UVB and UVA) induce similar mutations in human skin cells. *J. Invest. Dermatol.* **126,** 667–675 (2006).

177. Fairbanks, B. D., Schwartz, M. P., Bowman, C. N. & Anseth, K. S. Photoinitiated polymerization of PEG-diacrylate with lithium phenyl-2,4,6-trimethylbenzoylphosphinate: polymerization rate and cytocompatibility. *Biomaterials* **30,** 6702–6707 (2009).

178. Chemicals, C. S. & Segment, C. E. Ciba IRGACURE 2959 Ciba IRGACURE 2959. *Coating* 2–4 (2001).

179. Yanagawa, F., Sugiura, S. & Kanamori, T. Hydrogel microfabrication technology toward three dimensional tissue engineering. *Regen. Ther.* **3,** 45–57 (2016).

180. Zorlutuna, P. *et al.* Microfabricated biomaterials for engineering 3D tissues. *Adv. Mater.* **24,** 1782–1804 (2012).

181. Verhulsel, M. *et al.* A review of microfabrication and hydrogel engineering for micro-organs on chips. *Biomaterials* **35,** 1816–1832 (2014).

182. Leitão, D. C., Amaral, J. P., Cardoso, S. & Reig, C. in *Giant Magnetoresistance (GMR) Sensors: From Basis to State-of-the-Art Applications* 31–45 (Springer Berlin Heidelberg, 2013). doi:10.1007/978-3-642-37172-1_2

183. Sung, J. H., Yu, J., Luo, D., Shuler, M. L. & March, J. C. Microscale 3-D hydrogel scaffold for biomimetic gastrointestinal (GI) tract model. *Lab Chip* **11,** 389–392 (2011).

184. Xia, Y. N. & Whitesides, G. M. Soft lithography. *Annu. Rev. Mater. Sci.* **37,** 551–575 (1998).

185. Khademhosseini, A. *et al.* Molded polyethylene glycol microstructures for capturing cells within microfluidic channels. *Lab Chip* **4,** 425–430 (2004).

186. Afrimzon, E. *et al.* Hydrogel microstructure live-cell array for multiplexed analyses of cancer stem cells, tumor heterogeneity and differential drug response at single-element resolution. *Lab Chip* **16,** 1047–1062 (2016).

187. Occhetta, P. *et al.* Fabrication of 3D cell-laden hydrogel microstructures through photo-mold patterning. *Biofabrication* **5,** 35002 (2013).

188. Suh, K. Y., Seong, J., Khademhosseini, A., Laibinis, P. E. & Langer, R. A simple soft lithographic route to fabrication of poly(ethylene glycol) microstructures for protein and cell patterning. *Biomaterials* **25,** 557–563 (2004).

189. Rivest, C. *et al.* Microscale hydrogels for medicine and biology: synthesis, characteristics and applications. *J. Mech. Mater. Struct.* **2,** 1103–1119 (2007).

190. Yeh, J. *et al.* Micromolding of shape-controlled, harvestable cell-laden hydrogels. *Biomaterials* **27,** 5391–5398 (2006).

191. Jeong, H.-H., Lee, J.-H., Noh, Y.-M., Kim, Y.-G. & Lee, C.-S. Generation of uniform agarose microwells for cell patterning by micromolding in capillaries. *Macromol. Res.* **21,** 534–540 (2013).

192. Cuchiara, M. P., Gould, D. J., McHale, M. K., Dickinson, M. E. & West, J. L. Integration of self-assembled microvascular networks with microfabricated PEG-based hydrogels. *Adv. Funct. Mater.* **22,** 4511–4518 (2012).

193. Khademhosseini, A. *et al.* Micromolding of photocrosslinkable hyaluronic acid for cell encapsulation and entrapment. *J. Biomed. Mater. Res. - Part A* **79,** 522–532 (2006).

194. Tekin, H. *et al.* Responsive Microgrooves for the Formation of Harvestable Tissue Constructs. *Langmuir* **27,** 5671–5679 (2011).

195. Golden, A. P. & Tien, J. Fabrication of microfluidic hydrogels using molded gelatin as a sacrificial element. *Lab Chip* **7,** 720–725 (2007).

196. Khademhosseini, A. & Langer, R. Microengineered hydrogels for tissue engineering. *Biomaterials* **28,** 5087–5092 (2007).

197. Costello, C. M. *et al.* Synthetic small intestinal scaffolds for improved studies of intestinal differentiation. *Biotechnol. Bioeng.* **111,** 1222–1232 (2014).

198. Szymanski, J. M. & Feinberg, A. W. Fabrication of freestanding alginate microfibers and microstructures for tissue engineering applications. *Biofabrication* **6,** 24104 (2014).

199. Levato, R. *et al.* Biofabrication of tissue constructs by 3D bioprinting of cell-laden microcarriers. *Biofabrication* **6,** 35020 (2014).

200. Kolesky, D. B. *et al.* 3D bioprinting of vascularized, heterogeneous cell-laden tissue constructs. *Adv. Mater.* **26,** 3124–3130 (2014).

201. Wu, Z. *et al.* Bioprinting three-dimensional cell-laden tissue constructs with controllable degradation. *Sci. Rep.* **6,** 24474 (2016).

202. Malda, J. *et al.* 25th anniversary article: Engineering hydrogels for biofabrication. *Adv. Mater.* **25,** 5011–5028 (2013).

203. Gao, G., Yonezawa, T., Hubbell, K., Dai, G. & Cui, X. Inkjet-bioprinted acrylated peptides and PEG hydrogel with human mesenchymal stem cells promote robust bone and cartilage formation with minimal printhead clogging. *Biotechnol. J.* **10,** 1568–1577 (2015).

204. Skardal, A. *et al.* Photocrosslinkable Hyaluronan-Gelatin Hydrogels for Two-Step Bioprinting. *Tissue Eng. Part A* **16,** 2675–2685 (2010).

205. Duan, B., Hockaday, L. A., Kang, K. H. & Butcher, J. T. 3D Bioprinting of heterogeneous aortic valve conduits with alginate/gelatin hydrogels. *J. Biomed. Mater. Res. Part A* **101A,** 1255–1264 (2013).

206. Gudapati, H., Dey, M. & Ozbolat, I. A comprehensive review on droplet-based bioprinting: Past, present and future. *Biomaterials* **102,** 20–42 (2016).

207. Maher, P. S., Keatch, R. P., Donnelly, K., Mackay, R. E. & Paxton, J. Z. Construction of 3D biological matrices using rapid prototyping technology. *Rapid Prototyp. J.* **15,** 204–210 (2009).

208. Murphy, S. V & Atala, A. 3D bioprinting of tissues and organs. *Nat. Biotechnol.* **32,** 773–785 (2014).

209. Guillotin, B. *et al.* Laser assisted bioprinting of engineered tissue with high cell density and microscale organization. *Biomaterials* **31,** 7250–7256 (2010).

210. Koch, L. *et al.* Skin tissue generation by laser cell printing. *Biotechnol. Bioeng.* **109,** 1855–1863 (2012).

211. Yan, J., Huang, Y. & Chrisey, D. B. Laser-assisted printing of alginate long tubes and annular constructs. *Biofabrication* **5,** 15002 (2013).

212. Beebe, D. J., Mensing, G. a & Walker, G. M. Physics and applications of microfluidics in biology. *Annu. Rev. Biomed. Eng.* **4,** 261–286 (2002).

213. Wan, J. Microfluidic-Based Synthesis of Hydrogel Particles for Cell Microencapsulation and Cell-Based Drug Delivery. *Polymers (Basel).* **4,** 1084–1108 (2012).

214. Matsunaga, Y. T., Morimoto, Y. & Takeuchi, S. Molding Cell Beads for Rapid Construction of Macroscopic 3D Tissue Architecture. *Adv. Mater.* **23,** H90–H94 (2011).

215. Daniele, M. A., Boyd, D. A., Adams, A. A. & Ligler, F. S. Microfluidic Strategies for Design and Assembly of Microfibers and Nanofibers with Tissue Engineering and Regenerative Medicine Applications. *Adv. Healthc. Mater.* **4,** 11–28 (2015).

216. Hwang, C. M., Khademhosseini, A., Park, Y., Sun, K. & Lee, S. H. Microfluidic chip-based fabrication of PLGA microfiber scaffolds for tissue engineering. *Langmuir* **24,** 6845–6851 (2008).

217. Park, D. Y. *et al.* One-stop microfiber spinning and fabrication of a fibrous cell-encapsulated scaffold on a single microfluidic platform. *Biofabrication* **6,** 24108 (2014).

218. Chaubaroux, C. *et al.* Cell Alignment Driven by Mechanically Induced Collagen Fiber Alignment in Collagen/Alginate Coatings. *Tissue Eng. Part C. Methods* **0,** 1–8 (2015).

219. Tamayol, A. *et al.* Fiber-based tissue engineering: Progress, challenges, and opportunities. *Biotechnol. Adv.* **31,** 669–687 (2013).

220. Panda, P. *et al.* Stop-flow lithography to generate cell-laden microgel particles. *Lab Chip* **8,** 1056 (2008).

221. Skoog, S. A., Goering, P. L. & Narayan, R. J. Stereolithography in tissue engineering. *J. Mater. Sci. Mater. Med.* **25,** 845–856 (2014).

222. Zhang, A. P. *et al.* Rapid fabrication of complex 3D extracellular microenvironments by dynamic optical projection stereolithography. *Adv. Mater.* **24,** 4266–4270 (2012).

223. Arcaute, K., Mann, B. K. & Wicker, R. B. Stereolithography of three-dimensional bioactive poly(ethylene glycol) constructs with encapsulated cells. *Ann. Biomed. Eng.* **34,** 1429–1441 (2006).

224. Chan, V. *et al.* Three-dimensional photopatterning of hydrogels using stereolithography for long-term cell encapsulation. *Lab Chip* **10,** 2062 (2010).

225. Stratakis, E., Ranella, A., Farsari, M. & Fotakis, C. Laser-based micro/nanoengineering for biological applications. *Progress in Quantum Electronics* **33,** 127–163 (2009).

226. Ciuciu, A. I. & Cywiński, P. J. Two-photon polymerization of hydrogels – versatile solutions to fabricate well-defined 3D structures. *RSC Adv.* **4,** 45504–45516 (2014).

227. Martens, P., Holland, T. & Anseth, K. S. Synthesis and characterization of degradable hydrogels formed from acrylate modified poly(vinyl alcohol) macromers. *Polymer (Guildf).* **43,** 6093–6100 (2002).

228. Rosales, A. M. & Anseth, K. S. The design of reversible hydrogels to capture extracellular matrix dynamics. *Nat. Publ. Gr.* **1,** 1–16 (2016).

229. Lewis, K. J. R. & Anseth, K. S. Hydrogel scaffolds to study cell biology in four dimensions. *MRS Bull* **38,** 260–268 (2013).

230. Koskela, J. Light-induced biomaterial microfabrication for advanced cell culturing–a comparative study. 103 (2010).

231. Ziaie, B. Hard and soft micromachining for BioMEMS: review of techniques and examples of applications in microfluidics and drug delivery. *Adv. Drug Deliv. Rev.* **56,** 145–172 (2004).

232. Voelkel, R. *et al.* Advanced mask aligner lithography: new illumination system. *Opt. Express* **18,** 20968–78 (2010).

233. Hahn, M. S. *et al.* Photolithographic patterning of polyethylene glycol hydrogels. *Biomaterials* **27,** 2519–2524 (2006).

234. Mazzoccoli, J. P., Feke, D. L., Baskaran, H. & Pintauro, P. N. Mechanical and cell viability properties of crosslinked low- And high-molecular weight poly(ethylene glycol) diacrylate blends. *J. Biomed. Mater. Res. - Part A* **93,** 558–566 (2010).

235. Cuchiara, M. P., Allen, A. C. B., Chen, T. M., Miller, J. S. & West, J. L. Multilayer microfluidic PEGDA hydrogels. *Biomaterials* **31,** 5491–5497 (2010).

236. Cha, C., Jeong, J. H., Shim, J. & Kong, H. Tuning the dependency between stiffness and permeability of a cell encapsulating hydrogel with hydrophilic pendant chains. *Acta Biomater.* **7,** 3719–3728 (2011).

237. Bernard, A. B., Lin, C.-C., Anseth, K. S., Ph, D. & Anseth, K. S. A Microwell Cell Culture Platform for the Aggregation of Pancreatic β-Cells. *Tissue Eng. Part C Methods* **18,** 583–592 (2012).

238. CHU, C. Engineering Matrix Properties for Stem Cell Culture and Gene Delivery. 107 (2012).

239. Guo, Q. *et al.* Light activated cell migration in synthetic extracellular matrices. *Biomaterials* **33,** 8040–8046 (2012).

240. McCall, J. D. & Anseth, K. S. Thiol-ene photopolymerizations provide a facile method to encapsulate proteins and maintain their bioactivity. *Biomacromolecules* **13,** 2410–2417 (2012).

241. Miller, J. S. *et al.* Rapid casting of patterned vascular networks for perfusable engineered three-dimensional tissues. *Nat. Mater.* **11,** 768–774 (2012).

242. Ross, A. E., Tang, M. Y. & Gemeinhart, R. a. Effects of Molecular Weight and Loading on Matrix Metalloproteinase-2 Mediated Release from Poly(Ethylene Glycol) Diacrylate Hydrogels. *AAPS J.* **14,** 482–490 (2012).

243. Nii, M. *et al.* The effects of interactive mechanical and biochemical niche signaling on osteogenic differentiation of adipose-derived stem cells using combinatorial hydrogels. *Acta Biomater.* **9,** 5475–5483 (2013).

244. Lin, L., Marchant, R. E., Zhu, J. & Kottke-Marchant, K. Extracellular matrix-mimetic poly(ethylene glycol) hydrogels engineered to regulate smooth muscle cell proliferation in 3-D. *Acta Biomater.* **10,** 5106–5115 (2014).

245. Bertassoni, L. E. *et al.* Hydrogel bioprinted microchannel networks for vascularization of tissue engineering constructs. *Lab Chip* **14,** 2202–11 (2014).

246. Kwag, H. R. *et al.* A Self-Folding Hydrogel In Vitro Model for Ductal Carcinoma. *Tissue Eng. Part C. Methods* **22,** 398–407 (2016).

247. Revzin, A. *et al.* Fabrication of Poly(ethylene glycol) Hydrogel Microstructures Using Photolithography. *Langmuir* **17,** 5440–5447 (2001).

248. Leach, J. B., Bivens, K. A., Patrick, C. W. & Schmidt, C. E. Photocrosslinked hyaluronic acid hydrogels: Natural, biodegradable tissue engineering scaffolds. *Biotechnol. Bioeng.* **82,** 578–589 (2003).

249. Hutson, C. B. *et al.* Synthesis and characterization of tunable poly(ethylene glycol): gelatin methacrylate composite hydrogels. *Tissue Eng. Part A* **17,** 1713–23 (2011).

250. Bencherif, S. A. *et al.* Influence of the degree of methacrylation on hyaluronic acid hydrogels properties. *Biomaterials* **29,** 1739–1749 (2008).

251. Prado, S. S., Weaver, J. M. & Love, B. J. Gelation of photopolymerized hyaluronic acid grafted with glycidyl methacrylate. *Mater. Sci. Eng. C* **31,** 1767–1771 (2011).

252. Burdick, J. A. & Prestwich, G. D. Hyaluronic acid hydrogels for biomedical applications. *Adv. Mater.* **23,** 41–56 (2011).

253. Kim, P., Jeong, H. E., Khademhosseini, A. & Suh, K. Y. Fabrication of non-biofouling polyethylene glycol micro- and nanochannels by ultraviolet-assisted irreversible sealing. *Lab Chip* **6,** 1432 (2006).

254. Weber, L. M., He, J., Bradley, B., Haskins, K. & Anseth, K. S. PEG-based hydrogels as an in vitro encapsulation platform for testing controlled β-cell microenvironments. *Acta Biomater.* **2,** 1–8 (2006).

255. Benton, J. A., DeForest, C. A., Vivekanandan, V. & Anseth, K. S. Photocrosslinking of Gelatin Macromers to Synthesize Porous Hydrogels That Promote Valvular Interstitial Cell Function. *Tissue Eng. Part A* **15,** 3221–3230 (2009).

256. Sahoo, S., Chung, C., Khetan, S. & Burdick, J. A. Hydrolytically Degradable Hyaluronic Acid Hydrogels with Controlled Temporal Structures. *Biomacromolecules* **9,** 1088–1092 (2008).

257. Nichol, J. W. *et al.* Cell-laden microengineered gelatin methacrylate hydrogels. *Biomaterials* **31,** 5536–5544 (2010).

258. Aubin, H. *et al.* Directed 3D cell alignment and elongation in microengineered hydrogels. *Biomaterials* **31,** 6941–6951 (2010).

259. Gumuscu, B., Bomer, J. G., Van Den Berg, A. & Eijkel, J. C. T. Photopatterning of Hydrogel Microarrays in Closed Microchips. *Biomacromolecules* **16,** 3802–3810 (2015).

260. Goubko, C. A., Majumdar, S., Basak, A. & Cao, X. Hydrogel cell patterning incorporating photocaged RGDS peptides. *Biomed. Microdevices* **12,** 555–568 (2010).

261. DeForest, C. A. & Anseth, K. S. Photoreversible patterning of biomolecules within click-based hydrogels. *Angew. Chemie - Int. Ed.* **51,** 1816–1819 (2012).

262. Tsang, V. L. *et al.* Fabrication of 3D hepatic tissues by additive photopatterning of cellular hydrogels. *FASEB J.* **21,** 790–801 (2007).

263. Dang, T.-D., Kim, Y. H., Choi, J. H. & Kim, G.-M. A novel simple preparation method of a hydrogel mold for PDMS micro-fluidic device fabrication. *J. Micromechanics Microengineering* **22,** 15017 (2012).

264. Dardano, P. *et al.* A photolithographic approach to polymeric microneedles array fabrication. *Materials (Basel).* **8,** 8661–8673 (2015).

265. Shim, T. S., Yang, S.-M. & Kim, S.-H. Dynamic designing of microstructures by chemical gradient-mediated growth. *Nat. Commun.* **6,** 6584 (2015).

266. Sato, T. *et al.* Long-term expansion of epithelial organoids from human colon, adenoma, adenocarcinoma, and Barrett's epithelium. *Gastroenterology* **141,** 1762–1772 (2011).

267. Ootani, A. *et al.* Sustained in vitro intestinal epithelial culture within a Wnt-dependent stem cell niche. *Nat. Med.* **15,** 701–706 (2009).

268. Spence, J. R. *et al.* Directed differentiation of human pluripotent stem cells into intestinal tissue in vitro. *Nature* **470,** 105–109 (2011).

269. Kim, H. J., Huh, D., Hamilton, G. & Ingber, D. E. Human gut-on-a-chip inhabited by microbial flora that experiences intestinal peristalsis-like motions and flow. *Lab Chip* **12,** 2165–74 (2012).

270. Buske, P. *et al.* On the biomechanics of stem cell niche formation in the gut - modelling growing organoids. *FEBS J.* **279,** 3475–3487 (2012).

271. Kimura, H., Yamamoto, T., Sakai, H., Sakai, Y. & Fujii, T. An integrated microfluidic system for long-term perfusion culture and on-line monitoring of intestinal tissue models. *Lab Chip* **8,** 741–6 (2008).

272. Kim, H. J. & Ingber, D. E. Gut-on-a-Chip microenvironment induces human intestinal cells to undergo villus differentiation. *Integr. Biol. (Camb).* **5,** 1130–40 (2013).

273. Ramadan, Q. *et al.* NutriChip: nutrition analysis meets microfluidics. *Lab Chip* **13,** 196–203 (2013).

274. Esch, M. B., Ueno, H., Applegate, D. R. & Shuler, M. L. Modular, pumpless body-on-a-chip platform for the co-culture of GI tract epithelium and 3D primary liver tissue. *Lab Chip* **16,** 2719–29 (2016).

275. Sin, A. *et al.* The Design and Fabrication of Three-Chamber Microscale Cell Culture Analog Devices with Integrated Dissolved Oxygen Sensors. *Biotechnol. Prog.* **20,** 338–345 (2004).

276. Mahler, G. J., Esch, M. B., Glahn, R. P. & Shuler, M. L. Characterization of a gastrointestinal tract microscale cell culture analog used to predict drug toxicity. *Biotechnol. Bioeng.* **104,** 193–205 (2009).

277. Esch, M. B. *et al.* On chip porous polymer membranes for integration of gastrointestinal tract epithelium with microfluidic 'body-on-a-chip' devices. *Biomed. Microdevices* **14,** 895–

906 (2012).

278. Yu, J., Carrier, R. L., March, J. C. & Griffith, L. G. Three dimensional human small intestine models for ADME-Tox studies. *Drug Discov. Today* **19,** 1587–1594 (2014).

279. Wang, Y. *et al.* A microengineered collagen scaffold for generating a polarized crypt-villus architecture of human small intestinal epithelium. *Biomaterials* **128,** 44–55 (2017).

280. Wang, L., Murthy, S. K., Barabino, G. A. & Carrier, R. L. Synergic effects of crypt-like topography and ECM proteins on intestinal cell behavior in collagen based membranes. *Biomaterials* **31,** 7586–7598 (2010).

281. Wang, L., Murthy, S. K., Fowle, W. H., Barabino, G. A. & Carrier, R. L. Influence of micro-well biomimetic topography on intestinal epithelial Caco-2 cell phenotype. *Biomaterials* **30,** 6825–6834 (2009).

282. Nalle, S. C. & Turner, J. R. Endothelial and epithelial barriers in graft-versus-host disease. *Adv. Exp. Med. Biol.* **763,** 105–131 (2012).

283. Lee, M., Dunn, J. C. Y. Y. & Wu, B. M. Scaffold fabrication by indirect three-dimensional printing. *Biomaterials* **26,** 4281–4289 (2005).

284. Salomon, J. *et al.* Contractile forces at tricellular contacts modulate epithelial organization and monolayer integrity. *Nat. Commun.* **8,** 13998 (2017).

285. Yang, W. C. *et al.* Engineering a biomimetic villus array for in vitro three-dimensional culture of intestinal epithelial cells. *J. Microelectromechanical Syst.* **21,** 1418–1425 (2012).

286. Yu, J., Peng, S., Luo, D. & March, J. C. In vitro 3D human small intestinal villous model for drug permeability determination. *Biotechnol. Bioeng.* **109,** 2173–2178 (2012).

287. Kim, S. H. *et al.* Three-dimensional intestinal villi epithelium enhances protection of human intestinal cells from bacterial infection by inducing mucin expression. *Integr. Biol. (Camb).* **6,** 1122–31 (2014).

288. Costello, C. M. *et al.* 3-D intestinal scaffolds for evaluating the therapeutic potential of probiotics. *Mol. Pharm.* **11,** 2030–2039 (2014).

289. Shaffiey, S., Jia, H., Keane, T. & Costello, C. Intestinal stem cell growth and differentiation on a tubular scaffold with evaluation in small and large animals. *Regenerative* **11,** 45–61 (2016).

290. Deng, X., Zhang, G., Shen, C., Yin, J. & Meng, Q. Hollow fiber culture accelerates differentiation of Caco-2 cells. *Appl. Microbiol. Biotechnol.* **97,** 6943–6955 (2013).

291. Chen, Y. *et al.* Robust bioengineered 3D functional human intestinal epithelium. *Sci. Rep.* **5,** 13708 (2015).

292. Pfluger, C. A., McMahon, B. J., Carrier, R. L. & Burkey, D. D. Precise, Biomimetic Replication of the Multi-Scale Structure of Intestinal Basement Membrane using Chemical Vapor Deposition. *Tissue Eng. Part A* **19,** 120926220547002 (2012).

293. Koppes, A. N. *et al.* Complex, multi-scale small intestinal topography replicated in cellular growth substrates fabricated via chemical vapor deposition of Parylene C. *Biofabrication* **8,** 35011 (2016).

294. Insa, C., Martinez, E. & Altay, G. Characterization of the physicochemical properties of Poly (ethylene glycol) diacrylate (PEGDA) hydrogels. (2015).

295. Beamish, J. A., Zhu, J., Kottke-Marchant, K. & Marchant, R. E. The effects of monoacrylated poly(ethylene glycol) on the properties of poly(ethylene glycol) diacrylate hydrogels used for tissue engineering. *J. Biomed. Mater. Res. - Part A* **92,** 441–450 (2010).

296. Arc, S., Hbo, L. & Microlithography, F. O. R. M Ercury Short Arc Lamps Hbo ® for Microlithography. *Quality* (2000).

297. Hermanson, G. T. *Bioconjugate Techniques*. *Bioconjugate Techniques* (2013). doi:10.1016/B978-0-12-382239-0.00024-8

298. Poellmann, M. J., Barton, K. L., Mishra, S. & Johnson, A. J. W. Patterned Hydrogel Substrates

for Cell Culture with Electrohydrodynamic Jet Printing. *Macromol. Biosci.* **11,** 1164–1168 (2011).

299. Nakajima, N. & Ikada, Y. Mechanism of amide formation by carbodiimide for bioconjugation in aqueous media. *Bioconjug. Chem.* **6,** 123–130 (1995).

300. Poellmann, M. J. & Johnson, A. J. W. Characterizing and patterning polyacrylamide substrates functionalized with n-hydroxysuccinimide. *Cell. Mol. Bioeng.* **6,** 299–309 (2013).

301. Audi, S. H. *et al.* Pulmonary reduction of an intravascular redox polymer. *Am J Physiol Lung Cell Mol Physiol* **280,** L1290-9 (2001).

302. Fonseca, K. B. *et al.* Injectable MMP-sensitive alginate hydrogels as hMSC delivery systems. *Biomacromolecules* **15,** 380–390 (2014).

303. Wang, H., Cai, L., Paul, A., Enejder, A. & Heilshorn, S. C. Hybrid elastin-like polypeptide-polyethylene glycol (ELP-PEG) hydrogels with improved transparency and independent control of matrix mechanics and cell ligand density. *Biomacromolecules* **15,** 3421–3428 (2014).

304. Natoli, M., Leoni, B. D., D'Agnano, I., Zucco, F. & Felsani, A. Good Caco-2 cell culture practices. *Toxicol. Vitr.* **26,** 1243–1246 (2012).

305. Bretscher, a & Weber, K. Villin: the major microfilament-associated protein of the intestinal microvillus. *Proc. Natl. Acad. Sci. USA* **76,** 2321–2325 (1979).

306. Versaevel, M., Grevesse, T. & Gabriele, S. Spatial coordination between cell and nuclear shape within micropatterned endothelial cells. *Nat. Commun.* **3,** 671 (2012).

307. No Title. Available at: http://medcell.med.yale.edu/systems_cell_biology/gi_tract_lab.php.

308. Yeste, J., Illa, X., Guimerà, A. & Villa, R. A novel strategy to monitor microfluidic in-vitro blood-brain barrier models using impedance spectroscopy. in (ed. van den Driesche, S.) 95180N (2015). doi:10.1117/12.2180567

309. Lucas-Garrote, B., Morais, S. & Maquieira, Á. Dual signal amplification for highly sensitive hybridization microassays on chemically activated surfaces. *Sensors Actuators B Chem.* (2016). doi:10.1016/j.snb.2016.10.109

310. Guimerà, A., Gabriel, G., Parramon, D., Calderón, E. & Villa, R. Portable 4 wire bioimpedance meter with bluetooth link. in *IFMBE Proceedings* **25,** 868–871 (2009).

311. Ando, Y., Mizutani, K. & Wakatsuki, N. Electrical impedance analysis of potato tissues during drying. *J. Food Eng.* **121,** 24–31 (2014).

312. Hwang, C. M. *et al.* Benchtop fabrication of PDMS microstructures by an unconventional photolithographic method. *Biofabrication* **2,** 45001 (2010).

313. Choi, M. *et al.* Light-guiding hydrogels for cell-based sensing and optogenetic synthesis in vivo. *Nat. Photonics* **7,** 987–994 (2013).

314. Beuermann, S., Paquet, D. A., McMinn, J. H. & Hutchinson, R. A. Determination of Free-Radical Propagation Rate Coefficients of Butyl, 2-Ethylhexyl, and Dodecyl Acrylates by Pulsed-Laser Polymerization. *Macromolecules* **29,** 4206–4215 (1996).

315. Kızılel, S., Pérez-Luna, V. H. & Teymour, F. Mathematical Model for Surface-Initiated Photopolymerization of Poly(ethylene glycol) Diacrylate. *Macromol. Theory Simulations* **15,** 686–700 (2006).

316. Dendukuri, D. *et al.* Modeling of Oxygen-Inhibited Free Radical Photopolymerization in a PDMS Microfluidic Device Modeling of Oxygen-Inhibited Free Radical Photopolymerization in a PDMS Microfluidic Device. *Macromolecules* **41,** 8547–8556 (2008).

317. Lalevée, J., El-Roz, M., Allonas, X. & Fouassier, J. P. Controlled photopolymerization reactions: The reactivity of new photoiniferters. *J. Polym. Sci. Part A Polym. Chem.* **45,** 2436–2442 (2007).

318. Liu, M., Li, M.-D., Xue, J. & Phillips, D. L. Time-Resolved Spectroscopic and Density Functional Theory Study of the Photochemistry of Irgacure-2959 in an Aqueous Solution. *J.*

Phys. Chem. A **118,** 8701–8707 (2014).

319. Chan, V. *et al.* Multi-material bio-fabrication of hydrogel cantilevers and actuators with stereolithography. *Lab Chip* **12,** 88–98 (2012).

320. The NIST Reference on Constants, Units, and Uncertainty. Available at: http://physics.nist.gov/cuu/index.html. (Accessed: 5th March 2017)

321. Lee, J. H., Prud'homme, R. K. & Aksay, I. a. Cure depth in photopolymerization: Experiments and theory. *J. Mater. Res.* **16,** 3536–3544 (2001).

322. Xiao, Y., He, L. & Che, J. An effective approach for the fabrication of reinforced composite hydrogel engineered with SWNTs, polypyrrole and PEGDA hydrogel. *J. Mater. Chem.* **22,** 8076 (2012).

323. Browning, M. B. & Cosgriff-Hernandez, E. Development of a Biostable Replacement for PEGDA Hydrogels. *Biomacromolecules* **13,** 779–786 (2012).

324. Bäckström, S. *et al.* Tailoring Properties of Biocompatible PEG-DMA Hydrogels with UV Light. *Mater. Sci. Appl.* **3,** 425–431 (2012).

325. Zhu, J., Tang, C., Kottke-Marchant, K. & Marchant, R. E. Design and Synthesis of Biomimetic Hydrogel Scaffolds with Controlled Organization of Cyclic RGD Peptides. *Bioconjug. Chem.* **20,** 333–339 (2009).

326. Williams, C. G., Malik, A. N., Kim, T. K., Manson, P. N. & Elisseeff, J. H. Variable cytocompatibility of six cell lines with photoinitiators used for polymerizing hydrogels and cell encapsulation. *Biomaterials* **26,** 1211–1218 (2005).

327. Sabnis, A., Rahimi, M., Chapman, C. & Nguyen, K. T. Cytocompatibility studies of an in situ photopolymerized thermoresponsive hydrogel nanoparticle system using human aortic smooth muscle cells. *J. Biomed. Mater. Res. Part A* **91A,** 52–59 (2009).

328. Arcaute, K. *et al.* Three-dimensional PEG hydrogel construct fabrication using stereolithography. *Mater. Res. Soc. Symp. Proc.* (2005).

329. Decker, C. & Jenkins, A. D. Kinetic Approach of O2 Inhibition in Ultraviolet and Laser Induced Polymerizations. *Macromolecules* 1241–1244 (1985). doi:10.1016/j.ab.2011.10.035

330. Ligon, S. C., Husár, B., Wutzel, H., Holman, R. & Liska, R. Strategies to Reduce Oxygen Inhibition in Photoinduced Polymerization. *Chem. Rev.* **114,** 557–589 (2014).

331. No Title. Available at: http://www.molecularhydrogenfoundation.org/concentration-and-solubility-of-h2/.

332. Lin, H. & Freeman, B. D. Gas Permeation and Diffusion in Cross-Linked Poly(ethylene glycol diacrylate). doi:10.1021/ma051686o

333. Krutkramelis, K., Xia, B. & Oakey, J. Monodisperse Polyethylene Glycol Diacrylate Hydrogel Microsphere Formation by Oxygen-Controlled Photopolymerization in a Microfluidic Device. *Lab Chip* **16,** 1457–1465 (2016).

334. Jamnongwong, M., Loubiere, K., Dietrich, N. & Hébrard, G. Experimental study of oxygen diffusion coefficients in clean water containing salt, glucose or surfactant: Consequences on the liquid-side mass transfer coefficients. *Chem. Eng. J.* **165,** 758–768 (2010).

335. Yasar, O. & Inceoglu, S. Compressive Evaluation of Polyethylene (Glycol) Diacrylate (PEGDA) for Scaffold Fabrication. in *Volume 2: Materials; Biomanufacturing; Properties, Applications and Systems; Sustainable Manufacturing* V002T03A004 (ASME, 2016). doi:10.1115/MSEC2016-8619

336. Jariwala, A. S. *et al.* Modeling effects of oxygen inhibition in mask-based stereolithography. *Rapid Prototyp. J.* **17,** 168–175 (2011).

337. Li, Y. *et al.* Fabrication of High-Aspect-Ratio 3D Hydrogel Microstructures Using Optically Induced Electrokinetics. *Micromachines* **7,** 65 (2016).

338. Bae, M., Divan, R., Suthar, K. J., Mancini, D. C. & Gemeinhart, R. a. Fabrication of

Poly(ethylene glycol) Hydrogel Structures for Pharmaceutical Applications using Electron beam and Optical Lithography. *J. Vac. Sci. Technol. B. Microelectron. Nanometer Struct. Process. Meas. Phenom.* **28,** C6P24-C6P29 (2010).

339. Born, M. & Wolf, E. Principles of optics. *Principles of Optics Electromagnetic Theory of Propagation INterference and Diffraction of Light 2nd edition by Max Born Emil Wolf New York NY Pergamon Press 1964* 1–952 (1999). doi:10.1016/S0030-3992(00)00061-X

340. Chuang, Y. J., Tseng, F. G. & Lin, W. K. Reduction of diffraction effect of UV exposure on SU-8 negative thick photoresist by air gap elimination. *Microsyst. Technol.* **8,** 308–313 (2002).

341. Zhang, J., Chan-Park, M. B., Miao, J. & Sun, T. T. Reduction of diffraction effect for fabrication of very high aspect ratio microchannels in SU-8 over large area by soft cushion technology. *Microsystem Technologies* **11,** 519–525 (2005).

342. Guvendiren, M., Burdick, J. A. & Yang, S. Solvent induced transition from wrinkles to creases in thin film gels with depth-wise crosslinking gradients. *Soft Matter* **6,** 5795 (2010).

343. Kim, H. & Lee, S. J. Stomata-Inspired Membrane Produced Through Photopolymerization Patterning. *Adv. Funct. Mater.* **25,** 4496–4505 (2015).

344. Viswanathan, P. *et al.* Mimicking the topography of the epidermal-dermal interface with elastomer substrates. *Integr. Biol. (Camb).* **8,** 21–9 (2016).

345. Leewis, C. M., de Jong, A. M., van IJzendoorn, L. J. & Broer, D. J. Simulations with a dynamic reaction–diffusion model of the polymer grating preparation by patterned ultraviolet illumination. *J. Appl. Phys.* **95,** 8352–8356 (2004).

346. Vergote, K., Deene, Y. De, Bussche, E. Vanden & Wagter, C. De. On the relation between the spatial dose integrity and the temporal instability of polymer gel dosimeters. *Phys. Med. Biol.* **49,** 4507–4522 (2004).

347. Fuxman, A. M., McAuley, K. B. & Schreiner, L. J. Modelling of polyacrylamide gel dosimeters with spatially non-uniform radiation dose distributions. *Chem. Eng. Sci.* **60,** 1277–1293 (2005).

348. Orakdogen, N. & Okay, O. Correlation between crosslinking efficiency and spatial inhomogeneity in poly(acrylamide) hydrogels. *Polym. Bull.* **57,** 631–641 (2006).

349. Sánchez, C. *et al.* Photoembossing of periodic relief structures using polymerization-induced diffusion: A combinatorial study. *Adv. Mater.* **17,** 2567–2571 (2005).

350. Saez, A., Ghibaudo, M., Buguin, A., Silberzan, P. & Ladoux, B. Rigidity-driven growth and migration of epithelial cells on microstructured anisotropic substrates. *Proc. Natl. Acad. Sci.* **104,** 8281–8286 (2007).

351. Pan, J. *et al.* Fabrication of a 3D hair follicle-like hydrogel by soft lithography. *J. Biomed. Mater. Res. - Part A* **101,** 3159–3169 (2013).

352. Lee, A. G., Arena, C. P., Beebe, D. J. & Palecek, S. P. Development of Macroporous Poly(ethylene glycol) Hydrogel Arrays within Microfluidic Channels. *Biomacromolecules* **11,** 3316–3324 (2010).

353. Lee, T. Y., Guymon, C. A., J??nsson, E. S. & Hoyle, C. E. The effect of monomer structure on oxygen inhibition of (meth)acrylates photopolymerization. *Polymer (Guildf).* **45,** 6155–6162 (2004).

354. Xie, J., Liu, X., Liang, J. & Luo, Y. Swelling properties of superabsorbent poly(acrylic acid- co -acrylamide) with different crosslinkers. *J. Appl. Polym. Sci.* **112,** 602–608 (2009).

355. Wu, Y., Liang, J., Horkay, F. & Libera, M. Antimicrobial loading into and release from poly(ethylene glycol)/poly(acrylic acid) semi-interpenetrating hydrogels. *J. Polym. Sci. Part B Polym. Phys.* **54,** 64–72 (2016).

356. Es-Haghi, H., Bouhendi, H., Marandi, G. B., Zohurian-Mehr, M. J. & Kabiri, K. Rheological Properties of Microgel Prepared with Long-Chain Crosslinkers by a Precipitation Polymerization Method. *J. Macromol. Sci. Part B* **51,** 880–896 (2012).

357. Lally, S., Liu, R., Supasuteekul, C., Saunders, B. R. & Freemont, T. Using osmotic deswelling

of microgel particles to control the mechanical properties of pH-responsive hydrogel composites. *J. Mater. Chem.* **21,** 17719 (2011).

358. Chen, B. *et al.* Highly stretchable and transparent ionogels as nonvolatile conductors for dielectric elastomer transducers. *ACS Appl. Mater. Interfaces* **6,** 7840–7845 (2014).

359. Tang, Q., Sun, X., Li, Q., Wu, J. & Lin, J. Synthesis of polyacrylate/polyethylene glycol interpenetrating network hydrogel and its sorption of heavy-metal ions. *Sci. Technol. Adv. Mater.* **10,** 15002 (2009).

360. Liao, D. *et al.* The effect of epidermal growth factor on the incremental Young's moduli in the rat small intestine. *Med. Eng. Phys.* **25,** 413–418 (2003).

361. Huang, G. *et al.* Engineering three-dimensional cell mechanical microenvironment with hydrogels. *Biofabrication* **4,** 42001 (2012).

362. Beer, M. V. Correlation of ligand density with cell behavior on bioactive hydrogel layers. (2011).

363. Wang, W.-H., Dong, J.-L., Baker, G. L. & Bruening, M. L. Bifunctional polymer brushes for low-bias enrichment of mono- and multi-phosphorylated peptides prior to mass spectrometry analysis. *Analyst* **136,** 3595 (2011).

364. de Campos Vidal, B. & Mello, M. L. S. Collagen type I amide I band infrared spectroscopy. *Micron* **42,** 283–289 (2011).

365. Drumheller, P. D. & Hubbell, J. A. Polymer networks with grafted cell adhesion peptides for highly biospecific cell adhesive substrates. *Anal. Biochem.* **222,** 380–8 (1994).

366. Lee, W., Lee, T. G. & Koh, W. G. Grafting of Poly(acrylic acid) on the Poly(ethylene glycol) Hydrogel Using Surface-initiated Photopolymerization for Covalent Immobilization of Collagen. *J. Ind. Eng. Chem.* **13,** 1195–1200 (2007).

367. Matsumoto, Y., Araki, T., Endo, T., Sueyoshi, K. & Hisamoto, H. Hydrogel Based 2D-Photonic Crystal Including Acrylic Acid for Biosensing Apprication. 2038–2040 (2014).

368. Kennedy, R. *et al.* In situ formed hybrid hydrogels from PEG based multifunctional hyperbranched copolymers: a RAFT approach. *Polym. Chem.* **5,** 1838 (2014).

369. Yeung, T. *et al.* Effects of substrate stiffness on cell morphology, cytoskeletal structure, and adhesion. *Cell Motil. Cytoskeleton* **60,** 24–34 (2005).

370. Kidoaki, S. & Sakashita, H. Rectified Cell Migration on Saw-Like Micro-Elastically Patterned Hydrogels with Asymmetric Gradient Ratchet Teeth. *PLoS One* **8,** e78067 (2013).

371. Moon, J. J., Hahn, M. S., Kim, I., Nsiah, B. A. & West, J. L. Micropatterning of Poly(Ethylene Glycol) Diacrylate Hydrogels with Biomolecules to Regulate and Guide Endothelial Morphogenesis. *Tissue Eng. Part A* **15,** 579–585 (2009).

372. Lilly, J. L., Romero, G., Xu, W., Shin, H. Y. & Berron, B. J. Characterization of molecular transport in ultrathin hydrogel coatings for cellular immunoprotection. *Biomacromolecules* **16,** 541–549 (2015).

373. Tomić, K., Veeman, W. S., Boerakker, M., Litvinov, V. M. & Dias, A. A. Lateral and rotational mobility of some drug molecules in a poly(ethylene glycol) diacrylate hydrogel and the effect of drug-cyclodextrin complexation. *J. Pharm. Sci.* **97,** 3245–3256 (2008).

374. Handorf, A. M., Zhou, Y., Halanski, M. A. & Li, W.-J. Tissue Stiffness Dictates Development, Homeostasis, and Disease Progression. *Organogenesis* **11,** 1–15 (2015).

375. Kuo, C.-H. R., Xian, J., Brenton, J. D., Franze, K. & Sivaniah, E. Complex Stiffness Gradient Substrates for Studying Mechanotactic Cell Migration. *Adv. Mater.* **24,** 6059–6064 (2012).

376. Hale, N. A., Yang, Y. & Rajagopalan, P. Cell Migration at the Interface of a Dual Chemical-Mechanical Gradient. *ACS Appl. Mater. Interfaces* **2,** 2317–2324 (2010).

377. Rothen-Rutishauser, B., Krämer, S. D., Braun, A., Günthert, M. & Wunderli-Allenspach, H. MDCK cell cultures as an epithelial in vitro model: cytoskeleton and tight junctions as indicators for the definition of age-related stages by confocal microscopy. *Pharm. Res.* **15,**

964–71 (1998).

378. Dukes, J. D., Whitley, P. & Chalmers, A. D. The MDCK variety pack: choosing the right strain. (2011). doi:10.1186/1471-2121-12-43

379. Kim, J.-H. & Asthagiri, A. R. Matrix stiffening sensitizes epithelial cells to EGF and enables the loss of contact inhibition of proliferation. *J. Cell Sci.* **124,** 1280–1287 (2011).

380. Imai, M., Furusawa, K., Mizutani, T., Kawabata, K. & Haga, H. Three-dimensional morphogenesis of MDCK cells induced by cellular contractile forces on a viscous substrate. *Sci. Rep.* **5,** 14208 (2015).

381. Leight, J. L., Wozniak, M. a., Chen, S., Lynch, M. L. & Chen, C. S. Matrix rigidity regulates a switch between TGF- 1-induced apoptosis and epithelial-mesenchymal transition. *Mol. Biol. Cell* **23,** 781–791 (2012).

382. Jin, X. *et al.* Comparison of MDCK-MDR1 and Caco-2 cell based permeability assays for anti-malarial drug screening and drug investigations. *J. Pharmacol. Toxicol. Methods* **70,** 188–194 (2014).

383. Hajjarian, Z. *et al.* Laser Speckle Rheology for evaluating the viscoelastic properties of hydrogel scaffolds. *Sci. Rep.* **6,** 37949 (2016).

384. Shen, Y., Hou, Y., Yao, S., Huang, P. & Yobas, L. In Vitro Epithelial Organoid Generation Induced by Substrate Nanotopography. *Sci. Rep.* **5,** 9293 (2015).

385. Cerchiari, A. *et al.* Formation of Spatially and Geometrically Controlled Three-Dimensional Tissues in Soft Gels by Sacrificial Micromolding. *Tissue Eng. Part C Methods* **21,** 541–547 (2015).

386. Millán, J. *et al.* Adherens junctions connect stress fibres between adjacent endothelial cells. *BMC Biol.* **8,** 11 (2010).

387. Chen, Y. *et al.* Engineering a biomimetic villus array for in vitro 3-dimensional culture of intestinal epithelial cells. in *2012 7th IEEE International Conference on Nano/Micro Engineered and Molecular Systems (NEMS)* 230–233 (IEEE, 2012). doi:10.1109/NEMS.2012.6196763

388. Lovett, D. B., Shekhar, N., Nickerson, J. A., Roux, K. J. & Lele, T. P. Modulation of Nuclear Shape by Substrate Rigidity. *Cell. Mol. Bioeng.* **6,** 230–238 (2013).

389. Roeder, R. *et al.* small-intestine submucosa (SIS), small-diameter vascular grafts. (1999).

390. DiMarco, R. L., Hunt, D. R., Dewi, R. E. & Heilshorn, S. C. Improvement of paracellular transport in the Caco-2 drug screening model using protein-engineered substrates. *Biomaterials* **129,** 152–162 (2017).

391. Yeste, J. *et al.* Geometric correction factor for transepithelial electrical resistance measurements in transwell and microfluidic cell cultures. *J. Phys. D. Appl. Phys.* **49,** 375401 (2016).

392. Illa, X. *et al.* A novel modular bioreactor to in Vitro study the hepatic sinusoid. *PLoS One* **9,** 1–5 (2014).

393. Schulzke, J. D., Bentzel, C. J., Schulzke, I., Riecken, E. O. & Fromm, M. Epithelial tight junction structure in the jejunum of children with acute and treated celiac sprue. *Pediatric research* **43,** 435–441 (1998).

394. Pageot, L. P. *et al.* Human cell models to study small intestinal functions: recapitulation of the crypt-villus axis. *Microsc. Res. Tech.* **49,** 394–406 (2000).

395. Fihn, B. M., Sjöqvist, a & Jodal, M. Permeability of the rat small intestinal epithelium along the villus-crypt axis: effects of glucose transport. *Gastroenterology* **119,** 1029–1036 (2000).

396. Beaulieu, J.-F. Differential expression of the VLA family of integrins along the crypt-villus axis in the human small intestine. *J. Cell Sci.* **102,** 427–36 (1992).

397. Lambolez, F. *et al.* Characterization of T cell differentiation in the murine gut. *J. Exp. Med.* **195,** 437–449 (2002).

398. MITSOMWANG, P., NAGASAWA, S., CHAIJIT, S., FUJIKURA, M. & MUTOH, Y. Effect of Underlay Stiffness on Cutting Profile of Polycarbonate Sheet during Wedge Indentation Process. *J. Adv. Mech. Des. Syst. Manuf.* **6,** 1168–1179 (2012).

399. Johnson, L. A. *et al.* Matrix stiffness corresponding to strictured bowel induces a fibrogenic response in human colonic fibroblasts. *Inflamm. Bowel Dis.* **19,** 891–903 (2013).

400. Linnankoski, J. *et al.* Paracellular porosity and pore size of the human intestinal epithelium in tissue and cell culture models. *J. Pharm. Sci.* **99,** 2166–2175 (2010).

401. Li, N. *et al.* Development of an improved three-dimensional in vitro intestinal mucosa model for drug absorption evaluation. *Tissue Eng. Part C. Methods* **19,** 708–19 (2013).

402. Fleisher, D. in (1999). doi:10.1201/9780203909478.pt2

403. Walter, E., Janich, S., Roessler, B. J., Hilfinger, J. M. & Amidon, G. L. HT29-MTX/Caco-2 Cocultures as an in Vitro Model for the Intestinal Epithelium: In Vitro–in Vivo Correlation with Permeability Data from Rats and Humans. *J. Pharm. Sci.* **85,** 1070–1076 (1996).

404. Ouasti, S. *et al.* Network connectivity, mechanical properties and cell adhesion for hyaluronic acid/PEG hydrogels. *Biomaterials* **32,** 6456–6470 (2011).

405. Chaudhuri, O. *et al.* Extracellular matrix stiffness and composition jointly regulate the induction of malignant phenotypes in mammary epithelium. *Nat. Mater.* **13,** 970–978 (2014).

406. Soofi, S. S., Last, J. A., Liliensiek, S. J., Nealey, P. F. & Murphy, C. J. The elastic modulus of Matrigel??? as determined by atomic force microscopy. *J. Struct. Biol.* **167,** 216–219 (2009).

407. Gaudet, C. *et al.* Influence of Type I Collagen Surface Density on Fibroblast Spreading, Motility, and Contractility. *Biophys. J.* **85,** 3329–3335 (2003).

408. Engler, A. *et al.* Substrate Compliance versus Ligand Density in Cell on Gel Responses. *Biophys. J.* **86,** 617–628 (2004).

409. Hagel, V., Haraszti, T. & Boehm, H. Diffusion and interaction in PEG-DA hydrogels. *Biointerphases* **8,** 32 (2013).

410. Hulse, W. L. & Forbes, R. T. A nanolitre method to determine the hydrodynamic radius of proteins and small molecules by Taylor dispersion analysis. *Int. J. Pharm.* **411,** 64–68 (2011).

411. Armstrong, J. K., Wenby, R. B., Meiselman, H. J. & Fisher, T. C. The Hydrodynamic Radii of Macromolecules and Their Effect on Red Blood Cell Aggregation. *Biophys. J.* **87,** 4259–4270 (2004).

412. Drury, J. L. & Mooney, D. J. Hydrogels for tissue engineering: Scaffold design variables and applications. *Biomaterials* **24,** 4337–4351 (2003).

413. DeForest, C. A. & Anseth, K. S. Cytocompatible click-based hydrogels with dynamically tunable properties through orthogonal photoconjugation and photocleavage reactions. *Nat. Chem.* **3,** 925–931 (2011).

414. Blaeser, A. *et al.* Biofabrication Under Fluorocarbon: A Novel Freeform Fabrication Technique to Generate High Aspect Ratio Tissue-Engineered Constructs. *Biores. Open Access* **2,** 374–384 (2013).

415. Altay, G. Engineering a Platform for the Basic Research of Migration and Differentiation of Intestinal Stem Cells. 1–7

416. Viswanathan, P. *et al.* Mimicking the topography of the epidermal–dermal interface with elastomer substrates. *Integr. Biol.* (2016). doi:10.1039/C5IB00238A

417. Lo, C.-M., Wang, H.-B., Dembo, M. & Wang, Y. Cell Movement Is Guided by the Rigidity of the Substrate. *Biophys. J.* **79,** 144–152 (2000).

418. Martín-Belmonte, F. *et al.* Cell-Polarity Dynamics Controls the Mechanism of Lumen Formation in Epithelial Morphogenesis. *Curr. Biol.* **18,** 507–513 (2008).

419. Engelberg, J. A., Datta, A., Mostov, K. E. & Hunt, C. A. MDCK Cystogenesis Driven by Cell

Stabilization within Computational Analogues. *PLoS Comput. Biol.* **7,** e1002030 (2011).

420. Yevick, H. G., Duclos, G., Bonnet, I. & Silberzan, P. Architecture and migration of an epithelium on a cylindrical wire. *Proc. Natl. Acad. Sci.* **112,** 5944–5949 (2015).

421. Sim, J. Y. *et al.* Spatial distribution of cell-cell and cell-ECM adhesions regulates force balance while main taining E-cadherin molecular tension in cell pairs. *Mol. Biol. Cell* **26,** 2456–2465 (2015).

8

Resum en Català

La major part dels actuals models de cultiu cel·lular *in vitro* no reprodueixen l'anatomia dels teixits i el comportament fisiològic de les cèl·lules *in vivo*. A més a més, proporcionen resultats enganyosos quan es comparen amb el teixit real. Les tecnologies de microfabricació es poden utilitzar per anar un pas més enllà dels models 2D convencionals, en el camp del cultiu de teixits *in vitro* i reproduir de forma fiable els microambients del teixits. Per l'epiteli de l'intestí prim, aquest enfocament s'ha explorat a través de la fabricació de scaffolds de col·lagen i poly (lactic-co-glycolic acid) que imiten les vellositats, mitjançant un procés seqüencial de motlles. Ha estat un enfocament innovador i interessant, i ha reportat resultats rellevants en quant a la importància del tridimensionalitat del models *in vitro* de epiteli intestinal. Tot i així, la naturalesa dels materials emprats no permet un ajust fi de les propietats del sistema, i el mètode de fabricació basat en emmotllament és laboriós, requerint diverses etapes de motlles intermedis.

Aquí es descriu un mètode simple i rendible per fabricar microestructures toves, que imiten les vellositats amb l'arquitectura 3D anatòmica. Utilitzem poly (ethylene glycol) diacrylated (PEGDA) i àcid acrílic, que formen hidrogels tous en copolimeritzar sota la llum UV, mitjançant fotolitografia. Hem demostrat que la nostra tecnologia permet produir monocapes funcionals de cèl·lules epitelials (Caco-2) polaritzades.

Els hidrogels són materials en polimèrics que formen xarxes tridimensionals amb un alt contingut d'aigua, que permet una fàcil difusió de factors solubles i oxigen. Els hidrogels fets de PEG posseeixen propietats químiques i mecàniques altament ajustables i s'han convertit en materials molt utilitzats per imitar la matriu extracel·lular i les membranes basals dels teixits. Per obtenir les microestructures que imiten la tridimensionalitat de les vellositats, es van utilitzar màscares binaries. Aquestes màscares presenten uns patrons en els que

les zones fosques impedeixen el pas de la llum, mentre que les finestres son transparents. En el nostre cas es van utilitzar màscares amb patrons circulars per fabricar estructures en forma de pillar, en un procés de polimerització depenent de la llum UV. Durant aquest procés, diversos factors, com ara el temps d'exposició UV, la concentració de fotoiniciador i el pes molecular del PEGDA i la seva concentració, es van estudiar per entendre els mecanismes que permeten la formació de microestructures toves amb uns valors de relació d'aspecte alts. Després, aquestes variables es van ajustar per controlar les dimensions de les microestructures i per tal d'obtenir hidrogels microestructurats que imitin les dimensions de les vellositats que es troben en l'intestí prim, així com les seves propietats físico-químiques i mecàniques.

Per permetre l'adhesió cel·lular i el creixement de, el PEGDA, que no és bioactiu i per tant repèl l'adhesió tan de proteïnes com de cèl·lules, es va copolimeritzar amb àcid acrílic per així treure profit dels grups carboxílics de l'àcid acrílic per incorporar-hi covalentment diverses proteïnes de la matriu extracel·lular. Després de la copolimerització, es va demostrar que els hidrogels mostraven grups carboxil exposats. A més a més es va confirmar que mitjançant la reacció d'acoblament per EDC/NHS les proteïnes es mantenen covalentment unides al hidrogel al llarg del temps. D'altra banda hem establert la relació entre PEGDA i àcid acrílic que permet obtenir microestructures similars, en dimensions i forma, a les de les vellositats. A més a més, la funcionalització dels hydrogels amb proteïnes de la membrana basal va ser adequada. Els nostres resultats mostren que la quantitat de proteïna unida covalentment al hidrogel depèn de la quantitat d'àcid acrílic empleat, que ofereix una manera de controlar la densitat de lligant al hidrogel, independentment de les propietats mecàniques. Tenint en compte l'espectre de rigidesa del epiteli intestinal, es van aconseguir hydrogels microestructurats que mostraven propietats mecàniques en aquets rang.

Els hidrogels microestructurats i funcionlaitzats per tal d'imitar les vellositats, han demostrat ser adequats per al creixement cel·lular. En primer lloc, l'adhesió cel·lular en els hidrogels es va assajar mitjançant el cultiu de fibroblasts, que van cobrir les microestructures en 7 dies. A continuació, es van utilitzar cèl·lules epitelials MDCK per determinar la idoneïtat dels hidrogels microestructurats en desenvolupar monocapes epitelials. Finalment, hem utilitzat cèl·lules epitelials del tipus Caco-2 (àmpliament utilitzades en els models de la barrera intestinal) per validar la funcionalitat del nostre sistema com a model *in vitro* de l'epiteli intestinal. Les cèl·lules Caco-2 van ser sembrades en els hidrogels microestructurats que imiten les vellositats, i es van mantenir en cultiu durant 21 dies. Els nostres resultats mostren que les cèl·lules Caco-2 van ser capaces d'adherir-s'hi i dividir-se, a més van formar una monocapa epitelial de cèl·lules polaritzades seguint la línia de les microestructures, d'una manera similar a les

vellositats. Aquest resultats es van demostrar per l'expressió de marcadors epitelials a la part apical de les cèl·lules i la forma, posició i l'orientació dels nuclis cel·lulars. En comparació amb els cultius tradicionals en membranes 2D, les monocapes de cèl·lules Caco-2 crescudes sobre els hidrogels microestructurats van mostrar signes d'una millor polarització cel·lular, semblants a les cèl·lules epitelials de l'intestí.

També hem estat capaços de transferir amb èxit aquesta plataforma, els hidrogels microestructurats, sobre les de membranes poroses de policarbonat dels Transwell®. Amb aquesta tecnologia, actualment estem treballant en la realització d'assajos de permeabilitat paracel·lular i transcel·lular per avaluar l'acompliment del nostre sistema en comparació amb l'estàndard de monocapes epitelials de Caco-2. D'altra banda, hem avaluat la resistència elèctrica transepithelial (TEER) de les monocapes crescudes sobre els hidrogels microestructurats, i els nostres resultats de les mesures de TEER han confirmat la formació de barreres de cèl·lules epitelials funcionals, amb valors de TEER més propers a la situació *in vivo* que els mesurats per monocapes convencionals, evidenciant així els resultats prometedors de la plataforma per ser aplicada en el camp de l'absorció del fàrmacs, la toxicitat i el modelatge de malalties

Els nostres resultats són compatibles amb la hipòtesi que la geometria de les vellositats millora la fisiologia cel·lular i, per tant, la funció de barrera. En aquest punt, es requereixen més esforços per dissenyar un conjunt robust i compatible amb els models estàndard (Transwell®) per realitzar mesuraments sistemàtics de la permeabilitat i el transport.

A causa de la simplicitat i la versatilitat del mètode de fabricació dissenyat, els hidrogels microestructurats fets PEGDA i àcid acrílic poden tenir aplicacions incomptables. El mètode es pot utilitzar per dissenyar models més complexos de mucosa intestinal, mitjançant la incorporació d'altres tipus de cèl·lules com ara les cèl·lules caliciformes, cèl·lules mare intestinals, cèl·lules immunes i fins i tot bacteris comensals o patògens. A més, a causa de la plasticitat proa l'hora de modificar les propietats d'aquesta material, la metodologia es pot estendre a altres teixits epitelials que presenten arquitectures 3D rellevants per la seva funcionalitat, com ara la còrnia, l'esòfag o la pell.

9 Appendix: Journal articles

Protein patterning on hydrogels by direct microcontact printing: application to cardiac differentiation

RSC ADVANCES
Volume: 4 Issue: 55 Pages: 29120-29123
DOI: 10.1039/c4ra03374d
Published: 2014

A. G. Castaño,*[a] V. Hortigüela,[ab] A. Lagunas,[bc] C. Cortina,[e] N. Montserrat,[bf] J. Samitier[bcd] and E. Martínez[abd]

[a]*Biomimetic systems for cell bioengineering, Institute for Bioengineering of Catalonia (IBEC), C/Baldiri Reixac 10-12, 08028 Barcelona, Spain*
[b]*Centro de Investigación Biomédica en Red en Bioingeniería, Biomateriales y Nanomedicina (CIBER-BBN), C/María de Luna 11, Edificio CEEI, 50018 Zaragoza, Spain*
[c]*Nanobioengineering, Institute for Bioengineering of Catalonia (IBEC), C/Baldiri Reixac 10-12, 08028 Barcelona, Spain*
[d]*Department of Electronics, University of Barcelona, C/Martí i Franquès 1, 08028 Barcelona, Spain*
[e]*Oncology program, Institute for Research in Biomedicine (IRB Barcelona), C/Baldiri Reixac 10, 08028 Barcelona, Spain*
[f]*Center of Regenerative Medicine in Barcelona, Barcelona Biomedical Research Park (PRBB), C/Doctor Aiguader, 88, 7a Planta, 08003 Barcelona, Spain*

An extended microcontact printing technique to chemically pattern hydrogels is reported. The procedure employs standard polydimethylsiloxane stamps and requires minor pre-processing of the hydrogels by freeze-drying. Micropatterned Matrigel™ and gelatin hydrogels induce NIH-3T3 cell alignment and elongation. Furthermore, human embryonic stem cells cultured on fibronectin-patterned hydrogels display beating foci earlier than those cultured on non-patterned substrates

Mesopattern of immobilised bone morphogenetic protein-2 created by microcontact printing and dip-pen nanolithography influence C2C12 cell fate

RSC ADVANCES
Volume: 4 Issue: 100 Pages: 56809-56815
DOI: 10.1039/c4ra10311d
Published: 2014

S. Oberhansl,[ac] A. G. Castaño,[bc] A. Lagunas,[ac] E. Prats-Alfonso,[e] M. Hirtz,*[f] F. Albericio,[e] H. Fuchs,[fg] J. Samitier[acd] and E. Martinez*[bcd]

**Corresponding authors*
[a]*Nanobioengineering group, Institute for Bioengineering of Catalonia (IBEC), 08028 Barcelona, Spain*
[b]*Biomimetic systems for cell engineering group, Institute for Bioengineering of Catalonia (IBEC), 08028 Barcelona, Spain*
[c]*Centro de Investigación Biomédica en Red en Bioingeniería, Biomateriales y Nanomedicina, CIBER-BBN, Spain*
[d]*Department of Electronics, University of Barcelona, 08028 Barcelona, Spain*
[e]*Institute for Research in Biomedicine (IRB), Department of Organic Chemistry, University of Barcelona, CIBER-BBN, Barcelona Science Park, 08028 Barcelona, Spain*
[f]*Institute of Nanotechnology (INT) and Karlsruhe Nano Micro Facility (KNMF), Karlsruhe Institute of Technology (KIT), Eggenstein-Leopoldshafen, Germany*
[g]*Westfälische Wilhelms-Universität and Center for Nanotechnology (CeNTech), Münster, Germany*

Dip-pen nanolithography and microcontact printing were used to fabricate mesopatterned substrates for cell differentiation experiments. A biotin–thiol was patterned on gold substrates and subsequently functionalised with streptavidin and biotinylated bone morphogenetic protein-2 (BMP-2). The feasibility of mesopatterned substrates containing immobilised BMP-2 was proven by obtaining similar differentiation outcomes compared to the growth factor in solution. Therefore, these substrates might be suitable for replacing conventional experiments with BMP-2 in solution.

Large-scale dendrimer-based uneven nanopatterns for the study of local arginine-glycine-aspartic acid (RGD) density effects on cell adhesion

NANO RESEARCH
Volume: 7 Issue: 3 Pages: 399-409
DOI: 10.1007/s12274-014-0406-2
Published: MAR 2014

Anna Lagunas[1,2], Albert G. Castaño[2,1], Juan M. Artés[2,3], Yolanda Vida[4,5], Daniel Collado[4,5], Ezequiel Pérez-Inestrosa[4,5], Pau Gorostiza[2,1,6], Silvia Claros[7,1], José A. Andrades[7,1], and Josep Samitier[1,2,8]

[1]*Networking Biomedical Research Center in Bioengineering, Biomaterials and Nanomedicine (CIBER-BBN), Spain*
[2]*Institute for Bioengineering of Catalonia (IBEC), Baldiri-Reixac 15-21, Barcelona 08028, Spain*
[3]*Physical Chemistry Department, University of Barcelona (UB), Martí i Franquès 1-11, Barcelona 08028, Spain*
[4]*Andalusian Centre for Nanomedicine and Biotechnology (BIONAND), Severo Ochoa 35, Málaga 29590, Spain*
[5]*Organic Chemistry Department, University of Málaga (UMA), Campus Teatinos, Málaga 29071, Spain*
[6]*Institució Catalana de Recerca i Estudis Avançats (ICREA), Spain*
[7]*Cell Biology, Genetics and Physiology Department, University of Málaga (UMA), Campus Teatinos, Málaga 29071, Spain*
[8]*Electronics Department, University of Barcelona (UB), Martí i Franquès 1-11, Barcelona 08028, Spain*

Cell adhesion processes are governed by the nanoscale arrangement of the extracellular matrix (ECM), being more affected by local rather than global concentrations of cell adhesive ligands. In many cell-based studies, grafting of dendrimers on surfaces has shown the benefits of the local increase in concentration provided by the dendritic configuration, although the lack of any reported surface characterization has limited any direct correlation between dendrimer disposition and cell response. In order to establish a proper correlation, some control over dendrimer surface deposition is desirable. Here, dendrimer nanopatterning has been employed to address arginine-glycine-aspartic acid (RGD) density effects on cell adhesion. Nanopatterned surfaces were fully characterized by atomic force microscopy (AFM), scanning tunneling microscopy (STM) and X-ray photoelectron spectroscopy (XPS), showing that tunable distributions of cell adhesive ligands on the surface are obtained as a function of the initial dendrimer bulk concentration. Cell experiments showed a clear correlation with dendrimer surface layout: Substrates presenting regions of high local ligand density resulted in a higher percentage of adhered cells and a higher degree of maturation of focal adhesions (FAs). Therefore, dendrimer nanopatterning is presented as a suitable and controlled approach to address the effect of local ligand density on cell response. Moreover, due to the easy modification of dendrimer peripheral groups, dendrimer nanopatterning can be further extended to other ECM ligands having density effects on cells

RSC Advances

COMMUNICATION

View Article Online
View Journal | View Issue

Protein patterning on hydrogels by direct microcontact printing: application to cardiac differentiation†

Cite this: *RSC Adv.*, 2014, **4**, 29120

Received 14th April 2014
Accepted 20th June 2014

DOI: 10.1039/c4ra03374d

www.rsc.org/advances

A. G. Castaño,*[a] V. Hortigüela,[ab] A. Lagunas,[bc] C. Cortina,[e] N. Montserrat,[bf] J. Samitier[bcd] and E. Martínez[abd]

An extended microcontact printing technique to chemically pattern hydrogels is reported. The procedure employs standard polydimethylsiloxane stamps and requires minor pre-processing of the hydrogels by freeze-drying. Micropatterned Matrigel™ and gelatin hydrogels induce NIH-3T3 cell alignment and elongation. Furthermore, human embryonic stem cells cultured on fibronectin-patterned hydrogels display beating foci earlier than those cultured on non-patterned substrates.

Hydrogels are networked materials with high water content, which allows easy diffusion of soluble factors and oxygen. Due to their biocompatibility and swelling properties, hydrogels are widely used for mammalian cell cultures. Because of their mechanical and chemical properties, hydrogels mimic extracellular matrix architecture and have become trendy materials to resemble soft tissues.[1–3] Protein patterning of biocompatible surfaces, like hydrogels, plays an important role mimicking chemical heterogeneity of native tissues where cells collectively arrange in complex functional structures.[4–7] In particular, cardiac microenvironment has been replicated through fibronectin patterns to obtain more realistic cardiac cell cultures.[8–11]

Protein patterning has been extensively applied to stiff substrates; however the patterning of soft, sticky materials such as hydrogels is not straightforward. Several works have been published reporting successful chemical patterning of hydrogels. Most of them rely on complex techniques such as jet printing,[12] microfluidics,[13,14] and photo-immobilization strategies[15–17] to generate micropatterns of biomolecules on hydrogels. Microcontact printing and related techniques are the most widely used to create molecular patterns onto surfaces because of their high versatility, easy procedure and low cost.[18] However, these straightforward methods could exhibit an inefficient application on very soft or tacky substrates such as hydrogels.[19] Attempts to expand microcontact printing to hydrogels are based on the use of agarose hydrogel stamps,[20,21] the use of intermediate poly(vinyl alcohol) layers,[19] require sequential steps on glass slides,[22] require substantial chemical modification of the hydrogels,[23,24] or need complex combination with stereolithography methods.[25]

Herein we present a simple and versatile method to create protein micropatterns on soft hydrogels by direct microcontact printing without the need of hydrogel chemical modifications, intermediate layers, or multiple steps. As in the conventional method, we keep on using polydimethylsiloxane (PDMS) stamps. To make hydrogels able to withstand the stamping procedure and to avoid sticking or slip effects, hydrogels are freeze-dried prior to the printing procedure. To prove the success of this expanded technique we choose to print protein features onto Matrigel™ and gelatin substrates, which are hydrogels commonly used in stem cell culture.[26,27] We achieved the protein printing on these hydrogels, the micropatterns remained after reconstitution and during cell culture, and they successfully guided cellular alignment. The applicability of the extended microcontact printing approach has been validated in promoting cardiac differentiation. In a preliminary study, human embryonic stem cells have been seeded on fibronectin micropatterned hydrogels until beating foci were observed. Micropatterned substrates displayed promising results, as beating foci were observed earlier than on nonpatterned substrates.

[a]*Biomimetic systems for cell bioengineering, Institute for Bioengineering of Catalonia (IBEC), C/Baldiri Reixac 10-12, 08028 Barcelona, Spain. E-mail: agarciac@ibecbarcelona.eu*

[b]*Centro de Investigación Biomédica en Red en Bioingeniería, Biomateriales y Nanomedicina (CIBER-BBN), C/María de Luna 11, Edificio CEEI, 50018 Zaragoza, Spain*

[c]*Nanobioengineering, Institute for Bioengineering of Catalonia (IBEC), C/Baldiri Reixac 10-12, 08028 Barcelona, Spain*

[d]*Department of Electronics, University of Barcelona, C/Martí i Franquès 1, 08028 Barcelona, Spain*

[e]*Oncology program, Institute for Research in Biomedicine (IRB Barcelona), C/Baldiri Reixac 10, 08028 Barcelona, Spain*

[f]*Center of Regenerative Medicine in Barcelona, Barcelona Biomedical Research Park (PRBB), C/Doctor Aiguader, 88, 7a Planta, 08003 Barcelona, Spain*

† Electronic supplementary information (ESI) available: Experimental details, Fig. S1–S4 and Video 1. See DOI: 10.1039/c4ra03374d

For the microcontact printing process, the hydrogels were freeze-dried (Fig. 1). First, Matrigel™ (at dilutions ranging from 1/40 to 1/10 v/v in DMEM) and gelatin (at dilutions ranging from 0.05% to 0.5% w/v in Milli-Q water) were poured on piranha-activated glass slides. After gelation (2 h at 37 °C), the excess of solution was removed and samples were rinsed with Milli-Q water to avoid the presence of salts. Subsequently, samples were freeze-dried by immersion in liquid nitrogen and vacuum dried for 24 hours at −50 °C and 0.06 mbar of pressure.

After checking the hydrogel surface by scanning electron microscopy (SEM), those dilutions leading to homogeneous distribution of the material on the surface were selected (Fig. S1 in the ESI†). They correspond to 0.1 w/v for gelatin and 1/40 v/v for Matrigel™. To ensure that cell-adhesive properties of the hydrogels were not modified by the freeze-drying process, substrates were reconstituted and NIH-3T3 cells were cultured. After 4 hours of culture, NIH-3T3 cells preserved the typical fibroblast morphology and no significant differences in cell adhesion percentages were found between the freeze-dried and the control hydrogels (Fig. S4 in the ESI†).

Microcontact printing process was then carried out on freeze-dried hydrogels (Fig. 2). PDMS stamps featuring lines of several width and pitch combinations, from 2 μm to 20 μm, were employed to pattern streptavidin, laminin, and fibronectin proteins (Fig. S2 in the ESI†). No chemical modification of the hydrogel surface was performed; the proteins were immobilized by physical adsorption. The success of the printing procedure (uniformity, reproducibility and stability) was checked by fluorescence microscopy before reconstitution and 24 hours after the addition of 10 mM PBS buffer (Fig. 2). Dehydration is accompanied by an increase in stiffness of hydrogel-like materials such as collagen fibrils, which ensures the successful transfer of the pattern.[28,29]

It was observed that the procedure did not alter the pattern dimensions when the hydrogels were reconstituted. Protein patterning was observed on the surface and showed limited diffusion within a region ~8 μm thick into the bulk of the hydrogels (Fig. S3 in the ESI†). Once the printing was accomplished, fibronectin lines of 20 μm in width were printed onto freeze-dried Matrigel™ and gelatin hydrogels. Such size was selected in accordance to the results found in literature demonstrating successful cell alignment.[5,30,31] Thereafter, NIH-3T3 cells were seeded at a cell density of 10^4 cells per cm^2 under serum starvation conditions to highlight the effects of the micropattern. Unlike most of the works within this field, we have not passivated the non-patterned regions of the micropatterned surfaces, so cells were able to adhere freely to all over the sample surface in a way that mimics better the *in vivo* situation. After 4 hours of culture, both gelatin and Matrigel™ hydrogels showed significant alignment of NIH-3T3 cells on the patterned regions with respect to non-patterned substrates, used as controls (Fig. 3 and S5 in the ESI†). In particular, on patterned gelatin more than 60% of cells showed actin fibers and nuclei aligned with the pattern direction within an angle of 30°, while on patterned Matrigel™ the percentage increased up to 70% (Fig. 3d and S5d in the ESI†). Moreover, cells were elongated because of the pattern effects (Fig. 3e).

Once pattern effects on cell guidance were demonstrated on NIH-3T3 cells, the applicability of the technique was further extended to cardiac differentiation studies. For this purpose, disaggregated human embryonic stem cells (hESC) were seeded on fibronectin patterned hydrogels and non-patterned hydrogels, and their differentiation toward cardiac lineage cells was monitored for 30 days. During this differentiation assay, hESC cultured on micropatterned hydrogels displayed cell alignment

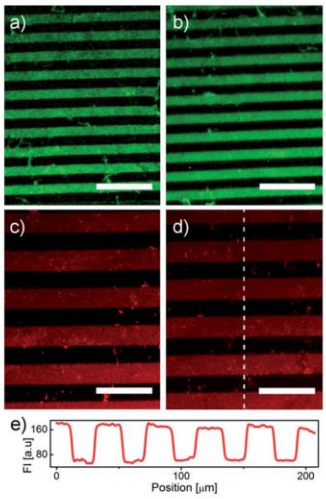

Fig. 2 Fluorescence microscopy images of hydrogels patterned with streptavidin Texas Red® conjugate. 5 μm wide lines printed on freeze-dried Matrigel (a) before and (b) after reconstitution. (Scale bar: 30 μm.) 20 μm wide lines printed on freeze-dried gelatin (c) before and (d) after reconstitution. (Scale bar: 60 μm.) (e) Fluorescence intensity profile corresponding to dash line of (d), showing the uniformity of the printing.

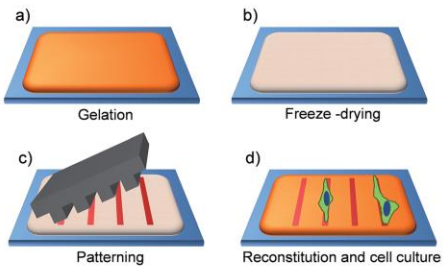

Fig. 1 Schematics of hydrogel micropatterning process. (a) After the gelation process, the hydrogels were freeze-dried (b) to enable the application of the microcontact printing technique (c). Then, the hydrogel were reconstituted (d) and cells were cultured.

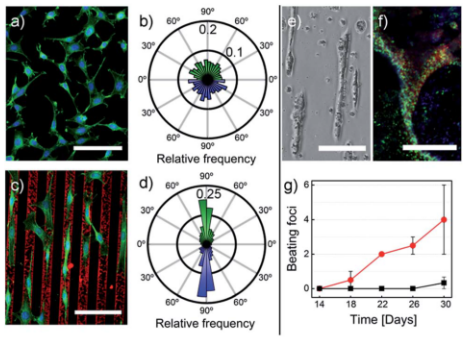

Fig. 3 Cell alignment on micropatterned gelatin and application in cardiac differentiation. Fluorescence microscopy pictures of NIH-3T3 mouse embryonic fibroblasts cultured on (a) non-patterned and (c) patterned gelatin (fibronectin lines 20 μm in width) hydrogels after 4 hours of culture. Cell nuclei are stained in blue, actin cytoskeleton in green and fibronectin in red. Scale bar: 100 μm. Normalized histograms (bin = 10°) depicting the distribution of the angles between cell cytoskeleton fibers (in green) and cell nuclei (in blue) with the pattern direction on (b) non-patterned (d) and patterned gelatin hydrogels. Human embryonic stem cells (hESCs) cultured on micropatterned gelatin with cardiac differentiation medium. (e) Elongated hESC cells following the pattern direction after 24 hours. Scale bar: 125 μm. (f) Beating colony from hESC on patterned gelatin at day 30, expressing GATA4 (stained in blue) and ASA (stained in red) cardiac markers. Scale bar: 200 μm. (g) Plot of the number of beating foci as a function of the culture time on patterned (red) and non-patterned (black) gelatin substrates (mean ± SEM).

at early culture stages (24 h) (Fig. 3e), expressed cardiac markers (GATA4 and alpha sarcomeric actin (ASA))(Fig. 3f), and beating foci (Video 1 in the ESI†) appeared at earlier time points than non-patterned substrates (day 18 *versus* day 30) (Fig. 3f and g). Through these results we demonstrate the beneficial effects of the anisotropy introduced on the substrate by the micropattern on the cardiac differentiation process.

One of the major advantages of human embryonic stem cells (hESCs) arises in their dual ability to self-renew and differentiate into all the cell types of the body. While differentiation of hESCs into cardiomyocytes has been well reported the process remains still inefficient.[32–35] So far intense research has been documented in the use of specific media culture combinations[33,34] or the use of specific cardiac-related genes[35] promoting cardiac differentiation. Hydrogels have been previously reported as potential candidates for hESCs differentiation towards cardiomyocytes due to their tunable composition and physical properties.[36] In that regard, we believe that the development of hydrogel-based strategies favoring cardiac differentiation will represent a major finding in the field of pluripotent stem cells differentiation and regenerative medicine. Because of its versatility, compatibility with standard cell culture methodology and minor modification of the hydrogel surface, we believe our patterning strategy to be advantageous for such applications.

Conclusions

In conclusion, we have developed a simple, straightforward procedure to create protein micropatterns applicable to hydrogels. This procedure employs the robust, well-proven microcontact printing technique with PDMS stamps and requires minor pre-processing of the hydrogels by freeze-drying. Matrigel™ and gelatin hydrogels have been successfully micropatterned using this methodology. We found that NIH-3T3 cells adhere well on patterned hydrogels, and aligned and elongated following the patterns. Moreover, in a preliminar study, we obtained hESC-derived cardiac lineage cells at earlier time points on patterned hydrogels than on non-patterned hydrogels. The described extended microcontact printing technique will be useful in cell culture platforms such as stem cells, where the use Matrigel™ or gelatin hydrogels is required.

Acknowledgements

Authors acknowledge the financial support of CIBER-BBN (Instituto de Salud Carlos III) with assistance from the European Regional Development Fund, the Commission for the Universities and Research of the Generalitat de Catalunya (2009 SGR 505) and the "Fundación Botín" (Santander, Spain). This work was also financially supported by the CARDIO-STEM Project (PLE2009-0147), funded by the MICINN under the National Program for the internationalization of R&D, TERCEL-ISCIII-MINECO, Cardiocel and Fundación Cellex.

Notes and references

1 C. A. DeForest and K. S. Anseth, *Annu. Rev. Chem. Biomol. Eng.*, 2012, **3**, 421–444.
2 H. Geckil, F. Xu, X. Zhang, S. Moon and U. Demirci, *Nanomedicine*, 2010, **5**, 469–484.
3 M. W. Tibbitt and K. S. Anseth, *Biotechnol. Bioeng.*, 2009, **103**, 655–663.
4 J. W. Nichol and A. Khademhosseini, *Soft Matter*, 2009, **5**, 1312–1319.
5 V. Gauvreau and G. Laroche, *Bioconjugate Chem.*, 2005, **16**, 1088–1097.
6 K. Kolind, K. W. Leong, F. Besenbacher and M. Foss, *Biomaterials*, 2012, **33**, 6626–6633.
7 E. Martínez, A. Lagunas, C. Mills, S. Rodríguez-Seguí, M. Estévez, S. Oberhansl, J. Comelles and J. Samitier, *Nanomedicine*, 2009, **4**, 65–82.
8 N. Badie and N. Bursac, *Biophys. J.*, 2009, **96**, 3873–3885.
9 A. F. G. Godier-Furnémont, T. P. Martens, M. S. Koeckert, L. Wan, J. Parks, K. Arai, G. Zhang, B. Hudson, S. Homma and G. Vunjak-Novakovic, *Proc. Natl. Acad. Sci. U. S. A.*, 2011, **108**, 7974–7979.
10 E. Serena, S. Zatti, E. Reghelin, A. Pasut, E. Cimetta and N. Elvassore, *Integr. Biol.*, 2010, **2**, 193–201.
11 C. Y. Tay, H. Yu, M. Pal, W. S. Leong, N. S. Tan, K. W. Ng, D. T. Leong and L. P. Tan, *Exp. Cell Res.*, 2010, **316**, 1159–1168.

12 M. J. Poellmann, K. L. Barton, S. Mishra and A. J. W. Johnson, *Macromol. Biosci.*, 2011, **11**, 1164–1168.
13 H. Zhang, J. N. H. Shepherd and R. G. Nuzzo, *Soft Matter*, 2010, **6**, 2238–2245.
14 A. Kunze, M. Giugliano, A. Valero and P. Renaud, *Biomaterials*, 2011, **32**, 2088–2098.
15 P. Musoke-Zawedde and M. S. Shoichet, *Biomed. Mater.*, 2006, **1**, 162–169.
16 Y. Luo and M. S. Shoichet, *Biomacromolecules*, 2004, **5**, 2315–2323.
17 C. A. DeForest, B. D. Polizzotti and K. S. Anseth, *Nat. Mater.*, 2009, **8**, 659–664.
18 Y. Xia and G. M. Whitesides, *Angew. Chem., Int. Ed.*, 1998, **37**, 550–575.
19 H. Yu, S. Xiong, C. Y. Tay, W. S. Leong and L. P. Tan, *Acta Biomater.*, 2012, **8**, 1267–1272.
20 M. Mayer, J. Yang, I. Gitlin, D. H. Gracias and G. M. Whitesides, *Proteomics*, 2004, **4**, 2366–2376.
21 D. Weibel, A. Lee, M. Mayer, S. F. Brady, D. Bruzewicz, J. Yang, W. DiLuzio, J. Clardy and G. M. Whitesides, *Langmuir*, 2005, **21**, 6436–6442.
22 X. Tang, M. Y. Ali and M. T. Saif, *Soft Matter*, 2012, **8**, 7197–7206.
23 M. R. Hynd, J. P. Frampton, N. Dowell-Mesfin, J. N. Turner, W. Shain and J. Neurosci, *Methods*, 2007, **162**, 255–263.
24 M. R. Burnham, J. N. Turner, D. Szarowski and D. L. Martin, *Biomaterials*, 2006, **27**, 5883–5994.
25 V. Chan, M. B. Collens, J. H. Jeong, K. Park, H. Kong and R. Bashir, *Virtual Phys. Prototyp.*, 2012, **7**, 219–228.
26 A. R. Greenlee, T. A. Kronenwetter-Koepel, S. J. Kaiser and K. Liu, *Toxicol. in Vitro*, 2005, **19**, 389–397.
27 H. Baharvand, M. Azarnia, K. Parivar and S. K. Ashtiani, *J. Mol. Cell. Cardiol.*, 2005, **38**, 495–503.
28 K. T. Maciel, R. M. Carvalho, R. D. Ringle, C. D. Preston and D. H. Pashley, *J. Dent. Res.*, 1996, **75**, 1851–1858.
29 E. A. Talman and D. R. Boughner, *Ann. Thorac. Surg.*, 2001, **71**, S375–S378.
30 S. Rohr, *Circ. Res.*, 1991, **68**, 115–116.
31 P. Camelliti, A. D. McCulloch and P. Kohl, *Microsc. Microanal.*, 2005, **11**, 249–259.
32 M. Pucéat, *Methods*, 2008, **45**, 168–171.
33 T. Neri, S. Stefanovic and M. Pucéat, *J. Cardiovasc. Pharmacol.*, 2010, **56**, 16–21.
34 G. Blin, T. Neri, S. Stefanovic and M. Pucéat, *Curr. Stem Cell Res. Ther.*, 2010, **5**, 215–226.
35 J. E. Dixon, E. Dick, D. Rajamohan, K. M. Shakesheff and C. Denning, *Mol. Ther.*, 2011, **19**, 1695–1703.
36 S. Gerecht, J. A. Burdick, L. S. Ferreira, S. A. Townsend, R. Langer and G. Vunjak-Novakovic, *Proc. Natl. Acad. Sci. U. S. A.*, 2007, **104**, 11298–11303.

RSC Advances

COMMUNICATION

View Article Online
View Journal | View Issue

Cite this: *RSC Adv.*, 2014, 4, 56809

Received 12th September 2014
Accepted 27th October 2014

DOI: 10.1039/c4ra10311d

www.rsc.org/advances

Mesopattern of immobilised bone morphogenetic protein-2 created by microcontact printing and dip-pen nanolithography influence C2C12 cell fate†

S. Oberhansl,[ac] A. G. Castaño,[bc] A. Lagunas,[ac] E. Prats-Alfonso,[e] M. Hirtz,*[f] F. Albericio,[e] H. Fuchs,[fg] J. Samitier[acd] and E. Martinez*[bcd]

Dip-pen nanolithography and microcontact printing were used to fabricate mesopatterned substrates for cell differentiation experiments. A biotin–thiol was patterned on gold substrates and subsequently functionalised with streptavidin and biotinylated bone morphogenetic protein-2 (BMP-2). The feasibility of mesopatterned substrates containing immobilised BMP-2 was proven by obtaining similar differentiation outcomes compared to the growth factor in solution. Therefore, these substrates might be suitable for replacing conventional experiments with BMP-2 in solution.

Introduction

Chemical surface modifications for cell adhesion, migration and differentiation experiments have been extensively described for both the microscale (from 20 μm upwards) and the nanoscale (from 500 nm downwards). By definition,[1,2] micropatterning or "cell patterning" is used to place cells in a certain manner on the substrate or dictate their shape, which, in turn, has been shown to highly influence cell fate (see the review of M. Théry for a detailed summary[3]). On the other hand, nanopatterns are usually applied for controlling cell-substrate interactions and are known to influence cell adhesion,[4] proliferation and differentiation.[5] Nevertheless, few examples so far are located in the "gap" between micro- and nanoscale features. Graham and co-workers denominated patterns with features smaller than 10 μm mesopatterns to clearly distinguish them from conventional micropatterns.[6] On these mesopatterns cells are able to spread across various features and overcome possible pattern restrictions.[7,8] This characteristic allows for tuning and controlling the concentration and spatial arrangement of an immobilised molecule.[9] Protein patterns with features between 1 and 10 μm are easily obtained by microcontact printing (μCP), even though inefficient molecule transfer can be a drawback.[1] For patterning with μCP, a silicon master is fabricated *via* photolithography and subsequently used to produce a PDMS stamp. The molecule transfer occurs by placing an inked stamp in contact with a surface. A very interesting alternative for the fabrication of protein mesopattern is the nanofabrication technique dip-pen nanolithography (DPN),[6,10] which allows direct and controlled deposition of biomolecules. DPN is an AFM-based direct-writing technique where a sharp cantilever is used to deposit molecules *via* a water meniscus or as ink droplets. In contrast to μCP, DPN is a maskless technique and time and cost expensive fabrication of masters is not necessary, thus providing easy flexibility in pattern design. DPN furthermore permits multiplexing, *i.e.* writing with different inks at the same time.[11] To our knowledge, mesopatterns have to date been used exclusively for studying cell adhesion, migration and guidance, mostly by immobilising extra cellular matrix (ECM) proteins or their components.[7,12] Other biologically relevant molecules, like growth factors, have not yet been applied to mesopatterns. Influencing cellular growth, proliferation and differentiation, growth factors are known to not only have dose-dependent effects on cells, but also their distribution and spatial organisation are crucial. Therefore, cell differentiation experiments call for enhanced control over distribution and local density of the respective factor. For example, bone morphogenetic

[a]*Nanobioengineering group, Institute for Bioengineering of Catalonia (IBEC), 08028 Barcelona, Spain*

[b]*Biomimetic systems for cell engineering group, Institute for Bioengineering of Catalonia (IBEC), 08028 Barcelona, Spain. E-mail: emartinez@ibecbarcelona.eu*

[c]*Centro de Investigación Biomédica en Red en Bioingeniería, Biomateriales y Nanomedicina, CIBER-BBN, Spain*

[d]*Department of Electronics, University of Barcelona, 08028 Barcelona, Spain*

[e]*Institute for Research in Biomedicine (IRB), Department of Organic Chemistry, University of Barcelona, CIBER-BBN, Barcelona Science Park, 08028 Barcelona, Spain*

[f]*Institute of Nanotechnology (INT) and Karlsruhe Nano Micro Facility (KNMF), Karlsruhe Institute of Technology (KIT), 76344, Eggenstein-Leopoldshafen, Germany. E-mail: michael.hirtz@kit.edu*

[g]*Westfälische Wilhelms-Universität and Center for Nanotechnology (CeNTech), Münster, Germany*

† Electronic supplementary information (ESI) available: Materials and methods, surface functionalisation protocols, cell culture protocol and in-detail fabrication process of DPN patterned substrates. See DOI: 10.1039/c4ra10311d

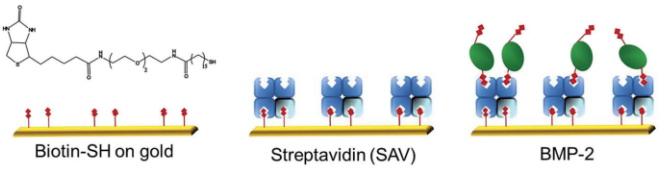

Fig. 1 Schematic representation of the functionalisation steps for the gold substrates: biotin–thiol, streptavidin and bone morphogenetic protein-2 (BMP-2).

protein-2 (BMP-2) is known to have a dose-dependent effect.[13] Surface immobilisation is thought to have advantages over presenting a growth factor in solution. Immobilised BMP-2 can in principle bind their receptors on the cell surface without being internalised, thus extending the signalling time.[14] Pohl *et al.* mention as advantages targeted presentation and control over the local density of a factor.[15] Furthermore, the loss of the signalling molecule due to diffusion in the culture medium can be avoided, which leads to its sustained influence.[16] Our group has successfully applied a sandwich complex, for the covalent immobilisation of BMP-2 on substrates, most importantly maintaining its biological activity.[17,18]

In this communication, we present the proof of concept that mesopatterns are suitable for cell differentiation experiments. For the fabrication of the mesopatterns, DPN was employed as well as μCP, which served as a reference patterning technique. Both techniques were used to deposit a biotin–thiol molecule.[19] Gold substrates with a homogeneous layer of biotin–thiol were used as control. Further derivatisation with streptavidin and lastly biotinylated bone morphogenetic protein-2 (BMP-2) ensured that BMP-2 was anchored in a stable and directional manner on the substrate (see Fig. 1). The response of myoblastic C2C12 cells to the immobilised BMP-2 was analysed and quantified by staining for the early differentiation marker osterix.

Results and discussion

Deposition of biotin–thiol *via* μCP was straight-forward: the elastomeric stamp with round features of 5 μm in diameter was incubated in a solution of biotin–thiol in ethanol. The biotin–thiol was transferred onto the gold by placing the stamp in contact with the surface. The remaining free space between the pattern was passivated against unspecific cell adhesion with polyethylene-glycol. For deposition of biotin–thiol *via* DPN, a carrier molecule was used, namely 1,2-dioleoyl-*sn-glycero*-3-phosphocholine (DOPC). This strategy was chosen because the deposition rate of biotin–thiol without a carrier molecule was very slow (see Fig. S2†).[20] By using DOPC as a carrier, dwell times of 0.2 s could be obtained (compared to around 60 s without the use of DOPC). As stated by Derda *et al.*,[21] substrates suitable for cell experiments have to have a patterned area of minimum 0.25 mm^2. Due to the vast reduction in needed dwell time by utilising the carrier ink DOPC instead of pure biotin–thiol (0.2 s instead of 60 s), patterning on this area size scale became feasible, with typical writing times of 30–40 min per sample of 2.36 mm^2. After allowing the biotin–thiol to bind to the gold, the carrier lipid was washed away. Though DPN, in contrast to μCP, can pattern only comparably small areas in one writing step, patterning of sufficiently large areas for cell culture experiments can be achieved by using cantilever arrays and an adequate writing strategy. The fabrication process, reaching a homogeneous mesopattern over a large area, is given in Fig. S3–S6.† Fig. S7† shows the darkfield microscopy image of an optimised mesopattern of DOPC containing biotin–thiol on gold, with a total pattern area of 2.36 mm^2. The homogeneity of the pattern is satisfying, because all dots have similar diameters with a narrow distribution. The mean dot size was determined to be 4.01 ± 0.90 μm in diameter.

An overview over all the substrates used for cell experiments can be found in Table 1. Experiments with BMP-2 in solution have been carried out in a representative experiment.[18]

After immobilising biotin–thiol on the substrates, they were incubated with streptavidin, leading to a transformation of the biotin pattern into a streptavidin pattern. Subsequently, half of the substrates were functionalised with biotinylated BMP-2 binding to the streptavidin features, while the other half, without BMP-2, served as negative control. For cell differentiation experiments, C2C12 myoblastic cells were seeded on the substrates. BMP-2 is known to play a very important role in the C2C12 cell fate: in the presence of BMP-2 they will differentiate towards osteoblasts.[22] Without BMP-2, they will stay in the myoblastic lineage. Quantification of osteogenic differentiation was performed as described below (see Fig. 7): cells with a "hollow", *i.e.* black nucleus have not started to differentiate towards osteoblast lineage cells. Cells which are homogeneously stained or have a pronounced green nucleus have started to differentiate towards osteoblasts. Fig. 2 shows a representative fluorescence image of C2C12 cells on a substrate prepared by μCP with (+) and without (−) BMP-2. The solid white arrows indicate cells which have started to differentiate

Table 1 Pattern parameters for all substrates

	Homogeneous	μCP	DPN
Method	Immersion	Microcontact printing	Dip-pen nanolithography
Feature size	Monolayer	5 μm round	4 μm dots
Spacing	—	5 μm	22 μm

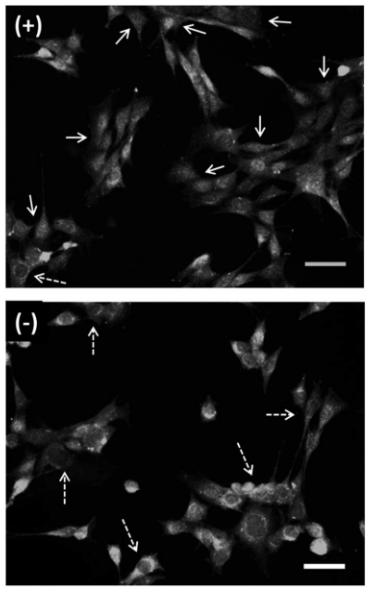

Fig. 2 Fluorescence microscopy images of C2C12 myoblastic cells on microcontact printed substrates with BMP-2 (+) and without BMP-2 (−). (Dashed) white arrows indicate cells which have (not) differentiated towards the osteoblastic regime. The scale bars equal 50 μm.

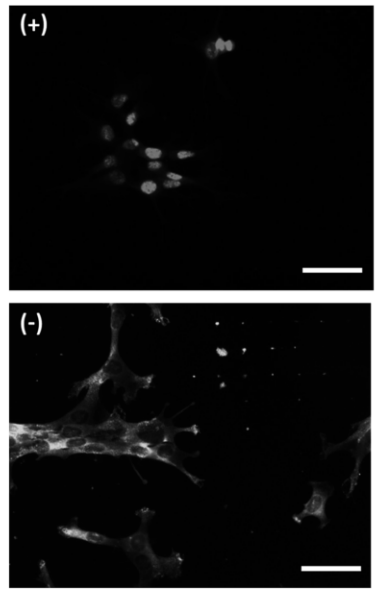

Fig. 3 Fluorescence microscopy images of C2C12 myoblastic cells on substrates fabricated by dip-pen nanolithography, with BMP-2 (+) and without BMP-2 (−). The scale bars equal 50 μm.

towards osteoblast lineage cells. The dashed white arrows indicate cells which are not in the osteoblastic regime. As expected, more cells have differentiated towards osteoblast lineage cells on the BMP-2 containing substrates.

For the substrates without BMP-2 (−), less cells adhered to the substrate. This might be explained by the fact that streptavidin slows down cell adhesion, acting as an anti-adhesive matrix towards both proteins and cells: cell adhesion was found to be initiated after 18 h.[23] Since staining for osterix was performed after 24 h, the cells had only little time to adhere and spread. This was also observed for cells on the other substrates without BMP-2 (DPN and homogeneous). Fig. 3 shows the fluorescence images of C2C12 cells on substrates fabricated with DPN. The substrate containing BMP-2 (+) clearly shows that all cells in the image have osterix located inside the nucleus, whereas the substrate without BMP-2 (−) shows only empty nuclei. Nevertheless, the efficiency of the DPN substrates did not reach 100%: apart from differentiated cells, there were also many cells with an empty nucleus, even though located on top of the BMP-2 pattern (data not shown).

On the basis of evaluated images for all substrates, the percentage of differentiated cells was calculated and is represented in Fig. 4. Significant differences were obtained between respective substrates with/without BMP-2. Precise values for the percentage of cell differentiation towards osteoblast lineage

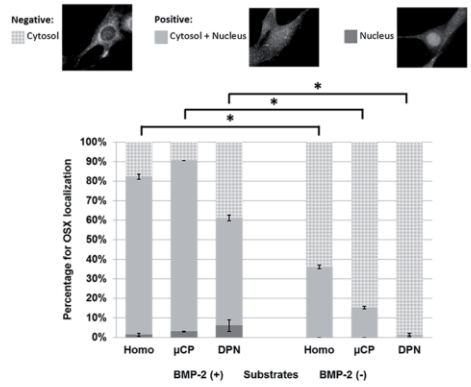

Fig. 4 Graph representing the percentage of the fluorescently marked protein osterix (OSX) localised in the cytosol (light grey), cytosol and nucleus (grey) and mostly in the nucleus (dark grey). The left side shows the substrates with BMP-2, the right side the substrates without BMP-2. At least 80 cells were evaluated per substrate and all substrates were prepared triplicate. For statistical purposes ANOVA was performed with a value of $\alpha = 0.05$.

cells are given in Table 2. For comparison, when working with BMP-2 in solution, the reported percentages are around 90%.[24]

The obtained values for the percentage of differentiated cells can all be attributed to the differences in BMP-2 surface density. The values for the respective BMP-2 surface density were estimated (see Experimental section below) and are presented in Table 2. Overall density refers to the amount of BMP-2 molecules on the whole substrate; local density refers to the density of BMP-2 molecules in one pattern feature, *i.e.* per round feature or per dot (for detailed definition see Fig. 6 below). For "homogeneous" (therefore featureless) substrates, both densities are the same, because, in contrast to the spatially confined localisation of BMP-2 on the patterned substrates, the homogeneous substrates are assumed to have a random BMP-2 distribution.

The lower percentage of cell differentiation found for DPN substrates in comparison to μCP substrates might be attributed to the different overall BMP-2 density, since the local density in one "pattern feature (round or dot)" of the array and the feature size are comparable. The only difference is the spacing between the features, leading to a smaller overall density and a decrease of the cell surface area stimulated by the BMP-2. Also, it has been shown in our group that by applying a BMP-2 surface concentration gradient, differences in cell differentiation are obtained. Differentiation values higher than 80% are obtained for overall BMP-2 surface concentrations of ≥2 pmol cm^{-2},[18] being in accordance with the values reported here.

The lower percentage for cell differentiation on the homogeneous substrates (~82%) when compared to the μCP substrates (~91%) can most likely be attributed to the differences in local BMP-2 density. When administered in solution, it has been reported that the concentration of BMP-2 has an effect on the cell differentiation outcome.[13] When immobilised on surfaces, BMP-2 surface density is also known to play an important role in stem cell differentiation.[25] BMP-2 receptors naturally exist in the cell membrane in multiple forms of preassembled oligomers and monomers.[26] BMP-2 surface immobilisation can lead to regions with high ligand local densities (like in the microcontact printed spots), which can improve dramatically the occupancy of BMP-2 receptors. Furthermore, surface immobilisation restricts BMP-2 diffusion and avoids its complete detachment from the receptor.[27] Interaction of BMP-2 with a single receptor, in turn, can lead to receptor oligomerisation[28] and thus increase the overall signalling. The percentage of cell differentiation for the microcontact printed substrates corresponds to what has been found for cell differentiation in solution (90%), leading to the conclusion that this type of substrates could replace cell experiments with BMP-2 in solution.

To further evaluate the differences among the values of cell differentiation for all substrates containing BMP-2, a frequency analysis was performed. The best result was obtained for DPN prepared substrates (see Fig. 5).

All cells identified as positive for differentiation are completely differentiated, being reflected in the cells having a green nucleus (as shown in the images of Fig. 5). This result may be related with a better performance of the DPN technique in terms of pattern homogeneity when compared to μCP.[1]

Table 2 Percentage of differentiated C2C12 myoblastic cells towards osteoblast lineage cells in comparison to the values of BMP-2 surface coverage and density for the three substrates used in cell culture experiments: dip-pen nanolithography (DPN), microcontact printing (μCP) and without pattern feature (homogeneous)

Substrate (+BMP-2)	Homogeneous	μCP	DPN
Percentage of differentiated cells (%)	82 ± 3	91 ± 1	61 ± 3
Overall surface coverage BMP-2	35.5%	28.3%	2.6%
Overall BMP-2 density (pmol cm^{-2})	4.44	3.53	0.33
Local surface coverage BMP-2	35.5%	100%	100%
Local BMP-2 density (amol μm^{-2})	0.04	0.13	0.13

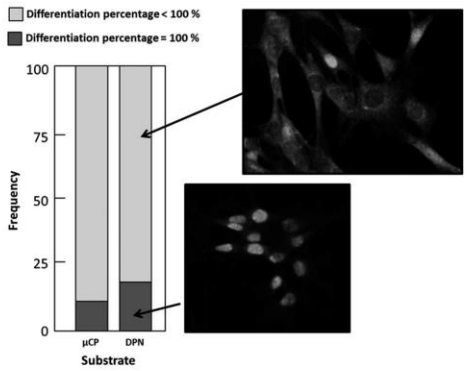

Fig. 5 Frequency analysis for the values of cell differentiation, comparing the microcontact printed substrates (μCP) to the ones prepared with dip-pen nanolithography (DPN).

Conclusions

In conclusion, we have shown that mesopatterned substrates are suitable for cell differentiation experiments. μCP is a fast and reproducible patterning method for a total pattern area of around 1 cm^2. These substrates are suitable to replace conventional experiments with BMP-2 in solution. On the other hand, DPN allows the facile and flexible variation of the pattern spacing, because it is a maskless technique. Even though cell differentiation for the substrates fabricated with DPN is not as high as reported for BMP-2 in solution, this approach is very promising and has a lot of potential as flexible platform for this kind of cell response studies. While patterns can be changed on the go without the need of fabricating new masters, the main argument often brought forward against using DPN for large area cell studies is the intrinsic limited area throughput. However, the presented study shows that adequate area sizes can be produced with reasonable expenditure of time thanks to the reduced dwell times enabled by the use of carrier inks.

Experimental

Estimating the BMP-2 surface density

The estimations started from the underlying biotin–thiol layer. It was assumed that both, the homogeneous (homo) and the microcontact printed (μCP) substrates have a monolayer of biotin–thiol. For the substrates fabricated with dip-pen nanolithography (DPN), prior calculations had to be done: in order to estimate the approximate quantity of deposited DOPC and biotin–thiol, the mean dot size for the arrays was determined as 4.01 ± 0.90 μm (mean dot area 53.20 ± 23.89 μm^2; determined from 100 random dots in the array). Furthermore, a recently published work determined the mass transfer of DOPC doing dip-pen nanolithography.[29] Following these calculations, we take into account that dot areas >65 μm^2 have a mass transfer of 1.59 ± 0.10 pg ink per dot and dot areas <65 μm^2 have a mass transfer of 0.08 ± 0.02 pg ink per dot, since the dots are bigger at the beginning of the array and get smaller during patterning because of ink loss (for the calculated dots, 72% are bigger than 65 μm^2 and 28% smaller). The estimated number of molecules is therefore 2.48×10^8 (for bigger dots) and 1.25×10^7 (for smaller dots). Thus it can be deduced that for bigger dots 411.82 amol of biotin–thiol are deposited and for smaller dots 20.72 amol. These values are only estimated since the humidity during deposition varied and ranged from 35% to 55% and was therefore not fixed as for the work of Fuchs and co-workers.

Further combination of the obtained values for number of molecules deposited and dot areas obtained from the images leads to the estimation of biotin–thiol molecules per surface area: around 2.5×10^6 molecules per μm^2 for all dots, which corresponds to 4.1 amol μm^{-2} biotin–thiol (in more detail: 3.1×10^5 molecules per μm^2 for small droplets and 2.7×10^6 molecules per μm^2 for big droplets).

In order to be able to calculate if a monolayer of biotin–thiol was formed in the spots, the stearic acid molecule was chosen as approach. This comparison is based on the structural similarity which both molecules present due to their aliphatic chain and they should very likely arrange themselves in a similar way. If we estimate that one molecule of stearic acid ($M = 284$ g mol^{-1}) occupies 21 Å^2 (taken from ref. 30) we can calculate that there is a density of 4.76×10^6 molecules μm^{-2} for the stearic acid. For the biotin–thiol, the values for large droplets correspond to a closed monolayer whereas the values for the smaller droplets correspond to a spaced-out monolayer.

Assuming furthermore, that even if there was no complete monolayer (substrates DPN), the size of the protein streptavidin ($4.5 \times 4.5 \times 5.3$ nm^3)[31] will be able to overcome possible "holes" in the monolayer. Since a sufficient amount of streptavidin was provided during incubation, the calculated values are based on a monolayer of streptavidin for all substrates.

We hypothesise that each molecule of streptavidin will bind 1 molecule of BMP-2 since their dimensions are very similar (BMP-2 (ref. 32): $7 \times 3.5 \times 2.5$ nm^3). Therefore, the density of BMP-2 depends only on the amount of BMP-2 provided during incubation. The local values indicate the density of BMP-2 on the pattern features. Since the homogeneous substrate does not have any areas where BMP-2 could not bind and a random but homogeneous distribution is assumed for the whole surface, the local and the overall densities are the same. The patterned substrates, on the other hand, exhibit regions without streptavidin (the passivated areas), where BMP-2 cannot bind. Therefore, the overall area for BMP-2 attachment is smaller. This area was calculated taking into account the pattern parameters and is reflected in the overall surface coverage of BMP-2. The resulting values for the overall density of BMP-2 show a decrease in the density from the substrates homo to μCP to DPN. An interesting point to highlight here is that the assembly of BMP-2 on the substrates homo is random, whereas on the substrates μCP and DPN, the assembly is guided by the pattern features and most accurately localised.

The terms local and overall density are also depicted in Fig. 6, whereas local density is indicated in red, referring to the density of BMP-2 molecules in 1 pattern feature (round or dot). Overall density refers to the amount of BMP-2 on the whole substrate. Since the homogeneous substrates (homo) don't have pattern features and the BMP-2 distribution is random, both densities are the same.

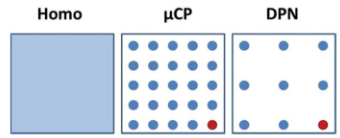

Fig. 6 Schematic figure representing the BMP-2 densities of the substrates homo, μCP and DPN. The red color indicates the local density of BMP-2.

Osterix as early differentiation marker

Quantification of osteogenic differentiation was performed by staining for a so called "early differentiation" marker. It has been reported that osterix (OSX) is induced rapidly in C2C12 cells by BMP-2 during the first 24 h of administration,[33] making it an ideal candidate for fast assessment of cell differentiation. The quantification of OSX positive cells (*i.e.* cells starting to have differentiated towards osteoblasts) was based on the criteria defined by the group of Polak who reported that OSX was activated and translocated from the cell cytosol into the nucleus during preosteoblast stages of osteoblastic lineage differentiation.[34] Therefore, all cells with a void nucleus are counted as negative and all cells with a homogeneous colouring or a pronounced green nucleus are counted as positive for differentiation towards the osteoblastic regime (see Fig. 7).

Frequency analysis

A frequency analysis is based on the individual analysed images (at least 18 images per sample) and their respective differentiation rates. This means that each of the images taken into account are evaluated for their respective differentiation

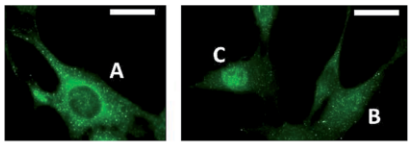

Fig. 7 Osterix staining of C2C12 myoblastic cells. The cell on the left side (A) shows an empty nucleus and is considered negative for differentiation. On the other hand, the cells on the right side are positive for differentiation because they are homogeneously green (B) or have a brighter green nucleus (C). The scale bars equal 25 μm.

percentages and, in the case of 100% differentiation, classified as yes (100%) or no (<100%).

Acknowledgements

CIBER-BBN is an initiative funded by the VI National R&D&i Plan 2008–2011, Iniciativa Ingenio 2010, Consolider Program, CIBER Actions and financed by the Instituto de Salud Carlos III with assistance from the European Regional Development Fund. The Nanobioengineering group has support from the Commission for Universities and Research of the Department of Innovation, Universities, and Enterprise of the Generalitat de Catalunya (2009 SGR 505). This study was supported by "Fundación M. Botín", Santander, Spain. Part of the work was carried out with support of the European Community. We appreciate the support of the European Research Infrastructure EUMINAfab (funded under the FP7 specific program Capacities, Grant Agreement Number 226460) and its partner at the Karlsruhe Institute of Technology (KIT). This work was partly carried out with the support of the Karlsruhe Nano Micro Facility (KNMF, www.kmf.kit.edu), a Helmholtz Research Infrastructure at Karlsruhe Institute of Technology (KIT, www.kit.edu). We thank Miriam Funes for technical help. The IRB group has support of CICYT (CTQ2012-30930) and Generalitat of Catalunya (2009SGR1024).

Notes and references

1 J. Y. Lim and H. J. Donahue, *Tissue Eng.*, 2007, **13**, 1879.
2 K. Kolind, K. W. Leong, F. Besenbacher and M. Foss, *Biomaterials*, 2012, **33**, 6626.
3 M. Théry, *J. Cell Sci.*, 2010, **123**, 4210.
4 M. Arnold, E. A. Cavalcanti-Adam, R. Glass, J. Blümmel, W. Eck, M. Kantlehner, H. Kessler and J. P. Spatz, *ChemPhysChem*, 2004, **5**, 383.
5 (*a*) K. Y. Lee, E. Alsberg, S. Hsiong, W. Comisar, J. Linderman, R. Ziff and D. Mooney, *Nano Lett.*, 2004, **4**, 1501; (*b*) J. M. Curran, R. Chen, R. Stokes, E. Irvine, D. Graham, E. Gubbins, D. Delaney, N. Amro, R. Sanedrin, H. Jamil and J. A. Hunt, *J. Mater. Sci.: Mater. Med.*, 2010, **21**, 1021; (*c*) L. R. Giam, M. D. Massich, L. Hao, L. S. Wong, C. C. Mader and C. A. Mirkin, *Proc. Natl. Acad. Sci. U. S. A.*, 2012, **109**, 4377.
6 D. G. Thompson, E. O. McKenna, A. Pitt and D. Graham, *Biosens. Bioelectron.*, 2011, **26**, 4667.
7 C. S. Chen, J. L. Alonso, E. Ostuni, G. M. Whitesides and D. E. Ingber, *Biochem. Biophys. Res. Commun.*, 2003, **307**, 355.
8 G. Csucs, R. Michel, J. W. Lussi, M. Textor and G. Danuser, *Biomaterials*, 2003, **24**, 1713.
9 M. Ventre, F. Causa and P. A. Netti, *J. R. Soc., Interface*, 2012, **9**, 2017.
10 (*a*) R. D. Piner, J. Zhu, F. Xu, S. Hong and C. A. Mirkin, *Science*, 1999, **283**, 661; (*b*) E. J. Irvine, A. Hernandez-Santana, K. Faulds and D. Graham, *Analyst*, 2011, **136**, 2925; (*c*) C.-C. Wu, D. N. Reinhoudt, C. Otto, V. Subramaniam and A. H. Velders, *Small*, 2011, **7**, 989; (*d*) S. Sekula-Neuner, J. Maier, E. Oppong, A. C. B. Cato, M. Hirtz and H. Fuchs, *Small*, 2012, **8**, 585.
11 (*a*) S. Sekula, J. Fuchs, S. Weg-Remers, P. Nagel, S. Schuppler, J. Fragala, N. Theilacker, M. Franzreb, C. Wingren, P. Ellmark, C. A. Borrebaeck, C. A. Mirkin, H. Fuchs and S. Lenhert, *Small*, 2008, **4**, 1875; (*b*) P. L. Stiles, *Nat. Methods*, 2010, **7**, I.
12 (*a*) C. S. Chen, M. Mrksich, S. Huang, G. M. Whitesides and D. E. Ingber, *Science*, 1997, **276**, 1425; (*b*) A. Offenhäusser, S. Böcker-Meffert, T. Decker, R. Helpenstein, P. Gasteier, J. Groll, M. Möller, A. Reska, S. Schäfer, P. Schulte and A. Vogt-Eisele, *Soft Matter*, 2007, **3**, 290; (*c*) C.-J. Pan, H.-Y. Ding and Y.-X. Dong, *Colloids Surf., B*, 2013, **102**, 730; (*d*) N. P. Westcott, W. Luo and M. Yousaf, *J. Colloid Interface Sci.*, 2014, **430**, 207.
13 (*a*) J. van den Dolder, A. J. E. de Ruijter, P. H. M. Spauwen and J. A. Jansen, *Biomaterials*, 2003, **24**, 1853; (*b*) I. Song, B. S. Kim, C.-S. Kim and G.-I. Im, *Biochem. Biophys. Res. Commun.*, 2011, **408**, 126.
14 E. Yamachika, H. Tsujigiwa, N. Shirasu, T. Ueno, Y. Sakata, L. Fukunaga, N. Mizukawa, M. Yamada and T. Sugahara, *J. Biomed. Mater. Res., Part A*, 2009, **88**, 599.
15 T. L. Pohl, J. H. Boergermann, G. K. Schwaerzer, P. Knaus and E. A. Cavalcanti-Adam, *Acta Biomater.*, 2012, **8**, 772.
16 Y. N. Zhao, J. Zhang, X. Wang, B. Chen, Z. F. Xiao, C. Y. Shi, Z. L. Wei, X. L. Hou, Q. B. Wang and J. W. Dai, *J. Controlled Release*, 2010, **141**, 30.
17 A. Lagunas, J. Comelles, E. Martínez and J. Samitier, *Langmuir*, 2010, **26**, 14154.
18 A. Lagunas, J. Comelles, S. Oberhansl, V. Hortigüela, E. Martínez and J. Samitier, *Nanomedicine: Nanotechnology, Biology and Medicine*, 2013, **9**, 694.
19 E. Prats-Alfonso, F. Garcia-Martin, N. Bayo, L. J. Cruz, M. Pla-Roca, J. Samitier, A. Errachid and F. Albericio, *Tetrahedron*, 2006, **62**, 6876.
20 S. Oberhansl, PhD thesis, University of Barcelona, Spain, October, 2012, pp. 153–155.
21 R. Derda, L. Li, B. P. Orner, R. L. Lewis, J. A. Thomson and L. L. Kiessling, *ACS Chem. Biol.*, 2007, **2**, 347.
22 H. M. Ryoo, M. H. Lee and Y. J. Kim, *Gene*, 2006, **366**, 51.
23 M. Lehnhert, M. Gorbahn, M. Klein, B. Al-Nawas, I. Köper, W. Knoll and M. Veith, *J. Biomed. Mater. Res., Part A*, 2012, **100**, 388.

24 T. Katagiri, A. Yamaguchi, M. Komaki, E. Abe, N. Takahashi, T. Ikeda, V. Rosen, J. M. Wozeny, A. Fujisawa-Sehara and T. Suda, *J. Cell Biol.*, 1994, **127**, 1755.
25 W. Luo, E. W. L. Chan and M. N. Yousaf, *J. Am. Chem. Soc.*, 2010, **132**, 2614.
26 K. Heinecke, A. Seher, W. Schmitz, T. D. Mueller, W. Sebald and J. Nickel, *BMC Biol.*, 2009, **7**, 59.
27 T. Crouzier, L. Fourel, T. Boudou, C. Albigès-Rizo and C. Picart, *Adv. Mater.*, 2011, **23**, H111.
28 T. Kirsch, J. Nickel and W. Sebald, *EMBO J.*, 2000, **19**, 3314.
29 S. Biswas, M. Hirtz and H. Fuchs, *Small*, 2011, **7**, 2081.
30 Taken from http://www.philasim.org/newmanual/exp21.pdf, accessed, July 2012.
31 W. Knoll, M. Zizelsperger, T. Liebermann, S. Arnold, A. Badia, M. Liley, D. Piscevic, F.-J. Schmitt and J. Spinke, *Colloids Surf., A*, 2000, **161**, 115.
32 M. Laub, T. Seul, E. Schmachtenberg and H. P. Jennissen, *Mater. Sci. Eng.*, 2001, **32**, 926.
33 M. Hayashi, S. Maeda, H. Aburatani, K. Kitamura, H. Miyoshi, K. Miyazono and T. Imamura, *J. Biol. Chem.*, 2008, **283**, 565.
34 G. Tai, I. Christodoulou, A. E. Bishop and J. M. Polak, *Biochem. Biophys. Res. Commun.*, 2005, **333**, 1116.

Nano Res
DOI (automatically inserted by the publisher)
Review Article/Research Article Please choose one

Large-Scale Dendrimer-Based Uneven Nanopatterns for the Study of Local RGD Density Effects on Cell Adhesion

Anna Lagunas,(✉)[1,2] Albert G. Castaño,[2,1] Juan M. Artés,[2,3,†] Yolanda Vida,[4,5] Daniel Collado,[4,5] Ezequiel Pérez-Inestrosa,[4,5] Pau Gorostiza,[2,1,6] Silvia Claros,[7,1] José A. Andrades,[7,1] and Josep Samitier[1,2,8]

[1]Networking Biomedical Research Center in Bioengineering, Biomaterials and Nanomedicine (CIBER-BBN)
[2]Institute for Bioengineering of Catalonia (IBEC), Baldiri-Reixac 15-21, Barcelona 08028 Spain
[3]Physical Chemistry Department, University of Barcelona (UB), Martí i Franquès 1-11, Barcelona 08028 Spain
[4]Andalusian Centre for Nanomedicine and Biotechnology (BIONAND), Severo Ochoa 35, Málaga 29590 Spain
[5]Organic Chemistry Department, University of Málaga (UMA), Campus Teatinos, Málaga 29071 Spain
[6]Institució Catalana de Recerca i Estudis Avançats (ICREA)
[7]Cell Biology, Genetics and Physiology Department, University of Málaga (UMA), Campus Teatinos, Málaga 29071 Spain
[8]Electronics Department, University of Barcelona (UB), Martí i Franquès 1-11, Barcelona 08028 Spain
[†]Present address: Electrical and Computer Engineering department, University of California Davis, 95616 Davis CA

Received: day month year / Revised: day month year / Accepted: day month year (automatically inserted by the publisher)

ABSTRACT

Cell adhesion process is governed by the nanoscale arrangement of the extracellular matrix (ECM), being more affected from local than from global concentration of cell adhesive ligands. Dendrimers grafted on surfaces showed the benefits of the local increase in concentration provided by the dendritic configuration, in many cell-based studies; although the lack of any surface characterization has limited a direct correlation with dendrimer disposition and cell response. In order to establish a proper correlation, some control in dendrimer surface deposition is desirable. Here, dendrimer nanopatterning is applied to address arginine-glycine-aspartic acid (RGD) density effects on cell adhesion. Nanopatterned surfaces were fully characterized by atomic force microscopy (AFM), scanning tunneling microscopy (STM) and X-ray photoelectron spectroscopy (XPS), showing that tunable distributions of cell-adhesive ligands on the surface are obtained as a function of the initial dendrimer bulk concentration. Cell experiments showed a clear correlation with dendrimer surface layout: substrates presenting regions of high local ligand density resulted in a higher percentage of adhered cells and a higher degree of maturation of focal adhesions (FAs). Therefore, dendrimer nanopatterning is presented as a suitable and controlled approach to address the effect of local ligand density in cell response. Moreover, due to the easy modification of dendrimer peripheral groups, dendrimer nanopatterning can be further extended to other ECM ligands with density effects on cells.

KEYWORDS

Dendrimer, RGD, AFM, STM, cell adhesion, focal adhesions.

Address correspondence to Anna Lagunas. alagunas@ibecbarcelona.eu

Introduction

For an adherent cell exposed to a surface, the early steps of cell-surface interaction are mediated mainly by integrins [1,2]. These molecules are heterodimeric transmembrane proteins that recognize and become activated by certain aminoacid sequences present in the extracellular matrix (ECM) proteins. Upon integrin activation, cytoplasmic protein recruitment leads to the formation of transient focal complexes at the cell periphery. These complexes can disassemble or eventually evolve into mature focal adhesions (FAs) that link to the cytoskeleton and mediate strong adhesion to the substrate [3]. Like many cell membrane receptors that aggregate into clusters to produce sustained signaling effects [4], integrin clustering is required for transient focal complexes to grow into mature FAs. The clustering of integrins and thus cell adhesion is governed mainly by the physiological arrangement of the ECM [5-7].

Experimental evidence of ECM organization at the nanoscale steered the production of synthetic nanopatterned surfaces directed towards identifying the geometric cues that initiate and guide cell adhesion [8,9]. Nanopatterning of ECM motives for the study of cell-surface interactions at the nanoscale highlighted the relevance of ECM ligand presentation to cells on receptor clustering, with cell-adhesion being favored more from local than from global ligand concentrations [10-12]. In that sense, dendritic molecules presenting a highly branched and easily tunable size and chemical structure emerged as ideal scaffolds for the construction of surfaces devoted to the study of ligand density effects on cells. Dendrimers grafted onto surfaces, and in situ modified through their peripheral groups for specific cell interactions [13-15], showed the benefits of the local increase in ligand density in cell adhesion [16,17], morphology [18,19], and migration events [20]. Griffith and co-workers presented the first systematic study on the effects of ECM ligand clustering on cell adhesion and migration [21]. They used star polyethylene oxide tethers modified with the adhesion ligand YGRGD to demonstrate that cell motility can be varied by regulating nanoscale ligand density, with a clustered presentation enhancing cell migration speeds. The main drawback in this study is the lack of any surface characterization on ligand disposition.

In order to facilitate the correlation between ligand surface disposition and cell response, it is desirable to exert some degree of control on the deposition of dendrimers on the surface. For sufficient low-charged surfaces, dendrimers can be patterned on the nanometer scale in a liquid-like order with large and well-defined spacing at low ionic strengths [22]. Dendrimer adsorption onto surfaces has been extensively studied and addressed through different surface characterization techniques such as fourier transform infrared-external reflection spectroscopy (FTIR-ERS) and ellipsometry [23], atomic force microscopy (AFM) [24,25], and scanning tunneling microscope (STM)[26] among others. Here, dendrimer nanopatterning is applied for the first time to create uneven distributions of the cell adhesive motive arginine-glycine-aspartic acid (RGD) to address nanoscale ligand density effects on cell adhesion. In contrast with other nanopatterning techniques [8], due to its simplicity, dendrimer nanopatterning can be straightforwardly scaled up to large surface areas, therefore being fully compatible with cell culture protocols. Surfaces derived from RGD-tailored dendrimers nanopatterning were fully characterized by AFM, STM and x-ray photoelectron spectroscopy (XPS). Surface analysis showed that tunable local ligand densities were obtained as a function of the initial bulk concentration. Cell experiments showed that dendrimer nanopatterns sustained cell adhesion and were preferential sites to establish the first cell-substrate interactions. Results demonstrated that dendrimers can mediate integrin clustering at high surface local RGD densities, leading to the formation of mature FAs. Dendrimer nanopatterning is therefore presented as a suitable approach for the study of RGD presentation on cell adhesion process and, due to the easy modification of the peripheral chemical groups in dendrimers, it can be further extended to other ECM ligands with clustering effects on cells.

1. Experimental

1.1 Dendrimer nanopatterning on Au(111) substrates

Deionized water (18 MΩ cm^{-1} Milli-Q, Millipore) was used to prepare all solutions and for rinsing samples. Surface nano-patterning was conducted as previously described [22,26] by immersing flame-annealed 1.4x1.1 cm Au(111) on mica substrates (Spi Supplies) on aqueous solutions of the RGD-tailored dendrimer RGD-Cys-D1 (see Electronic Supplementary Material (ESM) for RGD-Cys-D1 synthesis details) for 16 h (pH = 5.6, T = 293K). All solutions were sonicated and filtered (MILLEX RB Filter Sterile, Millipore) previously. Dendrimer stock solution was used within 6 months of preparation. RGD-Cys-D1 nanopatterning was followed by copious rinsing with water and drying with argon.

1.2 Patterning imaging and data analysis.

Nanopatterned substrates were imaged by AFM in a Dimension 3100 AFM instrument (Veeco Instruments) operated in tapping mode in air. Silicon AFM probes (Budget Sensors) with a spring constant k = 40 N/m and a resonant frequency ν = 300 kHz were used. Image thresholds were obtained manually from AFM height images and processed with Image J 1.44p freeware (http://imagej.nih.gov/ij). Particle positions were used to obtain minimum inter-particle distances (d_{min}) using a custom-generated MATLAB code (The MATHWORKS, Inc.; ESM). d_{min} values were analyzed with OriginPro 8.5.0 SR1 (OriginLab Corp.). Mean minimum inter-particle spacing was obtained from fitting the resulting d_{min} distributions to a lognormal model (Figure S2 in ESM). At least four images were computed per sample in two independent experiments.

Probability contour plots for d_{min} were constructed from d_{min} values for each particle position and plotted in zeta using an adapted MATLAB code from http://www.eng.cam.ac.uk/help/tpl/programs/Matlab/matlabbyexample/ (see ESM). Threshold images were superimposed for clarity.

STM measurements in air were carried out in a PicoSPM microscope (Molecular Imaging) controlled by Dulcinea electronics (Nanotec Electronica) using WSxM 4.0 software [27]. Etched Pt0.8:Ir0.2 probes with a diameter of 0.25 mm were used (Agilent Technologies).

1.3 Preparation of control substrates.

Homogeneously modified substrates were prepared by immersing flame-annealed Au(111) substrates in a solution of RGD-PEG-SH and triethylene glycol mono-11-mercaptoundecyl ether (PEG-SH) from Sigma-Aldrich at a 1:100 molar ratio in 96% ethanol (Panreac) for 16 h at room temperature. RGD-PEG-SH was kindly supplied by Prof. F. Albericio's group at the Institute for Research in Biomedicine (IRB, Barcelona, Spain) [28]. Polyethylene glycol passivated substrates were prepared by immersion of flame-annealed Au(111) substrates in a 1 mM solution of PEG-SH in 96% ethanol for 16 h at room temperature. After incubation, substrates were thoroughly washed in ethanol and dried with argon. All solutions were sonicated and filtered prior to substrate incubation.

1.4 Cell culture and fluorescent staining.

All steps, including work on the cell culture, were performed in a sterile laminar flow hood, and only sterile materials, solutions and techniques were used. All cell culture reagents were purchased from Invitrogen S. A. NIH 3T3 mouse embryonic fibroblasts from passages 8-9 were cultured at 37 ºC and 10% CO_2 in Dulbecco's Modified Eagle Medium (D-MEM) liquid high glucose supplemented with 10% FBS, 1% L-glutamine, 1% penicillin-streptomycin and 1% sodium pyruvate. The medium was exchanged every second day. Nanopatterned surfaces were incubated in PBS for 15 min prior to use. After trypsinization, cells were seeded at a cell density of 4000 cells/cm^2 in D-MEM liquid high glucose supplemented with 1% FBS 1% L-glutamine, 1% penicillin-streptomycin and 1% sodium pyruvate, and incubated for 4.5 h at 37 ºC and 10% CO_2. Control experiments with homogeneously modified, polyethylene glycol-passivated and bare Au(111) substrates were performed. Post-incubation, non-adherent cells were removed by a gentle wash with PBS and the attached

cells were fixed with a 10% neutral buffered formalin solution from Sigma-Aldrich for 20 min and then washed with PBS. The remaining free aldehyde groups were blocked with 50 mM amonium chloride (NH_4Cl) from Merk Sharp & Dohme in PBS for 20 min at room temperature. Afterwards, samples were washed with PBS, and cells were permeabilized with a solution of 0.1% saponin (Fluka) in 1% BSA from Sigma-Aldrich in PBS for 10 min at room temperature. To visualize focal adhesions (FAs) and cell cytoskeleton actin fibers, rabbit monoclonal anti-paxillin [Y113] (Abcam) diluted 1:200 and phalloidin-FITC (0.5 mg/mL) from Sigma-Aldrich diluted 1:500 in 1% BSA in PBS were added and cells were incubated for 1 h at room temperature. Cells were washed with PBS and incubated for 1 h at room temperature with the secondary antibody goat anti-rabbit IgG (H+L) ALEXA FLUOR 568 (2 mg/ml) and Hoechst (10 mg/ml) for cell nuclei staining, both from Invitrogen S. A. and diluted 1:1000 in 1% BSA in PBS. After incubation, cells were washed with PBS, and samples mounted with FLUOROMOUNT aqueous mounting medium (Sigma-Aldrich).

1.5 Cell imaging and data analysis.

Cells were imaged by fluorescence microscopy with an Eclipse E1000 upright microscope (Nikon) equipped with a CCD camera and working with a green excitation G-2A long-pass emission filter for paxillin visualization, a FITC filter for actin fibers and a UV emission filter for cell nuclei.
In fluorescent micrographs, the number of adhered cells was identified by stained nuclei, and paxillin immunostaining was used to determine the size and number of FAs. ImageJ freeware image analysis was used for quantification. In cell adhesion experiments, 15 images with the 10X objective were computed per sample. For FA quantification, images corresponding to paxillin staining were converted to 8-bit files. The background was removed (rolling bar radius 10), and the resulting images were converted to binary by setting a threshold. Threshold values were determined empirically, and FAs were considered from 1 μm^2. A minimum of 30 cells per sample were analyzed.

1.6 Statistics.

At least three independent experiments were performed per sample with different cell batches. Quantitative data are displayed, showing average and standard error of the mean. Significant differences were judged using Student T-test with a *t* value of less than 0.05 considered statistically significant.

2. Results and Discussion

2.1 Nanopaterning of RGD-Cys-D1 dendrimers and characterization of surface disposition

Water-soluble polyamidoamine (PAMAM) G1 dendrimers were chosen to construct nanoscale cell adhesive clusters. The use of low generation PAMAM dendrimers (less than G5) is preferred since they have proven more biocompatible and less immunogenic than high generation ones [29]. In order to make dendrimers compatible with cell-based experiments and trigger cell adhesion, the primary amine surface groups on the outermost layer of the PAMAM dendrimers were functionalized with the cell adhesive linear RGD polypeptide (see ESM). PAMAM dendrimer-RGD peptide conjugates were synthesized as depicted in Scheme 1.
The maleimido-functionalized generation-1 PAMAM dendrimer was reacted chemoselectively with a single cysteine (Cys) at the C-terminus of RGD, by adapting a previously described procedure [30,31], to generate RGD-Cys-D1, which assembles eight copies of the RGD peptide.

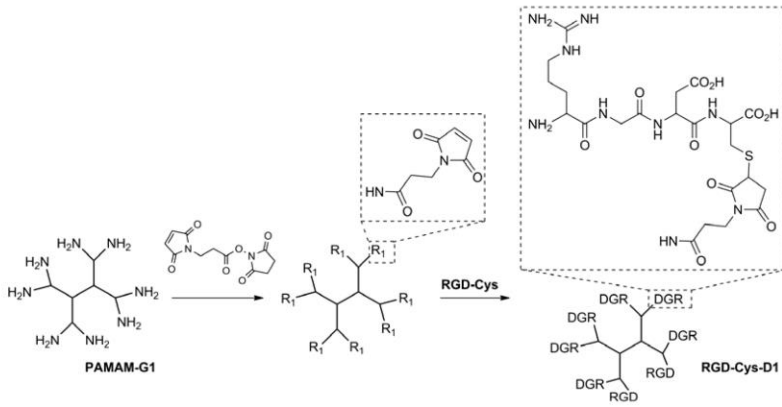

Scheme 1 Synthesis of RGD-Cys-D1 from PAMAM G1.

RGD-Cys-D1 dendrimers were patterned onto flame annealed Au(111) substrates by immersion in aqueous solutions of RGD-Cys-D1 of 10^{-8}- 10^{-2}% w/w concentration for 16 h (pH = 5.6, and T = 293K). The resulting, dendrimer nanopatterns were imaged by AFM and STM in air. For low bulk concentrations, up to 10^{-5} % w/w, isolated dendrimers of 4-5 nm in diameter can be observed (Fig. 1).

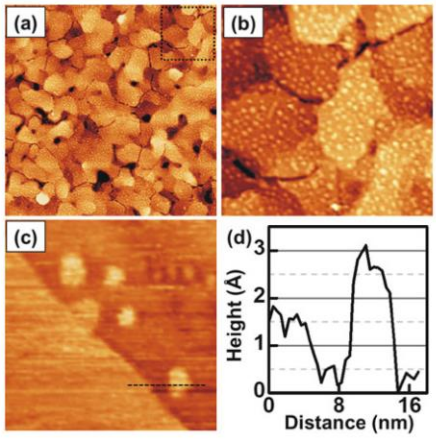

Figure 1 Surface characterization of RGD-Cys-D1 dendrimer nanopatterns on Au(111) with AFM and STM in air. (a) 5x5 μm representative AFM image obtained when patterning was conducted from a bulk concentration of 10^{-5}% w/w. (b) zoom-in from the dashed region in (a). (c) STM image obtained on nanopatterns from an initial bulk concentration of 10^{-8}% w/w (45x45 nm, Bias = 200 mV, Set point = 0.5 nA) and (d) height-distance profile obtained on the dashed region indicated in (c).

Minimum interparticle distances (d_{min}) obtained from AFM image thresholds (Fig. 2 and Fig. S2 in the ESM) were used to characterize the local density on the surface. Since dendrimers are unevenly distributed, individual inter-dendrimer spacing or even the mean inter-dendrimer spacing values calculated here from d_{min} distribution fittings (Fig. 2(b)) are not suitable to describe the local density [32]. Therefore, d_{min} values obtained for each particle position are plotted in zeta to construct the probability contour plots for d_{min} shown in Fig. 2(c) where high density RGD regions are highlighted. As shown in Figure 2(c), slight variations in the mean interligand spacing caused an abrupt increase of denser ligand regions. If we consider RGD-Cys-D1 dendrimers separated less than 70 nm, the percentage of dense areas increase from 7%, for surfaces derived from 10^{-8}% w/w bulk concentration, to 79%, for surfaces derived from 10^{-5}% w/w bulk concentration.

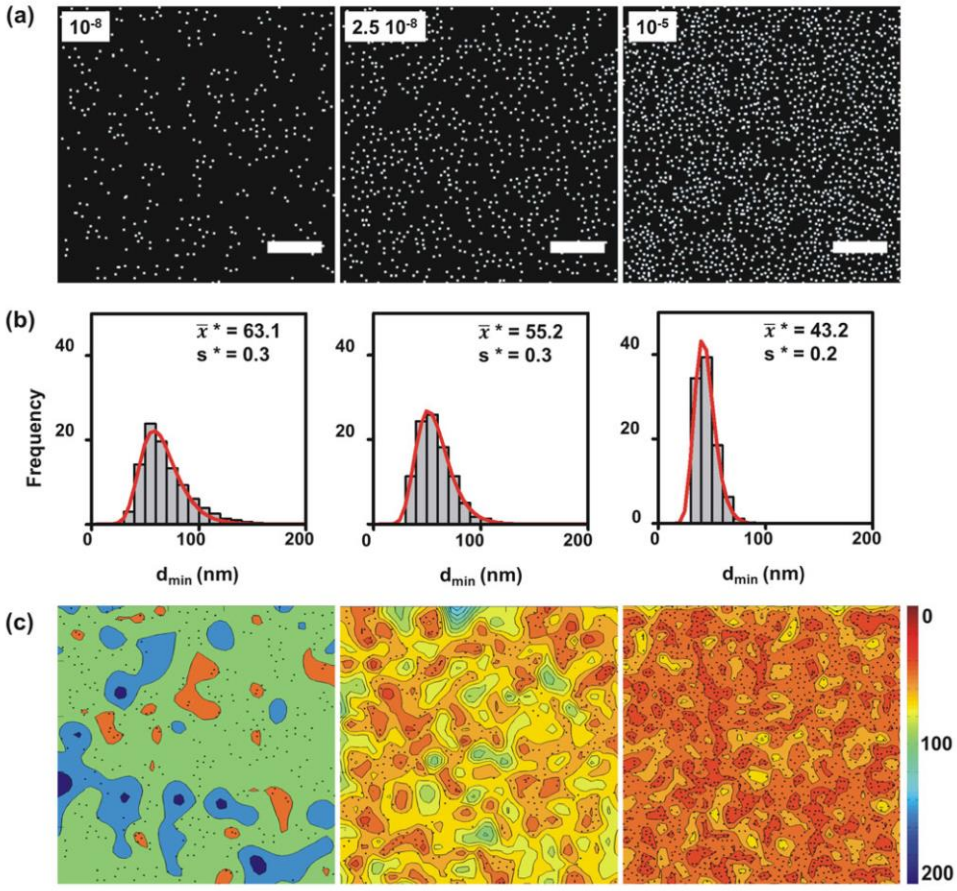

Figure 2 Nanopatterning of RGD-Cys-D1 on Au(111) surfaces. (a) Representative AFM image thresholds obtained from 10^{-8}, 2.5 10^{-8}, and 10^{-5} % w/w RGD-Cys-D1 bulk concentrations. Scale bar = 500 nm. (b) Minimum inter-particle distance (d_{min}) distributions. 63.1, 55.2 and 43.2 nm are the mean values of the shown distributions (s* stand for the standard deviation). The calculated minimum inter-particle distances for the corresponding ordered patterns are 117, 97, and 66 nm, respectively (c) Corresponding d_{min} probability contour plots obtained from images in (a) (superimposed). Color scale corresponds to d_{min} values in nanometers.

Patterning from high bulk concentrations, 10^{-2}% w/w for 16 h, resulted in dendrimer aggregation. AFM images (Fig. 3(a)) showed the presence of elongated structures with an estimated average size of 650 nm^2 (Fig. S3). High magnification images taken by means of scanning tunneling microscope (STM) revealed that these structures contained dendrimers assembled in a close-packed configuration (Fig. 3(b)). In order to elucidate whether aggregation occurred in solution or was a result of a surface-induced reorganization process, zeta potential was measured in the initial bulk RGD-Cys-D1 dendrimer solutions (Fig. S4 in the ESM). A zeta potential of -3.03 mV was recorded for the 10^{-2}% w/w bulk concentration,

indicating that for such high initial concentration, solution instability may lead to dendrimer aggregation and the subsequent deposition of the formed aggregates on the surface. The d_{min} probability contour plot (Fig. 3(d)) constructed from the threshold image in Fig. 3(c), showed that aggregation not only caused an increase of the local RGD density as expected but also increased the heterogeneity of the samples in terms of ligand distribution, if compared with nanopatterned surfaces from lower bulk concentrations.

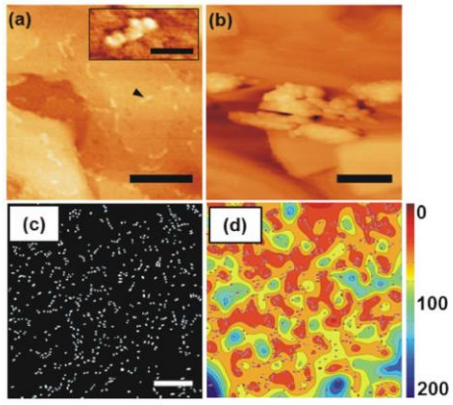

Figure 3 RGD-Cys-D1 nanopatterning on Au(111) surfaces from 10^{-2}% w/w bulk concentration. (a) AFM tapping image (scale bar = 250 nm) showing the presence of dendrimer aggregates. The inset corresponds to the magnified phase image of one of the aggregates (scale bar = 50 nm). (b) High magnification image of aggregates obtained by STM (scale bar = 50 nm). (c) AFM image threshold, scale bar = 500 nm and (d) the corresponding d_{min} probability contour plot. Aggregates are superimposed in dark red pointing out that they are points of high ligand density. Color scale corresponds to d_{min} values in nanometers. The calculated percentage of dense areas with particles (dendrimer aggregates) separated less than 70 nm is 28%.

2.2 Cell adhesion on dendrimer nanopatterns

Since the diameter of integrins in the cell membrane is around 10 nm [33] each dendrimer of 4-5 nm in diameter, although providing up to eight copies of the cell-adhesive RGD ligand, resulted in a single site for integrin binding [35]. Using dendrimer nanopatterning, a set of substrates of unevenly distributed RGD molecules with tunable local ligand density was obtained. Cell adhesion experiments were performed with NIH 3T3 mouse embryonic fibroblasts seeded at 4000 cells/cm^2 for 4.5 h. Serum starvation conditions were maintained at 1% of fetal bovine serum during the experiment in order to highlight the effect of the substrate [21]. Fluorescent micrographs of adhered cells on the samples were taken after cell fixation and nuclei staining (Fig. 4a). In this case, ready-to-use substrates were obtained, with no further passivation step required, as demonstrated by the percentage of adhered cells obtained for the negative controls (bare Au(111) and polyethylene glycol (PEG-SH) passivated Au(111) substrates; Fig. 4(b)). The low percentage of adhered cells observed in Au(111) substrates can be attributed to the well-known gold-induced protein denaturation effect [35]. Therefore, cell interactions with the nanopatterned surfaces could be attributed solely to RGD-Cys-D1-cell receptor interactions, without any passivation step that can mask the specific influence of the patterns on cell guidance [36].The percentage of adhered cells obtained from a bulk concentration of 10^{-8}% w/w, which was lower than of the negative controls, confirm that dendrimers are preferential sites to establish the first cell-substrate interactions, and pointed out that RGD clustering effect when provided solely by the dendritic conformation is in this case, not enough to reach high percentages of cell adhesion. This is in agreement with previous reports suggesting that a coverage limit of high density ligand regions is necessary in order to generate a sufficient cell response [11,21,38]. As the bulk concentration increased, the percentage of seeded cells adhered to the substrate after 4.5 h of incubation increased to 80% for a bulk concentration of 10^{-5}% w/w. Similar adhesion was obtained when dendrimers were presented as high density aggregates on the surface. In both cases statistical analysis showed that adhesion was significantly higher than in the homogeneously modified RGD-PEG-SH substrates (Fig. 4(b)). Since this finding could be attributed to an effect of global ligand density, we measured the elemental composition of the surface by XPS (see ESM). The atomic percentage of sulfur directly correlates with the number of RGD molecules, which differed between dendrimers and homogeneous

films. The sulfur/gold ratio was found to be very similar for substrates derived from 10^{-5} and 10^{-2}% bulk concentrations, resulting in 0.04±0.02 and 0.03±0.02, respectively; while much higher values were found for homogeneous surfaces, with a sulfur/gold ratio of 0.20±0.03. These observations indicate that uneven distributions of RGD obtained through RGD-Cys-D1 dendrimer nanopatterning sustain cell adhesion more efficiently than the corresponding homogeneous surfaces and highlight the relevance of local ligand density.

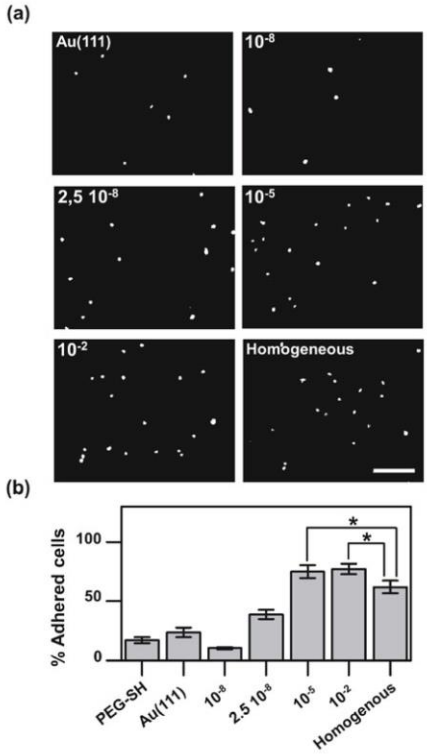

Figure 4 Cell adhesion on RGD-Cys-D1 nanopatterned Au(111) substrates after 4.5 h incubation with a range of bulk concentrations compared with that achieved on Au(111) and homogeneously modified surfaces. (a) Representative fluorescent microscopy images of cell nuclei stained with Hoechst. Scale bar = 200 μm. (b) Percentage of adhered cells presented as the mean with the standard error.

2.3 RGD-Cys-D1 nanopattern influence on FA formation and maturation

Since cell-matrix junctions are strongly influenced by local ligand density [12], we examined FA formation. The signal transduction adaptor protein paxillin, which is involved in FA formation from its early stages [38] was fluorescently labeled and monitored at high magnification (Figure 5a). No mature FAs developed below a bulk concentration of 2.5 10^{-8}% w/w (Figure 5b). This is in agreement with results reported by Cavalcanti-Adam et al. [39], who found that FA dynamics is significantly delayed in overlarge inter-ligand spacing. Here, the absence of high density RGD regions in surfaces produced from bulk concentrations below 2.5 10^{-8}% w/w. In such surfaces, the weak cell to surface interaction may favor easy cell detachment which can also contribute to the low percentage of adhered cells obtained (Fig. 4). Accordingly, an increase of bulk concentration to 10^{-5}% w/w, and hence an increase of local RGD density, increased the number of mature FAs. Substrates derived from 10^{-2}% w/w bulk concentration rendering high density dendrimer aggregates resulted in a reduced number of FAs per cell compared to the number achieved from 10^{-5}% w/w, but much larger FA areas. XPS results (sulfur/gold ratio of 0.04±0.02, 0.03±0.02 for 10^{-5} and 10^{-2}% w/w bulk concentrations, respectively) showed that samples derived from 10^{-5} and 10^{-2}% w/w bulk concentrations presented a similar amount of RGD on their surfaces. However, the area covered with high surface particle density ($d < 70$ nm) is very different in both cases. Therefore, the observed cell behavior should be due to the RGD local distribution in each case. With fewer cell adhesive anchor points, 10^{-2}% bulk concentration derived surfaces made cells develop a lower number of FAs than in 10^{-5}% w/w bulk concentration derived ones but, as predicted by Cavalcanti-Adam et al. [39], the increased local ligand density when aggregation occurs, caused FA maturation to be favored for 10^{-2}% w/w vs. 10^{-5}% w/w surfaces for the same period of time. These

results are also supported by theoretical studies on integrin-ligand binding performed by Irvine et al. [40] which revealed that an increase in local ligand density enhances ligand-receptor affinity of neighboring integrins, thus favoring receptor clustering and reinforcing cell adhesion. In addition, Comisar et al. [41], using an integrin binding/clustering model, obtained that integrin cluster size is increased with increasing RGD distribution heterogeneity.

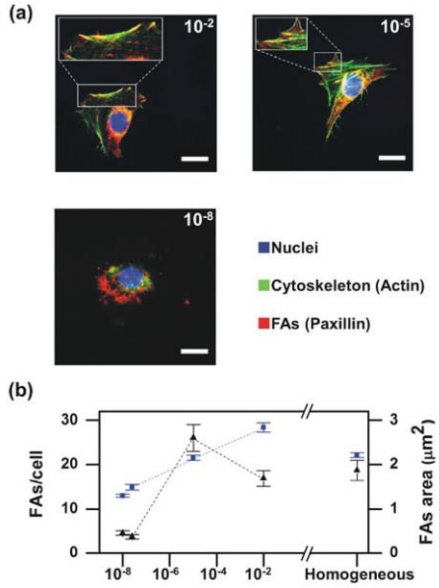

Figure 5 (a) Fluorescent micrographs of representative cells after 4.5 h in culture on the corresponding substrates. Insets show the magnified portion of FAs formed at the cell periphery. Scale bar = 20 μm. (b) Plot of the number of FAs per cell (black triangles) and FA area (blue squares) obtained from various bulk concentrations (logarithmic scale) and from the homogeneous surface (FAs were considered from 1 μm^2. The error bars correspond to the standard errors of the mean. Dashed lines are eye guides).

3. Conclusions

Dendrimer nanopatterning approach is presented to address RGD local density effects on cell adhesion. To this end, PAMAM G1 dendrimers had been chemically modified with the cell adhesive RGD peptide, in a way that each dendrimer assembled eight copies of RGD, and patterned on Au(111) substrates. AFM and STM surface analysis showed that RGD-tailored dendrimers are unevenly distributed on the surface and that tunable local RGD densities were obtained as a function of the initial bulk concentration. Probability contour plots for the minimum interparticle distance (d_{min}) were constructed from AFM images to visualize the surface high density RGD regions. Surface imaging also showed that dendrimer aggregate deposition took place at high initial bulk concentrations (10^{-2}% w/w) as a result of solution instability. Cell adhesion experiments demonstrate that dendrimer-based nanopatterns sustained cell adhesion, and provided cell guidance for the first cell to substrate interactions. Dendrimers assist FA assembly and maturation at high local RGD surface densities. Our results point out the relevance of surface local ligand density particularly in the case of dendrimer aggregates. If compared to 10^{-5}% bulk concentration, with a similar value of surface ligand density, the higher degree of segregation in 10^{-2}% derived surfaces, resulted in fewer but more mature FAs.

In conclusion, dendrimer nanopatterning has been successfully applied to the study of surface RGD presentation on cell adhesion studies, which were supported with an in detail surface characterization. Moreover, the versatility introduced by dendrimers which include a facile chemical modification of their peripheral groups and an easy tunable size, makes dendrimer nanopatterning suitable to be extended to the study of other ECM ligands with clustering effects on cells.

Acknowledgements

Authors thank Professor A. Hari Reddi for fruitful discussions and M. López for help in STM measurements. Authors also thank M. Sanmartí for its help in Zeta potential measurements. This work was supported by Centro de Investigación Biomédica en Red en Bioingeniería, Biomateriales y Nanomedicina (CIBER-BBN), Spain; the Nanobioengineering group at the Institute for Bioengineering of Catalonia (IBEC) receives support from the Commission for Universities and Research of the Department of Innovation, Universities and Enterprise of the Generalitat de Catalunya (2009 SGR 505). In addition, research leading to these results received support from the Spanish Ministry of Science and Education; Ministry of Economy and Competitiveness (Red TerCel; FIS PI10/02529); the Andalusian Government (P07-CVI-2781, PAIDI BIO-217, PI-0729-2010); Fundación Botín, Santander, Spain; CICYT (CTQ2009-07758; CTQ2010-20303); Commission for Universities and Research of the Department of Innovation, Universities and Enterprise of the Generalitat de Catalunya (2009 SGR 505).

Electronic Supplementary Material: further details of the synthesis and characterization of RGD-Cys-D1 dendrimers, detailed MATLAB code for d_{min} calculation and the corresponding probability contour plots construction, d_{min} calculation and cluster size estimation from AFM images and Zeta potential measurements and detailed XPS experimental are available in the online version of this article.

References

[1] Mager, D. M.; LaPointe, V.; Stevens, M. M. Exploring and Exploiting Chemistry at the Cell Surface. *Nat. Chem.* **2011**, *3*, 582-589.

[2] Geiger, B.; Spatz, J. P.; Bershadsky, A. D. Environmental Sensing Through Focal Adhesions. *Nat. Rev. Mol. Cell Biol*. **2009**, *10*, 21-33.

[3] Geiger, B.; Bershadsky, A.; Pankov, R.; Yamada, K. Transmembrane Extracellular Matrix–Cytoskeleton Crosstalk. *Nat. Rev. Mol. Cell Biol*. **2001**, *2*, 793-804.

[4] Vogel, V.; Sheetz, M. Local Force and Geometry Sensing Regulate Cell Functions. *Nat. Rev. Mol. Cell Biol*. **2006**, 7, 265-275.

[5] Smith, M. L.; Gourdon, D.; Little, W. C.; Kubow, K. E., Eguiluz, R. A.; Luna-Morris, S.; Vogel, V. Force-Induced Unfolding of Fibronectin in the Extracellular Matrix of Living Cells. *PLoS Biol.* **2007**, *5*, 2243-2254.

[6] Jiang, F.; Hörber, H.; Howard, J.; Müller, D. J. Assembly of Collagen into Microribbons: Effects of pH and Electrolytes. *J. Struct. Biol.* **2004**, *148*, 268-278.

[7] Abrams, G. A.; Goodman, S. L.; Nealey, P. F.; Franco, M.; Murphy, C. J. Nanoscale Topography of the Basement Membrane Underlying the Corneal Epithelium of the Rhesus Macaque. *Cell Tissue Res.* **2000**, *299*, 39-46.

[8] Christman, K. L.; Enriquez-Rios, V. D.; Maynard, H. D. Nanopatterning Proteins and Peptides. *Soft Matter* **2006**, *2*, 928-939.

[9] Falconnet, D.; Csucs, G.; Grandin, H. M.; Textor, M. Surface Engineering Approaches to Micropattern Surfaces for Cell-based Assays. *Biomaterials* **2006**, *27*, 3044-3063.

[10] Arnold, M.; Schwieder, M.; Blümmel, J.; Cavalcanti-Adam, E. A.; López-Garcia, M.; Kessler, H.; Geiger, B.; Spatz, J. P. Cell interactions with hierarchically structured nano-patterned adhesive surface. *Soft Matter*. **2009**, *5*, 72-77.

[11] Malmström, J.; Christensen, B.; Jakobsen, H. P.; Lovmand, J.; Foldbjerg, R.; Sorensen, E. S.; Sutherland, D. S. Large area protein patterning reveals nanoscale control of focal adhesion development. *Nano Lett.* **2010**, 10, 686-694.

[12] Deeg, J. A.; Louban, I.; Aydin, D.; Selhuber-Unkel, C.; Kessler, H.; Spatz, J. P. Impact of local versus global ligand density on cellular adhesion. *Nano Lett.* **2011**, *11*, 1469-1476.

[13] Rolland, O.; Turrin, C.-O.; Caminade, A.-M.;Majoral, J. P. Dendrimers and nanomedicine: multivalency in action. *New J. Chem*. **2009**, *33*, 1809-1824.

[14] Saovapakhiran, A.; D'Emanuele, A. Attwood, D.; Penny, J. Surface modification of PAMAM dendrimers modulates the mechanism of cellular internalization. *Bioconjugate Chem*. **2009**, *20*, 693-701.

[15] Albertazzi, L.; Fernandez-Villamarin, M.; Riguera, R.; Fernandez-Megia, E. Peripheral functionalization of dendrimers regulates internalization and intracelular trafficking in living cells. *Bioconjugate Chem*. **2012**, *23*, 1059-1068.

[16] Mikhail, A. S.; Jones, K. S.; Sheardown, H. Dendrimer-grafted cell adhesion peptide-modified PDMS. *Biotechnol. Prog*. **2008**, *24*, 938-944.

[17] Kino-oka, M.; Kim, J.; Kurisaka, K.; Kim, M.-H. Preferential growth of skeletal myoblasts and fibroblasts in co-culture on a dendrimer-immobilized surface. *J. Biosci. Bioeng.* **2013**, *115*, 96-99.

[18] Lomba, M.; Oriol, L.; Sánchez-Somolinos, C.; Grazú, V.; Moros, M.; Serrano, J. L.; Martínez De la Fuente, J. Cell adhesión on surface patterns generated by the photocrosslinking of hyperbranched polyesters with a trisdiazonium salt. *React. Funct. Polym*. **2013**, *73*, 499-507.

[19] Kim, M. –H.; Kino-oka, M.; Morinaga, Y.; Sawada, Y.; Kawase, M.; Yagi, K.; Taya, M. Morphological regulation and aggregate formation of rabbit chondrocytes on dendrimer-immobilized surfaces with D-glucose display. *J. Biosci. Bioeng.* **2009**, *107*, 196-205.

[20] Kim, M. –H.; Kino-oka, M.; Kawase, M.; Yagi, K.; Taya, M. Synergistic effect of D-glucose and epidermal growth factor display on dynamic behaviors of human epithelial cells. *J. Biosci. Bioeng.* **2007**, *104*, 428-431.

[21] Maheshwari, G.; Brown, G.; Lauffenburger, D. A.; Wells, A.; Griffith, L. G. Cell adhesion and motility depend on nanoscale RGD clutering. *J. Cell Sci.* **2000**, *113*, 1677-1686.

[22] Pericet-Camara, R.; Cahill, B. P.; Papastavrou, G.; Borkovec, M. Nano-patterning of Solid Substrates by Adsorbed Dendrimers *Chem. Commun.* **2007**, *3*, 266-268.

[23] Tokuhisa, H.; Zhao, M.; Baker, L. A.; Phan, V. T.; Dermody, D. L.; Garcia, M. E.; Peez, R. F.; Crooks, R. M.; Mayer, T. M. Preparation and characterization of dendrimer monolayers and dendrimer-alkanethiol mixed monolayers adsorbed to gold. *J. Am. Chem. Soc.* **1998**, *120*, 4492-4501.

[24] Pericet-Camara, R.; Papastavrou, G.; Borkovec, M. Atomic force microscopy study of the adsorption and electrostatic self-organization of poly(amidoamine) dendrimers on mica. *Langmuir*, **2004**, *20*, 3264-3270.

[25] Li, J.; Piehler, L. T.; Qin, D.; Baker, J. R.; Tomalia, D. A. Visualization and characterization of poly(amidoamine) dendrimers by atomic force microscopy. *Langmuir*, **2000**, *16*, 5613-5616.

[26] Mertz, L.; Hitz, J.; Hubler, U.; Weyermann, P.; Diederich, F.; Murer, P.; Seebach, D.; Widmer, I.; Stöhr, M.; Güntherodt, H. –J. STM investigation on single, physisorbed dendrimers. *Single Mol.* **2002**, *5*, 295-299.

[27] Horcas, I.; Fernández, R.; Gómez-Rodríguez, J. M.; Colchero, J.; Gómez-Herrero, J.; Baro, A. M. WSXM: A Software for Scanning Probe Microscopy and a Tool for Nanotechnology. *Rev. Sci. Instrum.* **2007**, *78*, 13705-13713.

[28] Prats-Alfonso, E.; García-Martín, F.; Bayo, N.; Cruz, L. J.; Pla-Roca, M.; Samitier, J.; Errachid, A.; Albericio, F. Facile Solid-phase Synthesis of Biotinylated Alkyl Thiols. *Tetrahedron* **2006**, *62*, 6876-6881.

[29] Boas, U.; Heegaard, P. M. H. Dendrimers in Drug Research. *Chem. Soc. Rev.* **2004**, *33*, 43-63.

[30] Zhou, M.; Bentley, D.; Ghosh, I. Helical Supramolecules and Fibers Utilizing Leucine Zipper-Displaying Dendrimers. *J. Am. Chem. Soc.* **2004**, *126*, 734-735.

[31] Zhou, M.; Ghosh, I.; Noncovalent Multivalent Assembly of Jun Peptides on a Leucine Zipper Dendrimer Displaying Fos Peptides. *Org. Lett.* **2004**, *20*, 3561-3564.

[32] Huang, J.; Gräter, S. V.; Corbellini, F.; Rinck, S.; Bock, E.; Kemkemer, R.; Kessler, H.; Ding, J.; Spatz, J. P. Impact of order and disorder in RGD nanopatterns on cell adhesion. *Nano Lett.* **2009**, *9*, 1111-1116.

[33] Xiong, J-P.; Stehle, T.; Zhang, R.; Joachimiak, A.; Frech, M.; Goodman, S. L.; Arnaout, M. A. Crystal Structure of the Extracellular Segment of Integrin αVβ3 in Complex with an Arg-Gly-Asp Ligand. *Science* **2002**, *296*, 151-155.

[34] Arnold, M.; Cavalcanti-Adam, E. A.; Glass, R.; Blümmel, J.; Eck, W.; Kantlehner, M.; Kessler, H.; Spatz, J. P. Activation of integrin function by nanopatterned adhesive interfaces. *ChemPhysChem*. **2004**, *5*, 383-388.

[35] Liu, L.; Chen, S.; Giachelli, C. M.; Ratner, B. D.; Jiang, S. Controlling Osteopontin Orientation on Surfaces to Modulate Endothelial Cell Adhesion. *J. Biomed. Mater. Res.* **2005**, *74A*, 23-31.

[36] Tatkiewicz, W. I.; Seras-Franzoso, J.; García-Fruitós, E.; Vazquez, E.; Ventosa, N.; Peebo, K.; Ratera, I.; Villaverde, A.; Veciana, J. Two-dimensional microscale engineering of protein-based nanoparticles for cell guidance. *ACS Nano* **2013**, *7*, 4774-4784.

[37] Lehnert, D.; Wehrle-Haller, B.; David, C.; Welland, U.; Ballestrem, C.; Imhol, B. A.; Bastmeyer, M. Cell behavior on micropatterned substrata: limits of extracellular matrix geometry for spreading and adhesion. *J. Cell Sci.* **2004**, *117*, 41-52.

[38] Schaller, M. D. Paxillin: a Focal Adhesion-associated Adaptor Protein. *Oncogene* **2001**, *20*, 6459-6472.

[39] Cavalcanti-Adam, E. A.; Volberg, T.; Micoulet, A.; Kessler, H.; Geiger, B.; Spatz, J. P. Cell Spreading and Focal Adhesion Dynamics Are Regulated by Spacing of Integrin Ligands. *Biophys. J.* **2007**, *92*, 2964-2974.

[40] Irvine, D. J.; Hue, K-A.; Mayes, A. M.; Griffith, L. G. Simulations of Cell-Surface Integrin Binding to Nanoscale-Clustered Adhesion Ligands. *Biophys. J.* **2002**, *82*, 120-132.

[41] Comisar, W. A.; Mooney, D. J.; Linderman, J. J. Integrin organization: linking adhesion ligand nanopatterns with altered cell responses. *J. Theor. Biol.* **2011**, *274*, 120-130.